ABSTRACT

Title of Dissertation: A COMPARISON OF LONGITUDINAL AND TRANSVERSE CROSS SECTIONS IN THE p(e,e′K$^+$)Λ and p(e,e′K$^+$)Σ^0 REACTIONS

Richard Matthew Mohring, Doctor of Philosophy, 1999

Dissertation directed by: Professor Elizabeth J. Beise
Department of Physics

Jefferson Lab Experiment E93-018 measured kaon electroproduction on hydrogen in two hyperon channels, p(e,e′K$^+$)Λ and p(e,e′K$^+$)Σ^0. Data in both channels were taken at three (3) different values of the virtual photon transverse linear polarization, ϵ, for each of four (4) values of Q^2 = (0.52, 0.75, 1.00, 2.00) GeV^2. Cross sections averaged over the azimuthal angle, ϕ, were extracted (i.e., $\sigma_T + \epsilon\sigma_L$) at each of these twelve points for each hyperon. Rosenbluth separations were performed to separate the longitudinal and transverse production cross sections.

A COMPARISON OF LONGITUDINAL AND TRANSVERSE CROSS SECTIONS IN THE $p(e,e'K^+)\Lambda$ and $p(e,e'K^+)\Sigma^0$ REACTIONS

by

Richard Matthew Mohring

Dissertation submitted to the Faculty of the Graduate School of the
University of Maryland, College Park in partial fulfillment
of the requirements for the degree of
Doctor of Philosophy
1999

Advisory Committee:

Professor Elizabeth J. Beise, Chairperson/Advisor
Professor Chia-Cheh Chang
Professor Philip G. Roos
Professor Michael A. Coplan
Dr. Herbert Breuer

DEDICATION

To my wife, my dearest Jenny

ACKNOWLEDGEMENTS

I would like to begin by thanking my parents, Richard and Linda Mohring, for giving me the kind of upbringing that I hope Jenny and I can give our own future children one day. Including my sister, Karalyn, and my grandmother, Mary Behrman, I am blessed to have such a generous and caring family. This dissertation is a direct result of the love and support you all have given me my whole life.

Much of the inspiration that lead me to physics graduate school came from classes I attended given by Yuan Li, Daniel Murnick, and Earl Shaw at Rutgers-Newark and by O. L. Russo, Nuggehalli Ravindra, and Murray Lieb at NJIT. My original roots in physics can be traced to Mr. Weston at East Brunswick High School who showed us how wonderful and challenging it could be to endeavor to understand how things work.

I am certain that many graduate students are not as fortunate as I have been to have worked for a research group composed of scientists who are not only technically adept, but are the kind of folks you enjoy having lunch with. It has been a pleasure working for the Experimental Nuclear Physics group at Maryland with Phil Roos, Nick Chant, George Chang, Jim Kelly, Betsy Beise, and Herbert Breuer. Things within the group were always run smoothly and pleasantly by

our capable Administrative Assistant, Judy Myrick. Also, I was able to work with several talented postdocs: Pete Markowitz, Fraser Duncan, Allison Lung, and Lars Ewell.

Special thanks to the members of my defense committee for taking the time to read through this work. Particularly, George suggested several important changes, and suggestions from Betsy resulted in a totally revamped (and much better) approach to the introductory chapter. Herbert made nothing short of a Herculean effort with his meticulous editing (which at first was rather intimidating!) and I believe that his suggestions palpably improved this document.

My thanks go to Betsy for being willing to take me on as a student in July 1993 essentially before either of us had begun working at the University. For the last six years, Betsy has always shown confidence in my ability to work on my own, has supported my results, and has been a friend beyond her capacity as an advisor. I also thank her for sending me to Boston for what were my earliest experimental experiences, working on the SAMPLE experiment at MIT-Bates. I am also grateful to Phil for recruiting me to Maryland and for always having an open door whether it be for advice, a simple chat, or to discuss physics.

The whole Jefferson Lab experience was possible only through the hard work and dedication of a tremendous number of skilled scientists and technicians. A certain-to-be-incomplete list of people whom I wish to thank for their efforts and contributions to my thesis work follows: Dave Abbott, Kétévi Assamagan,

Kevin Bailey, Keith Baker, Kevin Beard, Joe Beaufait, Betsy Beise, Paul Brindza, Herbert Breuer, Roger Carlini, Bill Cummings, Fraser Duncan, Jim Dunne, Rolf Ent, Mike Fowler, Haiyan Gao, Don Geesaman, Paul Guèye, Steve Hickson, Roy Holt, Paul Hood, Thia Keppel, Steve Knight, Steve Lassiter, Allison Lung, Dave Mack, Naomi Makins, Pete Markowitz, Mike Miller, Joe Mitchell, Hamlet Mkrtchyan, Tom O'Neill, Dave Potterveld, John Price, Jörg Reinhold, Ralph Segel, Paul Stoler, Vardan Tadevosyan, Liquang Tang, Bill Vulcan, Pat Welch, Steve Wood, Chen Yan, and Ben Zeidman.

While at Jefferson Lab, I had the privilege of working closely with an incredibly talented and cool group of graduate students. I wish the best of luck to them all: John Arrington, Derek van Westrum, Dipangkar Dutta, Chris Bochna, Dave Meekins, Bart Terburg, Chris Cothran, Chris Armstrong, Valera Frolov, Kenneth Gustafsson, Adrian Honegger, Jochen Volmer, Ioana Niculescu, Pawel Ambrozowicz, Kathy McCormick, Dave Gaskell, and my fellow kaon hunters: Gabriel Niculescu, Doug Koltenuk, Jinseok Cha, and Wendy Hinton.

I would like to thank the spokesperson for E93-018, Keith Baker of Hampton University, for granting me the opportunity to work on the experiment and for making the three hour drive up to Maryland on several occasions for analysis discussions. I would also like to thank Henk Blok, Dave Mack, Don Geesaman, and Steve Cotanch for valuable conversations during the analysis phase. The experiment itself was a success due to the efforts of the entire E93-018 and E91-

016 collaborations, and notably their heroic postdocs: Paul Guèye and Jörg Reinhold. Thank you for sharing all the long nights at the lab and the myriad hours spent shackled in front of computers – what a long "strange" trip it's been.

A fundamental precept of surviving graduate school is to not lose sight of the other side of life. Thanks to: my dear friends from back home – Andy Baharlias, Steve Goldman, Ian Plotkin, and Ron Lieberman for hanging around while their science friend went off and played with subnuclear particles for six years; Steve, for our songwriting and his patience through periods of my being overwhelmed by work; Greg Cooper, Marcia Robson, and Mike Wiltberger for our many years of companionship; all of the folks who kept the tradition of Tuesday night wallyball alive; Sarah Workneh for a daily breath of fresh air at tea time; Christine Waite for her encouragement through eclectic phone calls and random mailings; the New York Yankees for affording me bragging rights by winning three World Series in the last four years; the students in the ENP group during my graduate career: Mohammed Khayat, Farida Adimi, Jeff Huffman, Tao Gu, Tom Payerle, Chafiq Halli, Rob Brown, Glenn Collins, Kenneth Gustafsson, Damon Spayde, Andrés Collinucci, and Mary Claire Herda; and especially to Kenneth and Damon for their camaraderie and for listening to my blathering while the blue cupboard was overflowing.

Sadly, two of my friends passed away during my years at Maryland. First, Eric Candell, a graduate student from RPI on SAMPLE, died suddenly in May

1995. From my perspective as a new student, Eric stood out as the type of scientist to aspire towards being. More recently, Ernie Knouse from the department's Electronics Development Group died in March 1999. I only knew him for a few short years, but I can understand the profound sense of loss felt by all those in and around the department whose lives he touched. We miss you, Ernie.

I wish to tip my cap to SURA/Jefferson Lab and to the University of Maryland Graduate School for Fellowship support, and to the National Science Foundation for indirect support.

Finally, I want to express my gratitude to my lovely wife, Jennifer, but I find that the words come slowly. It is daunting to approach the task of elucidating in one short paragraph the depths of my love and appreciation for her. Jenny came with me to the foreign land of Maryland, held me up in times when stress began to overwhelm me, took a genuine interest in my work, waited for me while I lived away during the experiment, proofread my thesis draft...and the list goes on and on. Her endless reservoir of support for me and my work were invaluable in the pursuit of this dissertation, and I look forward to having the rest of our lives together in which I can thank her.

TABLE OF CONTENTS

LIST OF TABLES

LIST OF FIGURES

Chapter 1

Introduction and Previous Data

1.1 Introduction

One of the most intriguing areas of intermediate energy nuclear physics (i.e., energies of a few GeV) is the interface between a hadron description and a quark description of nuclei and subnuclear processes. A hadron description such as Quantum Hadrodynamics (QHD) considers a multitude of mesons and baryons* such as pions, kaons, protons, neutrons, Δ, Λ, and Σ^0 to be the fundamental objects which interact with one another. The properties of the particles and strengths of the interactions between them are phenomenologically determined by experiments (e.g., hadron-hadron scattering, photoproduction, radiative capture, electroproduction), and the use of symmetry relations (e.g., duality, crossing symmetry) between reactions [CWJ93].

*See Section 1.1.3 for a short discussion of mesons and baryons.

On the other hand, one can explicitly consider that the hadrons are composite particles composed of fundamental objects: quarks and gluons. The theory of Quantum Chromodynamics (QCD) does so, and is generally accepted as a correct reductionistic theory from which the parameters of QHD could, in principle, be deduced [Cot89]. Unfortunately, many practical calculations using QCD are very difficult (if at all possible) primarily due to the fact that for a given quark-gluon interaction the strength of the QCD coupling grows to greater than unity as the transferred momentum is decreased. Because of this, QCD can only be solved via perturbation theory for momentum transfers above some as yet undetermined threshold [GS94].

The experimental capabilities of the Thomas Jefferson National Accelerator Facility (TJNAF*, Jefferson Lab, JLab) make it well-suited to the task of studying subnuclear dynamics in this energy regime. The electron beam at Jefferson Lab is high-intensity (capable of 200 μA), has 100% duty factor, and can run at high energies (up to 4 GeV at the time of this experimental work). In the experimental halls, Jefferson Lab utilizes high-resolution large acceptance spectrometers, high-power cryogenic targets, and high-resolution detectors with fast electronics. This allows for measurements with fairly low event rates to be made with improved statistical and systematic errors relative to earlier facilities.

*Prior to May 24, 1996 the lab was known as CEBAF, the Continuous Electron Beam Accelerator Facility. The address of the laboratory is: Jefferson Lab, 12000 Jefferson Avenue, Newport News, VA 23606, USA.

This dissertation presents an analysis of data taken during Jefferson Lab experiment E93-018 [Bak93] studying the electroproduction reaction, $p(e, e'K^+)Y$, in two hyperon channels, Y= (Λ, Σ^0). The remainder of this first chapter begins with a brief discussion of a typical electroproduction experiment and an overview of kaon electroproduction. Then, the mathematical formalism used for this particular study is presented, followed by a discussion of the underlying physics motivation behind experiment E93-018. Finally, results of earlier experimental and theoretical work are collected and summarized.

Chapter 2 describes in detail the experimental apparatus used for taking data during E93-018. Chapter 3 discusses the data analysis procedures including the calculation of detector efficiencies and other corrections. Chapter 4 explains the Monte Carlo simulation of the experiment and how it is implemented for the extraction of cross sections. Chapter 5 presents the results of the analysis.

Appendix A presents specific details of the SOS aerogel Čerenkov detector that are not touched upon in Chapter 2. Appendix B is a collection of useful conventions and definitions used during the analysis.

1.1.1 Coincidence Electroproduction Experiments

In general, a coincidence electroproduction experiment allows for the properties of both the target nucleus and a produced particle to be measured. This is accomplished by probing the target with a beam of electrons, and detecting

the scattered probe and produced ejectile simultaneously. The use of an electron beam as a probe is particularly desirable because electron interactions are well understood via the theory of Quantum Electrodynamics (QED), avoiding many of the complications that arise from the influence of the strong interaction* in a technique such as hadron-hadron scattering.

1.1.2 Elementary Kaon Electroproduction

A diagram of the elementary† kaon electroproduction reaction

$$\mathrm{e} + \mathrm{p} \rightarrow \mathrm{e}' + \mathrm{K}^+ + (\Lambda \text{ or } \Sigma^0) \ ,$$

that was studied by E93-018 is shown in Figure 1.1. An incident electron (labeled e), scatters by radiating a virtual photon (γ_v). The scattered electron (e') travels at a polar angle θ_e with respect to the direction of the incident beam, and is detected in a spectrometer (the High Momentum Spectrometer, HMS). The plane defined by the incident electron and scattered electron is referred to as the "scattering plane". The virtual photon carries momentum and energy from the electron beam and interacts with a proton target to form a kaon (K^+) and a hyperon (Y, which for E93-018 is either a Λ or Σ^0). The kaon travels at a polar angle θ_{qK} with respect to the virtual photon direction and is detected in a second

*The strong interaction can potentially come into play through "final state interactions" between several produced particles, or a produced particle and residual nuclei.

†The reaction is referred to as "elementary" because the target is a single proton, as opposed to an $A > 1$ nucleus having more than one proton and/or a number of neutrons.

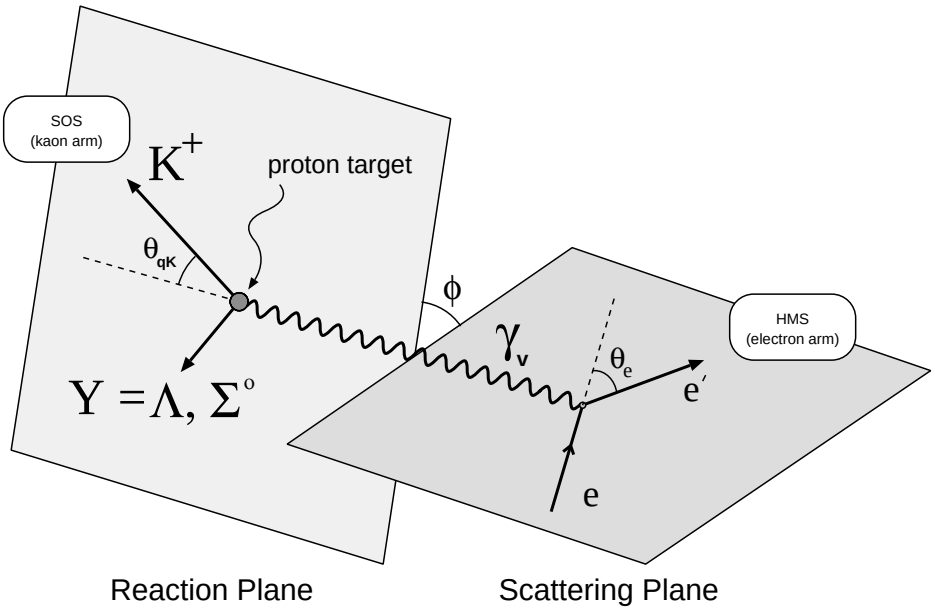

Figure 1.1: Definition of the kaon electroproduction reaction. Note the azimuthal angle, ϕ, between the scattering and reaction planes with respect to the direction of the virtual photon.

spectrometer (the Short Orbit Spectrometer, SOS). The plane defined by the produced kaon and produced hyperon is referred to as the "reaction plane". The azimuthal angle, ϕ, is the angle between the scattering plane and reaction plane. The details of the measurement, such as the beam, target, and spectrometers are discussed in Chapter 2.

1.1.3 Mesons and Baryons

A hadron is defined as a particle that is composed of quarks and/or anti-quarks and interacts via the strong force. Hadrons are typically subdivided into two classes: mesons and baryons. Mesons are composed of quark-antiquark ($q\bar{q}$) pairs, while baryons are composed of quark triplets (qqq). Table 1.1 lists some

Particle	Quarks	Mass (MeV)	Charge	Isospin $\lvert I, I_z\rangle$	Spin	Parity
up quark	u	$\approx 1-5$	$+\frac{2}{3}\,e$	$\lvert\frac{1}{2},+\frac{1}{2}\rangle$	$\frac{1}{2}$	+
down quark	d	$\approx 3-9$	$-\frac{1}{3}\,e$	$\lvert\frac{1}{2},-\frac{1}{2}\rangle$	$\frac{1}{2}$	+
strange quark	s	$\approx 60-170$	$-\frac{1}{3}\,e$	$\lvert 0,0\rangle$	$\frac{1}{2}$	+
π^-	$\bar{u}d$	139.57	$-1e$	$\lvert 1,-1\rangle$	0	−
π^+	$u\bar{d}$	139.57	$+1e$	$\lvert 1,+1\rangle$	0	−
K^+	$u\bar{s}$	493.68	$+1e$	$\lvert\frac{1}{2},+\frac{1}{2}\rangle$	0	−
p	uud	938.27	$+1e$	$\lvert\frac{1}{2},+\frac{1}{2}\rangle$	$\frac{1}{2}$	+
n	udd	939.57	0	$\lvert\frac{1}{2},-\frac{1}{2}\rangle$	$\frac{1}{2}$	+
Λ	uds	1115.68	0	$\lvert 0,0\rangle$	$\frac{1}{2}$	+
Σ^0	uds	1192.64	0	$\lvert 1,0\rangle$	$\frac{1}{2}$	+

Table 1.1: Properties of the three lightest quarks (u,d,s) and a selection of mesons and baryons that are composed of them. Compiled from [HZ98].

properties of the three lightest quarks, and a selection of mesons and baryons that are composed of them. The kaon is the lightest meson that contains a strange quark. In the case of the K^+, an up quark is paired with an anti-strange quark. Technically, these definitions are in terms of "valence quarks", as will be discussed in Section 1.6.

Stable, everyday matter is primarily composed of hadrons which do not contain any strange (valence) quarks. Baryons containing strange quarks are given the name "hyperons". In E93-018, the hyperon, Λ or Σ^0, that is produced concurrently with the kaon is a baryon that contains a single strange quark. The Λ and Σ^0 differ in their isospin and their mass; the less massive Λ is isoscalar ($I = 0$), whereas the more massive Σ^0 is isovector ($I = 1$). For an introductory

level discussion of the quark model, please see a reference such as [HM84, Clo79].

1.2 Mathematical Formalism

In order to facilitate a discussion of the reaction that was measured by E93-018, the relevant mathematical conventions and notations are presented in this section. For further discussion of notations and selected derivations, please see Appendix B.

1.2.1 Specific Notations

Throughout the document, the expanded four-vector notation

$$x^\mu = (x_0, \mathbf{x}) \tag{1.1}$$

is used and should be obvious by context. A metric is chosen such that Lorentz invariant contractions between four-vectors are given by

$$x^\mu y_\mu = x_0 y_0 - \mathbf{x} \cdot \mathbf{y} \ \text{, and} \tag{1.2}$$

$$x^\mu x_\mu = x_0 x_0 - \mathbf{x} \cdot \mathbf{x} = (x_0, \mathbf{x})^2 = (x_0)^2 - |\mathbf{x}|^2 \ . \tag{1.3}$$

Three-vectors such as $\mathbf{x}$ are typically represented in bold face, although they appear occasionally (particularly in figures for clarity) as $\vec{x}$. Unit vectors are given with the notation $\hat{\mathbf{x}} \equiv \mathbf{x}/|\mathbf{x}|$.

Equations that are part of a derivation are enumerated by appending the suffixes "d1, d2, ..." to the equation number of the final result.

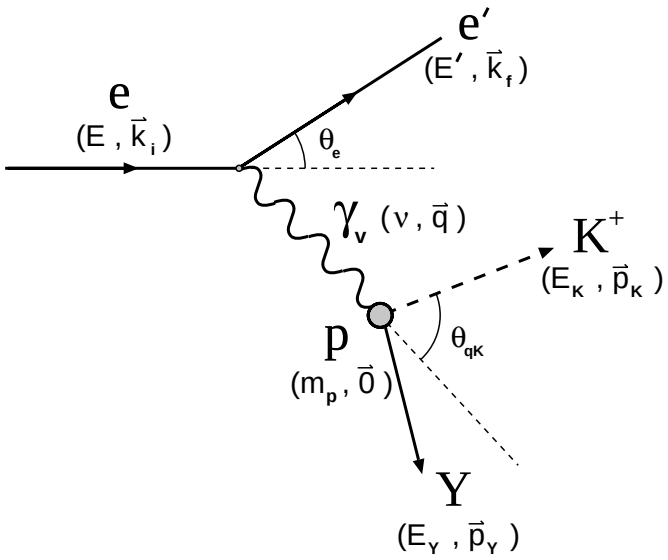

Figure 1.2: Kaon electroproduction in the laboratory frame.

Furthermore, throughout this document, the velocity, v, of a particle is often given as a fraction of the speed of light *in vacuo*: $\beta \equiv v/c$. As a matter of convention, the term "velocity" will be used when referring to β.

Lastly, unless otherwise stated, values are given in natural c.g.s. units such that $\hbar = c = 1$.

1.2.2 Electroproduction / Virtual Photoproduction

The kaon electroproduction reaction considered by E93-018 is depicted in Figure 1.2. The exclusive five-fold differential electroproduction cross section for this process can be expressed in terms of a virtual photoproduction cross section, $\frac{d^2\sigma}{d\Omega_K^*}$ (sometimes simply called $\frac{d\sigma}{d\Omega_K^*}$), multiplied by a virtual photon flux factor, Γ_0 [DL72, HM84, NL90]. The electroproduction cross section can then

be written in terms of the scattered electron energy, E', electron Lab frame solid angle, $d\Omega'_e \equiv d\sin\theta_e\, d\phi_e$, and kaon Center-of-Momentum frame* (CM) solid angle, $d\Omega^*_K \equiv d\sin\theta^*_{qK}\, d\phi$, as

$$\frac{d^5\sigma}{dE' d\Omega'_e d\Omega^*_K} = \Gamma_0(E', \Omega'_e) \left(\frac{d^2\sigma}{d\Omega^*_K}\right) , \tag{1.4}$$

with

$$\Gamma_0(E', \Omega'_e) = \frac{\alpha}{2\pi^2} \frac{(W^2 - m_p^2)}{2\, m_p^2} \frac{E'}{E} \frac{1}{Q^2} \frac{1}{(1-\epsilon)} . \tag{1.5}$$

In this expression, W is the total CM energy of the (virtual photon + proton) system, Q^2 is the square of the four-momentum transfer carried by the virtual photon†, and ϵ is the transverse linear polarization of the virtual photon, given by

$$\epsilon = \frac{1}{1 + 2\,\frac{|\mathbf{q}|^2}{Q^2}\,\tan(\frac{\theta_e}{2})} . \tag{1.6}$$

Rather than use Equation 1.4, the form of the virtual photoproduction cross section used for this analysis is

$$\frac{d^5\sigma}{dQ^2 dW\, d\phi_e d\Omega^*_K} = \Gamma(Q^2, W) \left(\frac{d^2\sigma}{d\Omega^*_K}\right) \tag{1.7}$$

where the transformation between the spaces $(E', \Omega'_e) \leftrightarrow (Q^2, W)$ is incorporated into the virtual photon flux, Γ, via

$$\Gamma(Q^2, W) = \Gamma_0(E', \Omega'_e) \times \frac{W}{2m_p\, E\, E'} = \frac{\alpha}{4\pi^2} \frac{(W^2 - m_p^2)}{2\, m_p^2\, E^2} \frac{W}{Q^2} \frac{1}{(1-\epsilon)} . \tag{1.8}$$

*Note that the CM frame referred to is always that of the (virtual photon + proton) system.

†Expressions for W and Q^2 are given in Section B.1.

Because we do not measure any of the incoming or outgoing polarizations of the particles involved, the virtual photoproduction cross section can be decomposed neatly into four contributions from various combinations of virtual photon polarizations, as

$$\frac{d^2\sigma}{d\Omega_K^*} = \left(\frac{d^2\sigma_T}{d\Omega_K^*}\right) + \epsilon\left(\frac{d^2\sigma_L}{d\Omega_K^*}\right) + \sqrt{2\epsilon(\epsilon+1)}\left(\frac{d^2\sigma_{LT}}{d\Omega_K^*}\right)\cos\phi + \epsilon\left(\frac{d^2\sigma_{TT}}{d\Omega_K^*}\right)\cos 2\phi \ , \tag{1.9}$$

or more compactly,

$$\frac{d^2\sigma}{d\Omega_K^*} = \sigma_T + \epsilon\,\sigma_L + \sqrt{2\epsilon(\epsilon+1)}\,\sigma_{LT}\cos\phi + \epsilon\,\sigma_{TT}\cos 2\phi \ , \tag{1.10}$$

where:

- σ_T is the cross section due to transversely polarized virtual photons,
- σ_L is the cross section due to longitudinally polarized virtual photons,
- σ_{LT} is the cross section due to interference between transversely polarized and longitudinally polarized virtual photons,
- σ_{TT} is the cross section due to interference between the two different states of transversely polarized virtual photons,
- ϵ is the virtual photon transverse linear polarization, and,
- ϕ is the azimuthal angle between the scattering and production planes (as depicted in Figure 1.1).

If one integrates the cross section in Equation 1.10 over all $\phi \in (0, 2\pi)$, the interference terms vanish*, leaving only the combined contributions from the

*Because the ϕ dependence of the interference terms is entirely given by $\cos\phi$ and $\cos 2\phi$, the integral over ϕ reduces to $\int_0^{2\pi}\cos\phi = \int_0^{2\pi}\cos 2\phi = 0$.

Point	$\langle Q^2 \rangle$ GeV^2	$\langle W \rangle$ GeV	$\langle \epsilon \rangle$ (for Λ)	E GeV	$\mathrm{P_{HMS}} = E'$ GeV	θ_{HMS} deg	$\mathrm{P_{SOS}}$ GeV	θ_{SOS} deg
1	0.52	1.84	0.552	2.445	0.833	29.27°	1.126	13.40°
2	0.52	1.84	0.771	3.245	1.633	18.03°	1.126	16.62°
3	0.52	1.84	0.865	4.045	2.433	13.20°	1.126	18.34°
4	0.75	1.84	0.462	2.445	0.725	37.95°	1.188	13.42°
5	0.75	1.84	0.724	3.245	1.526	22.44°	1.188	17.62°
6	0.75	1.84	0.834	4.045	2.326	16.23°	1.188	19.75°
7	1.00	1.81	0.380	2.445	0.635	47.30°	1.216	13.40°
8	1.00	1.81	0.678	3.245	1.435	26.80°	1.216	18.20°
9	1.00	1.81	0.810	4.045	2.236	19.14°	1.216	20.78°
10	2.00	1.84	0.363	3.245	0.844	50.59°	1.634	13.42°
11	2.00	1.84	0.476	3.545	1.145	41.11°	1.634	15.67°
12	2.00	1.84	0.613	4.045	1.645	31.83°	1.634	18.14°

Table 1.2: Kinematical settings measured in E93-018. Note that there are three settings of the virtual photon polarization, ϵ, for each of four values of Q^2. Data were taken in the Λ and Σ^0 channels simultaneously. For ease of discussion, the settings have been labeled as Point 1 through Point 12 in increasing order of Q^2, and with increasing order of ϵ within each Q^2 setting.

transverse and longitudinal cross sections, $\sigma_T + \epsilon\sigma_L$. Then, by measuring the cross section at several values of the virtual photon polarization, ϵ, the cross sections σ_T and σ_L can be separated. The experimental setup for E93-018 was such that at each of the four values of Q^2 that were examined, full $\phi \in (0, 2\pi)$ coverage was measured at three (3) different values of the virtual photon polarization, ϵ, as listed in Table 1.2. Note that $\mathrm{P_{HMS}} = E'$ and $\mathrm{P_{SOS}} = |\mathbf{p_K}|$.

A least-squares fitting routine was then used to fit a linear dependence of $(\sigma_T + \epsilon\sigma_L)$ vs. ϵ. The results of the fit were used to extract the separated values of σ_T (the $\epsilon = 0$ intercept of the fitted line) and σ_L (the slope of the fitted line)

for each Q^2, for each of the Λ and Σ^0 channels. This technique is typically called a "Rosenbluth separation", or simply an "L/T separation". The procedure for extracting the cross sections is discussed in detail in Chapters 4 and 5.

1.3 Physics Motivation for E93-018

The general goals of Jefferson Lab experiment E93-018 were as follows:

First, E93-018 set out to extract L/T separated cross sections in the Λ and Σ^0 channels. As mentioned in Section 1.1, data is needed to evaluate the parameters in phenomenological models. The extraction of precise L/T separated cross sections will hopefully aid in constraining the theoretical models, and in turn, give information about the reaction mechanisms.

Second, a strong decrease in the ratio of Σ^0/Λ cross sections is seen with increasing Q^2 in previous experimental data (see Section 1.4). Examining the production ratio for σ_L and σ_T separately may give some insight into the production mechanism, as will be discussed in Section 1.5.

Third, by examining the dependence of the longitudinal part of the cross section as a function of the Mandelstam variable t, one can potentially extract information about the charge form factor of the kaon. This technique has been used for the extraction of the pion form factor (see [DL72]).

Fourth, experiments are planned at JLab and other facilities to study kaon electroproduction off $A > 1$ nuclei. A thorough study of the elementary reaction

$p(e, e'K^+)Y$ such as that studied by E93-018 is an important starting point for extracting an A dependence.

Finally, other experiments, particularly in Hall A (e.g., [Mar94]) and Hall B (e.g., [MH93]) at Jefferson Lab will take further measurements of the elementary reaction. Data from E93-018 will serve as a useful reference for these experiments.

1.4 Previous Data

Several exploratory measurements of kaon electroproduction were made prior to the running of E93-018. These earlier experiments were performed between 1972 and 1979 at facilities such as the Cambridge Electron Accelerator (CEA), the Wilson Synchrotron Laboratory (Harvard-Cornell) and the Deutsches Elektronen-Synchrotron (DESY). One of these experiments [Beb77a] separated the longitudinal and transverse contributions to the Λ and Σ^0 cross sections for three values of Q^2. However, only two values of ϵ were measured for each kinematic setting in that experiment, and consequently the uncertainties on the L/T separated results were very large. Another experiment [Bra79] focused on pion electroproduction, but also had a sample of kaons from which the cross section $\left(\frac{d\sigma}{dt}\right)$ was extracted, although the experiment was not optimized for studying kaons.

The existing world data for $\left(\frac{d^2\sigma}{d\Omega_K^*}\right)$ is listed in Table 1.3. The rightmost column shows the cross sections scaled to $\langle W \rangle = 2.15$ GeV, $\theta_{CM} = 0^\circ$ using the

W	Q^2	ϵ	$\langle\theta_{CM}\rangle$	$\frac{d^2\sigma}{d\Omega_K^*}\,\Lambda$	$\frac{d^2\sigma}{d\Omega_K^*}\,\Sigma^0$	$\frac{d^2\sigma}{d\Omega_K^*}\,\Lambda$	$\frac{d^2\sigma}{d\Omega_K^*}\,\Sigma^0$
GeV	GeV^2		deg	Unscaled (nb/sr)		Scaled (nb/sr)	
CEA [Bro72, Beb77b]							
2.17	0.18	0.85	5.9	533* ± 84	—	546 ± 86	—
2.17	0.29	0.88	5.9	449* ± 57	94 ± 48	460 ± 58	95 ± 49
2.17	0.40	0.86	5.9	398 ± 46	60 ± 40	408 ± 47	61 ± 40
2.17	0.76	0.81	5.9	287 ± 42	75 ± 33	295 ± 43	76 ± 33
2.17	1.17	0.78	5.9	277 ± 45	—	285 ± 46	—
1.93	0.29	0.93	6.0	732 ± 140	336 ± 147	686 ± 131	333 ± 146
2.10	0.29	0.90	6.0	369 ± 90	192 ± 84	366 ± 89	190 ± 83
2.48	0.29	0.74	6.0	350 ± 33	123 ± 29	431 ± 41	145 ± 34
Harvard-Cornell [Beb77b]							
2.17	1.18	0.94	8.0	251 ± 43	73 ± 30	263 ± 45	75 ± 31
2.15	1.98	0.94	9.1	193 ± 22	17 ± 12	203 ± 23	17 ± 12
2.17	3.98	0.88	9.0	78 ± 15	10 ± 10	85 ± 16	10 ± 10
2.85	1.36	0.87	10.4	142 ± 31	24 ± 25	230 ± 50	36 ± 37
2.51	3.46	0.85	10.0	97 ± 29	5 ± 8	130 ± 39	6 ± 10
Harvard-Cornell [Beb74, Beb77b]							
2.67	0.62	0.86	7.8	267 ± 26	35 ± 15	375 ± 37	46 ± 20
2.66	1.20	0.86	8.4	169 ± 12	38 ± 8	238 ± 17	50 ± 11
2.66	2.00	0.82	7.5	137 ± 13	6 ± 6	193 ± 18	8 ± 8
2.20	1.18	0.94	7.4	272 ± 19	35 ± 12	288 ± 20	36 ± 12

*Reference [Beb77b] incorrectly reports these two cross sections as 553 and 499 nb/sr, respectively. They are given correctly in reference [Bro72], as can be confirmed by examining the quoted extrapolations of the cross section and the quoted ratios of Σ^0/Λ.

Table 1.3: Previous world data on $\frac{d^2\sigma}{d\Omega_K^*}$ for p(e,e′K$^+$)Λ/Σ^0, shown unscaled and scaled to $\langle W\rangle = 2.15$ GeV, $\theta_{CM} = 0°$. The scaling procedure is discussed in more detail in Chapter 4. The scaling used here corresponds to Equations 4.13 and 4.20.

parameterizations that are discussed in some detail in Chapter 4 and are given by Equations 4.13 and 4.20. The points are scaled in W and θ_{CM} so that they can be directly compared with one another and are plotted as a function of Q^2

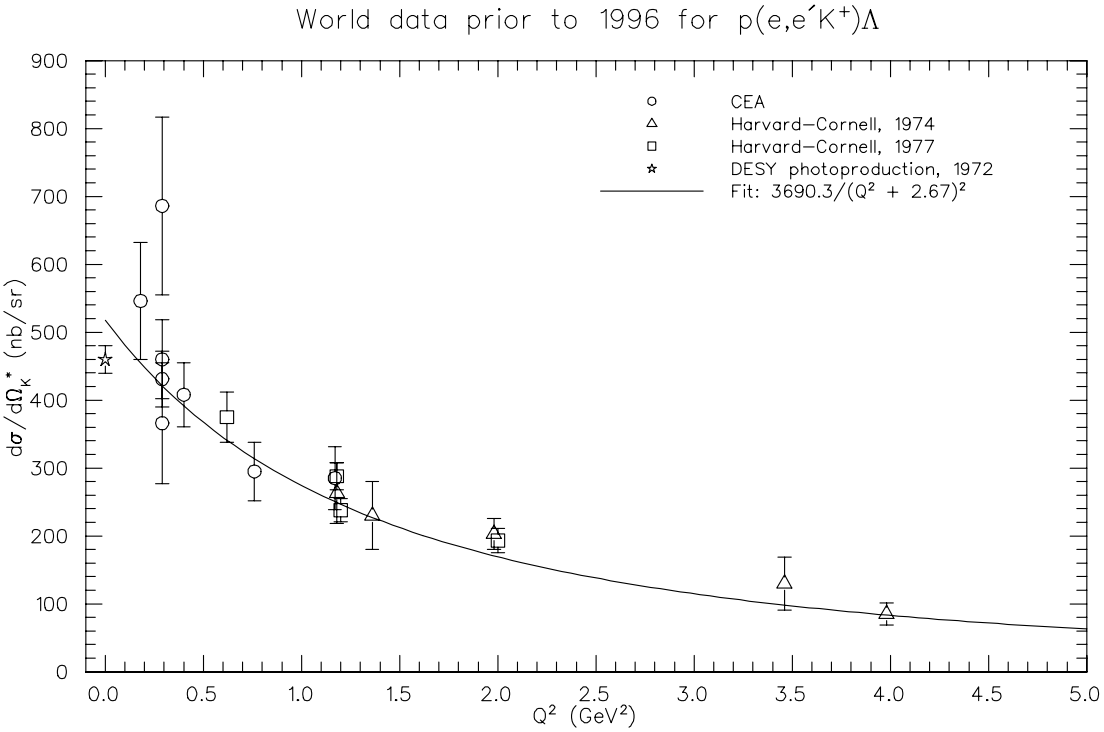

Figure 1.3: Previous world data for p(e,e′K$^+$)Λ. This graph shows the scaled Λ cross sections from Table 1.3, at $\langle W \rangle = 2.15$ GeV, $\theta_{CM} = 0°$. The curve is a fit to a $(Q^2 + 2.67)^{-2}$ dependence, as in [Beb77a].

in Figure 1.3 (for the Λ) and Figure 1.4 (for the Σ^0). A photoproduction point from [Fel72] is included at $Q^2 = 0$ on both plots, also scaled to $\langle W \rangle = 2.15$ GeV, $\theta_{CM} = 0°$. One can see that both cross sections decrease quickly with Q^2, although the Σ^0 cross section falls off considerably faster than the Λ cross section. This decrease in the ratio of Σ^0/Λ production is the topic of Section 1.6.

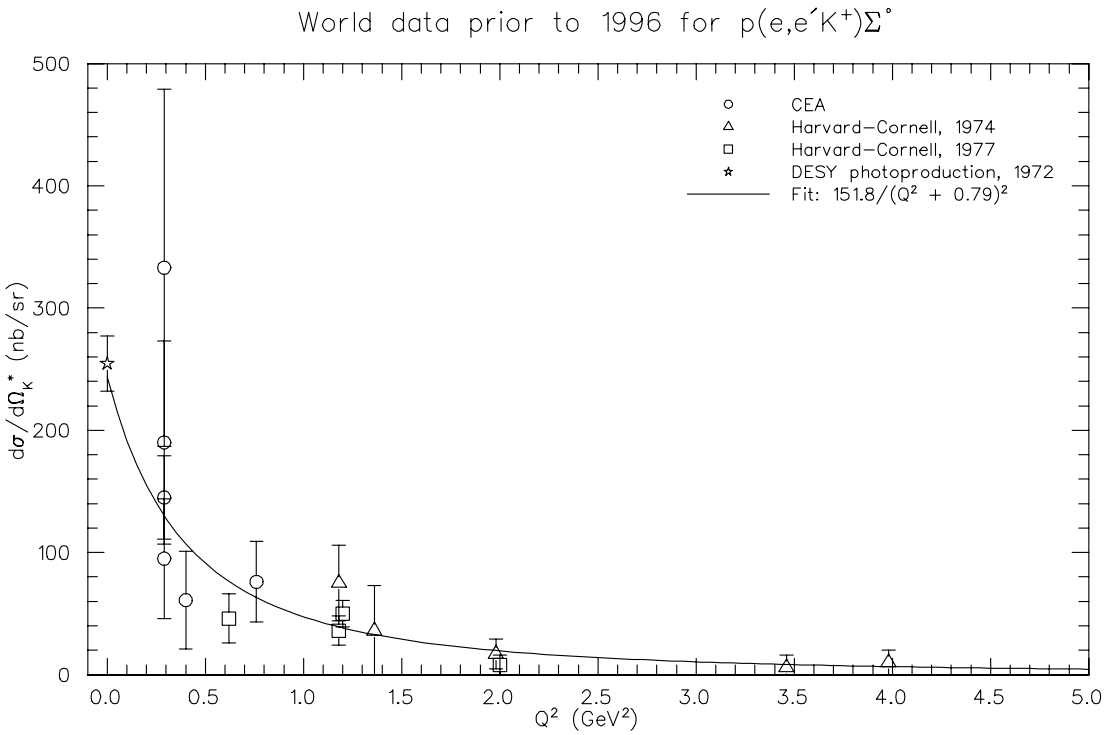

Figure 1.4: Previous world data for p(e,e′K$^+$)Σ^0. This graph shows the scaled Σ^0 cross sections from Table 1.3, at $\langle W \rangle = 2.15$ GeV, $\theta_{CM} = 0°$. The curve is a fit to a $(Q^2 + 0.79)^{-2}$ dependence, as in [Beb77a].

1.5 Model Descriptions

1.5.1 Introduction

In the past thirty years, there has been a wealth of scholarly interest in providing theoretical models to explain meson electroproduction. The models that consider kaons all attempt to reproduce all the available data from both kaon production and radiative kaon capture, while attempting to maintain consistency with SU(3) symmetry constraints on the coupling constants [WJC92]. The energy regime addressed by these models is low enough that they are each formulated

using the principles of QHD. However, the models are explicitly constructed such that they yield the proper perturbative QCD (pQCD) results at higher energies [CWJ93]. The most recent theoretical efforts can be broken into two categories, isobaric models and Regge models, and are discussed in the following two sections.

1.5.2 Isobaric Models

The approach taken in an isobaric model is to explicitly calculate kaon production amplitudes from tree-level (i.e., only one particle exchanged) QHD Feynman diagrams. Typically, a selection of diagrams from s, t, and u-channel processes* such as those depicted in Figure 1.5 are considered with limits on the properties of the propagators. For example, in David *et al.* [DFLS96] the authors sum over s-channel nucleonic resonances up to and including spin 5/2, u-channel hyperonic resonances of spin 1/2, and t-channel kaonic resonances K*(892) and K1(1270). In the WJC model [WJC92], a different selection of s and u channel resonances are included. Each vertex in these diagrams is associated with a particular coupling constant. The coupling constants used in several isobaric models are listed for comparison in Table 1.4 and Table 1.5. The various isobaric models share the property that they initially include only spin 1/2 baryonic resonances (although the specific resonances differ) and determine the remaining coupling constants from performing phenomenological fits to the data. The coupling con-

*Please refer to Table B.3 for definitions of s, t, and u.

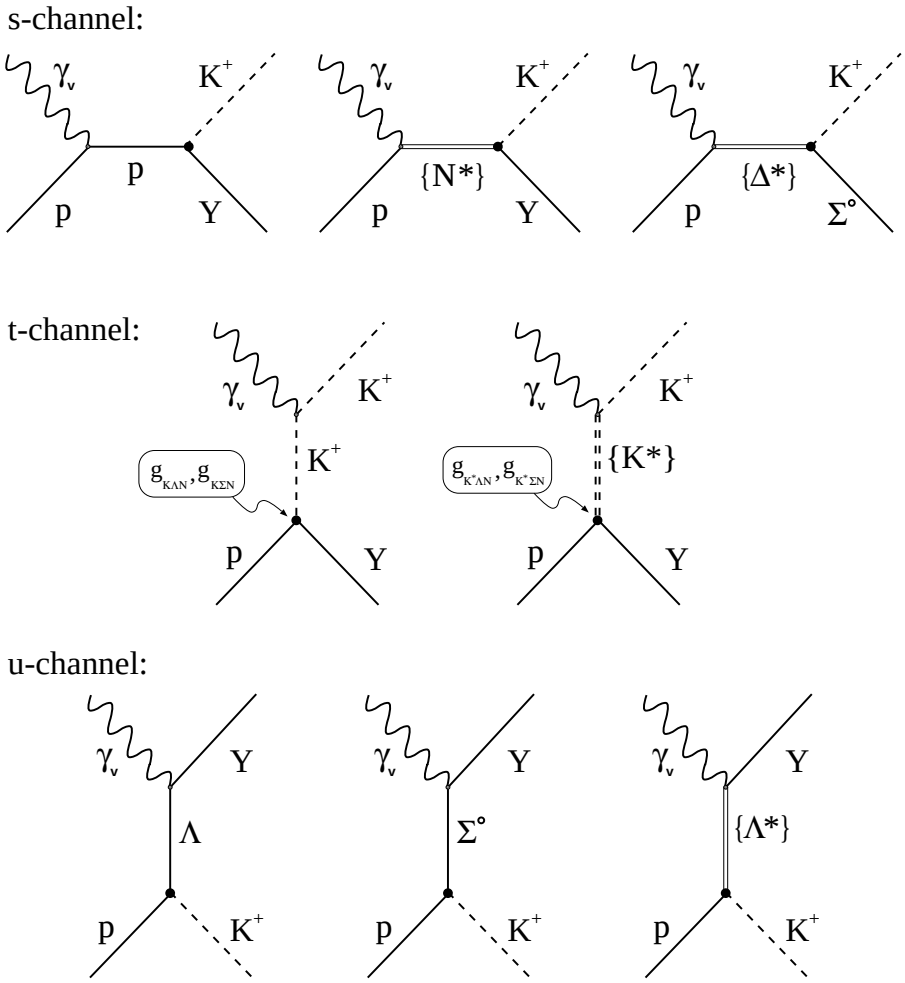

Figure 1.5: Feynman diagrams for kaon electroproduction considered in an isobaric model. The couplings in the t-channel ($g_{K\Lambda N}$, etc...) are shown explicitly. A description of the actual resonances and couplings used can be found in Table 1.4 and Table 1.5. Note that the s-channel processes involving Δ^* resonances are forbidden by isospin conservation for Λ production.

stants, which are the parameters of the theory, are not well-constrained due to the lack of available data.

One can see differences in the various models for quantities such as $g_{K\Lambda N}$ in Table 1.4. This is in part due to the overall lack of quality kaon production and scattering data from which the parameters were extracted. One issue that these

Particle		(I)J$^\pi$	Coupling	Model Description		
				AS	WJC	SL
Λ		(0)1/2$^+$	$g_{K\Lambda N}/\sqrt{4\pi}$	-4.17 ± 0.75	-2.38	-3.16 ± 0.01
Σ		(1)1/2$^+$	$g_{K\Sigma N}/\sqrt{4\pi}$	1.18 ± 0.66	0.27	0.91 ± 0.10
K*	K*(892)	(1/2)1$^-$	$G_V/4\pi$	-0.43 ± 0.07	-0.16	-0.05 ± 0.01
			$G_T/4\pi$	0.20 ± 0.12	0.08	0.16 ± 0.02
K1	K1(1270)	(1/2)1$^+$	$G_{V1}/4\pi$	-0.10 ± 0.06	0.02	-0.19 ± 0.01
			$G_{T1}/4\pi$	-1.21 ± 0.33	0.17	-0.35 ± 0.03
N1	N(1440)	(1)1/2$^+$	$G_{N1}/\sqrt{4\pi}$	-1.41 ± 0.60		-0.01 ± 0.12
N4	N(1650)	(0)1/2$^-$	$G_{N4}/\sqrt{4\pi}$		-0.04	
N6	N(1710)	(1)1/2$^+$	$G_{N6}/\sqrt{4\pi}$		-0.06	
N7	N(1720)	(1)3/2$^+$	$G^a_{N7}/4\pi$			-0.04 ± 0.01
			$G^b_{N7}/4\pi$			-0.14 ± 0.04
N8	N(1675)	(2)5/2$^-$	$G^a_{N8}/4\pi$			-0.63 ± 0.10
			$G^b_{N8}/4\pi$			-0.05 ± 0.56
L1	Λ(1405)	(0)1/2$^-$	$G_{L1}/\sqrt{4\pi}$		-0.07	-0.31 ± 0.06
L3	Λ(1670)	(0)1/2$^-$	$G_{L3}/\sqrt{4\pi}$	-3.17 ± 0.86		1.18 ± 0.09
L5	Λ(1810)	(1)1/2$^+$	$G_{L5}/\sqrt{4\pi}$			-1.25 ± 0.20
S1	Σ(1660)	(1)1/2$^+$	$G_{S1}/\sqrt{4\pi}$			-4.96 ± 0.19

Table 1.4: Coupling constants used for exchanged particles in isobaric models for the KΛ channels. The models shown are compiled in [DFLS96] and come from the following references: AS = [AS90], WJC = [WJC92], SL = [DFLS96].

differences reflect is that the various models disagree as to the relative importance of the resonances entering the calculation. Further information on the various isobaric models can be found in [DFLS96, WJC92, JC88, WJC90, JC90, WJC91, AS90, MBHW95].

Particle		(I)J$^\pi$	Coupling	Model Description		
				MBH	WJC	SL
Λ		$(0)1/2^+$	$g_{K\Lambda N}/\sqrt{4\pi}$	0.51	-2.38	-3.23 ± 0.17
Σ		$(1)1/2^+$	$g_{K\Sigma N}/\sqrt{4\pi}$	0.13	0.27	0.80 ± 0.10
K*	K*(892)	$(1/2)1^-$	$G_V/4\pi$	0.05	0.11	0.02 ± 0.01
			$G_T/4\pi$	0.05	-0.14	-0.07 ± 0.02
K1	K1(1270)	$(1/2)1^+$	$G_{V1}/4\pi$		-0.13	-0.05 ± 0.01
			$G_{T1}/4\pi$		0.07	0.23 ± 0.04
N1	N(1440)	$(1)1/2^+$	$G_{N1}/\sqrt{4\pi}$			-0.95 ± 0.11
N4	N(1650)	$(0)1/2^-$	$G_{N4}/\sqrt{4\pi}$	0.08	0.09	
N6	N(1710)	$(1)1/2^+$	$G_{N6}/\sqrt{4\pi}$	0.57	0.47	
N7	N(1720)	$(1)3/2^+$	$G^a_{N7}/4\pi$			-0.04 ± 0.02
			$G^b_{N7}/4\pi$			-0.53 ± 0.06
N8	N(1675)	$(2)5/2^-$	$G^a_{N8}/4\pi$			2.02 ± 0.20
			$G^b_{N8}/4\pi$			3.91 ± 0.57
L1	Λ(1405)	$(0)1/2^-$	$G_{L1}/\sqrt{4\pi}$		0.46	-0.42 ± 0.03
L3	Λ(1670)	$(0)1/2^-$	$G_{L3}/\sqrt{4\pi}$			-0.10 ± 0.09
L5	Λ(1810)	$(1)1/2^+$	$G_{L5}/\sqrt{4\pi}$			6.01 ± 0.23
S1	Σ(1660)	$(1)1/2^+$	$G_{S1}/\sqrt{4\pi}$			-1.72 ± 0.21
D1	Δ(1620)	$(0)1/2^-$	$G_{D1}/\sqrt{4\pi}$		-0.03	
D2	Δ(1900)	$(0)1/2^-$	$G_{D2}/\sqrt{4\pi}$	0.07	-0.06	
D3	Δ(1910)	$(1)1/2^+$	$G_{D3}/\sqrt{4\pi}$	0.30	-0.51	0.43 ± 0.04
D4	Δ(1232)	$(1)3/2^+$	$G^a_{D4}/4\pi$			-0.47 ± 0.06
			$G^b_{D4}/4\pi$			-1.88 ± 0.14
D7	Δ(1920)	$(1)3/2^+$	$G^a_{D7}/4\pi$			0.05 ± 0.01
			$G^b_{D7}/4\pi$			0.29 ± 0.04

Table 1.5: Coupling constants used for exchanged particles in isobaric models for the KΣ channels. The models shown are compiled in [DFLS96] and come from the following references: MBH = [MBHW95], WJC = [WJC92], SL = [DFLS96].

1.5.3 Regge Models

A second class of models are those that utilize Regge theory [Col77]. We will consider the recent model due to Vanderhaegen, Guidal, and Laget (VGL) [VGL98], which is based on earlier work of Levy, *et al.* [LMR73a, LMR73b]. These models were originally developed to describe pion photoproduction data, of which there is a relative abundance. In this type of model, the Feynman diagram approach is modified such that at higher energies the standard single particle Feynman propagator, $1/(t - m^2)$, is replaced by a "Regge propagator" that accounts for the exchange of a family of particles with the same internal quantum numbers [GLV97a].

For example, the pseudoscalar hadronic current for *photoproduction* via t-channel kaon exchange (for the Λ channel) can be written as

$$J^{\mu}_{K:t-\mathrm{exch}} \propto i\, e \not{\kappa} \bar{Y}_f \, (\kappa - p_K)^{\mu} \times \mathcal{P}^{\mathrm{K}}_{\mathrm{Regge}} \times \, g_{K\Lambda N} \, \gamma^5 \, N_i \ , \tag{1.11}$$

where e is the electron charge, $\kappa^{\mu} = (q - p_K)^{\mu}$ is the four-vector of the exchanged kaon, Y_f is the Lambda spinor, q^{μ} is the photon four-vector, p^{μ}_K is the kaon four-vector, $g_{K\Lambda N}$ is the coupling constant at the (proton + Λ + K^+) vertex, and N_i is the proton spinor. The Regge propagator, $\mathcal{P}^{\mathrm{K}}_{\mathrm{Regge}}$, is of the form,

$$\mathcal{P}^{\mathrm{K}}_{\mathrm{Regge}} = \left(\frac{s}{s_0}\right)^{\alpha_K(t)} \left(\frac{\pi \alpha^{'}_K(t)}{\sin \pi \alpha_K(t)}\right) \left(\frac{\mathcal{S}_K + e^{-i\pi\alpha_K(t)}}{2}\right) \left(\frac{1}{\Gamma(1 + \alpha_K(t))}\right) \ , \tag{1.12}$$

where s is the conventional Mandelstam variable (i.e., $s = W^2$), s_0 is a mass scale (typically $s_0 = 1$ GeV^2), α_K and $\alpha^{'}_K$ represent the Regge trajectory as

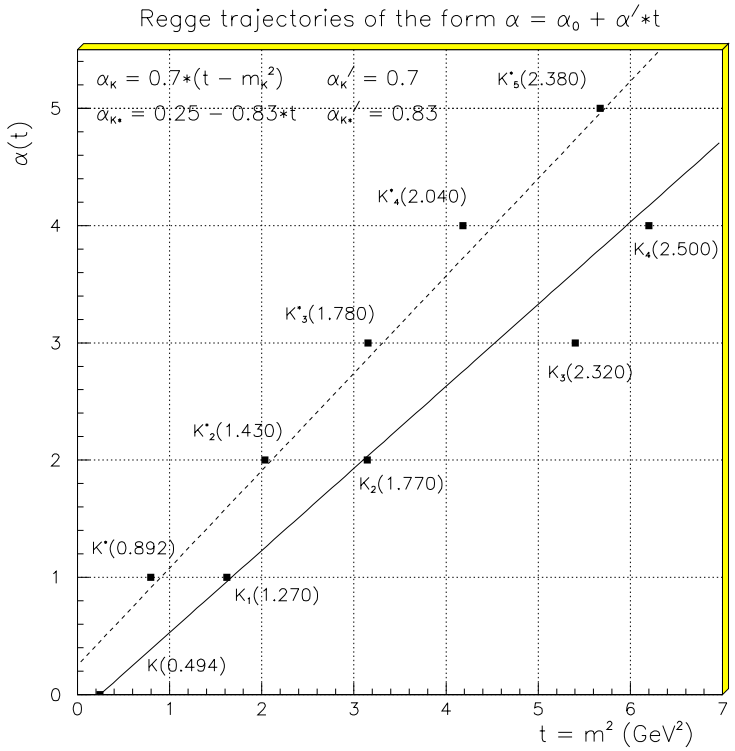

Figure 1.6: K and K* Regge trajectories, taken from [GLV97a].

shown in Figure 1.6, $\mathcal{S}_K = \pm 1$ is the signature of the trajectory, and Γ is the standard Gamma function. Equation 1.12 has the property that it reduces to the Feynman propagator as one approaches the first pole on the trajectory (i.e., $t \to m_K^2$). A similar current operator and propagator can be constructed for the pseudovector coupling of the K* mesons. It should be noted that in the VGL model, the only parameters are those of the first materialization of the trajectories with the external particles ($g_{K\Lambda N}, g_{K^*\Lambda N}$,...), which are determined so as to describe all existing high energy data [GLV97a, GLV99].

The extension of the photoproduction model to electroproduction is ac-

complished by multiplying the gauge invariant t-channel K and K* diagrams by a form factor*. For the VGL model this is given as a monopole form factor,

$$F_{K,K^*}(Q^2) = \frac{1}{1 + Q^2/\Lambda^2_{K,K^*}} \ , \tag{1.13}$$

where Λ^2_{K,K^*} are mass scales that are essentially free parameters, but can be fixed so as to fit the high Q^2 behavior of the separated electroproduction cross sections, σ_T and σ_L. It should be noted that the effective charge radius of the K$^+$ can be related to Λ^2_K via the expression [Won90, GLV99]

$$\langle r^2_K \rangle \equiv -\,6\,\frac{dF_K}{dQ^2}\bigg|_{Q^2=0} = \frac{6}{\Lambda^2_K} \ . \tag{1.14}$$

Further details regarding the VGL Regge model can be found in [GLV97b, GLV97a, VGL98].

1.6 Discussion of the Σ^0/Λ Ratio

The p(e, e′K$^+$)Λ and p(e, e′K$^+$)Σ^0 results collected in Figures 1.3 and 1.4 show that the ratio of cross sections for the two channels Σ^0/Λ decreases rapidly as Q^2 is increased. Nachtmann [Nac72, Nac74] and Close [Clo74] showed that the decrease of the ratio Σ^0/Λ could be anticipated through the use of an argument based on isospin. Although these arguments lack the sophistication of the kaon models presented in the previous sections, the qualitative picture presented in

*The isobaric models such as WJC also include electromagnetic form factors, however the functional forms used differ between models [WJC92, AS90].

this section is at least of historical interest, as it describes one of the motivations for performing E93-018 [Bak93].

In a simple quark-parton model, the nucleon is composed of point-like partons (charged quarks and charge-neutral gluons) that each carry some fraction, x (referred to as "Bjorken x"), of the overall momentum of the nucleon. This fraction x can be written as $x = Q^2/2M\nu$, where M is the nucleon mass and ν is the photon energy. Using this variable, one can consider deep-inelastic electron scattering from a single nucleon* as a preface to the Σ^0/Λ electroproduction ratio. In the scattering process, a virtual photon radiated by the electron interacts with one of the quarks. Of use will be the nucleon structure function F_2^e, defined as

$$F_2^e(x) = \sum_i e_i^2 \, x \, f_i(x) \ , \tag{1.15}$$

where the sum (i) is over the constituent quarks, e_i is the quark charge, and $f_i(x)$ represents the probability distribution of quarks in x. The functions $f_i(x)$ are normalized such that the sum over all quarks, i, and integral over all x is

$$\sum_i \int dx \, x \, f_i(x) = 1 \ . \tag{1.16}$$

If we restrict ourselves to only consider the presence of $(u, \bar{u})$, $(d, \bar{d})$, and $(s, \bar{s})$ quarks within the nucleon, Equation 1.15 can be expanded to give F_2^e for

*See, for example, [HM84].

the proton as

$$\frac{F_2^{ep}(x)}{x} = \left(\frac{2}{3}\right)^2 [u^p(x) + \bar{u}^p(x)] + \left(\frac{1}{3}\right)^2 [d^p(x) + \bar{d}^p(x)] + \left(\frac{1}{3}\right)^2 [s^p(x) + \bar{s}^p(x)] \tag{1.17}$$

where $u^p(x)$ is the probability distribution of u quarks within the proton, and similarly for the $\{\bar{u}, d, \bar{d}, s, \bar{s}\}$ quarks. Likewise, for the neutron we have,

$$\frac{F_2^{en}(x)}{x} = \left(\frac{2}{3}\right)^2 [u^n(x) + \bar{u}^n(x)] + \left(\frac{1}{3}\right)^2 [d^n(x) + \bar{d}^n(x)] + \left(\frac{1}{3}\right)^2 [s^n(x) + \bar{s}^n(x)] \ . \tag{1.18}$$

Assuming SU(2) isospin symmetry, the distribution of u quarks within the proton (uud) should be the same as the distribution of d quarks within the neutron (udd), and so on, giving

$$u(x) \equiv u^p(x) = d^n(x) \tag{1.19}$$

$$d(x) \equiv d^p(x) = u^n(x) \tag{1.20}$$

$$s(x) \equiv s^p(x) = s^n(x) \tag{1.21}$$

Each of the quark distributions can be separated into contributions from "valence quarks" and "sea quarks". The sea quarks must appear in $q\bar{q}$ pairs, and can be pictured as being radiated from the valence quarks, as in Figure 1.7. The individual quark distributions decompose into:

$$u(x) = u_{\text{val}}(x) + u_{\text{sea}}(x) \qquad \bar{u}(x) = \bar{u}_{\text{sea}}(x) \tag{1.22}$$

$$d(x) = d_{\text{val}}(x) + d_{\text{sea}}(x) \qquad \bar{d}(x) = \bar{d}_{\text{sea}}(x) \tag{1.23}$$

$$s(x) = s_{\text{sea}}(x) \qquad \bar{s}(x) = \bar{s}_{\text{sea}}(x) \ . \tag{1.24}$$

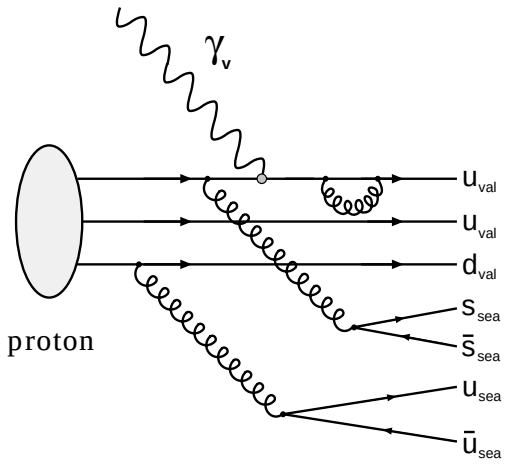

Figure 1.7: A proton shown as a three valence quark (uud) state with radiated gluons and sea quarks ($u\bar{u}$ and $s\bar{s}$). A virtual photon is shown interacting with one of the valence quarks.

For the purposes of this discussion, it is assumed that the sea quark distributions are flavor independent and are given by

$$S(x) \equiv u_{\rm sea}(x) = \bar{u}_{\rm sea}(x) = d_{\rm sea}(x) = \bar{d}_{\rm sea}(x) = s_{\rm sea}(x) = \bar{s}_{\rm sea}(x) \ . \tag{1.25}$$

The nucleon structure functions of Equation 1.17 and Equation 1.18 can then be written as

$$\frac{1}{x}F_2^{ep}(x) = \frac{1}{9}\left[4u_{\rm val}(x) + d_{\rm val}(x)\right] + \frac{4}{3}S(x) \tag{1.26}$$

$$\frac{1}{x}F_2^{en}(x) = \frac{1}{9}\left[u_{\rm val}(x) + 4d_{\rm val}(x)\right] + \frac{4}{3}S(x) \ , \tag{1.27}$$

leading to the ratio of neutron/proton structure functions,

$$\frac{F_2^{en}(x)}{F_2^{ep}(x)} = \frac{\frac{1}{9}\left[u_{\rm val}(x) + 4d_{\rm val}(x)\right] + \frac{4}{3}S(x)}{\frac{1}{9}\left[4u_{\rm val}(x) + d_{\rm val}(x)\right] + \frac{4}{3}S(x)} \ . \tag{1.28}$$

The upper and lower limits of this expression can be found by ignoring the sea quark contributions, $S(x)$. The ratio in Equation 1.28 must then lie in the

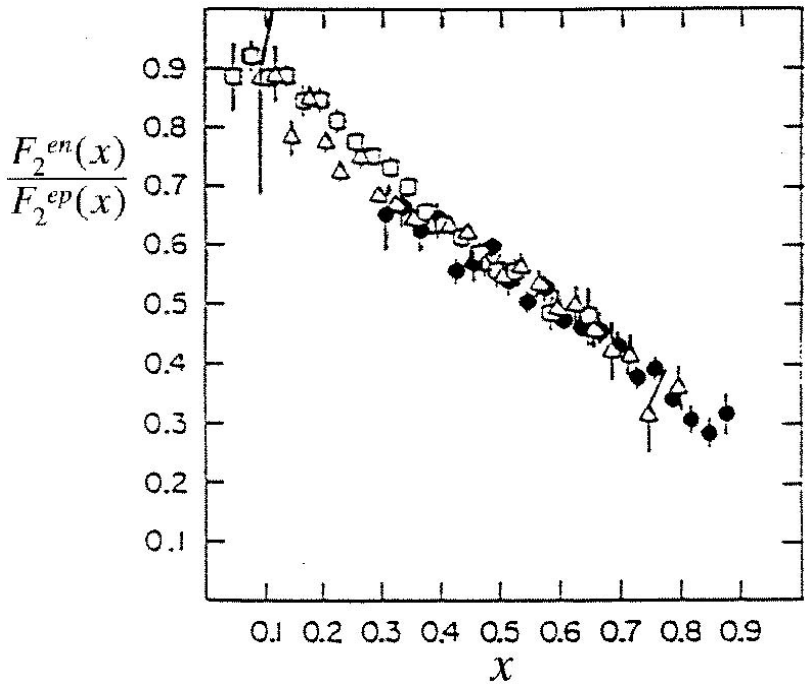

Figure 1.8: Ratio of neutron/proton structure functions F_2^{en}/F_2^{ep} as a function of Bjorken x measured by SLAC [Bod74].

range

$$\frac{1}{4} \leq \frac{F_2^{en}(x)}{F_2^{ep}(x)} \leq 4 \ . \tag{1.29}$$

In fact, this ratio was measured at SLAC (see Figure 1.8) and varies between 1/4 as $x \to 1$, to 1 as $x \to 0$. The lower limit of 1/4 shown by the data could be interpreted in the context of Equation 1.28 to mean that as one approaches $x = 1$ for scattering off a proton, $u_{\rm val} \gg d_{\rm val}$, and the probability of interacting with a u quark, $u_{\rm val}$, approaches 1. The upper limit of 1 as $x \to 0$ is consistent with interactions with the sea quarks, S, dominating over interactions with the valence quarks in Equation 1.28. This is reasonable to expect because of the Bremsstrahlung-type radiation of gluons (and hence the abundance of sea quarks)

will increase logarithmically at small x [Clo79].

In a separate paper, Cleymans and Close [CC75] write the proton wavefunction as a single quark which interacts with the virtual photon plus a spectator two-quark core in an isospin state of $I = 0$ or $I = 1$. The proton wavefunction is constructed as

$$\left|P\right\rangle = \cos\varphi(x)\ \left|P_\beta\right\rangle + \sin\varphi(x)\ \left|P_\alpha\right\rangle\ , \tag{1.30}$$

where $|P_\beta\rangle$ is a state of a quark plus an $I = 0$ core, $|P_\alpha\rangle$ is a state of a quark plus an $I = 1$ core, and the mixing angle φ is *a priori* arbitrary and signifies the relative importance of the two states.

The state $|P_\beta\rangle$ has $I = 0$ and therefore must be a ud quark pair in a symmetric isospin state accompanied by a u quark. One can immediately write its wave function as

$$\left|P_\beta\right\rangle \equiv \left|I_{\rm tot}^{\rm core},\ I_z^{\rm core}; q\right\rangle = \left|0, 0; u\right\rangle\ . \tag{1.31}$$

The state $|P_\alpha\rangle$ has $I = 1$ and can either be a uu quark pair accompanied by a d quark, or a ud quark pair in an antisymmetric isospin state accompanied by a u quark. Combining these two states with the proper Clebsch-Gordon coefficients gives

$$\left|P_\alpha\right\rangle = \sqrt{\frac{2}{3}}\ \left|1, 1; d\right\rangle - \sqrt{\frac{1}{3}}\ \left|1, 0; u\right\rangle\ . \tag{1.32}$$

The interaction of the virtual photon with a quark within the proton is

weighted by the charge of the participating quark, and can be written as

$$\left|\gamma P\right\rangle = \frac{2}{3}\ \cos\varphi(x)\ \left|0,0;u\right\rangle + \sin\varphi(x)\left(-\frac{1}{3}\sqrt{\frac{2}{3}}\ \left|1,1;d\right\rangle - \frac{2}{3}\sqrt{\frac{1}{3}}\ \left|1,0;u\right\rangle\right)\ . \tag{1.33}$$

Likewise, for an interaction with a neutron, one obtains

$$\left|\gamma N\right\rangle = -\frac{1}{3}\ \cos\varphi(x)\ \left|0,0;d\right\rangle + \sin\varphi(x)\left(-\frac{1}{3}\sqrt{\frac{1}{3}}\ \left|1,0;d\right\rangle - \frac{2}{3}\sqrt{\frac{2}{3}}\ \left|1,-1;u\right\rangle\right)\ . \tag{1.34}$$

From these expressions, the ratio of the structure functions F_2^{en}/F_2^{ep} becomes

$$\eta \equiv \frac{F_2^{en}(x)}{F_2^{ep}(x)} = \frac{\langle\gamma N|\gamma N\rangle}{\langle\gamma P|\gamma P\rangle} = \frac{\cos^2\varphi + 3\sin^2\varphi}{4\cos^2\varphi + 2\sin^2\varphi}\ . \tag{1.35}$$

As we have seen in Figure 1.8, as $x \to 1$, experimental results indicate that the ratio η approaches 1/4, which implies a mixing angle of $\varphi = 0$ in Equation 1.35. This translates into the proton wavefunction of Equation 1.30 becoming

$$\left|P\right\rangle\ \underset{\varphi=0}{\longrightarrow}\ \left|P_\beta\right\rangle = \left|0,0;u\right\rangle\ , \tag{1.36}$$

as $x \to 1$, and, consistent with the earlier discussion, the scattering predominantly taking place on a u quark.

In other words, as x (or in our case, Q^2) increases, within this model one expects the scattering to take place on a u quark, leaving behind an $I = 0$ core. This $I = 0$ core would become a Λ in the exclusive kaon production case via the creation of an $s\bar{s}$ pair, as depicted in Figure 1.9.

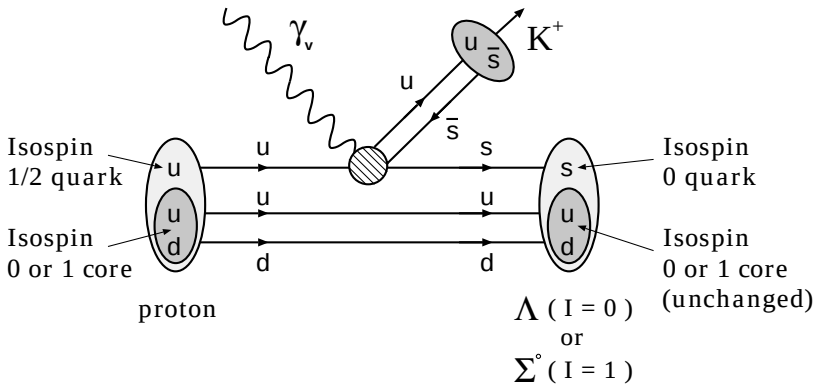

Figure 1.9: Cartoon diagram of kaon electroproduction. The virtual photon interacts with a u quark and leaves behind an $I = 0$ or $I = 1$ core. An $s\bar{s}$ pair is formed by the field Hamiltonian and splits up to produce a kaon and a hyperon. The $I = 0$ core state plus an s quark becomes a Λ, while an $I = 1$ core state becomes a Σ^0.

If the sea quarks are included in the calculation from the beginning, one gets an expression for the ratio of Σ^0/Λ production as a function of x to be

$$\frac{w(\Sigma^0)}{w(\Lambda)} = \frac{4\eta - 1 - 18\,(1-\eta)\,\delta}{9 - 6\eta}\ , \tag{1.37}$$

where w represents the probability of making either a Λ or Σ^0, and $\delta \geq 0$ is a measure of the contribution from $\{\bar{u}, \bar{d}, s, \bar{s}\}$ sea quarks as given by Nachtmann in [Nac74].

From examining Figure 1.8, Nachtmann proposes the simple form for the ratio η as a function of x:

$$\eta(x) = \begin{cases} (1-x) & 0 \leq x \leq 0.4 \\ \\ \frac{1}{12}(10 - 7x) & 0.4 \leq x \leq 1 \end{cases}\ . \tag{1.38}$$

An upper limit for the Σ^0/Λ production ratio is obtained by Nachtmann by neglecting δ. A lower limit can be shown to correspond to approximately $\delta = 0.7$

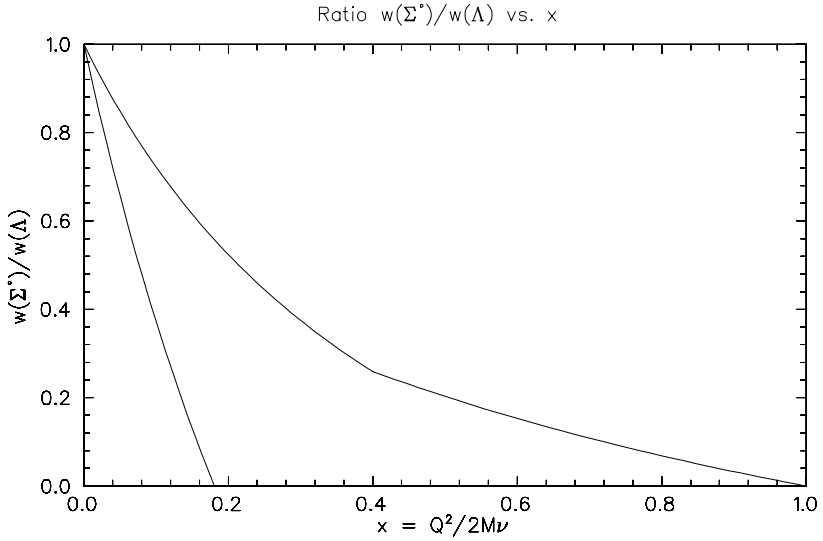

Figure 1.10: The upper and lower limits for the Σ^0/Λ production ratio given by Equation 1.39 as a function of Bjorken x.

[Nac74], leading to bounds on the ratio

$$\frac{4\eta - 1 - 18(1-\eta)(0.7)}{9 - 6\eta} \lesssim \frac{w(\Sigma^0)}{w(\Lambda)} \leq \frac{4\eta - 1}{9 - 6\eta} \,, \tag{1.39}$$

which are plotted in Figure 1.10.

Additionally, it should be noted that the ratio Σ^0/Λ is found to be zero with increasing Q^2 independent of quark-parton model, due to SU(3) symmetry considerations alone [CC75].

These arguments strictly apply to the transverse cross section, σ_T, only [Nac74]. This admits a second possibility for the decrease of the ratio Σ^0/Λ with increasing Q^2. If the production cross sections are dominated by contributions from σ_L as Q^2 increases, the ratio Σ^0/Λ could decrease by virtue of the fact that the couplings $g^2_{\Sigma NK} \ll g^2_{\Lambda NK}$. This relationship between the coupling constants is found by the various isobaric models of Section 1.5.2, and also from SU(3)

symmetry considerations [Fey72]. Thus, the separation of the Λ and Σ^0 cross sections into their longitudinal and transverse components, and the subsequent inspection of the Σ^0/Λ ratio, may help to shed light on the reaction mechanisms for kaon electroproduction.

Chapter 2

Experimental Apparatus and Data Acquisition

2.1 Overview

Data acquisition for experiment E93-018 (and also E91-016) took place in Hall C of Jefferson Lab during the period from August through November 1996. Electrons from the CEBAF accelerator with energies up to 4045 MeV* were incident at 100% duty factor (i.e., "continuous wave" or "CW") upon a 4.36 cm long liquid hydrogen target located in an evacuated scattering chamber. The scattered electrons were detected in the High Momentum Spectrometer (HMS), and the electroproduced kaons (along with background pions and protons) were detected in the Short Orbit Spectrometer (SOS). The detector elements themselves are housed in concrete-shielded huts located at the exit of each spectrometer. The signals from the detectors were relayed to remote electronics (located in the

*The specific settings are shown in Table 1.2.

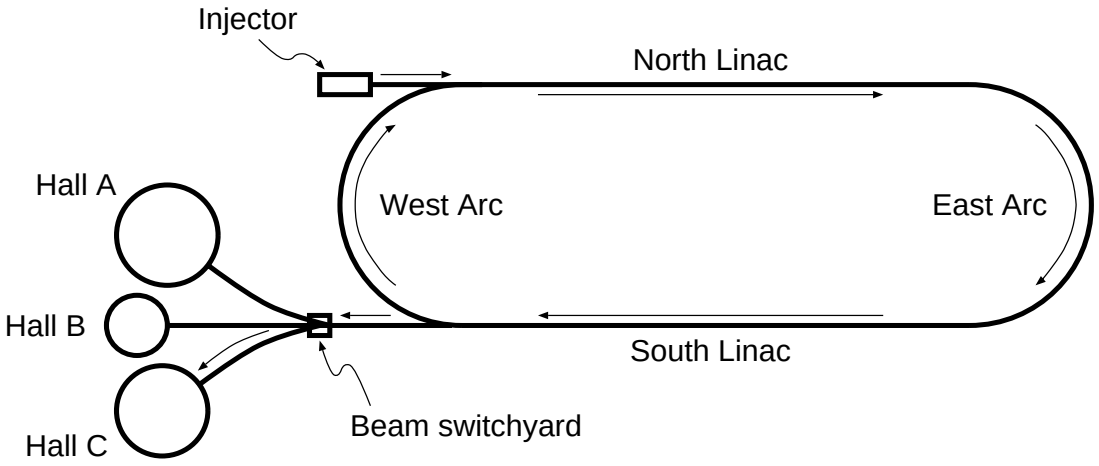

Figure 2.1: Schematic top view of the CEBAF accelerator.

"Hall C counting house") to be processed and recorded by the data acquisition system. This chapter discusses in detail the apparatus used and data taking for E93-018.

2.2 Accelerator

A schematic diagram of the accelerator is shown in Figure 2.1. Electrons from the injector are sent into the north linac at an energy of 45 MeV. In the north linac section, the electrons are accelerated through superconducting niobium RF resonant cavities and, in a standard tune, gain 400 MeV in energy. The beam is then guided through the east arc and into the south linac, where it is accelerated for another 400 MeV energy gain. The beam can then either be sent directly to the Beam SwitchYard (BSY) for distribution to the experimental halls, or the beam can be steered through the west arc for another pass through the two

linacs, thereby acquiring another 800 MeV of energy. This recirculation process can be repeated up to four times, resulting in simultaneous beams that make a maximum of five passes through both linacs, yielding energies from 845 MeV to 4045 MeV in steps of 800 MeV. The same linacs are used for acceleration in each pass, but because the simultaneous beams from different passes are at different energies, different beam pipes with their own magnets are necessary to steer the beam around the arcs. It should also be noted that for one kinematic setting in E93-018, the accelerator was tuned so that the beam would acquire only $\sim$ 700 MeV per pass (and only $\sim$ 39 MeV at the injector), resulting in a five-pass beam with an energy of 3539 MeV. This was the first time that a non-standard beam energy was used in a Jefferson Lab experiment.

The CW beam is not truly "continuous" in that it has a microstructure consisting of approximately 2 ps long pulses [Ree97] occurring at a frequency of 1497 MHz, dictated by the RF power used in the resonant cavities [Leg96]. At the BSY, every third pulse can be delivered to each of the three experimental halls, resulting in a frequency of 499 MHz for each hall (i.e., short pulses spaced about 2 ns apart). At the time of this writing, the accelerator is capable of simultaneously delivering beams of different energy to all three experimental halls, although at the time of the experiment, simultaneous delivery was achieved into only Halls A and C, as Hall B was not yet fully operational. Further information regarding the accelerator can be found in [Leg96, Dur96].

2.3 Beamline and Instrumentation

For a Hall C experiment such as E93-018, the beam is sent from the BSY into the Hall C arc, which directs the beam into the Hall C beamline. Measurements of the beam profile and position are made in the arc using high-resolution superharp scanners [Yan94]. The transverse size of the beam was measured several times during the experiment, and was typically found to be about 200 μm FWHM.

By using the superharps to measure the absolute beam position at the entrance, middle, and exit of the arc, it was possible to extract the beam energy from knowledge of the dispersive characteristics of the arc dipoles. This was not done concurrently with data taking as it used the destructive measurements made by the superharps, and also required the deactivation of all the focusing elements in the arc. The details of this measurement can be found in [GTY96, Dut95]. The beam energy can also be measured using several "physics techniques" that are independent of the arc measurement [Arr98]. These techniques rely on measuring (a) differential recoil between inclusive elastic scattering processes in light and heavy nuclei, (b) comparison of the ground state to the first excited state in inclusive scattering from carbon, and (c) measurement of elastic ^{1}H(e,e$'$p) scattering.

Resonant cavity Beam Position Monitors (BPMs) are situated along both the arc and the Hall C beamline and allowed for a continuous measurement of

the beam position and angle at the target. The accuracy of the absolute position measurement was determined to be ± 1.0 mm, with a relative position uncertainty of approximately 0.1 mm. Details regarding the BPMs (hardware, calibration) can be found in [Guè96].

The last major elements of the beamline instrumentation are the three Beam Current Monitors (BCMs), and the Unser current monitor. The BCMs are cylindrical resonant cavities similar to the BPMs, and provided a continuous (relative) measurement of the current during each data run. The Unser monitor (a parametric DC current transformer) has a very stable gain characteristic, and was used as an absolute current calibration for the BCMs. BCM calibration runs were taken periodically during E93-018, and using the information from the Unser monitor, a global software parameter file was generated so that the amount of incident charge could be extracted from the BCM information for each data run. Further details about the charge measurement can be found in Section 3.6.11, and in [Nic95], [Arm99], and [HCD].

2.4 Beam Rastering

Because the CEBAF electron beam has such a small transverse size and is at high current, the power density is sufficient to potentially cause damage to the

target and/or the beam dump*. Therefore, two separate rastering systems, one "fast" and one "slow", are in place to decrease the power density at the target and the dump, respectively.

The "fast raster", which is used to protect the target, is located along the beamline just before the entrance to Hall C (see Figure 2.4). The raster consists of two sets of steering magnets, for the horizontal and the vertical directions. For E93-018, the beam was steered sinusoidally at 17.0 kHz (vertical) and 24.2 kHz (horizontal) such that the position at the target varied by ± 0.5 mm. These frequencies were selected to ensure very many cycles before the raster pattern retraces itself.

The "slow raster" (also known as the "dump raster"), which is used to protect the beam dump, is located just before the scattering chamber along the Hall C beamline. This raster was not used during the running of E93-018 because the beam currents were low enough (viz., always much less than 80 μA) that multiple scattering in the Helium-filled exit beam pipe was sufficient to decrease the beam power density at the dump below a problematic level.

*Most of the electrons in the beam actually pass through the target without interaction. The excess beam travels beyond the target through a Helium-filled beam pipe that extends out of Hall C through an exit tunnel, and is absorbed by the "beam dump". The beam dump is a large aluminum (primarily alloy 6061-T6) cylinder with an aluminum/water heat exchanger [Wis97].

2.5 Scattering Chamber and Targets

This experiment implemented both solid and cryogenic targets. The targets were located in an evacuated cylindrical aluminum scattering chamber (123.2 cm diameter) located at the spectrometer pivot. The solid targets were used for spectrometer checkout and calibration. For example, data were taken with a ^{12}C target for the purpose of calibrating the optics as a function of extended target length (see Section 3.3). When not in use, the solid target ladder was mechanically lifted up and out of the beam path.

The cryogenic target ladder, shown in Figure 2.2, supports three independent circulation loops for cryogenic material, each of which contains a $\sim$4 cm and a $\sim$15 cm target cell. In E93-018, the primary target was a (4.36 $\pm$ 0.01) cm long liquid hydrogen (LH_2) target located in Loop 1 (see Figure 2.3). Loop 2 was empty, and Loop 3 contained liquid deuterium. The target cell was composed of aluminum (made from a beer can blank) with a convex beam entrance window (alloy 6061) of thickness (71 $\pm$ 3) μm, side wall (alloy 6061) of thickness (130 $\pm$ 5) μm, and a beam exit window (alloy 3004) of thickness (137 $\pm$ 5) μm [Dun97b].

The liquid hydrogen was cooled by a heat exchanger (not shown) in which the refrigerant was 15 K gaseous helium supplied by the CEBAF End Station Refrigerator (ESR). The LH_2 target was operated at 19 K and $\sim$ 24 psia (about 2 K subcooled below the boiling point). The temperature was measured using several Cernox carbon-glass resistors [DDW97] and was regulated by maintaining

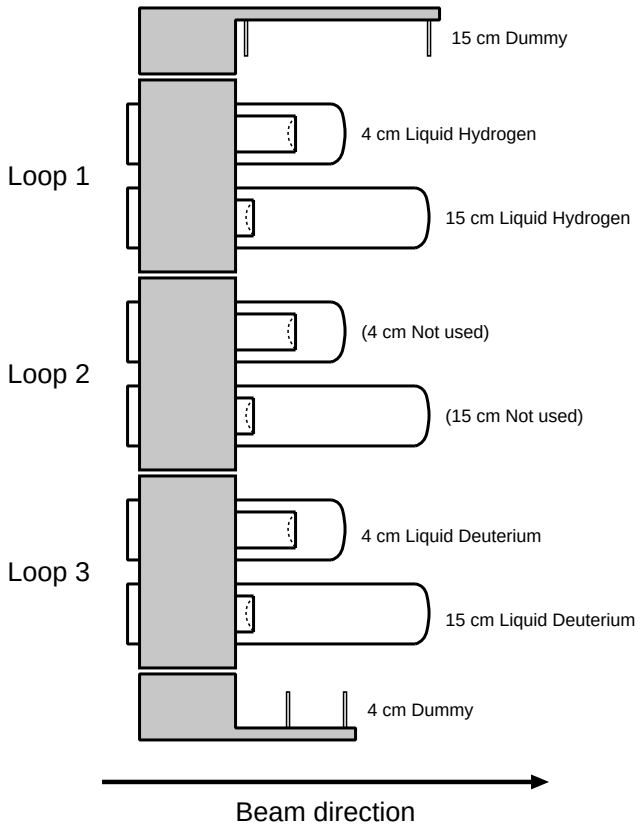

Figure 2.2: Cells in the cryogenic target stack. The plumbing associated with the circulation and cooling of the target material is not shown (see [Mee99]).

a constant heat load on the target liquid. The heat load was controlled by two independent heaters, high and low power. The low power heater was regulated in a temperature feedback loop by an Oxford ITC502 temperature controller. The high power heater was controlled in a feedback loop with beam current using EPICS (Experimental Physics Industrial Control System) software so as to maintain a constant heat load on the target. With no beam on the target, the software feedback loop activated the heaters to a user-controlled setpoint. When the beam was turned on, the heaters would decrease their power output to

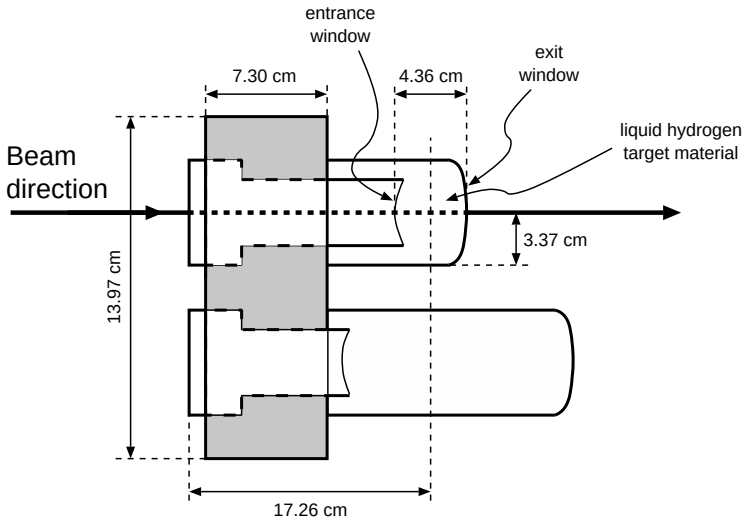

Figure 2.3: Schematic of Loop 1 liquid hydrogen targets showing the relevant dimensions.

compensate for the added current-dependent power deposition due to the beam passing through the target. The low power heater also compensated for smaller fluctuations, such as changes in the refrigerant temperature, by maintaining a fixed target temperature. Further details regarding the cryogenic target can be found in [Dun97a, Mee99, Ter99].

Also included on the cryotarget ladder were ∼4 cm and ∼15 cm "dummy" targets (see Figure 2.2). The dummy target used for E93-018 consisted of a pair of aluminum solid targets separated by ∼4 cm that were each approximately ten times the radiation length of the actual target windows. The upstream dummy target (alloy 5052) was 96.0 μm thick, and the downstream dummy target (alloy 3004) was 96.7 μm thick [Dun97b]. The dummy targets were purposely made

thicker than the actual cell windows so as to increase the speed with which the data could be taken, and also to simulate the radiative effects of the missing cryogenic material. Data taken with the dummy target were normalized to the actual window thicknesses and were then used to subtract the contribution of scattering from the target windows from the liquid hydrogen data.

2.6 HMS: The Electron Arm

A schematic top view of the layout of Hall C during E93-018 showing the relation between the spectrometers and the beamline/target chamber is depicted in Figure 2.4. The scattered electrons were detected in the High Momentum Spectrometer (HMS). The HMS is a magnetic spectrometer with three superconducting quadrupole magnets in sequence followed by a superconducting dipole, as shown in Figure 2.5. The dipole causes a vertical bend of 25° for the central ray. The specifications of the HMS are summarized in Table 2.1.

A 6.35 cm thick Heavymet* collimator with an octagonal aperture is located at the entrance of the spectrometer in order to define the angular acceptance, as shown in Figure 2.6. The quadrupoles are current regulated, and the dipole field is regulated by an NMR probe in a feedback loop. The currents/fields for each magnet were calculated for each desired central momentum and were set remotely from the counting house.

*An alloy of mostly tungsten, with 10% CuNi added for machinability.

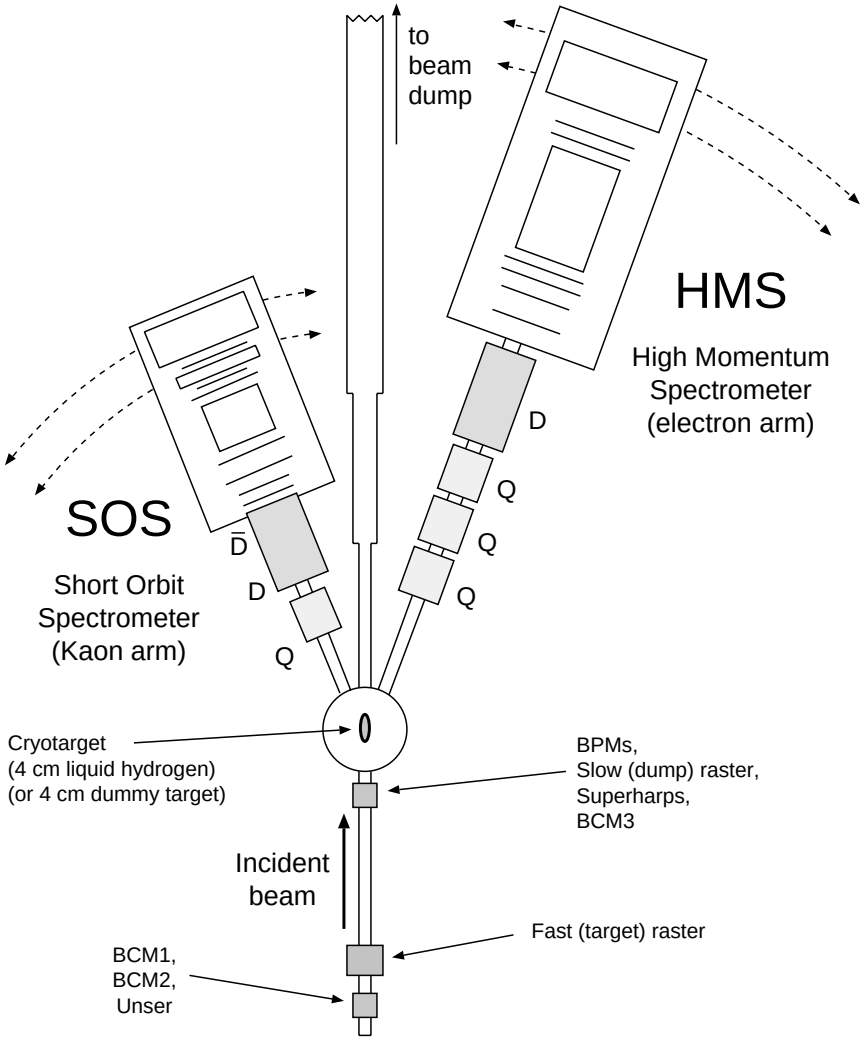

Figure 2.4: Schematic top view of Hall C spectrometer setup showing the location of the HMS and SOS relative to the target and incident beam.

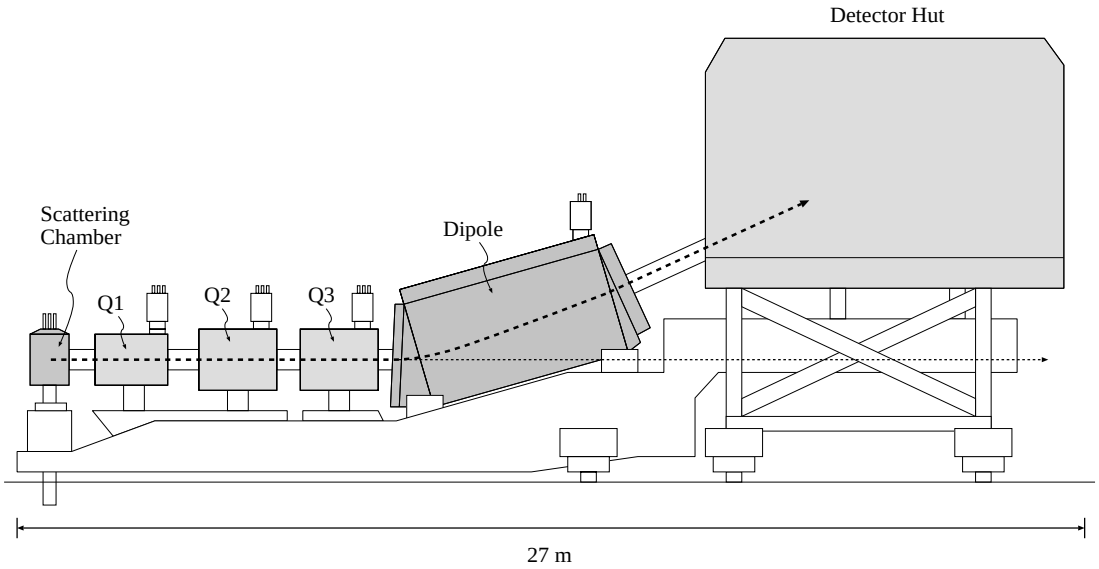

Figure 2.5: Schematic side view of the HMS carriage.

Maximum central momentum		7.5 GeV/c
Momentum acceptance		± 10 %
Dispersion		≈ 3.9 cm / %
Angular Acceptance	Horizontal (in-plane)	≈ ± 28 mrad
	Vertical (out-of-plane)	≈ ± 70 mrad
Solid Angle	Point target	≈ 7.0 msr
	∼4 cm LH_2 target	≈ 6.5 msr
Minimum central angle setting (E93-018)		13.2°
Optical length		26.0 m
Bend angle through dipole		25°

Table 2.1: Selected properties of the HMS.

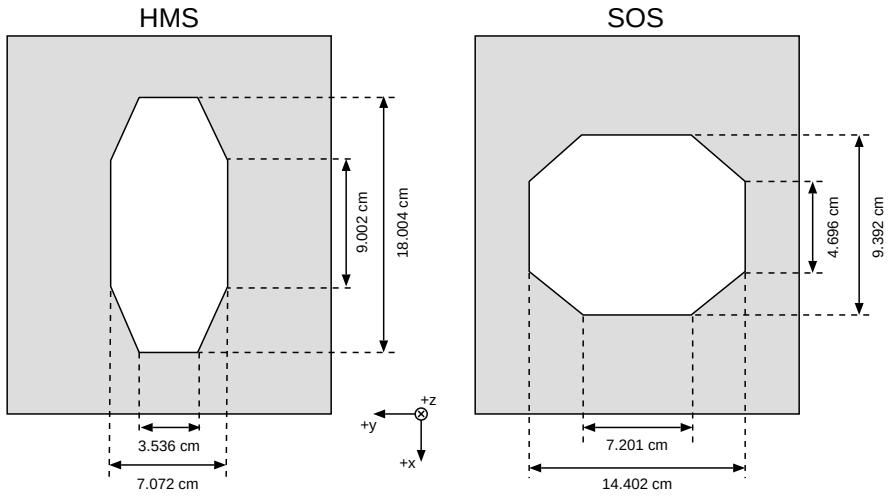

Figure 2.6: Dimensions of the HMS and SOS collimators, shown as viewed from the target location. The orientation of the collimators in the Beam coordinate system (see Section B.2) is given.

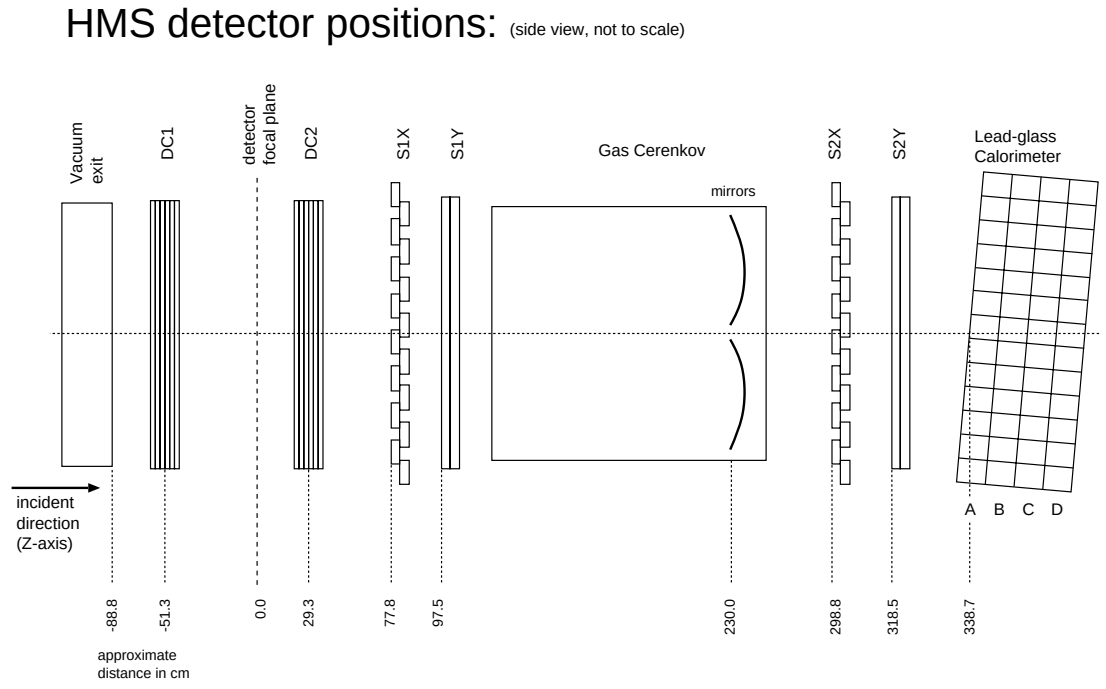

Figure 2.7: Schematic of the HMS detector package showing approximate detector locations in cm along the central ray (the horizontal dotted line). The detectors are all located within the concrete-shielded HMS detector hut.

Beyond the exit of the dipole, the vacuum system extends into the front of the HMS detector hut. The scattered particles pass out of vacuum through a Kevlar/Mylar window and are then incident upon the HMS detector stack, shown in Figure 2.7.

2.6.1 HMS Drift Chambers

The first detectors encountered by the scattered electrons are a pair of identical drift chambers (DCs) separated by 80.6 cm. Each of the HMS drift chambers contains six planes of wires, ordered X-Y-U-V-Y′-X′ , as in Figure 2.8. The X and X′ wires determine the dispersive coordinate (x, roughly vertical), the Y and Y′ wires determine the transverse coordinate (y, roughly horizontal), and the U and V planes are rotated by 15° in the clockwise and counterclockwise directions about the incident particle direction (z), respectively, with respect to the Y wires. The active area of each chamber is approximately $(x \times y) = (107 \times 52)$ cm^2.

An argon-ethane gas mixture (equal parts by weight, with a small amount of isopropyl alcohol) is circulated through the chambers at a rate between 400-800 cc/min. The sense wires are 25 μm gold-plated tungsten separated by 1 cm within a given plane. The field wires are 150 μm gold-plated Cu-Be and are held at negative high voltages ($\sim 1800 - 2500$ V) such that they generate equipotential surfaces that are approximately circular around each sense wire. A

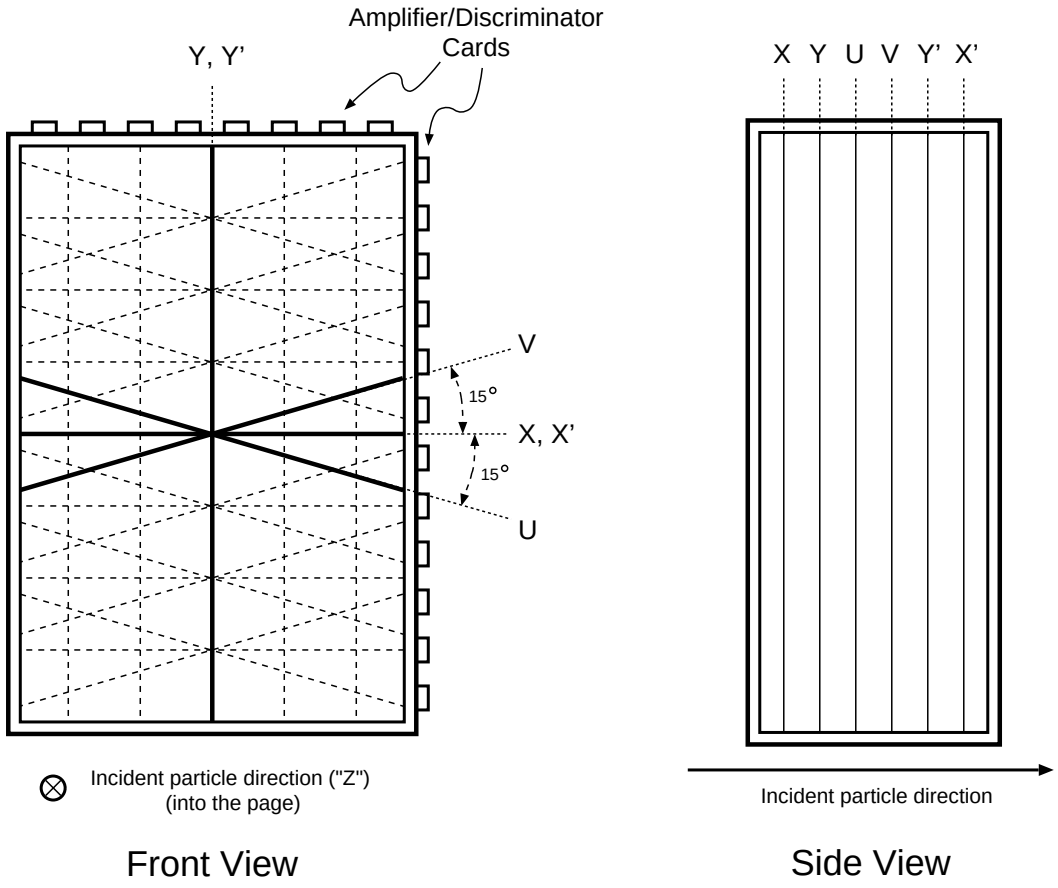

Figure 2.8: Schematic of an HMS drift chamber showing the orientations of the six wire planes.

single "cell" surrounding a sense wire in a given plane is shown in Figure 2.9.

When a charged particle passes through the chamber, it ionizes the gas mixture along its trajectory ("track") and the potential created by the field wires directs the liberated electrons to the sense wires nearest the track. The time that it takes these electrons to drift to the sense wire (up to about 100 ns) is proportional to the distance of the track from the sense wire.

The signals from each wire were amplified and discriminated on cards at-

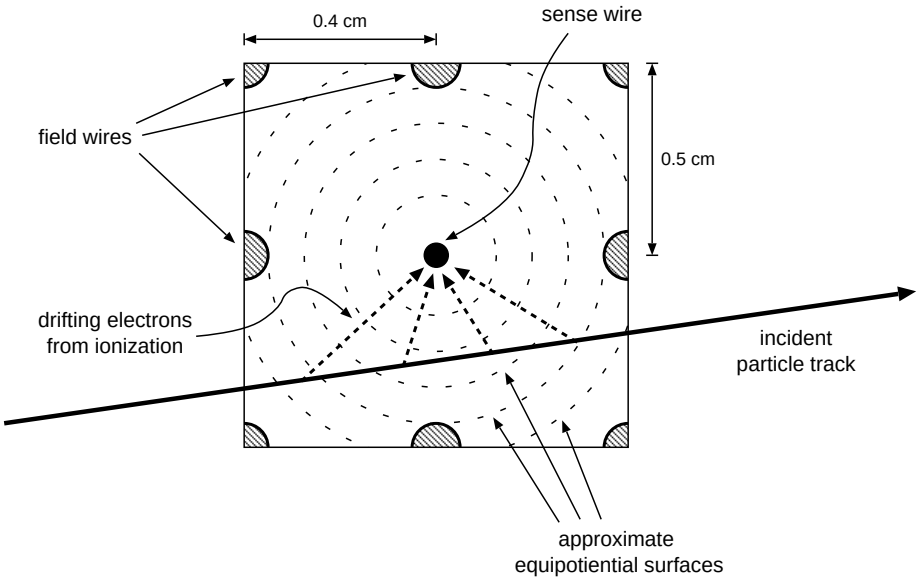

Figure 2.9: Cross section view of an idealized single cell in an HMS drift chamber. For details see text.

tached directly to the chambers and then sent as START signals to Lecroy 1877 multi-hit TDCs (Time-to-Digital Converters) located in the detector hut (the STOP signal was formed by the complete electron trigger which will be discussed in a subsequent section). By knowing the absolute position of the sense wires that were "hit" (from survey data) and the drift time from the TDCs, the position of the particle at each plane could be determined by the tracking software with resolution, $\sigma = 200 - 300\ \mu m$. The tracking software then uses the position information gathered from both drift chambers to reconstruct the trajectory of the particle through the hut (see Section 3.2). For further details regarding the HMS drift chambers, please refer to [Bak95].

Plane	Number of elements	Vertical Size Δx (cm)	Horizontal Size Δy (cm)	Thickness Δz (cm)
S1X	16	8.0	120.5	1.0
S1Y	9	75.5	8.0	1.0
S2X	16	8.0	120.5	1.0
S2Y	9	75.5	8.0	1.0

Table 2.2: HMS hodoscope information

2.6.2 HMS Scintillator Hodoscopes

The HMS is also equipped with four planes of scintillator hodoscopes. Each plane is composed of multiple scintillator elements (called "bars" or "paddles"). Two of the planes have the elements arranged in the dispersive ("X", roughly vertical) direction, and the other two are distributed along the transverse ("Y", roughly horizontal). The planes are grouped into two X−Y pairs (S1X, S1Y) and (S2X, S2Y), and were situated as shown in Figure 2.7.

Each element is a long narrow bar of BC404 scintillator material optically coupled on both ends to UVT lucite light-guides attached to 2" diameter Philips XP2282B photomultiplier tubes (PMTs). The bars were wrapped in one layer of aluminum foil and two layers of Tedlar to ensure light-tightness. The elements in a given plane are staggered (as shown for the "X" planes in Figure 2.7) so that they overlap by 0.5 cm to prevent gaps between them. Table 2.2 lists the number of elements in each plane along with their dimensions.

The analog signals from the PMTs are routed via a patch panel to the

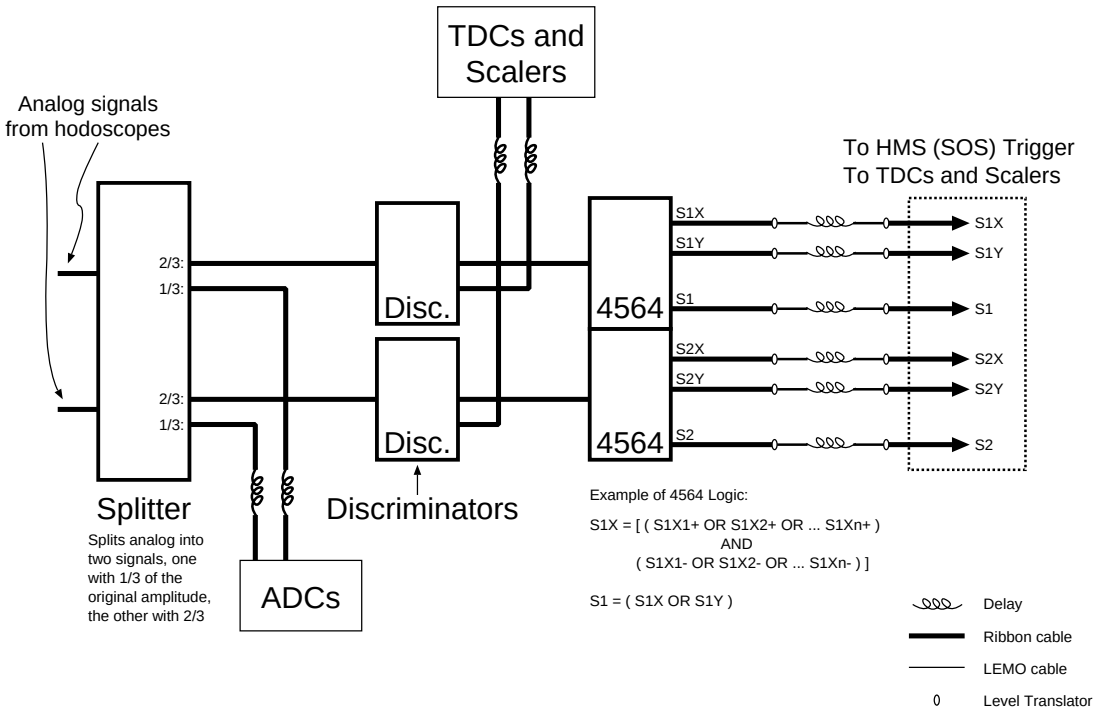

Figure 2.10: HMS/SOS hodoscope electronics diagram. For details see text.

electronics racks in the counting house. Figure 2.10 depicts the setup of the hodoscope electronics. The analog signals are split at a voltage divider into two signals (with 1/3 and 2/3 amplitude). The smaller signals are sent through ~ 400 ns of cable delay and then into Analog-to-Digital Converters (ADCs) to record pulse heights from each bar that was hit. The larger signals are discriminated (Philips PS7106), and one set of NIM outputs is sent (with appropriate delays) to TDCs (for timing information) and also to VME scalers. The other set of outputs is utilized for the trigger logic and sent directly into a Lecroy 4564 logic module.

The Lecroy 4564 first generates the logical OR of all the discriminated

signals from tubes on one side of a given plane. For example, the signal **S1X+** can be expressed as **S1X+** $\equiv$ (**S1X1+** OR **S1X2+** OR **S1X3+** OR ... **S1X16+**), where the notation "**S1Xn+**" represents the PMT located on the n^{th} element of plane S1 on the positive-x side of the central ray. There are an equivalent set of signals for the "**−**" side of each plane. Then, these signals are combined into six outputs: For each plane (using signals from the S1X plane as an example) a quantity analogous to **S1X** $\equiv$ (**S1X+** AND **S1X−**), is output (i.e., four outputs **S1X**, **S1Y**, **S2X**, and **S2Y**). Also, the X−Y pairs are further combined to form **S1** $\equiv$ (**S1X** OR **S1Y**), and **S2** $\equiv$ (**S2X** OR **S2Y**). These logical outputs are then sent to the main trigger logic (and also to scalers to be recorded).

The hodoscope arrays serve two purposes: (1) they provide an integral part of the trigger for each spectrometer (the NIM signals), and (2) they allow for measurement of the Time-Of-Flight (TOF) of the particle (from the TDC and ADC information). From the TOF and a knowledge of the z-positions of the hodoscope planes, the velocity ($\beta = v/c$) of the incident particle can be calculated. The TOF calculation is discussed further in Section 3.4. The timing resolution of the hodoscopes in the HMS was about $\sigma \sim 100$ ps per plane, allowing for an RMS resolution in velocity of $\Delta\beta \approx 0.017$ for $\beta = 1$ electrons.

2.6.3 HMS Particle Identification (PID): Gas Čerenkov

In addition to electrons, some negatively charged pions (π^-) traversed the spectrometer and were detected by the HMS in E93-018. These pions were a background that had to be identified so that they could either be rejected online by the trigger or corrected for in the offline analysis. All of the HMS momentum settings for E93-018 were high enough such that pions could not be fully separated from electrons solely on the basis of their velocity as calculated from TOF due to insufficient resolution. Thus, to accomplish π^-/e^- separation, both a gas Čerenkov detector and a lead-glass calorimeter are included in the detector stack.

The HMS gas Čerenkov is generally operated as a "threshold Čerenkov" detector. A threshold Čerenkov detector discriminates between species of charged particles on the basis of whether or not their velocity is above a certain value. This is accomplished by exploiting the fact that a charged particle will radiate energy ("Čerenkov light") if it travels through a medium at a velocity larger than the speed of light in that medium. This condition is given by

$$\beta > \beta_{\text{threshold}}, \quad \text{or} \quad \beta > 1/n, \tag{2.1}$$

where n is the refractive index of the medium. Therefore, if n is chosen judiciously, particle identification can be made on the basis of the presence or absence of light in the threshold Čerenkov detector. A more detailed discussion of Čerenkov radiation and threshold detectors is presented in Appendix A which describes the SOS aerogel Čerenkov detector.

The HMS gas Čerenkov detector is a large cylindrical tank (diameter of $\sim$ 150 cm, length of $\sim$ 152 cm) situated in the middle of the detector stack between the hodoscope pairs S1 and S2 (Figure 2.7). During E93-018, the detector was filled with CO_2 gas at room temperature and atmospheric pressure. The refractive index of the gas was $n = 1.00041$, yielding a threshold velocity of $\beta_{\text{threshold}} = 0.999593$. For the $\sim$ 1 GeV HMS momenta used in E93-018, electrons were always well above the threshold and therefore radiated Čerenkov light. However, pions (or any heavier particles) did not exceed the threshold velocity for any of the E93-018 momentum settings* and hence did not produce Čerenkov light.

Light from a radiating particle is collected inside the detector by two mirrors located towards the back of the cylinder, and is focused upon two 5 inch Burle 8854 PMTs. The signals from each PMT are brought upstairs to the counting house, and each is split in a fashion similar to the hodoscope signals. One pair of analog signals is sent through cable delay to an ADC. The other pair of signals is summed at a linear fan-in (Philips 740) and then discriminated to give NIM logic signals. The logic signals called **Č**, along with its complement, **NOT Č**, are sent directly to the pretrigger logic (and also to scalers and TDCs), and are used in conjunction with the signals from the lead-glass calorimeter in order to reject pions.

*For example, at $|\mathbf{p}| = 1$ GeV, an electron has $\beta = 0.99999987$, while a π^- has $\beta = 0.9904$.

2.6.4 HMS Particle ID: Lead-Glass Calorimeter

As mentioned earlier, a lead-glass calorimeter was also utilized for π^-/e^- separation. When a high energy electron enters the lead-glass material, it radiates Čerenkov light until it quickly interacts with the fields of the nuclei and radiates photons via Bremsstrahlung. These Bremsstrahlung photons can then produce secondary electron-positron pairs that also radiate Čerenkov light and/or more Bremsstrahlung photons, and those photons undergo similar processes. The thickness of lead-glass was chosen so that this cascading shower of particles continues until all of the energy of the incident electron is exhausted and a light signal approximately proportional to the original electron energy is created.

On the other hand, pions that enter the lead-glass radiate Čerenkov light, but do not produce a Bremsstrahlung shower. In fact, most pions will not be stopped inside the lead-glass detector, unless they undergo a strong interaction with a nucleus in the lead-glass. In this case, the most likely mechanism is the charge exchange reaction $\pi^- p \rightarrow \pi^\circ n$. The π° quickly decays to two photons, which then will cause an electromagnetic shower. This effect is the dominant cause of misidentifying pions as electrons in the calorimeter.

The HMS calorimeter consists of ($10 \times 10 \times 70$) cm^3 blocks of TF1 lead-glass (density = 3.86 g/cm^3, radiation length = 2.54 cm, $n = 1.67$) arranged in four planes (A, B, C, D) of 13 blocks each (see Figure 2.7). An electron loses the majority its energy in the first plane of blocks, plane A. The entire calorimeter

is tilted at an angle of 5° relative to the central ray as in Figure 2.7 in order to prevent any losses that would result from particles traveling through the spaces between blocks.

The energy deposited in each lead-glass block is detected by a 3-inch PMT (Philips XP3462B) located on one side of the block. The blocks were wrapped with layers of aluminized Mylar and Tedlar to improve light collection and to ensure light-tightness. Also, the PMTs were gain-matched in hardware to within 20% for use in the trigger [Mkr96].

The analog signals from the PMTs on each block are sent to the counting house where each signal is split in a fashion similar to the hodoscope/Čerenkov signals. One set of analog signals is sent through cable delays to ADCs. The other set is summed using linear fan-ins (Philips 740) to produce analog signals representing the amount of energy deposited into planes A, B, C, and D individually. Two copies of the signal from plane A (called **PRSUM**) are discriminated separately, one at a high threshold (**PRHI**) and one at a lower threshold (**PRLO**), representing gates on two different amounts of energy deposition into the first layer of the calorimeter. The signals from all four planes are also summed together (**SHSUM**) and discriminated to produce a signal (**SHLO**) providing a gate on the total energy deposited in the calorimeter. The NIM signals thus generated are sent directly to the pretrigger logic (and also to scalers and TDCs), and are used in the rejection of pions. The implementation of particle identification

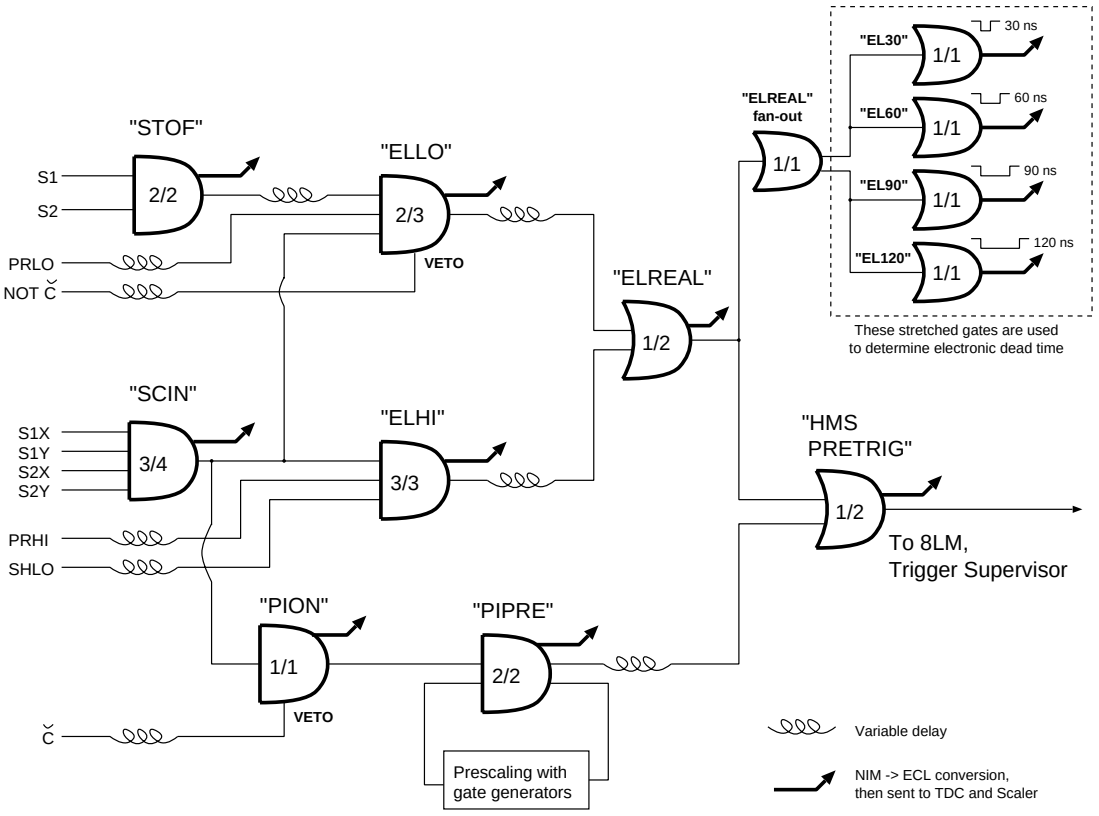

Figure 2.11: HMS pretrigger logic diagram. In quotation marks are given the Hall C specific names for the signals emerging from the units. The notation i/j indicates that the logic selected requires i input signals to be present in coincidence out of the j possible inputs. For further information see text.

(PID) in the electron pretrigger will be discussed in detail in the next section.

2.6.5 HMS Pretrigger

The logic signals created from the various HMS detectors are combined to form the electron pretrigger (**HMS PRETRIG**), as shown in Figure 2.11. The electron pretrigger logic is designed such that whenever an HMS event meets a set of selection criteria (i.e., it has appropriate signals from the detectors), an

HMS PRETRIG signal is sent to the coincidence logic.

Such criteria were set up in hardware, rather than exclusively in the offline software analysis, to reduce both dead time and data size. If the rate of background particles is high relative to the rate of useful particles, the data acquisition system can waste time accepting uninteresting events while being "dead" to interesting events in the meantime. Also, as one accumulates uninteresting events in an experiment, an increasingly greater amount of storage space becomes necessary to record the data. With the selection criteria in a hardware pretrigger, uninteresting events can be thrown out quickly, preventing the data acquisition system from wasting time and space on them. In E93-018, the hardware pretrigger was set to be as loose as possible while maintaining an acceptably low dead time in the data acquisition system.

The central part of the standard Hall C electron pretrigger is the scintillator information. Two different signals (called **STOF** and **SCIN**) are utilized in parallel to give two different conditions (**ELHI** and **ELLO**) for an event to be accepted as a valid electron event:

1. **ELHI**:

   SCIN is formed when 3 of the 4 signals from the hodoscope planes (**S1X**, **S1Y**, **S2X**, **S2Y**) are present. The **SCIN** signal is also sometimes simply referred to as "the 3/4 signal." Requiring 3/4 planes rather than strictly 4/4 reduces the sensitivity of the trigger to the effects of problems in

any single hodoscope paddle, and allows for the calculation of the hodoscope efficiencies (see Section 3.6.1).

A 3/3 coincidence, **ELHI**, is then formed from the AND of **SCIN**, **PRHI**, and **SHLO**. Thus, **ELHI** requires that an event not only has valid scintillators, but also eliminates a significant fraction of the pions by placing a relatively strong restriction that the event has a large lead-glass signal.

2. **ELLO**:

   STOF is formed from the AND of **S1** and **S2**, and hence requires that at least one hodoscope paddle in each of the front and back X−Y pairs S1 and S2 fired. This is the minimum amount of hodoscope information that is sufficient to calculate the time of flight and also helps to prevent random signals from being accepted as valid pretriggers. Note that **STOF** is less restrictive than **SCIN**.

   ELLO is then formed by first requiring that 2 of the 3 signals **STOF**, **PRLO**, and **SCIN** are present. Then, the presence of a signal from the gas Čerenkov detector is required by vetoing **ELLO** on the signal **NOT Č**. As opposed to the **ELHI** signal which relies on the lead-glass, **ELLO** is primarily dependent on the gas Čerenkov.

Continuing with the pretrigger logic, the OR of **ELHI** and **ELLO** is taken to form **ELREAL**. This design is implemented so that the pretrigger is not likely

to become too strict, thereby throwing out good electron events, if either the lead-glass or gas Čerenkov have a hardware problem during data taking. Two copies of the **ELREAL** signal are generated, one which goes to **HMS PRETRIG**, and another which is fanned out to four signals **EL30**, **EL60**, **EL90**, and **EL120**. The latter four signals will be discussed the Section 3.6.3 dealing with the calculation of the electronic live time.

There is an additional third logic path that is designed specifically to accept a fraction of the background pion events for diagnostic purposes. The gate **PION** is simply a 3/4 signal (**SCIN**) that has no Čerenkov signal (implemented by vetoing the **PION** gate on the signal **Č**). The **PION** signal is then combined with a prescaling circuit to form **PIPRE**, which ensures that a low-rate sample of pions is sent along to the data acquisition system.

Finally, the OR of **ELREAL** and **PIPRE** forms the signal **HMS PRETRIG**, which is forwarded to the coincidence electronics (the 8LM and Trigger Supervisor, to be discussed in Section 2.10).

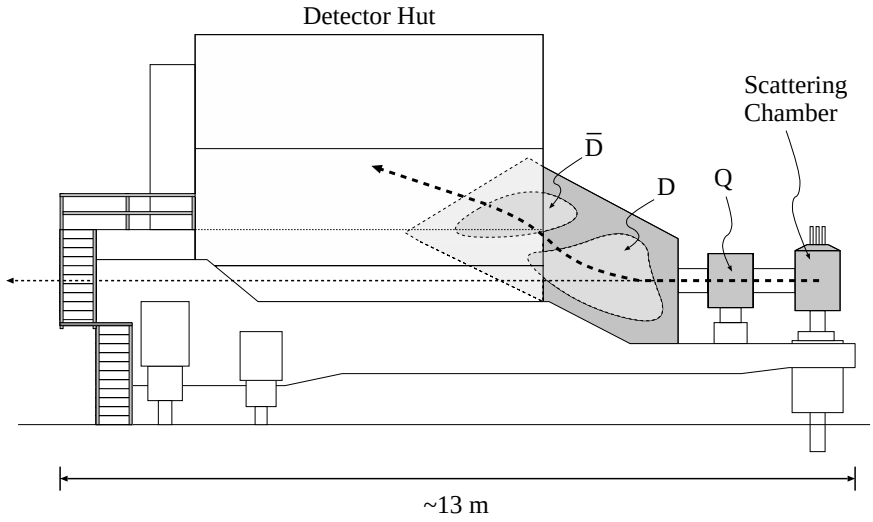

Figure 2.12: Schematic side view of the SOS carriage.

2.7 SOS: The Hadron (Kaon) Arm

The electroproduced kaons were detected in the Short Orbit Spectrometer (SOS). The SOS is a non-superconducting magnetic spectrometer with one quadrupole (Q) magnet followed by two dipoles (D and $\overline{\text{D}}$) which share a common yoke, as shown in Figure 2.12. The first dipole bends the central ray upward by 33°, and the second dipole bends the ray back downward by 15°, for a total of 18° upward. The specifications of the SOS are summarized in Table 2.3. A 6.35 cm thick Heavymet collimator with an octagonal aperture is located at the entrance of the spectrometer in order to define the angular acceptance as shown in Figure 2.6. As opposed to the HMS collimator which is "tall and thin" (see Table 2.1), the SOS collimator is "short and wide" (see Table 2.3). Each magnet is regulated by its own Hall probe in a feedback loop. The magnetic fields were calculated for

Maximum central momentum		1.75 GeV/c
Momentum acceptance		± 20 %
Dispersion		< 0.92 cm / %
Angular Acceptance	Horizontal (in-plane)	≈ ± 65 mrad
	Vertical (out-of-plane)	≈ ± 40 mrad
Solid Angle	Point target	≈ 7.5 msr
	∼4 cm LH_2 target	≈ 6.5 msr
Minimum central angle setting (E93-018)		13.4°
Optical length		7.4 m
Bend angle through dipole		18°

Table 2.3: Selected properties of the SOS.

each central momentum setting and were set remotely from the counting house.

The SOS was designed with a short flight path in order to facilitate experiments such as E93-018 which detect unstable, short-lived particles such as kaons or pions.

Beyond the exit of the second dipole, the vacuum system extends into the front of the SOS detector hut. The scattered particles pass out of vacuum through a Kevlar/Mylar window and are then incident upon the SOS detector stack as shown in Figure 2.13.

2.7.1 SOS Drift Chambers

As is the case for electrons in the HMS, the first detectors encountered by the hadrons are a pair of identical drift chambers (DCs) separated by 49.6 cm. Each of the SOS drift chambers contains six planes of wires, ordered X-X′-U-U′-

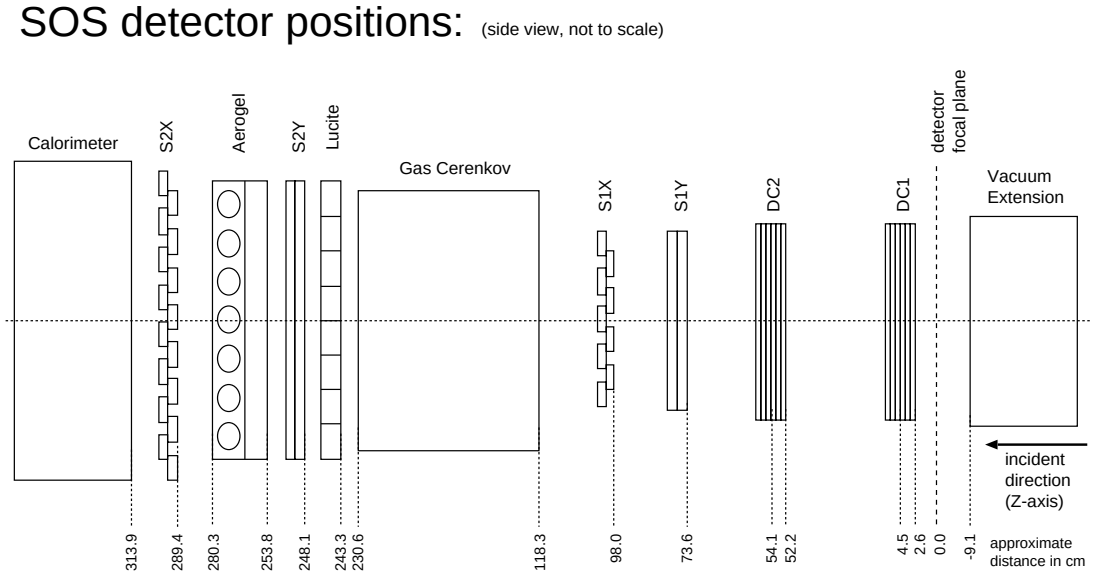

Figure 2.13: Schematic of the SOS detector package showing approximate detector locations in cm along the central ray (the horizontal dotted line). The detectors are all located within the concrete-shielded SOS detector hut.

V-V′, as in Figure 2.14. The X and X′ wires determine the dispersive coordinate (x, roughly vertical) and a combination of the U and V planes determine the transverse coordinate. The U and V planes are rotated by 60° in the clockwise and counterclockwise directions about the incident particle direction (z), respectively, relative to the X wires. The active area of each chamber is approximately $(x \times y) = (63 \times 40)$ cm^2.

Using the same gas handling system as the HMS, a similar argon-ethane gas mixture (equal parts by weight, with a small amount of isopropyl alcohol) is circulated through the chambers at a rate of $\sim$ 200 cc/min. The sense wires are 30 μm in diameter separated by 1 cm within a given plane. Between the wire planes are Al cathode foils, which are held at negative high voltages ($\sim$ 2000 V)

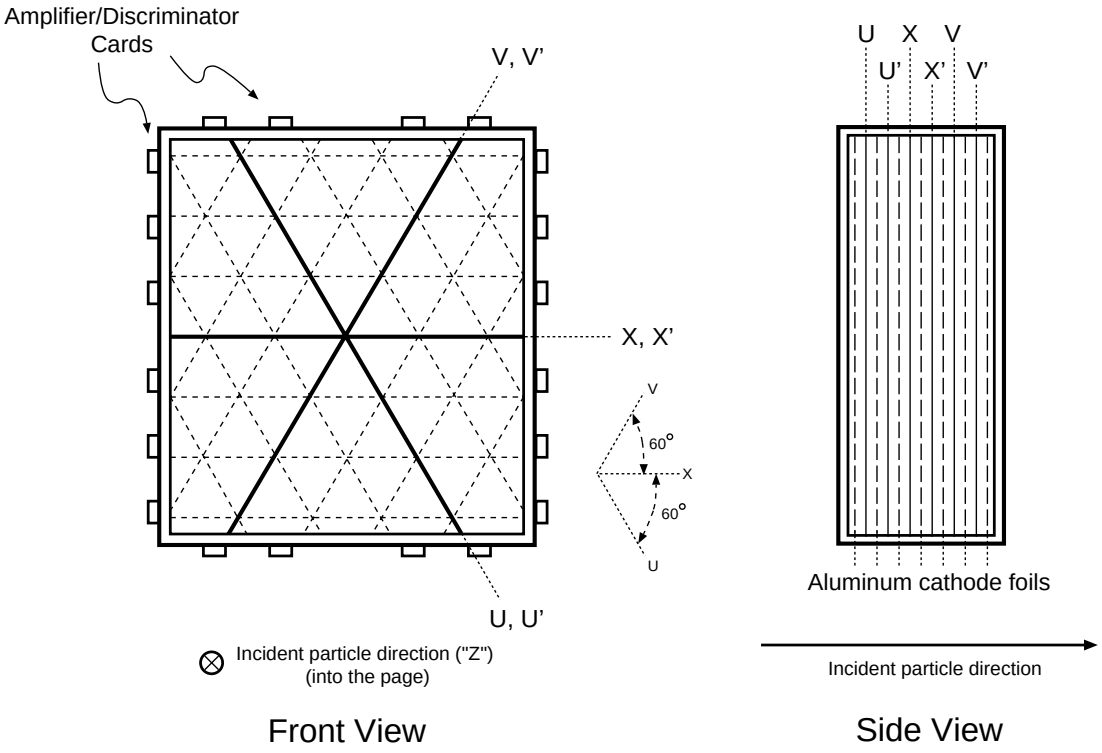

Figure 2.14: Schematic of an SOS drift chamber showing the orientations of the six wire planes.

along with the field wires (60 μm in diameter).

The principle of operation and electronic readout for the SOS drift chambers is virtually identical to that of the HMS chambers. That is, the signals from each wire are amplified and discriminated on cards attached directly to the chambers and then sent as START signals to Lecroy 1877 multi-hit TDCs located just outside the detector hut. The STOP signal is formed by the complete hadron trigger. The position of the particle at each plane can be determined by the tracking software with a resolution of $\sigma = 150$ μm.

Plane	Number of elements	Vertical Size Δx (cm)	Horizontal Size Δy (cm)	Thickness Δz (cm)
S1Y	9	63.5	4.5	1.0
S1X	9	7.5	36.5	1.0
S2Y	9	112.5	4.5	1.0
S2X	16	7.5	36.5	1.0

Table 2.4: SOS hodoscope information

2.7.2 SOS Scintillator Hodoscopes

The SOS is also equipped with four planes of scintillator hodoscopes. Each plane is composed of multiple scintillator elements and the planes are grouped into two Y−X pairs* (S1Y, S1X) and (S2Y, S2X), and are situated as shown in Figure 2.13.

The elements were built of materials identical to those used for the HMS paddles, except that the SOS bars were wrapped in different materials: one layer of aluminized Mylar and one layer of Tedlar. The elements in a given plane are again staggered so that they overlap by 0.5 cm to prevent gaps between them. Table 2.4 lists the number of elements in each plane and along with their dimensions.

The SOS hodoscope information was sent upstairs to the counting house and was processed in a way completely analogous to the HMS hodoscopes (see Section 2.6.2 and Figure 2.10). The resulting TOF resolution in the SOS was

*Note that the order in each pair is reversed from that of HMS.

better than 100 ps per plane (better than the HMS), but due to the short distances between the planes, the velocity resolution was similar to that of the HMS ($\Delta\beta \approx 0.017$ for $\beta = 1$ electrons). The value of beta calculated from TOF information was one of the important quantities used to distinguish kaons from other background particles.

2.7.3 SOS Particle ID: Aerogel Čerenkov

One of the greatest experimental challenges faced by experiment E93-018 was achieving adequate particle identification of a small sample of kaons amidst large backgrounds of both pions and protons. The three curves in Figure 2.15 represent the velocity of p, K^+, and π^+ as a function of their momentum. During E93-018 it was possible to differentiate between kaons and protons at all momentum settings using the velocity measurement from TOF only, as can be seen from the large separation in p/K^+ velocities*.

On the other hand, clean separation of π^+/K^+ by a direct measurement of the velocity was not possible due to the resolution of the TOF measurement. Because of this limitation, a special threshold Čerenkov detector was installed in the SOS detector stack explicitly for this purpose.

The Čerenkov radiator in this detector was a 9 cm thick slab of silica aerogel

*In fact, there was a lucite Čerenkov detector present during data taking which can be used to aid p/K^+ separation. It was used mainly for hardware proton rejection during a feasibility study for measuring kaon production off of a carbon target. This analysis does not use the information from the lucite Čerenkov.

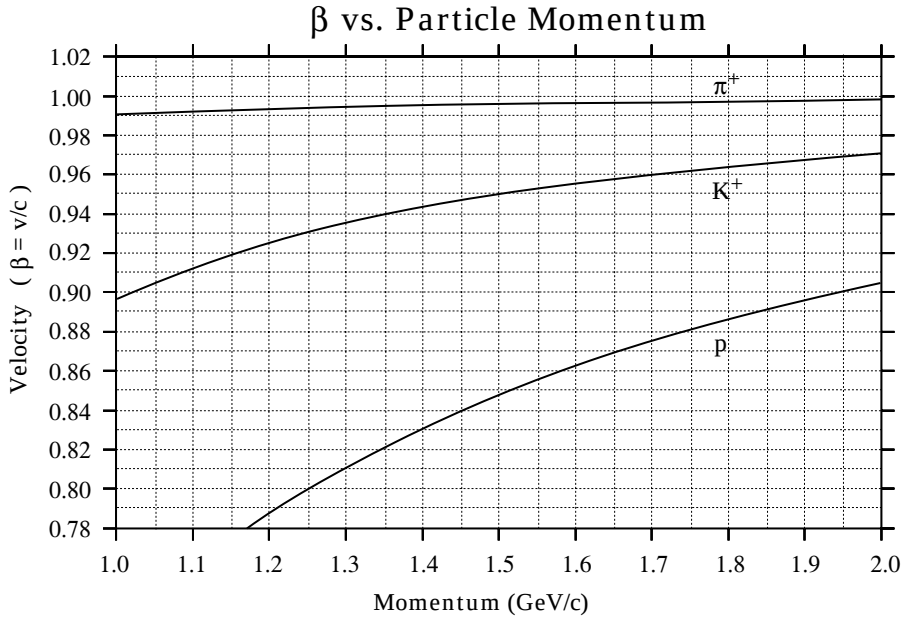

Figure 2.15: Velocity as a function of momentum for particles detected in the hadron arm (SOS). Note that this experiment was performed at central momenta ranging from $1.126 - 1.634$ GeV/c with a useful acceptance of $\pm 17\%$.

with an index of refraction measured to be 1.034 ± 0.001 at the time of E93-018 running. Silica aerogel is a compound of the form $n(SiO_2) + 2n(H_2O)$ with a low density, typically around 0.25 g/cm^3, about 90% air by volume [Bay82]. The aerogel material used for this detector was ordered from Airglass AB in Sweden* in 1993.

Using Equation 2.1, an index of refraction of $n = 1.034$ results in a threshold velocity of $\beta_{\text{threshold}} \approx 0.967$. As opposed to the HMS gas Čerenkov which uses mirrors to focus the light produced from particles traveling above threshold, light in the aerogel detector was collected using fourteen (14) 5-inch Burle 8854 PMTs mounted in a diffusely reflecting box.

*Address: Airglass AB, Box 150, S-245 00 Staffanstorp, Sweden

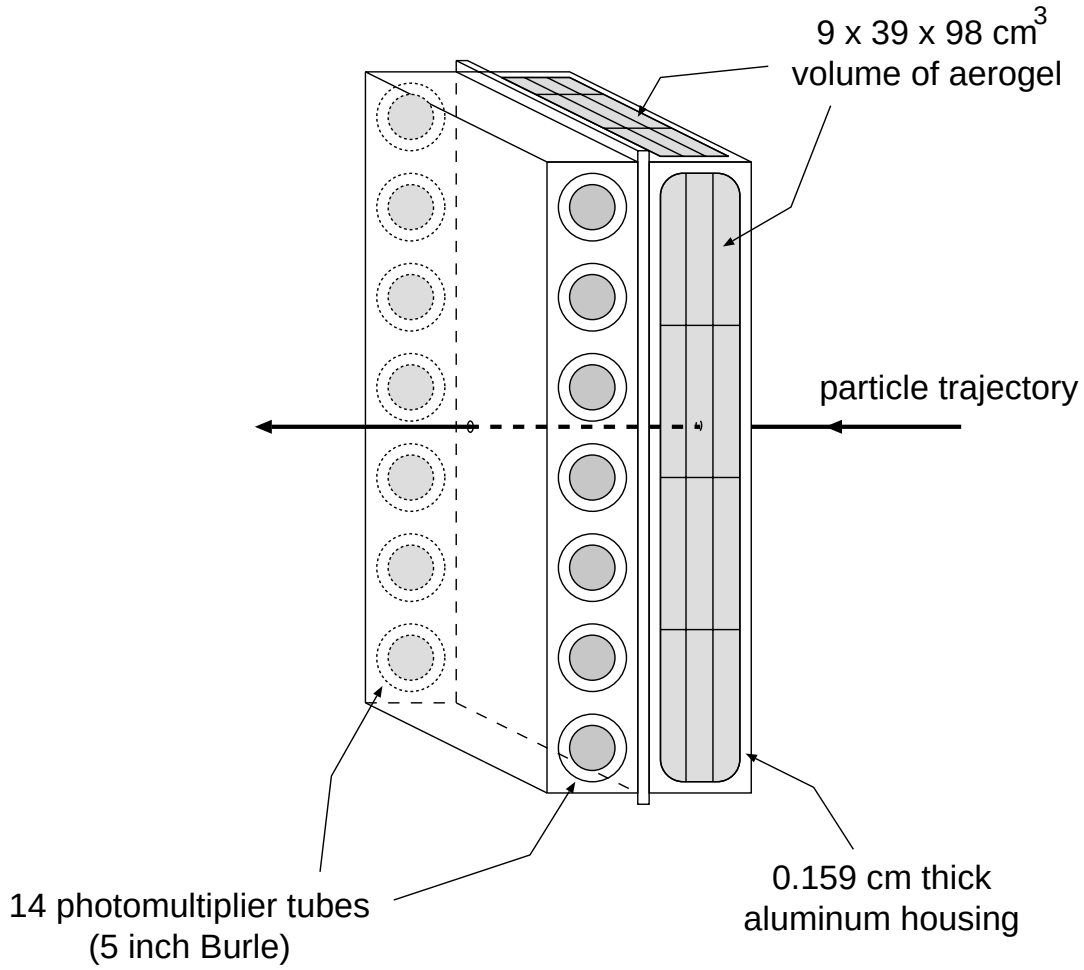

Figure 2.16: Diagram of the aerogel Čerenkov detector showing the location of the aerogel material and photomultipliers.

A view of the aerogel detector as it was mounted in the detector hut is shown in Figure 2.16. In this figure, particles are incident from the right and encounter the aerogel material first. Čerenkov light is produced in the forward direction and is reflected up to several times by the diffusely reflecting walls until it is either detected by one of the side-mounted PMTs or is absorbed by the walls or the aerogel material itself.

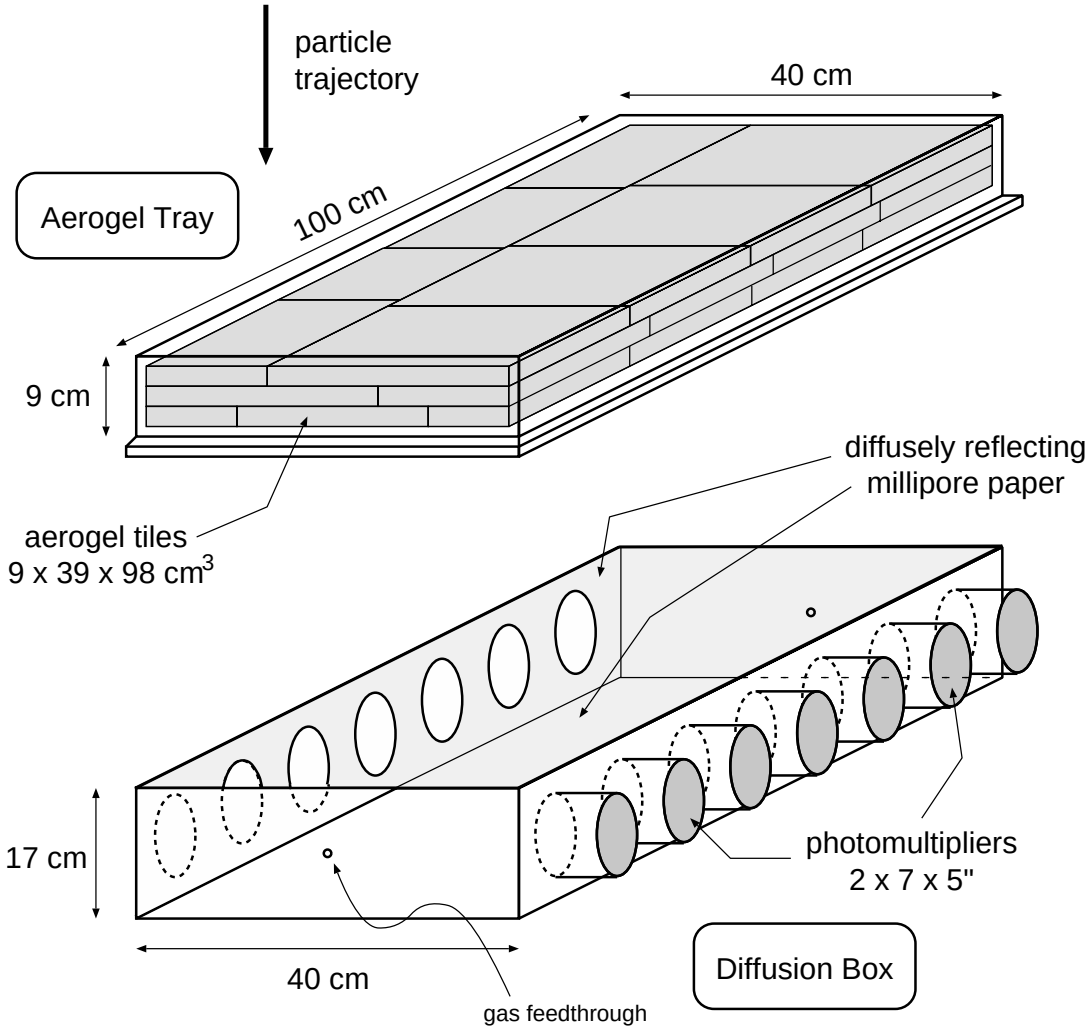

Figure 2.17: Exploded view of the aerogel Čerenkov detector. For details see text.

An exploded view of the aerogel detector is shown in Figure 2.17. The aerogel tiles $(3 \times 25 \times 25)$ cm^3 were cut and arranged into a three-layer slab $(9 \times 39 \times 98)$ cm^3. Care was taken to stagger the blocks so that there were no "cracks" through which particles could pass without hitting any aerogel material. This also made the slab more mechanically stable.

The slab of aerogel tiles was wrapped on all sides, except that facing the dif-

fusion box, with a layer of diffusely-reflecting Millipore paper* (diffuse reflectivity of $\sim 97\%$ for the wavelengths in question [Bay82]) and two layers of aluminized Mylar (specular reflectivity of $\sim 90\%$ [Lab93]). The entire package was wrapped around the 9 cm edge with sheets of 0.13 mm steel and was held in place within the aluminum housing with several thin wires.

Except for holes cut out for the phototube faces†, all of the remaining internal surfaces of both the aerogel tray and the diffusion box were covered with two layers of Millipore paper. The entire box was bolted shut and sealed with Teflon and electrical tape to be light-tight and also reasonably air-tight. The aerogel material is particularly hygroscopic (i.e., it absorbs water readily) and in order to prevent moisture from the air from contaminating the aerogel material, the detector was flushed continuously with dry air through gas feedthroughs located on opposite sides of the diffusion box.

The fourteen signals from the PMTs were split in the counting house into two sets of analog signals in a way completely analogous to the hodoscope signals (see Section 2.6.2). The larger signals were sent to ADCs, while the smaller analog signals were used to build an aerogel pretrigger for hardware rejection of pions, as will be discussed in the following section.

The full set of cuts used to separate π^+/K^+ will be discussed in Sec-

*The Millipore paper is actually a bright white chemical/biological filter paper with a pore size of 220 nm (Millipore Corp., Bedford, MA, 01730, Catalog No. GSWP 304 F0).

†The phototube faces were not flush with the walls of the diffusion box, but actually protruded in by about 5 mm. See Appendix A.7 regarding the aerogel fiducial region.

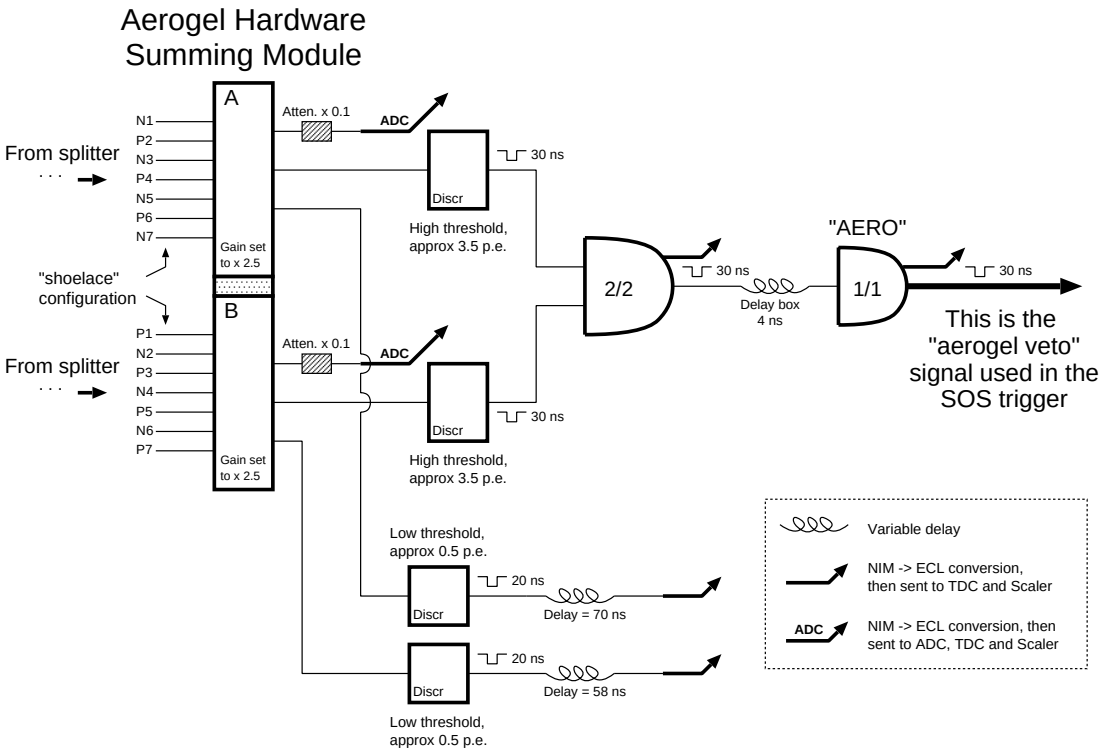

Figure 2.18: SOS Aerogel Čerenkov pretrigger logic diagram, described in detail in the text.

tion 3.5.2. More details regarding the aerogel Čerenkov detector can be found in Appendix A.

2.8 SOS Aerogel Pretrigger

An electronics diagram of the aerogel Čerenkov pretrigger logic is shown in Figure 2.18. The aerogel pretrigger summed the PMTs in hardware and vetoed the SOS pretrigger if the sum was less than a predetermined threshold.

The PMT signals were amplified and summed using a custom module built by the University of Maryland Electronics Development Group. Seven of the

tubes were added together in each independent half (A and B) of the module. Rather than simply summing each side, alternating tubes from the $+y$ and $-y$ sides of the detector (labeled P1-P7 and N1-N7, respectively, in Figure 2.18) were added together in a "shoelace" configuration in order to suppress any y-dependent inefficiencies.

Each of the half-sums A and B was output from the summing module and was sent into a discriminator (and also separately to scalers, ADCs, and TDCs for diagnostics). The threshold level of each discriminator was set to correspond to approximately 3.5 photoelectrons (p.e.) for each A and B (for a total of approximately 7 photoelectrons)*. These two logic signals were then logically ANDed to form the SOS aerogel pretrigger signal, **AERO**. This signal was sent to the main SOS pretrigger logic as a veto signal, and could optionally be used to reject pions at the trigger level.

2.9 SOS Pretrigger

At the heart of the SOS pretrigger shown in Figure 2.19, is a 3/4 scintillator signal **SCIN**, built in an identical way to its HMS counterpart. Unlike the HMS, there is no gas Čerenkov, lead-glass calorimeter, or **STOF** pathway in the SOS pretrigger. For E93-018, the other major difference from the HMS pretrigger was

*This is a fairly conservative threshold setting, as pions typically generated between 5-15 photoelectrons (see Section A.6).

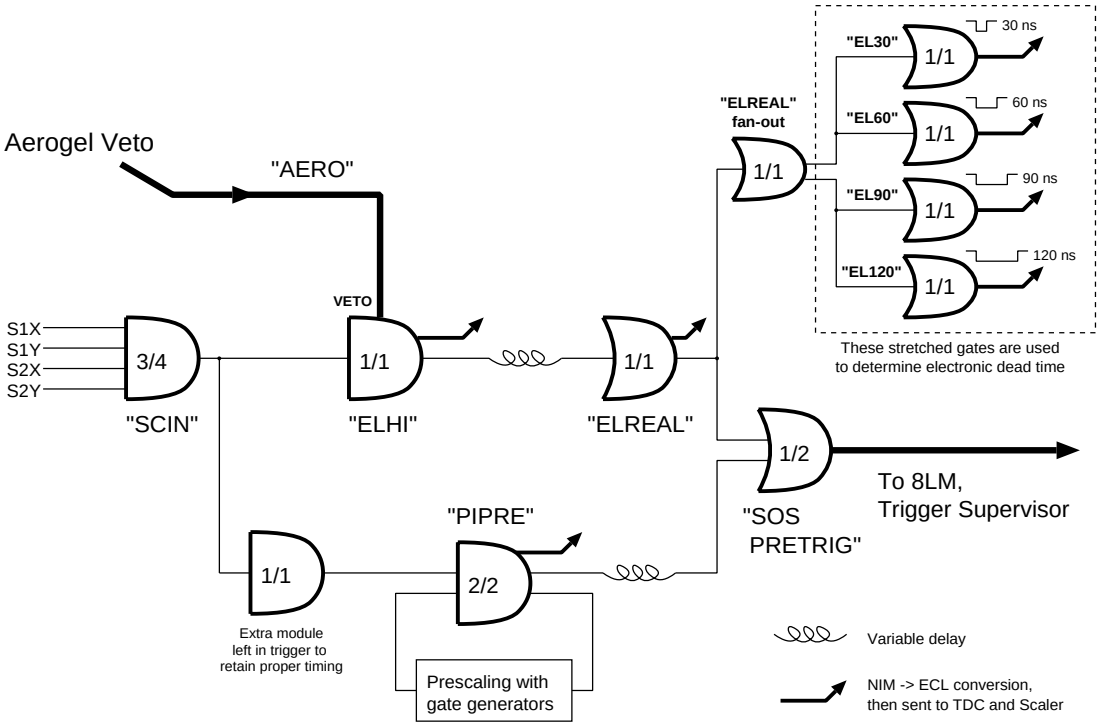

Figure 2.19: SOS pretrigger logic diagram. Notations are as in Figure 2.11. The Aerogel Veto signal **AERO** is generated by the SOS aerogel pretrigger, as shown in Figure 2.18.

the presence of the aerogel veto signal, **AERO**. The signal **SOS PRETRIG** was built from a good signal in 3/4 scintillator planes (**SCIN**) with the constraint that there was a signal of less than $\sim$7 p.e. in the aerogel detector (**AERO**).

2.10 COIN Logic: 8LM and Trigger Supervisor

Coincidences between the pretrigger signals from the two spectrometers are formed at a programmable logic module called the "8LM" (Lecroy 2365). The reading out of all of the detectors is controlled by a unit called the Trigger Supervisor (TS) which was custom built at Jefferson Lab. The diagram of the

logic involving the 8LM and TS is shown in Figure 2.20.

First, let us define the six inputs to the 8LM. The signal **TS GO** is always active when any run is in progress, the signal **TS EN1** is active whenever normal data taking (i.e., not taking pedestals) is in progress, and the signal **TS BUSY** is active while the TS is busy processing an event and its inputs are dead. These three signals are sent from the output of the TS to the input of the 8LM (note that these outputs are not shown emerging from the TS in Figure 2.20). The 8LM also takes as input the two spectrometer pretriggers, **HMS PRETRIG** and **SOS PRETRIG**, and a third signal called **PED PRETRIG**. The **PED PRETRIG** signal is only present for a short period at the beginning of each run when 1000 pedestal events are taken to measure the DC offsets in the ADCs.

The 8LM combines the three TS signals with the three **PRETRIG** signals to form eight outputs which are programmed as shown in Table 2.5. In particular, each of the signals **HMS PRETRIG** and **SOS PRETRIG** that are produced at the output of the 8LM are identical to their input signal of the same name, except that normal data taking must be in progress (i.e., **TS EN1** must be present). The signal **COIN PRETRIG** is produced during normal data taking (i.e., when **TS EN1** is present) whenever the 8LM receives overlapping **HMS PRETRIG** and **SOS PRETRIG** signals.

There are also four **TRIG** output signals corresponding to each of the four **PRETRIG** output signals. For a given event, these two types of output signals

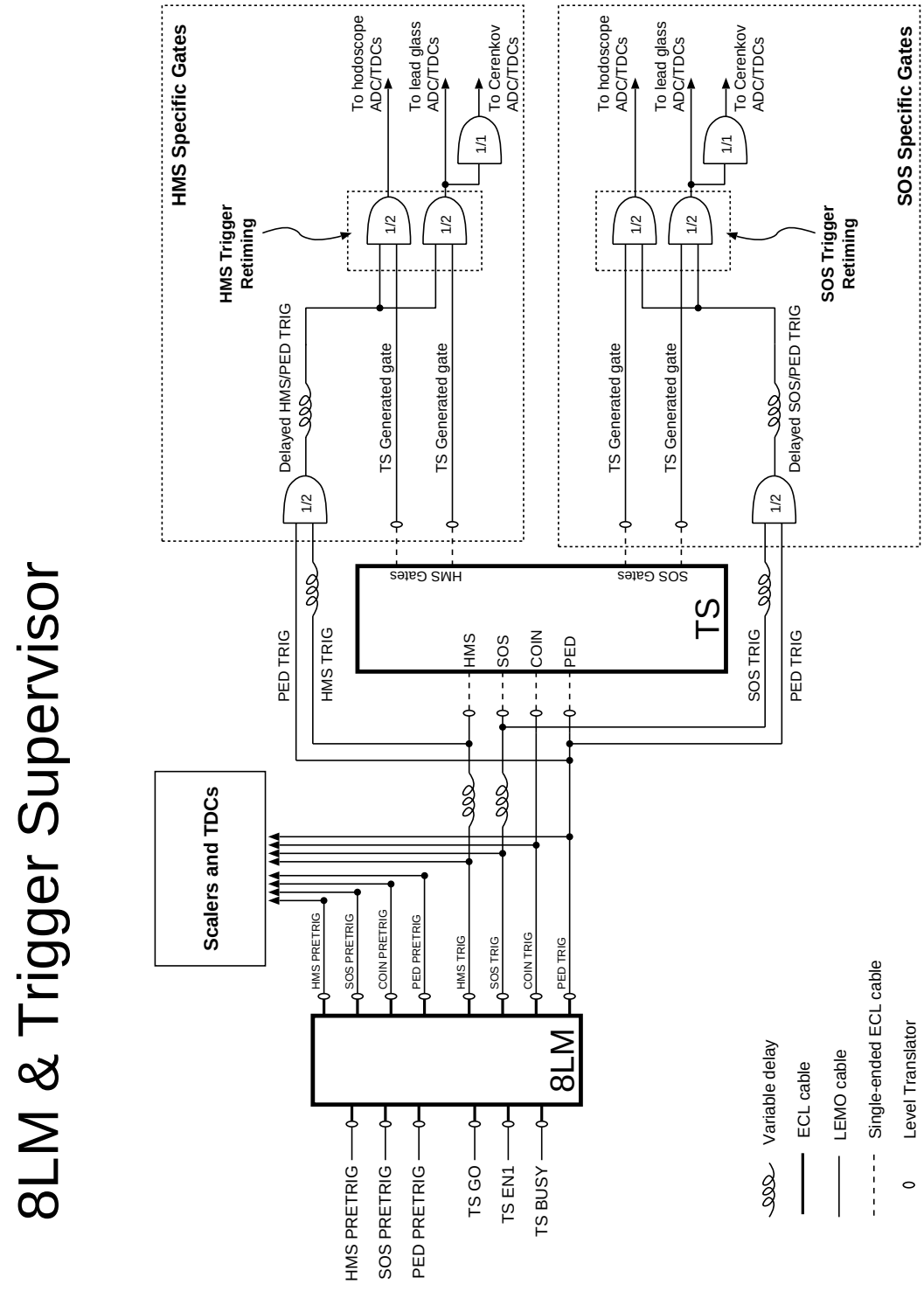

Figure 2.20: Coincidence logic diagram showing the use of the 8LM and Trigger Supervisor. A detailed description of this figure can be found in the text (Section 2.10).

Output Name	Definition (in terms of the 8LM inputs)			
HMS PRETRIG	**HMS PRETRIG**		**TS EN1**	
SOS PRETRIG		**SOS PRETRIG**	**TS EN1**	
COIN PRETRIG	**HMS PRETRIG**	**SOS PRETRIG**	**TS EN1**	
PED PRETRIG	**PED PRETRIG**	**TS GO**	NOT **TS EN1**	
HMS TRIG	**HMS PRETRIG**		**TS EN1**	NOT **TS BUSY**
SOS TRIG		**SOS PRETRIG**	**TS EN1**	NOT **TS BUSY**
COIN TRIG	**HMS PRETRIG**	**SOS PRETRIG**	**TS EN1**	NOT **TS BUSY**
PED TRIG	**PED PRETRIG**	**TS GO**	NOT **TS EN1**	NOT **TS BUSY**

Table 2.5: Summary of the programming of the 8LM. Each output signal that is listed is only generated when of each of the corresponding inputs are present. For example, **COIN PRETRIG** $\equiv$ **HMS PRETRIG** AND **SOS PRETRIG** AND **TS EN1**.

differ only in that the **TRIG** outputs require that the TS is ready to accept the event (i.e., **TS BUSY** is NOT present), whereas the **PRETRIG** signals are not affected by the status of **TS BUSY**.

During E93-018, the width of the **HMS PRETRIG** signal at the input of the 8LM was approximately 30 ns, and the width of the **SOS PRETRIG** signal was approximately 10 ns. Thus the effective coincidence time window was $\sim$40 ns wide for a **COIN TRIG** to be produced.

All of the signals produced by the 8LM are sent to TDCs and scalers to be recorded. These scalers are used for the calculation of the computer live time, as will be discussed in Section 3.6.4. The **TRIG** signals are forwarded to the TS, although the TS is programmed to prescale away virtually all of the singles events (i.e., events that are simply an **HMS TRIG** or an **SOS TRIG** without having formed a coincidence, **COIN TRIG**).

When the TS receives a **COIN TRIG** at its input, it then sends a pair of very long (> 100 μs) gate signals to the HMS/SOS readout electronics. Each signal is in turn ANDed with a delayed singles trigger (**HMS TRIG/SOS TRIG**) to send gates to the HMS/SOS ADCs and TDCs. This "retiming" using a delayed singles trigger is necessary because the timing of the long gates is set by whichever of the two spectrometer pretriggers reached the 8LM last. This timing would then be correct for the later spectrometer, but most likely incorrect for the earlier one, causing clipped/missed signals in the ADCs and offsets in the TDCs. Another way to interpret the setup is that the long TS output gate effectively enables the reading of the ADCs (or STARTing of the TDCs), while the delayed singles trigger sets the timing of when the read (or START) occurs.

2.11 Data Acquisition

The actual reading of the data and storage to disk, as well as the user interface, was managed by the CODA (CEBAF Online Data Acquisition) [Abb95] software system, running on an HP9000/735 workstation. The readout electronics (ADCs, TDCs, scalers) were located in FASTBUS and VME crates, which were managed by ROC (Read Out Controller) CPUs. The ROCs themselves were read directly by the CODA software via a parallel link over an FDDI/ethernet network. The CODA Event Builder software consolidated all of the data for each event from the various ROCs, added header information, and wrote the event to

disk. Also, information about the beam position, magnet settings, target status, and accelerator status were read out every 30 seconds using EPICS software.

Chapter 3

Data Analysis

3.1 Overview / The Replay ENGINE

The raw signals from the ADCs, TDCs, and scalers discussed in the previous chapter were stored by the data acquisition system as events in a raw data file for each run, called oct96_nnnnn.log. The raw data were processed using a modular FORTRAN code called the "replay ENGINE" [GW94]. The ENGINE decoded the raw data into arrays of specific detector responses. These arrays were then further processed and combined with additional experimental information such as the momentum and angle settings of the spectrometers, detector positions, and beam energy to yield information about the event such as the particle trajectories, momenta, velocities, energy deposition, and particle identification. The ultimate goal of the analysis was to determine the physics variables (such as Q^2, W, θ_e, $\mathbf{p_K}$, θ_{qK}...) of each event at the interaction vertex (i.e., at the target) and then

to measure the yield of electroproduced kaons as a function of a given subset of these variables.

The main results of the ENGINE were text files containing the information from the scalers (number of triggers, total incident charge, various detector efficiencies, etc...) and a PAW++ [Gro93] (a data manipulation and display program) ntuple containing the event-by-event quantities of interest. The use and interpretation of these files is the subject of the remainder of this chapter.

3.2 Tracking

In order to determine the trajectory of a detected particle at the target, one first must determine its trajectory inside the detector hut using the information from the drift chambers. The absolute positions of the drift chambers were known from survey: three coordinates were given for the center of each chamber, plus three angles describing their orientation relative to the optical axis of the spectrometer.

The tracking algorithm is straightforward. Typically, at least 5 of the 6 planes in each chamber are required to have at least a single wire "hit" before tracking is attempted. All intersections of non-parallel pairs of wires that were hit in each chamber are identified. Intersections that fall within a radius of 1.2 cm of one another are used to form so-called "space points". Next, all of the space points within a chamber are linked to form "stubs", which are essentially

miniature tracks. Finally, the algorithm loops over all of the space points in both chambers and performs a χ^2 minimization fit to a straight line track. The fitted tracks must be consistent with the stubs from each chamber. If multiple tracks are found, the track with the best χ^2 is kept. For details see [VW99].

The final track is then projected to the "detector focal plane" (hereafter referred to as simply the "focal plane"*) of the spectrometer to give the positions $x_{\rm fp}$, $y_{\rm fp}$, and slopes $x'_{\rm fp}$, $y'_{\rm fp}$ at $z = 0$. The focal plane is perpendicular to the central ray†, and $z = 0$ is located as shown in Figure 2.7 for the HMS, and Figure 2.13 for the SOS. These focal plane quantities are used in reconstructing the target quantities, and are discussed in Section 3.3. The focal plane values can also be projected to any z position in the (nearly magnetic-field free) detector hut, via:

$$x = x_{\rm fp} + (z)(x'_{\rm fp})$$

$$y = y_{\rm fp} + (z)(y'_{\rm fp})$$

which is useful for placing fiducial cuts and checks on the detectors.

*The detector focal plane is not identical to the true optical focal plane of the spectrometer. The HMS(SOS) optical focal plane is tilted at and angle of about 85°(70°) relative to the detector focal plane [Tan95].

†The central ray is defined by a measured particle with the exact nominal spectrometer momentum (i.e., $\delta = 0$, as defined in Section B.2.1) and travels through the hut along the line $x = 0, y = 0$.

3.3 Reconstruction of Target Quantities

Each magnetic spectrometer allows for the target quantities from which the detected particle originated*,

$$R_{\rm tar} = (R^{(1)}_{\rm tar}, R^{(2)}_{\rm tar}, R^{(3)}_{\rm tar}, R^{(4)}_{\rm tar}) \equiv (x'_{\rm tar}, y'_{\rm tar}, y_{\rm tar}, \delta)$$

to be reconstructed from a knowledge of the measured focal plane quantities,

$$F_{\rm fp} = (x_{\rm fp}, y_{\rm fp}, x'_{\rm fp}, y'_{\rm fp}).$$

Each of these reconstructed target quantities, $R^{(i)}_{\rm tar}$, is expressed in terms of the vector $F_{\rm fp}$ for each event through

$$R^{(i)}_{\rm tar} = \sum_{j,k,l,m=0}^{N} \mathcal{M}^{(i)}_{jklm} \, (x_{\rm fp})^j \, (y_{\rm fp})^k \, (x'_{\rm fp})^l \, (y'_{\rm fp})^m \tag{3.1}$$

where $\mathcal{M}^{(i)}$ represents a given row of the transport matrix for the spectrometer in question, and N is the order of the matrix ($N = 5$ for HMS, and $N = 6$ for SOS).

Initial values for the matrix elements are determined by a COSY INFINITY model [COS91] of each spectrometer. Data runs taken specifically for this purpose were used to optimize the matrix elements to best reflect the actual behavior of the spectrometer. For example, data for the optimization of the $x'_{\rm tar}$ and $y'_{\rm tar}$ matrix elements were taken with a special collimator called a "sieve slit" in place. The sieve slit is a solid piece of Heavymet with small holes drilled

*These quantities are defined in Appendix B.2.1.

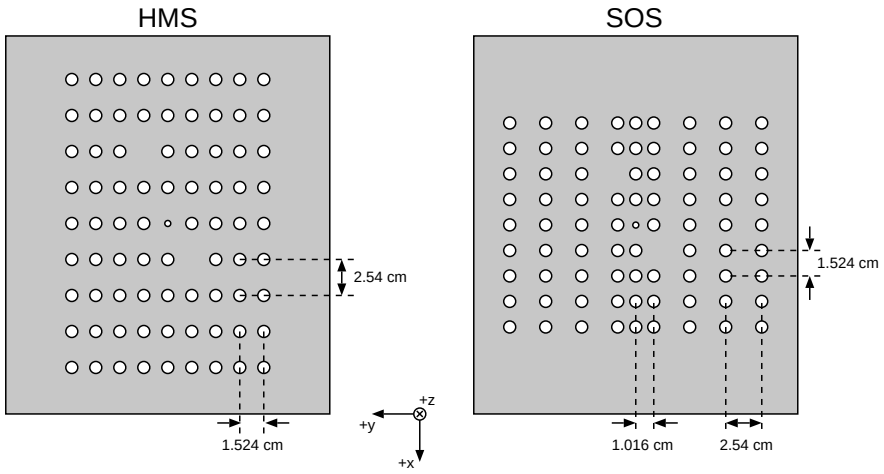

Figure 3.1: Dimensions of the HMS and SOS sieve slit collimators used for optics calibration in place of the normal collimators of Figure 2.6, shown as viewed from the target location.

through it, each hole centered at a measured value of $x'_{\rm tar}$ and $y'_{\rm tar}$ as in Figure 3.1. Electrons scattered from a thin carbon target were detected and could be reconstructed approximately back to the holes in the sieve slit. The missing holes allow for the proper left-right and up-down orientation to be established, while the smaller central hole is used to determine the angular reconstruction resolution. A fitting procedure described in [ADW97] modified the matrix elements to yield optimal agreement with the holes in the sieve slit after reconstruction. The matrix elements with dependences on δ and on $y_{\rm tar}$ were determined in a similar fashion, but with the additional variation of the spectrometer momenta and the target position*, respectively. More information about the matrix element optimization

*A thin carbon target which was slanted at an angle of 30° with respect to the horizontal was used for this measurement. By changing the vertical distance that the target was lowered into the beam path, the z_B position of the interaction was varied. See Appendix B for details regarding the various coordinate systems used.

can be found in references [ADW97], [Dut99], and [HCD].

3.4 TOF / Velocity Determination

In each spectrometer, the velocities of the detected particles were calculated using the timing information from the scintillator hodoscopes. The time that each scintillator bar was hit (relative to a common start) was corrected for pulse-height variation (i.e., variation in the triggering of the leading-edge discriminators), for the time it took the light to travel through the scintillator to reach the PMT, and for any offsets arising due to differences in electronic delays and cable length.

The corrections were taken into account using the so-called "TOF code" [Arm95]. The input to this code is a file of timing and scintillator information generated by the running the ENGINE with a special software setting for a sample of either pions or electrons. In this code, the pulse-height variation is corrected for each hit in software by parameterizing the shape of the leading-edge of the pulse as a function of the size of the signal from the ADC information and fitting the TOF code information. The light travel time is corrected as a function of the position of the hit along the scintillator bar by fitting the time difference between signals from both ends of the bar.

Knowing *a priori* that the sample is, for example, entirely pions (with mass m_π), one can precisely calculate the velocity of each event from its measured

momentum, $|\mathbf{p}|$, and energy, E, via:

$$\beta_{\rm mom} = \frac{|\mathbf{p}|}{E} = \frac{|\mathbf{p}|}{\sqrt{|\mathbf{p}|^2 + m_\pi^2}}. \tag{3.2}$$

The position of each hodoscope that was hit is known, giving the distance, d, traveled between hits. Hence, the actual time, t, between hits can be calculated from knowing the velocity of the particle, using $t = d/(\beta c)$. The TOF code then adjusts the offsets for each TDC channel to give the proper value of the time for each event.

After all of the calibrations are set, the hodoscope information is used to calculate the velocity, $\beta_{\rm tof}$, for each event during a normal run. One constraint placed on the hodoscope hits used for the $\beta_{\rm tof}$ calculation is that they are required to have been consistent with the track (from the drift chambers) so as to not include spurious firings. A typical spectrum of hadron velocities in the SOS is shown in Figure 3.2. The measurement of $\beta_{\rm tof}$ in the SOS is an integral part of the kaon PID cuts to be discussed in Section 3.5.2.

During E93-018, prior to Run 11393, there was a problem with the SOS S2X TDC such that a bad value of the time was recorded up to 10% of the time, typically resulting in a grossly incorrect calculation of $\beta_{\rm tof}$ for those events. The effect was due to a hardware problem and was eliminated for the remainder of the experiment by replacing the faulty TDC. However, for all the runs prior to number 11393, it was important to take this intermittent effect into account, otherwise a cut on $\beta_{\rm tof}$ would unintentionally throw away good kaon events (and possibly

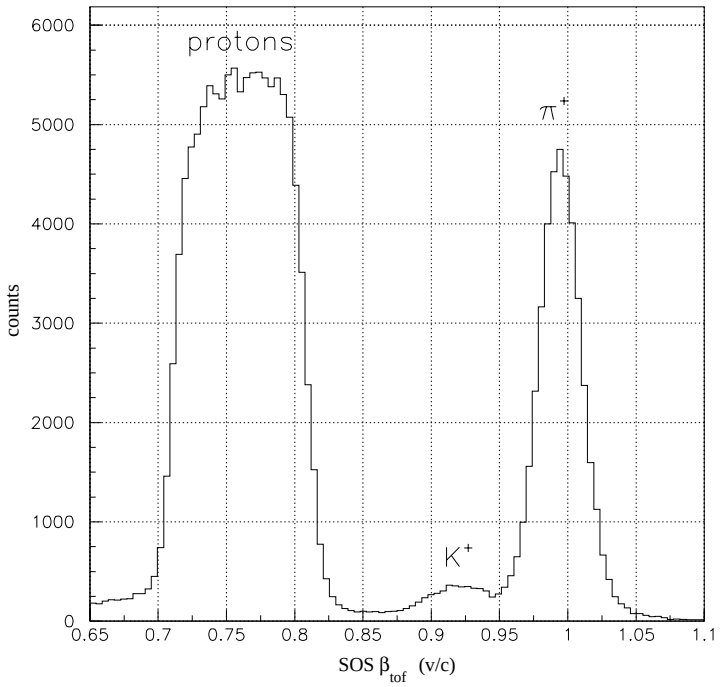

Figure 3.2: A typical $\beta_{\rm tof}$ spectrum for the SOS (with no aerogel in the trigger) for $\rm P_{SOS}$ = 1.126 GeV/c. Note that for a fixed momentum cut (shown here at $|\delta_{\rm SOS}|$ <17%), the protons span a wider range of velocities than the other particles due to their larger mass.

include extra background events). A modification of the standard routine used to calculate the velocity was made such that the S2X TDC was not included in the $\beta_{\rm tof}$ calculation in cases where the TDC value was determined to be affected. The full procedure for taking this effect into account is documented in [Kol99].

3.5 Particle Identification

3.5.1 HMS: Electron Identification

In E93-018, the sample of scattered electrons detected in the HMS was contaminated by a background of electroproduced pions (π^-). As discussed in Section 2.6.3, the HMS gas Čerenkov and HMS lead-glass calorimeter were used to perform π^-/e^- separation, because the velocity measurements from TOF in the HMS had insufficient resolution to separate them. A cut requiring greater than 3 photoelectrons in the gas Čerenkov was placed on the data; a typical electron generated $\mu = 12$ photoelectrons. No cut was placed on the calorimeter in software, although both detectors were in the trigger. A detailed study of these two detectors [Nic97] determined efficiencies of $\gtrsim 99.7\%$ for the calorimeter, and $\gtrsim 99.8\%$ for the Čerenkov. In this analysis, the detection efficiency is taken to be 99.8%, with an assigned error of 0.2%.

3.5.2 SOS: Kaon Identification

For the SOS, two separate software cuts were implemented to select kaons out of the proton and pion backgrounds: a cut on the velocity as measured from TOF information, and a cut on the number of photoelectrons detected in the aerogel Čerenkov detector.

The cut on $\beta_{\rm tof}$ was implemented as a cut on the quantity $(\beta_{\rm tof} - \beta_{\rm K})$,

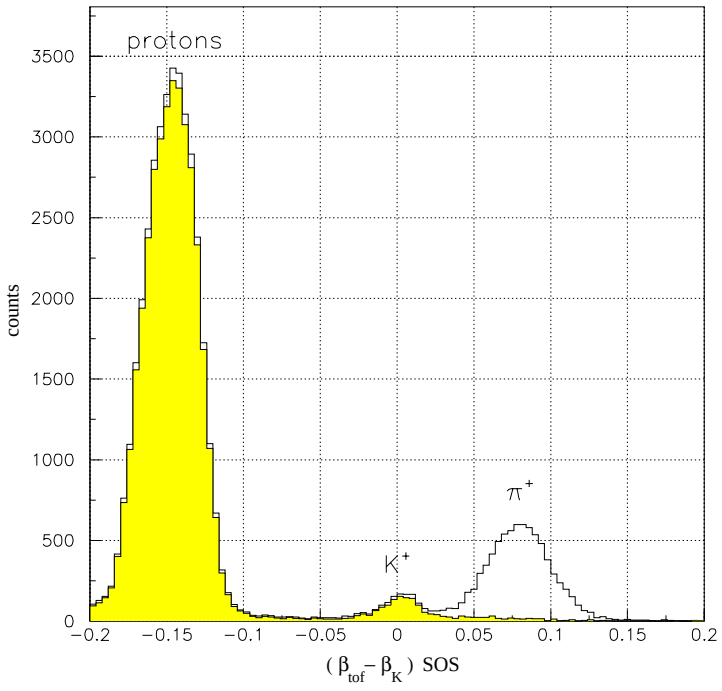

Figure 3.3: A typical $\beta_{\rm tof} - \beta_{\rm K}$ spectrum for the SOS, shown with (shaded) and without (unshaded) a software aerogel cut.

where $\beta_{\rm K}$ is the velocity as determined from momentum, making the assumption that the incident particle was indeed a kaon. In a manner similar to Equation 3.2, $\beta_{\rm K}$ is defined as:

$$\beta_{\rm K} \equiv \beta_{\rm mom}\,(\text{assuming a kaon}) = \frac{|\mathbf{p}|}{E} = \frac{|\mathbf{p}|}{\sqrt{|\mathbf{p}|^2 + m_K^2}}. \tag{3.3}$$

The unshaded spectrum* in Figure 3.3 shows the quantity $(\beta_{\rm tof} - \beta_{\rm K})$. In the analysis, a cut was placed at $\mid (\beta_{\rm tof} - \beta_{\rm K}) \mid < 0.04$, which eliminates all of the protons, and a significant fraction of the pions.

*As opposed to Figure 3.2, the aerogel was in the hardware trigger for the runs shown in Figure 3.3. This is why there are fewer pions relative to the kaons and protons in Figure 3.3.

The second cut was on the number of photoelectrons detected in the aerogel Čerenkov. This eliminated virtually all of the background pions that the $(\beta_{\rm tof} - \beta_{\rm K})$ cut did not reject. Furthermore, the (very few) pions that survived both of these cuts were effectively eliminated by the subtraction of the random background, as will be shown in Section 3.5.3. The shaded region in Figure 3.3 shows what remains after applying a cut requiring less than 3.5 photoelectrons in the aerogel detector. The efficiencies of these cuts are discussed in Section 3.6.

3.5.3 Coincidence Cuts

The events of interest in the data sample were coincidences made up of HMS (electron) signals paired with SOS (hadron) signals. However, it is possible that the two signals that made up the event were in fact uncorrelated and only formed a coincidence by random chance. The fraction of electron-kaon coincidences that were uncorrelated must be corrected for in order to arrive at the true electroproduction yield.

The random coincidences were dealt with by looking at the relative timing between the HMS and SOS signals, called the "coincidence time". The **COIN TRIG** signal started a TDC which was stopped by the **SOS TRIG** signal to form the "raw coincidence time" (an equivalent TDC was also present that was started by **COIN TRIG** and stopped by **HMS TRIG**). This value was corrected to account for variations in flight time arising from variations in particle velocity and

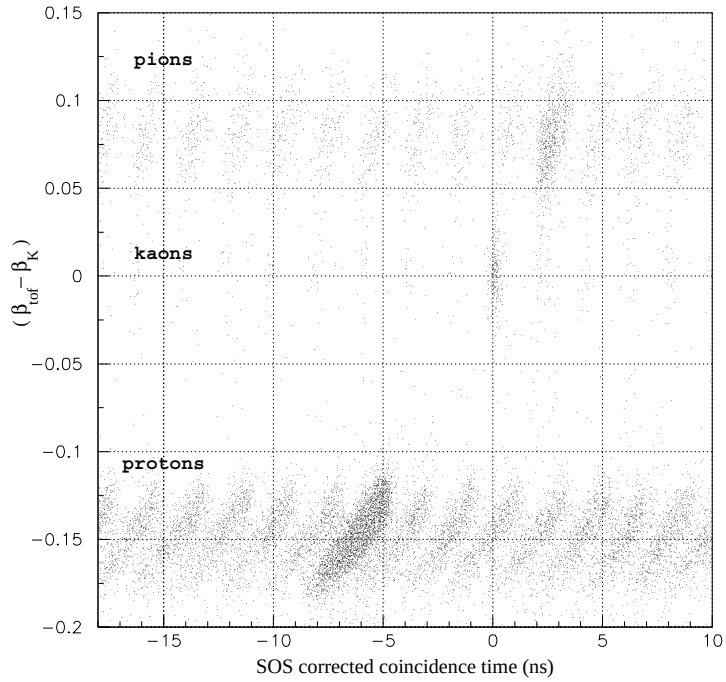

Figure 3.4: Plot of $(\beta_{\rm tof} - \beta_{\rm K})$ vs. SOS corrected coincidence time. Visible are three horizontal bands corresponding to protons, kaons, and pions. The coincidence time is offset such that the in-time kaons appear at 0 ns. See text for further details.

pathlength traveled through the spectrometers to yield the "corrected coincidence time" (for the SOS, this is referred to as "cointime(SOS)"). An offset was added to the corrected coincidence time such that events in which the electron and kaon originated from the same beam bunch would have a time of 0 ns. These coincidences are called "in-time", although it should be noted that they are still not necessarily correlated events.

Figure 3.4 shows $(\beta_{\rm tof} - \beta_{\rm K})$ for the SOS plotted versus the corrected coincidence time for a single run, without having applied the kaon PID cuts discussed

in the previous section. The three horizontal bands represent electron coincidences with protons (slower than kaons), kaons, and pions (faster than kaons). The in-time kaons are at 0 ns, in-time pion electroproduction events are in the heavily populated region at $\approx +2$ ns, and in-time electron-proton events* are smeared across the region of ≈ -8 ns to ≈ -5 ns. Events that do not have the electron and hadron in-time have an electron and hadron from different beam bunches, and are called "random coincidences". From the RF structure of the beam, these events have a coincidence time that is offset from the in-time peak by a multiple of $\sim$2 ns, as is evident in Figure 3.4.

After applying the $(\beta_{\rm tof} - \beta_{\rm K})$ and aerogel cuts, the distribution shown in Figure 3.4 reduces to that shown in the top half of Figure 3.5. Here, the random e-K events and the in-time peak are clearly visible. The lower half of the figure shows the one-dimensional projection of the upper half, namely the corrected coincidence time spectrum for these kaons. The in-time peak dominates over the purely random coincidences. The data is cut on the coincidence time around the peak, at $|\,\text{cointime(SOS)}\,| < 0.65$ ns.

The in-time kaon peak delimited by this cut on cointime(SOS) includes both "real coincidences" (i.e., the events we are interested in) and random coincidences. To estimate the amount of random background in the in-time peak, the average of five random peaks that are not in-time was used, with cuts shown as in Figure 3.5.

*These electron-proton events contained a large sample of p(e,e′p)ω and p(e,e′p)ρ°, which were analyzed as the subject of a separate thesis [Amb00].

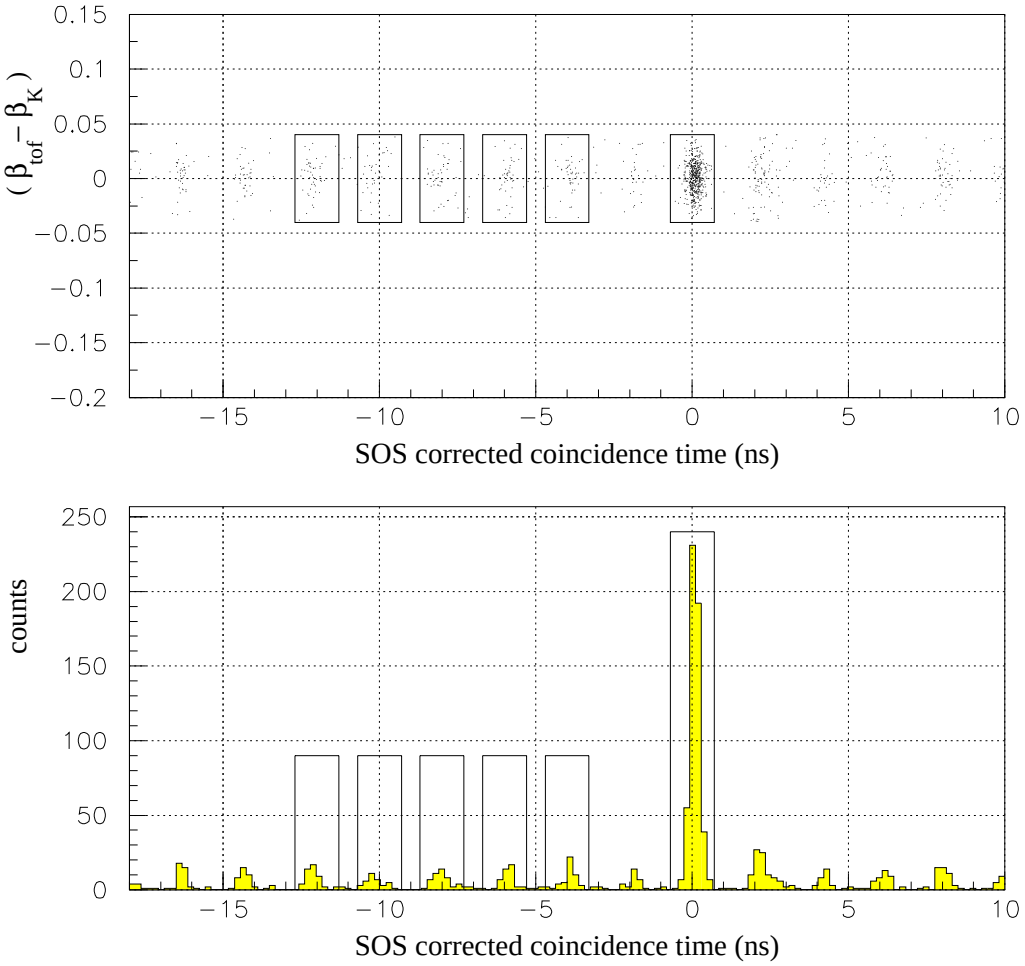

Figure 3.5: The upper panel shows $(\beta_{\rm tof} - \beta_{\rm K})$ vs. SOS corrected coincidence time, after applying cuts on $(\beta_{\rm tof} - \beta_{\rm K})$ and the aerogel. The single boxed region to the right is the in-time peak, and the five boxed regions to the left contain random coincidences. The lower panel shows the one-dimensional spectrum of SOS corrected coincidence times corresponding to the upper panel.

This average was subtracted from the in-time yield to give the "real" yield.

It was mentioned earlier in Section 3.5.2 that any pions that remained after the kaon PID cuts would be eliminated by this random subtraction. In

examining Figure 3.4, a few features are noteworthy. First, the cut defining the in-time kaon peak, $|\,\text{cointime(SOS)}\,| < 0.65$ ns, does not include the in-time pions, but only contains random pions. In other words, the coincidence timing cut alone eliminates a significant amount of the pion background. Second, if there are any remaining pions in the in-time kaon peak even after the PID cuts, the proportion of these background pion events will be the same in the random kaon peaks shown in Figure 3.5. This is because both the in-time and random kaon coincidence time cuts include *random* pions in the same way. Hence, the procedure of subtracting the random kaon counts from the in-time peak will also eliminate any remaining background pions.

One last feature regarding the coincidence time is of note. The actual value of the coincidence time for in-time kaons (defined as 0 ns) drifted from run to run by up to ± 2 ns as a function of temperature in the electronics room [Mac97]. Because of this effect, the coincidence time cut could not simply be placed at $|\,\text{cointime(SOS)}\,| < 0.65$ ns, but in fact it was necessary to extract the deviation Δt of the coincidence time centroid from 0 ns on a run-by-run basis. The cut applied for each run was thus $|\,\text{cointime(SOS)} - \Delta t\,| < 0.65$ ns.

3.5.4 Missing Mass Reconstruction

After all of the above cuts are placed, the missing mass, m_Y, of the produced hyperon can be reconstructed using Equation B.3. Figure 3.6 shows a histogram

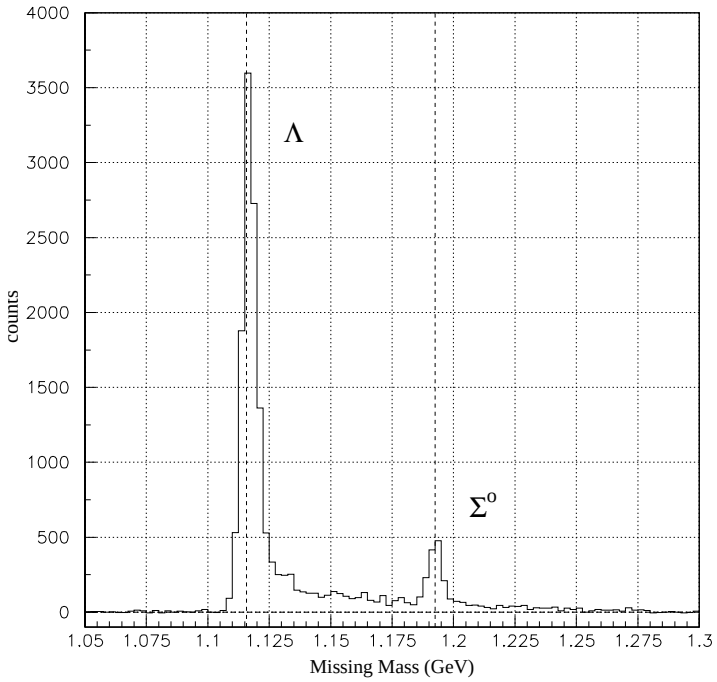

Figure 3.6: An example of a missing mass spectrum for $p(e,e'K^+)Y$ showing the Λ and Σ^0 peaks and radiative tails. The vertical dashed lines are located at the accepted Λ and Σ^0 masses (see Table 1.1). Note that this spectrum has already been corrected for random and dummy yields, as will be discussed in Section 3.5.5.

of the missing mass, showing peaks at the Λ and Σ^0 masses. The tails sloping off toward higher missing mass from each of these peaks are due to the effects of radiative processes. In these processes the incident electron, scattered electron, or produced kaon loses some energy by radiating a photon. As a result, there is some extra energy and momentum "missing" from what is measured, leading to an apparent increase in the calculated missing mass.

A cut was placed on the missing mass in order to separate the Λ and Σ^0

reaction channels. A cut of ($1.100 < m_Y < 1.155$) GeV was used in this analysis to identify Λ particles, as will be discussed in Section 5.3. The Λ yield had to be corrected for the number of Λ that were pushed by radiative processes to a missing mass above this cut. A similar procedure was implemented for the Σ^0, with a cut placed on the region ($1.180 < m_Y < 1.230$). However, the Σ^0 analysis was complicated by the fact that the Σ^0 peak sits on top of the Λ radiative tail (i.e., radiative processes push some of the Λ counts into the Σ^0 missing mass cut region). A Monte Carlo (MC) simulation was used to correct the yields for the effects of radiative processes. The MC is discussed in Chapter 4, and the implementation of the radiative corrections is discussed in Section 4.4.

3.5.5 Dummy Target Subtraction

The final source of background that needs to be taken into account is the number of events in the in-time kaon peak that have arisen from the beam interacting with the aluminum target walls instead of the liquid hydrogen. Data taken with the "dummy target" were used to estimate this background.

All of the same cuts that were applied to the regular data were also applied to the dummy target runs. The in-time kaon peak for the dummy run was corrected for random coincidences (within the dummy run) using the same procedure as described in Section 3.5.3.

Before subtracting the dummy yields from the LH_2 data yields, the dummy

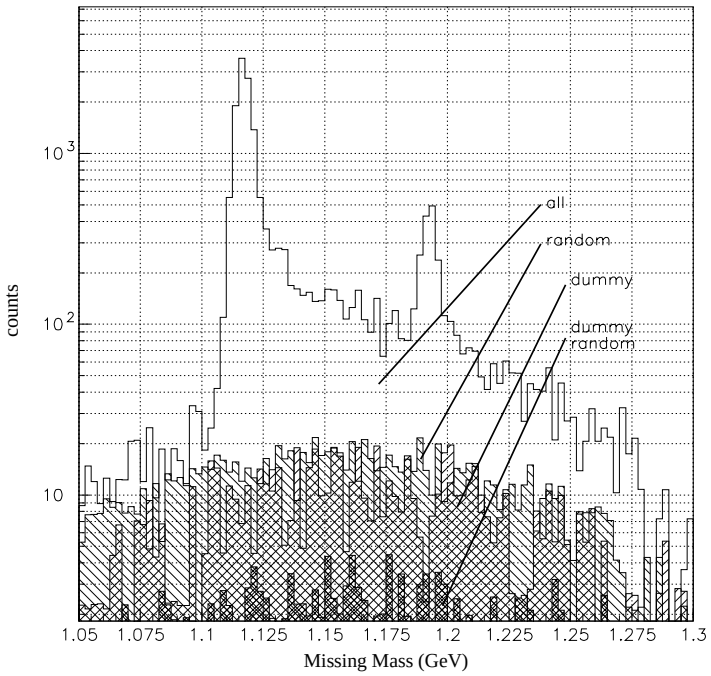

Figure 3.7: Relative size of random and dummy backgrounds discussed in Sections 3.5.3 and 3.5.5 shown in the missing mass (on a logarithmic scale) for the same setting as Figure 3.6 (Point 8).

yields were normalized to account for differences in the aluminum thickness (the dummy target foils were a factor of 9.27 times thicker than the actual target endcaps), and for the different amounts of incident charge in the combined dummy runs versus the combined LH_2 runs for a given kinematic setting.

The final data yield is then written in terms of the various backgrounds as:

$$Y_{\rm data} = (Y_{\rm in-time} - Y_{\rm random})_{\rm LH_2} - (Y_{\rm in-time} - Y_{\rm random})_{\rm DUMMY} \ . \qquad (3.4)$$

The size of the random and dummy contributions relative to the raw data for the run depicted in Figure 3.6 is shown in Figure 3.7 (on a logarithmic scale).

After the subtraction of these backgrounds, the bins in the unphysical region below the Λ production threshold fluctuate statistically about zero counts.

3.6 Corrections to the Data

After all the cuts were applied to the reconstructed SOS and HMS events and true $p(e,e'K^+)$ events were identified, the measured Λ and Σ^0 electroproduction yields had to be corrected for losses due to detection efficiencies, kaon decay, and kaon absorption. The following section describes the corrections applied to the data samples described in the previous section. The corrections and associated errors are summarized in Chapter 5 in Table 5.3.

3.6.1 Raw Scintillator (3/4) Efficiency

The trigger for each spectrometer required that three of the four scintillator planes fired. The efficiency of a single scintillator bar was typically better than 99.8%, as can be seen by comparing the number of events that fire 3/4 planes versus 4/4 planes. From this, the probability that one should have a hit in at least three of the four planes for a given event is

$$P_{3/4} = P_{1234} + P_{123} + P_{124} + P_{134} + P_{234} \tag{3.5}$$

where P_{1234} is the probability that all four planes had a hit, and P_{ijk} is the probability that only the three planes (i,j,k) fired without the fourth plane firing.

The scintillator trigger efficiency was computed on a run-by-run basis and was found to be effectively 100% for all settings, with an error of 0.1%.

3.6.2 Fiducial Tracking Efficiency

The efficiency of the drift chambers and tracking algorithm was also computed on a run-by-run basis. For each run, events that passed through the central scintillator bar on each of the four hodoscope planes were selected for the determination of the efficiency. These events were certain to have passed through the drift chambers, and barring inefficiencies, should have resulted in a good track. The tracking efficiency was computed by examining how many of these events that should have given a track did not, and was assumed to be indicative of the efficiency outside this fiducial region. Tracking efficiencies for the HMS were typically between $91 - 98\%$, whereas in the SOS they were a bit lower, at $83 - 93\%$. The lower tracking efficiency in the SOS was primarily due to the high rate (up to $\sim$ 700 kHz) of incident particles in the SOS. The error associated with these numbers is assigned to be 1.0%, from looking at the variations of the tracking efficiency as a function of incident particle rate.

3.6.3 Electronic Live Time

Another inefficiency that needs to be taken into account is the possibility that counts will be lost because the signals that created by the trigger logic are

of finite length. Most of the logic components in the trigger electronics do not recognize a new input while they are "busy" generating a signal at their output. For example, when a large signal reaches the input of a standard discriminator in the trigger logic, the unit will generate a pulse of 30 ns duration at its output. During that 30 ns period the unit is effectively "dead" to new input signals, and as a result, any subsequent signals arriving during that 30 ns dead time will be lost.

One can apply Poisson statistics to calculate the probability that a particular fraction of events will be lost by the trigger during a time t, given the rate R, of signals at the input. The probability of NOT receiving a count in an infinitesimal time dt is simply

$$P(\text{no count during } dt) = 1 - P(\text{count during } dt) = 1 - R\,dt\,. \tag{3.6}$$

The probability of NOT receiving a count in a finite time t is obtained by subdividing the time t into many smaller pieces of size dt, multiplying the probabilities for each of the $n = t/dt$ pieces together, and then taking the limit of $dt \to 0$:

$$P(\text{no count during } t) = \lim_{dt\to 0}(1 - R\,dt)^{t/dt} \equiv e^{-R\,t}\,. \tag{3.7}$$

Using this expression, it can be shown that the probability that the time between counts lies between t and $t + dt$ is

$$P(t)dt = P(\text{no count during } t) \times P(\text{count during } dt) = R\,e^{-R\,t}dt\,. \tag{3.8}$$

From this the electronic live time, L, can be calculated. This is the probability that a second event does not arrive before the first one is processed during a time τ, defined as the "limiting gate width" in the electronics in the trigger (this was 30 ns in the earlier example):

$$L = \int_{\tau}^{\infty} P(t)dt = \int_{\tau}^{\infty} R\, e^{-R\, t} dt = e^{-R\, \tau} \tag{3.9}$$

For $R\,\tau \ll 1$, the live time, L, can be approximated by its Taylor expansion $L = 1 - R\,\tau$. For this experiment, the worst case values are $R \lesssim 700$ kHz, and $\tau \approx 50$ ns, giving $R\,\tau \lesssim 0.035$.

The width of almost all of the output signals in the trigger logic during E93-018 was 30 ns. However, the hodoscope signals **S1X**, **S1Y**, **S2X**, and **S2Y** were each set to a width of 50 ns*, and resulted in a dead time consistent with a limiting gate width of that length.

The actual correction for electronic live time was made on a run-by-run basis for each spectrometer separately. The size, τ, of the limiting gate width and hence the correction, was measured by using the fanned-out copies of the 30 ns HMS(SOS) pretrigger signal, called **EL30**, **EL60**, **EL90**, and **EL120**. Each of these signals is adjusted to a width consistent with its name (e.g., the signal **EL60** is stretched to 60 ns) and is then sent directly into its own scaler. The units that create the **EL**$[T]$ signals are dead for T ns each time they accept an input, and as such will not generate gates for further events that arrive during

*See Hall C Logbook #10, p.110.

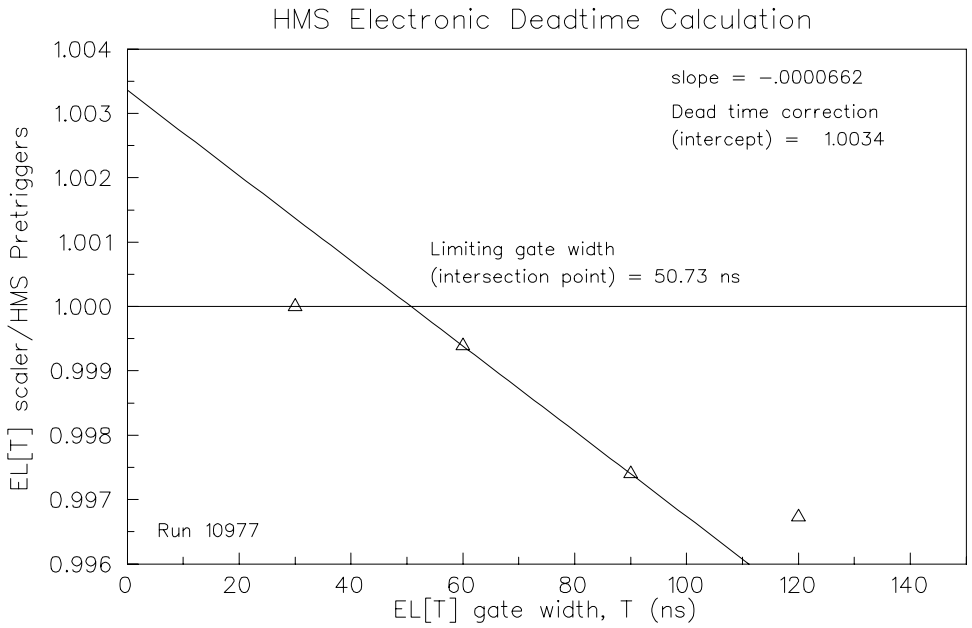

Figure 3.8: Verification of HMS electronic dead time correction as discussed in the text. An assumption has been made that the HMS scaler **EL120** was accidentally set to a width of 100 ns rather than 120 ns, and hence it was left out of the dead time fit.

the T ns gate width of its output. The principle is that the actual limiting gate width τ has already affected the rate of signals reaching the pretrigger, so all units **EL**$[T]$ with output width $T < \tau$ will generate the same number of signals as they receive at their inputs. Therefore, all of the inputs to these units will be counted in their respective scalers. On the contrary, scalers receiving signals generated by units with an output width $T > \tau$ will count fewer events by an amount proportional to RT due to the units being dead for a fraction of the time. One can then extrapolate to "zero gate width" to calculate how many counts one could have expected in the absence of electronic dead time, as is shown in Figure 3.8 and Figure 3.9.

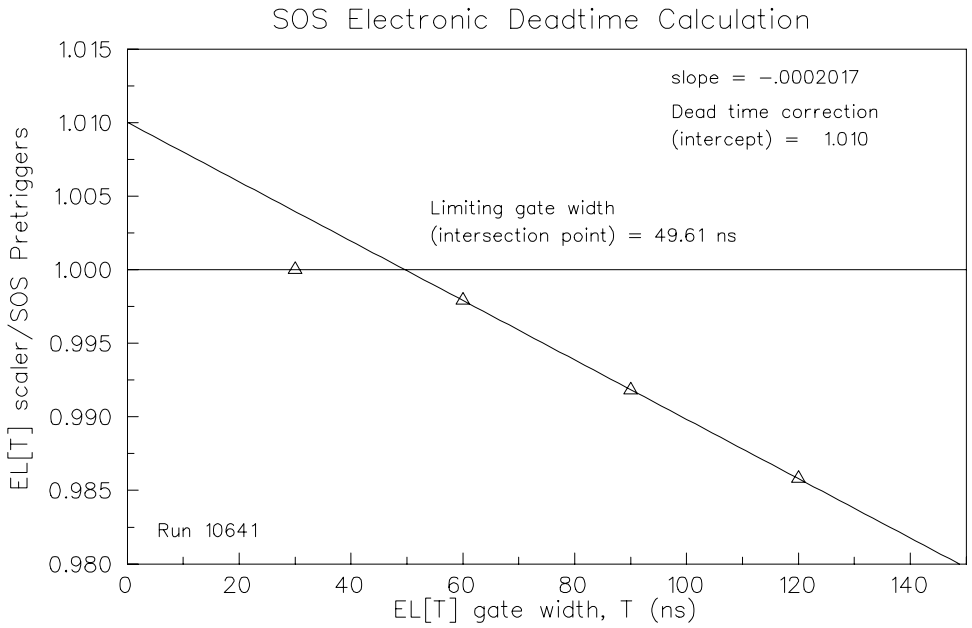

Figure 3.9: Verification of SOS electronic dead time correction similar to Figure 3.8. See text for details.

For the HMS, the pretrigger rates were quite low, and the corresponding electronic live times were typically very high, 99.6% or better. However, for the SOS (where the rates were up to $\sim$ 700 kHz) the electronic live time was significantly lower, ranging between $97.3 - 99.0\%$. The error on this correction was taken to be 0.1%.

3.6.4 Computer Live Time

Another (larger) source of dead time arises from the time it takes the data acquisition system to process an event. During normal running, the data acquisition system was run over a parallel link and in buffered mode. Under these conditions, the effective processing time is $\sim$ 125 μs, and the maximum accept-

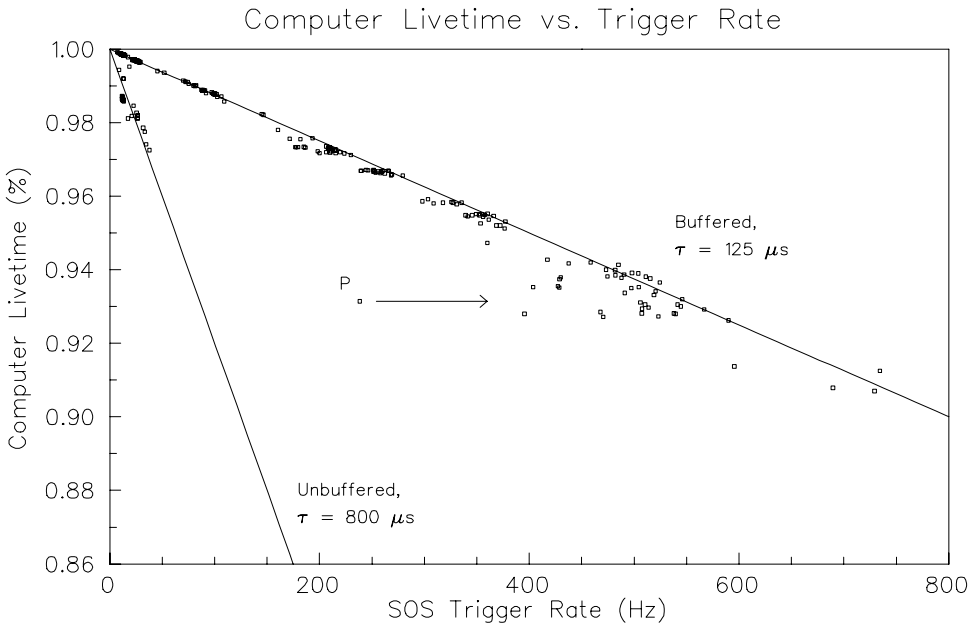

Figure 3.10: Verification of the computer live time correction by plotting the measured computer livetime vs. the SOS trigger rate. See text for details.

able event rate is around 2.5 kHz. Due to a problem with the data acquisition system during the experiment, some data were taken without buffering. In this mode, the processing time is ~ 800 μs.

In the coincidence electronics, a pretrigger is only converted into a trigger by the 8LM when the Trigger Supervisor (TS) is not busy. Therefore, the computer live time is calculated by dividing the number of triggers by the number of pretriggers formed by the 8LM. The dependence of the computer live time on the rate of triggers is shown in Figure 3.10 (the SOS is shown, but the HMS results are equivalent). The two distributions correspond to buffered and unbuffered running, and the lines are drawn proportional to $1 - R\,\tau$ for $\tau = 125$ μs and $\tau = 800$ μs, respectively. Points such as point "P" that are far away from the expected

line have a faulty calculation of the rate, but are shown here in order to maintain consistency with previously reported results of this effect (e.g., [Arr98]). In the normal output files from the ENGINE, the trigger rate is calculated as (number of SOS triggers)/(run time). The time used is unfortunately not the actual time with beam on, but the elapsed time of the run, which will be too large if there are periods without beam during the run. If one recalculates the trigger rate using the actual time with beam on, the resulting rate is increased such that the points agree with the expected line.

The computer live time was calculated on a run-by-run basis and ranged in size from $91 - 100\%$. The error on this correction was estimated to be 0.3% from measuring the deviations from the expected line, taking into account the aforementioned problem with the rate calculation.

3.6.5 TS Output Overlap Coincidence Blocking

As discussed in Section 2.10, coincidences between the HMS and SOS are formed at the 8LM and are forwarded to the Trigger Supervisor. Due to the details in the timing of the signals after the TS, a fraction of the events were recorded with incorrect detector responses, and in particular, with an incorrect value of coincidence time. This caused some otherwise good events to be thrown out by the $|\,\mathrm{cointime(SOS)}\,| < 0.65$ ns cut.

For the sake of clarity, let us consider a single SOS ADC channel. In order

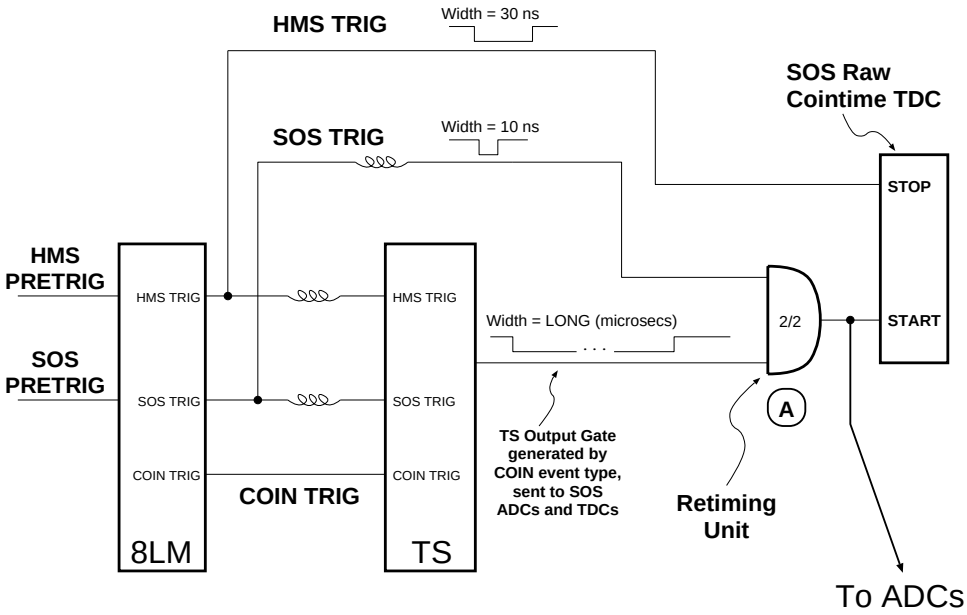

Figure 3.11: Close-up schematic of the Trigger Supervisor ADC/TDC gate retiming circuit for the SOS. The retiming takes place at unit "A", where a delayed SOStrigger is ANDed with the TS output gate. See text for details.

for the gates that read this ADC to arrive simultaneously with the analog signals, the very long gate output from the TS is retimed at unit A as shown in Figure 3.11 (and in Figure 2.20) using the **SOS TRIG** signal from the 8LM.

Normally, this **SOS TRIG** signal arises from the same **SOS PRETRIG** that formed the coincidence in question with an **HMS PRETRIG** at the 8LM input. This coincidence caused the 8LM to output the **COIN TRIG** that in turn caused the TS to output the long gate. In this case, the delays are set such that the retiming at unit A always results in a properly timed gate being sent to the ADCs, and the ADC information will be read correctly.

Alternatively, consider the case in which an **SOS PRETRIG** signal DOES

NOT form a coincidence at the 8LM, but arrives $\sim 60 - 70$ ns* *earlier* than a pair of **HMS PRETRIG/SOS PRETRIG** events that DO form a coincidence. Call the earlier single **SOS TRIG** formed by the 8LM a "blocking event". In this case, the TS will not output a gate upon receiving the blocking event (because it is set to prescale away everything it receives from the 8LM except for **COIN TRIG**s). However, this blocking event will still be sent along the retiming path towards unit "A". Now, when the real **COIN TRIG** reaches the TS about $\sim 60 - 70$ ns *later*, it does cause the TS to output the long gate. Unfortunately, the delays and timing were set such that it was possible for the blocking event to reach unit A at the same time as the very long gate, causing gates to be sent to the ADCs (and STARTs to be sent to the TDCs) with the improper early timing of the blocking event, rather than the proper timing of the actual SOS event that caused the **COIN TRIG** in the first place.

The gates sent to the SOS ADCs trigger them to read the information from the wrong event (or perhaps some combination of the blocking event and the real event), and the SOS TDCs record values that are $\sim 60 - 70$ ns higher than they should be. The bad SOS ADC values sometimes caused the TOF algorithm to fail. For instance, if there are too many scintillators hit, they may not be consistent with the track. Corrections for these events are taken into account

*Note that because the limiting gate width for the electronic dead time was $\tau = 50$ ns in each spectrometer, two singles triggers from the same spectrometer could not reach the 8LM any less than 50 ns apart (See Section 3.6.3).

separately as explained in Section 3.6.9.

The bad SOS TDC values caused the coincidence timing of otherwise good events to be well outside of the coincidence time cut. A typical spectrum of raw (uncorrected for pathlength) coincidence time is shown in Figure 3.12. Region I is the "main coincidence window" region of normal coincidences formed at the 8LM with a width of about 40 ns (30 ns from **HMS PRETRIG** and 10 ns from **SOS PRETRIG**). Region II is the "SOS blocking event" region in which the first 30 ns of Region I appear to be copied (with about 2% of the total events) to a time about 67 ns higher in coincidence time. The final 10 ns of the spectrum appear to be copied into a very tight region at around 242 ns. This is a self-timing peak caused by the HMS signal which will be discussed shortly.

Event sequences that could be responsible for various improper coincidence times are depicted in Figure 3.13. When an **HMS PRETRIG** and an **SOS PRETRIG** arrive at the 8LM, the later of the two sets the timing for the leading edge of the **COIN TRIG** that is generated. The timing of the TS gate signal is in turn dictated by when it receives the **COIN TRIG**. So, if the **HMS PRETRIG** is later at the 8LM as in diagram B, the timing of the TS GATE signal will be set by the HMS (and likewise by the SOS in a situation such as diagram C). Note that in diagram A, the **HMS PRETRIG** and an **SOS PRETRIG** arrive at the 8LM simultaneously, so both set the timing for the TS GATE.

The self-timing peak in Figure 3.12 arises from events in which an earlier

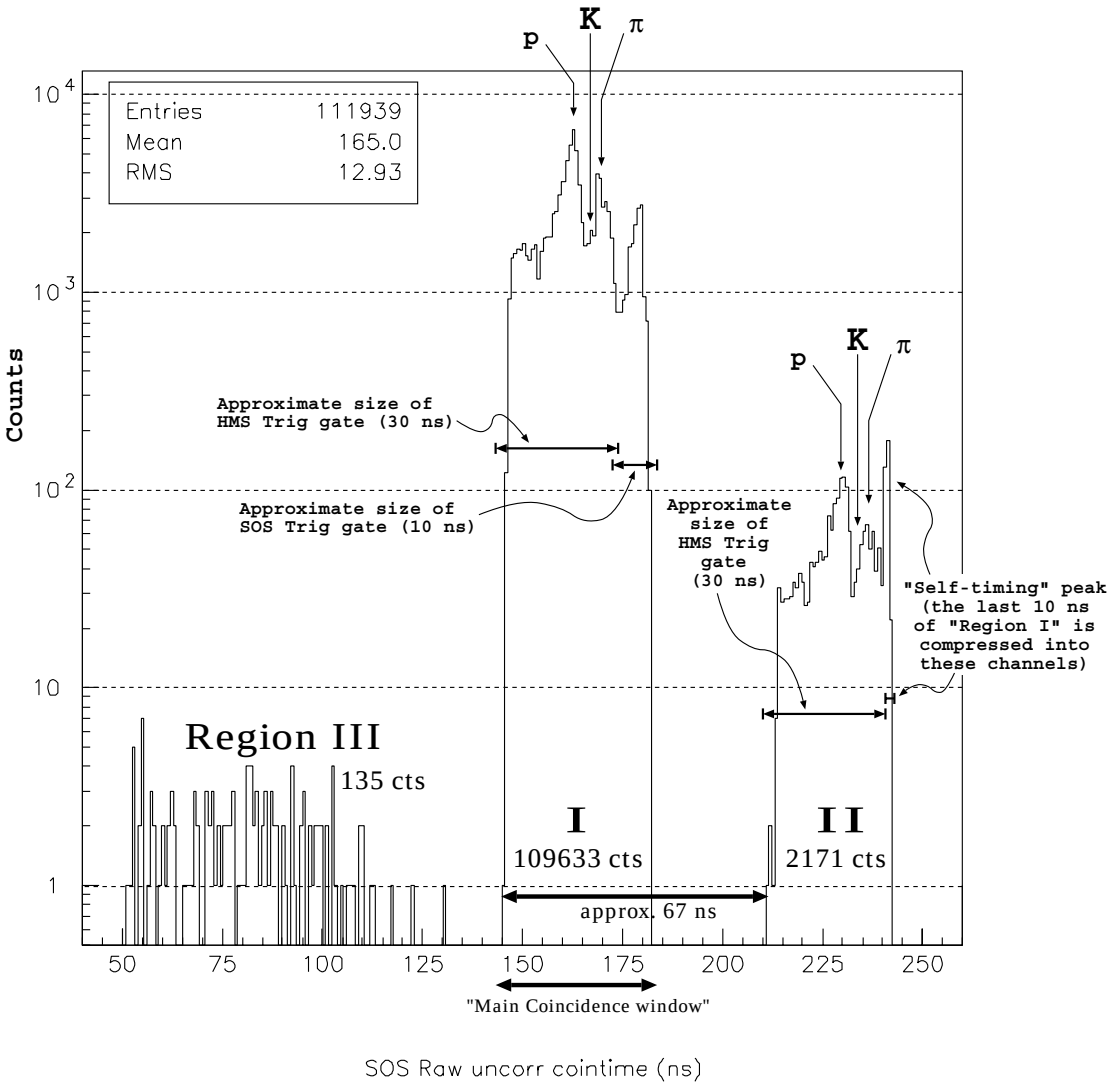

Figure 3.12: SOS raw (uncorrected) coincidence timing spectrum. Region I is the "main coincidence window", and events that are blocked are found in Regions II and III. Note that "cts" stands for "counts" in the figure. A detailed discussion is given in the text.

SOS TRIG overlaps the leading edge of the TS GATE signal in diagram A or B (or any relative timing between these two). In this case, the **HMS TRIG** sets the timing for both the START (by setting the timing of the TS GATE signal) and the STOP of the SCOINTIM raw coincidence time TDC. Hence, a

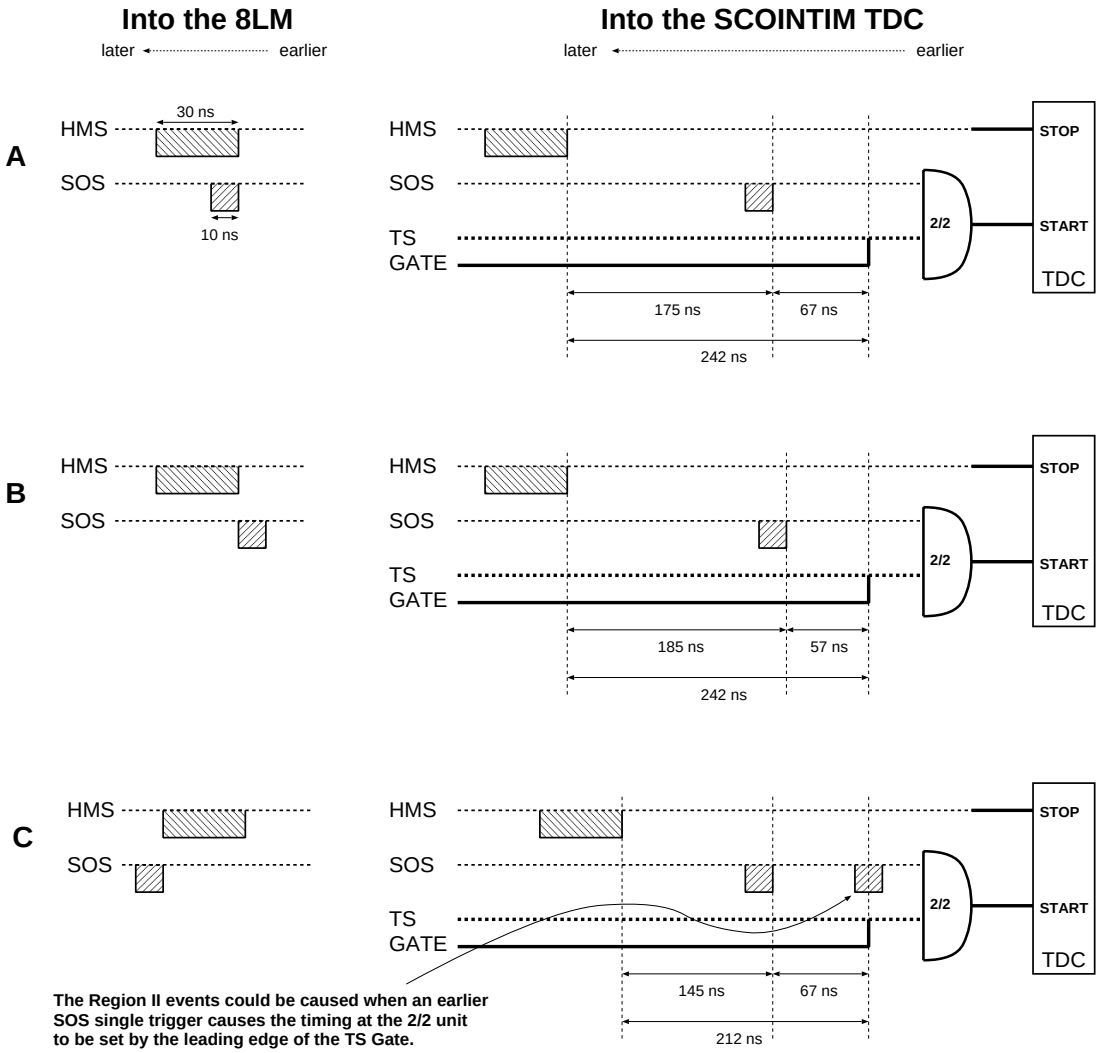

Figure 3.13: Hypothetical sequence of triggers that could cause events to be blocked, as discussed in detail in the text.

fixed time of 242 ns would be recorded for any blocked event in which the **HMS PRETRIG** was later than the **SOS PRETRIG** at the 8LM.

Region III is the equivalent coincidence blocking effect for events in which an **HMS TRIG** acts as the blocking event. The effect is dependent on the singles rates for each spectrometer, which accounts for why the SOS effect is much larger

than that for the HMS.

The exact mechanism for this effect was difficult to uncover after the fact, as the electronics had already been dismantled by the time the effect was investigated. One mechanism that was investigated here is discussed in [VW99] regarding an earlier Hall C experiment, E91-013. In that experiment, problems with coincidence timing spectra were thought to have been caused by loss of synchronization between the HMS and SOS fastbus crates when the data acquisition was run in buffered mode. However, the effect in E93-018 discussed here was also present when data were taken without buffering, and hence was not related to a buffering synchronization problem.

Regardless of the mechanism, it appears that the events in Regions II and Region III would have been recorded as perfectly good events had a singles event not blocked them. Therefore, the number of events outside of Region I relative to the total is taken as a correction for these blocked events. The effect ranged from $1.2 - 6.0\%$, depending on the **SOS TRIG** rate. The error on the correction is assigned at 0.5%.

In order to avoid confusion, it should be pointed out that the term "coincidence blocking" has been used to describe a completely different effect in Jefferson Lab experiment E89-008 which used both the HMS and SOS simultaneously as independent single arm electron spectrometers. The discussion that follows is paraphrased from [Arr98]. In their case, the TS was set to prescale away

all coincidences. However, if an **SOS TRIG** and an **HMS TRIG** happened to arrive at the TS within 7 ns of each other, the TS would override the prescaling circuit and would still accept the events together as a coincidence. The TS would then send long gates to both spectrometers, which could cause a mistiming in the ADC gates/TDC stops because the timing was not set up for coincidences. In summary, for experiment E89-008 the term "coincidence blocking" meant that good singles events were blocked by coincidences. This effect was not a factor for E93-018.

3.6.6 Kaon Decay Correction

The fact that kaons are unstable and have a short mean lifetime implies that a large fraction of the kaons which are created at the target decayed into secondary particles before they could be detected. The number of kaons that were actually detected was less than the true number of kaons produced in the reaction, and corrections for their decay had to be taken into account. Various decay channels are listed in Table 3.1.

For the sake of discussion, let us consider the hypothetical situation in which after a given kaon decayed, the produced decay particles themselves were never detected by the SOS. In this case, the number of detected kaons would be deficient by the fraction

$$\frac{N_{\text{detected}}}{N_{\text{at target}}} = e^{-\left(\frac{m\,d}{p\,\tau}\right)} \tag{3.10}$$

Decay channel	Branching fraction (Γ_i/Γ)
$K^+ \longrightarrow \mu^+ + \nu_\mu$	(63.51 $\pm$ 0.18)%
$K^+ \longrightarrow \pi^+ + \pi^\circ$	(21.16 $\pm$ 0.14)%
$K^+ \longrightarrow \pi^+ + \pi^+ + \pi^-$	(5.59 $\pm$ 0.05)%
$K^+ \longrightarrow e^+ + \pi^\circ + \nu_e$	(4.82 $\pm$ 0.06)%
$K^+ \longrightarrow \mu^+ + \pi^\circ + \nu_\mu$	(3.18 $\pm$ 0.08)%
$K^+ \longrightarrow \pi^+ + \pi^\circ + \pi^\circ$	(1.73 $\pm$ 0.04)%

Table 3.1: Primary K^+ decay modes listed with branching fractions (from [HZ98]).

where m is the kaon mass, d is the distance traveled to the detector, p is the momentum of the kaon, and $\tau_K \approx 12.4$ ns ($c\tau_K \approx 3.713$ m) is the mean lifetime of a kaon at rest [HZ98]. Both the distance traveled and the momentum of the kaons were measured, so this fraction could be used to compensate for the decays.

The choice of distance d to be used in Equation 3.10 has to be considered further, because at first glance it could have been taken to be anywhere inside the detector hut. If a kaon had survived up to ~8 cm into the aerogel, a decay that took place at any point beyond could not cause the detected event to fail the kaon cuts. This is for two reasons: First, the kaon would have already hit 3/4 scintillator planes, allowing for a valid hardware trigger and for a software $\beta_{\rm tof}$ calculation. Second, with only ~1 cm of aerogel material remaining to traverse, even a $\beta = 1$ decay fragment would be highly unlikely to generate enough Čerenkov light in the aerogel detector to cause the event to be vetoed with a threshold of 3.5 p.e. (see Section A.5). Because of these considerations, a kaon

was considered "detected" if it reached a plane ∼8 cm inside the aerogel material, or a distance of about 1016 cm from the target for the central ray of the SOS*. This was the distance (corrected for variations in path length through the spectrometer) that was used in calculating the decay fraction.

In reality, the decay particles were sometimes detected by some or all of the detector elements. This could lead to over-correction (double counting) if the decay fragments passed all the cuts and were mistaken for undecayed kaons because the value of N_{detected} in Equation 3.10 would be too large. Implementing decays in the Monte Carlo simulation showed that if the kaon decayed prior to reaching the detector hut, the decay particles were lost and were not detected. However, if the decay took place within the hut, some fraction of the decay particles would still be detected. Of these detected decay fragments, most did not pass the kaon cuts and were thrown out. What was left was a small number of decay particles which actually passed the kaon cuts and "mimicked" the undecayed kaon signal. A distribution of such events for the various decay channels (generated by Monte Carlo) is shown in Figure 3.14.

The decay correction was made on an event-by-event basis (due to flight pathlength differences from event to event) and was typically large, ranging from a factor of 2.5 to 4.0, with a scale error estimated to be 3.0%, plus a 1.0%

*Note that the decay correction is not very sensitive at the few cm level to the choice of this distance, d. The difference in the decay correction between choosing $d = 1016$ cm and $d = 1008$ cm is only 0.2%, while the difference between $d = 1016$ cm and $d = 1044$ cm (S2X) is 0.7%

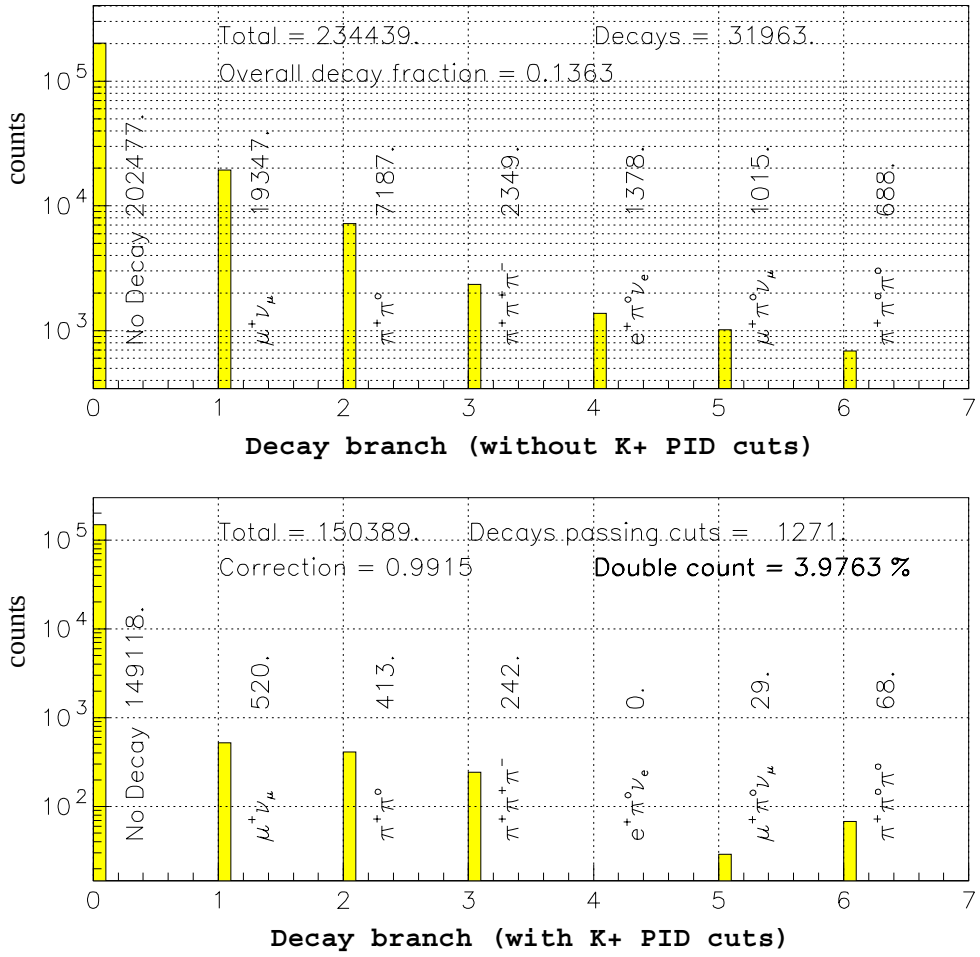

Figure 3.14: Simulated distribution of decay events that mimic a K^+ signal for Point 5. The upper panel shows that of the 234439 simulated kaons that reached the hut, 13.6% decayed into the channels shown. The lower panel shows the subset of these events that passed the kaon PID cuts. The 1271 decays in the lower panel would be inappropriately labelled as kaons.

error arising from determination of the path length. The fraction of the decay fragments that mimicked kaon signals for each setting is shown in Table 3.2. To account for the mimics, a reduction factor of $0.990 - 0.995$ was applied *after*

Point	SOS Momentum (GeV)	Double Count %
1	1.126	3.96%
2	1.126	4.17%
3	1.126	4.75%
4	1.188	3.72%
5	1.188	3.98%
6	1.188	4.53%
7	1.216	3.49%
8	1.216	4.00%
9	1.216	4.44%
10	1.634	2.27%
11	1.634	2.34%
12	1.634	2.55%

Table 3.2: Percentage of decay particles that mimic a K^+ signal as determined by the decay Monte Carlo simulation.

the main decay correction (i.e., as a secondary correction to the original decay correction), with an error in this second correction assigned to be 0.5%.

3.6.7 Kaon Absorption Through Materials

Some of the particles that were either scattered or produced at the target were lost through interactions with the various detectors and vacuum windows along their path. Table 3.3 lists the materials encountered by the scattered electrons, although the absorption of electrons by materials in the HMS was negligible*. However, for the kaons, the absorption correction was not negligible.

*Both tables were necessary for calculating the effects of multiple scattering in the Monte Carlo (see Section 4.3).

The materials that were encountered by the kaons up to the plane of detection are listed in Table 3.4.

A simple parameterization of the fraction of kaons lost to interaction is:

$$\frac{N_{\text{absorbed}}}{N_0} = \frac{N_A\, T}{\text{A}_{\text{eff}}}\, \sigma_0 \,, \tag{3.11}$$

where N_A is Avogadro's number, A_{eff} is the effective mass number of the material, T is the thickness in g/cm^2, and σ_0 is the total interaction cross section given by:

$$\sigma_0 = 21.065\, p_K^{-0.99}\, \text{A}_{\text{eff}}^{0.79} \,, \tag{3.12}$$

where p_K is the kaon momentum in GeV/c [KMT59]. Taking all of the materials into account gives the following expression for the absorption correction:

$$\text{Absorption correction} = 1.0 - \frac{0.06962}{p_K^{0.99}}. \tag{3.13}$$

The fraction of absorbed kaons ranged from $3 - 6\%$, and was corrected for on an event-by-event basis. The error in this correction was estimated to be 0.5% random (momentum dependency) and 0.5% due to an overall scale error in the size of the correction.

Material	ρ (g/cm^3)	Thick (cm)	λ (g/cm^2)	X (g/cm^2)	X/λ $\times 1000$
3.37 cm liquid hydrogen	0.0708	3.37	47.3	0.2386	5.04
5 mil Al target window	2.70	0.0127	88	0.0343	0.39
16 mil Al chamber window	2.70	0.0406	88	0.1096	1.25
Air (no vacuum coupling)	0.0012	15	75.0	0.0180	0.24
Kevlar (spectrometer entrance)	0.74	0.0381	70	0.0282	0.40
Mylar (spectrometer entrance)	1.39	0.0127	72	0.0177	0.25
Kevlar (spectrometer exit)	0.74	0.0381	70	0.0282	0.40
Mylar (spectrometer exit)	1.39	0.0127	72	0.0177	0.25
Air (exit through S2)	0.0012	256	75	0.3072	4.10
Mylar DC windows	1.39	0.0102	72	0.0142	0.20
Sense wires (eff.) W	19.3	0.0001	147.7	0.0019	0.01
Field wires (eff.) Cu/Be (50/50)	5.40	0.0068	87.9	0.0367	0.42
Ar/Ethane Gas	0.0015	16.6	70	0.0249	0.36
Polystyrene scint S1X	1.03	1.067	70	1.099	15.70
Polystyrene scint S1Y	1.03	1.067	70.0	1.099	15.70
Čerenkov windows (Al)	2.70	0.204	88.5	0.5508	6.22
N_2 gas	0.0013	150	64.2	0.195	3.04
Mirror support (Rohacell)	0.05	1.8	70.0	0.09	1.29
Mirror (SiO_2)	2.20	0.3	83.1	0.66	7.94
Polystyrene scint S2X	1.03	0.2668	70.0	0.2748	3.93
Total					67.13

Table 3.3: Materials in the HMS contributing to multiple scattering.

Material	ρ (g/cm^3)	Thick (cm)	λ (g/cm^2)	X (g/cm^2)	X/λ $\times 1000$
3.37 cm liquid hydrogen	0.0708	3.37	47.3	0.2386	5.04
5 mil Al target window	2.70	0.0127	88	0.0343	0.39
8 mil Al chamber window	2.70	0.0203	88	0.0548	0.62
Air (no vacuum coupling)	0.0012	15	75	0.0180	0.24
Kevlar (spectrometer entrance)	0.74	0.0127	70	0.0094	0.13
Mylar (spectrometer entrance)	1.39	0.0076	72	0.0106	0.15
Kevlar (spectrometer exit)	0.74	0.0381	70	0.0282	0.40
Mylar (spectrometer exit)	1.39	0.0127	72	0.0177	0.25
Air (DC 1 through S2)	0.0012	149	75	0.1788	2.38
Mylar cathode	1.39	0.0088	72	0.0122	0.17
Wire (effective) W	19.3	0.0024	147.7	0.0463	0.31
Ar/Ethane Gas	0.0015	3.7068	70	0.0056	0.08
Mylar cathode	1.39	0.0088	72	0.0122	0.17
Wire (effective) W	19.3	0.0024	147.7	0.0463	0.31
Ar/Ethane Gas	0.0015	3.7068	70	0.0056	0.08
Polystyrene scint S1Y	1.03	1.10	70	1.1330	16.19
Polystyrene scint S1X	1.03	1.04	70	1.0712	15.30
Čerenkov windows	1.39	0.060	70	0.0834	1.19
CO_2 gas (1 atm)	0.002	100	76.5	0.200	2.61
Mirror (Rohacell-Mylar-C)	—	—	70	0.45	6.43
Lucite	1.1600	2.5400	71.4	2.9464	41.27
Polystyrene scint S2Y	1.03	1.10	70.0	1.1330	16.19
Al housing for aerogel	2.70	0.159	88.0	0.4293	4.88
Aerogel (using 8 cm)	0.20	8	80.6	1.6	19.85
Total					134.63

Table 3.4: Materials in the SOS contributing to kaon absorption and multiple scattering.

3.6.8 Aerogel Cut Efficiency Correction

As stated earlier, one of the main tools used for particle identification was the cut on the number of photoelectrons yielded by the aerogel Čerenkov detector. The efficiency of this cut was directly measured using low-momentum pions. This was done for two main reasons. First, without using the aerogel cut to eliminate the pion background, it was impossible to obtain a clean enough sample of kaons to study the aerogel response. Second, many effects that might cause a kaon to "accidentally" fire the aerogel (such as knock-on electrons or scintillation) are primarily dependent on the velocity of the particle. With this in mind, the SOS was set to detect very low-momentum pions ($P_{SOS} = \{0.304, 0.417\}$ GeV/c) which were at a similar velocity ($\beta_\pi \approx \{0.91, 0.95\}$) to a typical kaon in the experiment. The aerogel cut was then varied, and the relative number of pions that were rejected as a function of this cut was recorded as in Table 3.5. For this analysis, a cut of 3.5 photoelectrons was used, yielding a correction of $(2.6 \pm 0.3)\%$.

3.6.9 Events with $\beta_{tof} = 0$

For some events, the TOF routines were unable to calculate a good value of β_{tof}, and as a result assigned a value of $\beta_{tof} = 0$. This was typically because the scintillators that were hit did not agree with the track that was found. Some of these events were caused by the problem with the S2X TDC discussed in Section 3.4, some caused by the TS coincidence blocking effect discussed in Section

Aerogel Photoelectrons	Cut efficiency %
0.5	$\approx 20\%$
1.5	5.6%
2.5	3.4%
3.5	2.6%
4.5	2.2%
5.5	1.9%
6.5	1.7%

Table 3.5: Efficiency of aerogel cut as a function of photoelectron threshold.

3.6.5, and others were simply because the TOF algorithm failed. The effect was treated as a global inefficiency.

The effect in the SOS was measured by looking at the number of events that pass all* of the kaon cuts *except* the cut on $(\beta_{\rm tof} - \beta_{\rm K})$. Some of these events have $\beta_{\rm tof} = 0$. The assumption is that the effect was particle independent, and as such the ratio of kaons to non-kaons for the $\beta_{\rm tof} = 0$ events should be the same as that for those with good $\beta_{\rm tof}$. This gives an effect that ranges in size from $1.0 - 4.2\%$, with an assigned error of 0.5%.

The HMS found very few events to have $\beta_{\rm tof} = 0$, and the correction was estimated to be $(0.2 \pm 0.2)\%$.

*This is only considering events in the main coincidence window so as to avoid double correcting for the TS coincidence blocking effect.

3.6.10 Target Length/Density

The length of the 4 cm liquid hydrogen target was measured to be 4.36 cm with an error of 0.2%. The density of the target (in the absence of beam power deposition) was known to an accuracy of 0.4% [Dun97b] .

As the beam passes through the target liquid, the power deposited can cause increases in temperature in the vicinity of the beam, and lead to local changes in the density. The effect increases with beam current and decreases as the raster amplitude is made larger. By examining changes in scattering rates as a function of beam current and raster amplitude, the target density decrease was measured to be $(-3.8 \pm 0.4)\%$ / 100 μA / mm of raster amplitude [Gus96]. For the conditions of E93-018, this translated to a reduction in density of 0.8% with an assigned error of 0.4%.

Finally, the results were corrected for the purity of the liquid hydrogen target, which was measured to be greater than 99.8%. A correction of 0.2% was used with an error assigned at 0.2% [Ter99].

3.6.11 Charge Measurement

The hardware used to measure the beam current was discussed in Section 2.3. In summary, there were two "working" BCMs during E93-018: BCM2, which was controlled by the Hall C users and was located just upstream of the entrance to the hall, and BCM3, which was controlled by the accelerator division

and was located just upstream of the target (see Figure 2.4). The readout electronics for BCM2 were located in the Hall C counting house electronics room, while the readouts for BCM3 were located in the Machine Control Center.

The stability of these two monitors relative to each other is shown in Figure 3.15 as a function of run number throughout E93-018. For the first half of the experiment (aside from scattered runs) this ratio fluctuated less than $\pm 1.5\%$. However, in the areas labeled as "Region A" and (in particular) "Region B", this ratio can be seen to behave erratically.

Region B corresponds to running taken from the evening of 30-Oct-96 through the afternoon of 31-Oct-96, during which period there was a failure of the climate control system in the Hall C electronics room. The electronics for BCM2 were thus affected and yielded inaccurate measurements of the charge. However, because the electronics for BCM3 were located elsewhere they were not affected by the temperature problems, as can be verified by examining the two BCMs independently during the run period. By looking at the ratio of the number of SOS pretriggers divided by the integrated charge from each run as measured by each BCM independently as in Figure 3.16, one clearly sees that although the BCM2 reading is unreliable in Region B, the BCM3 reading is quite stable. For runs after this failure, the readings from BCM2 were deemed unreliable. A similar, shorter failure of the climate control in the counting house was the cause of the fluctuations in Region A (18-Oct-96), and again BCM3 was fine. Also, note that

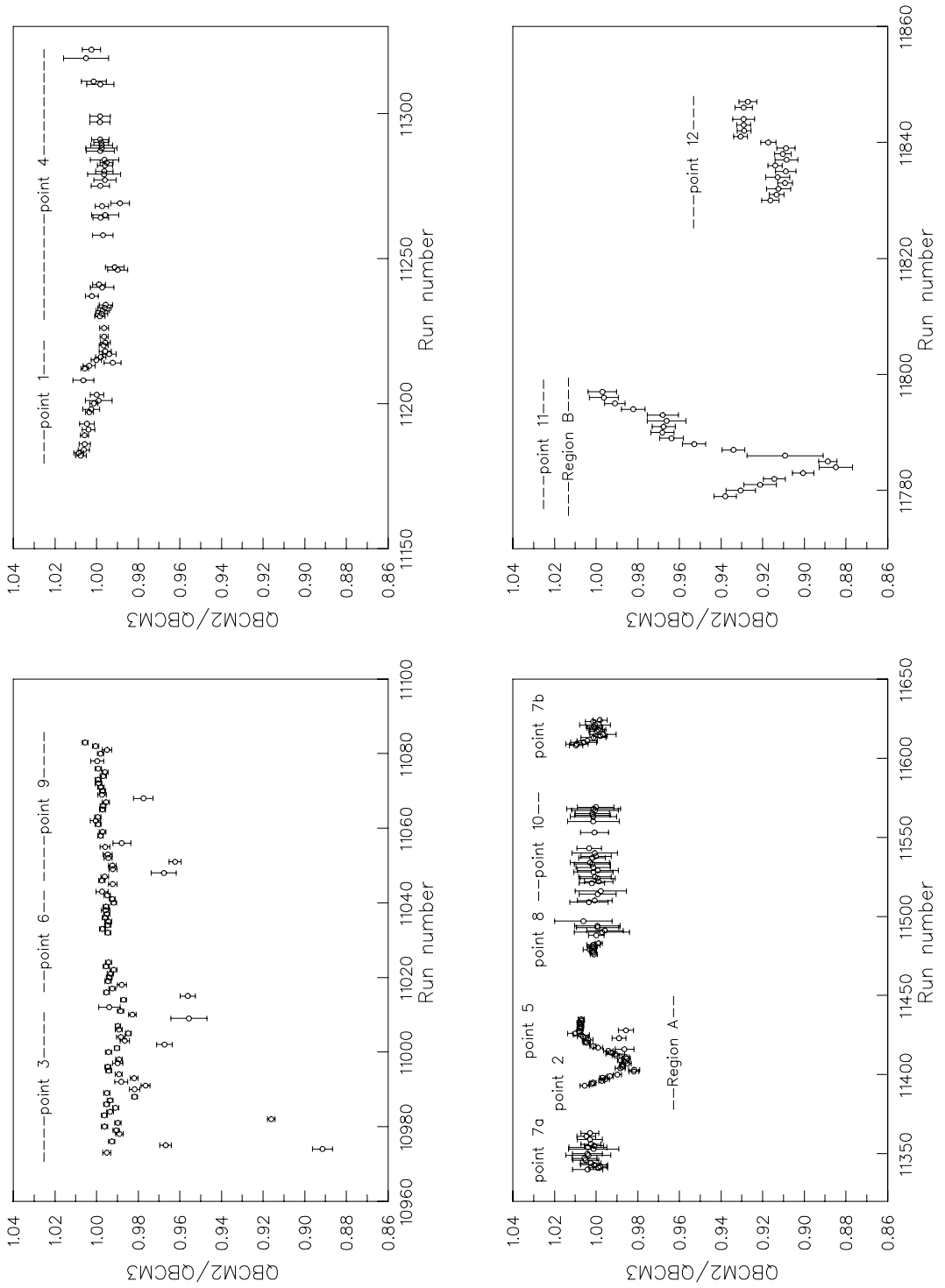

Figure 3.15: Ratio of charge measured from BCM2/BCM3. The figure is discussed in Section 3.6.11.

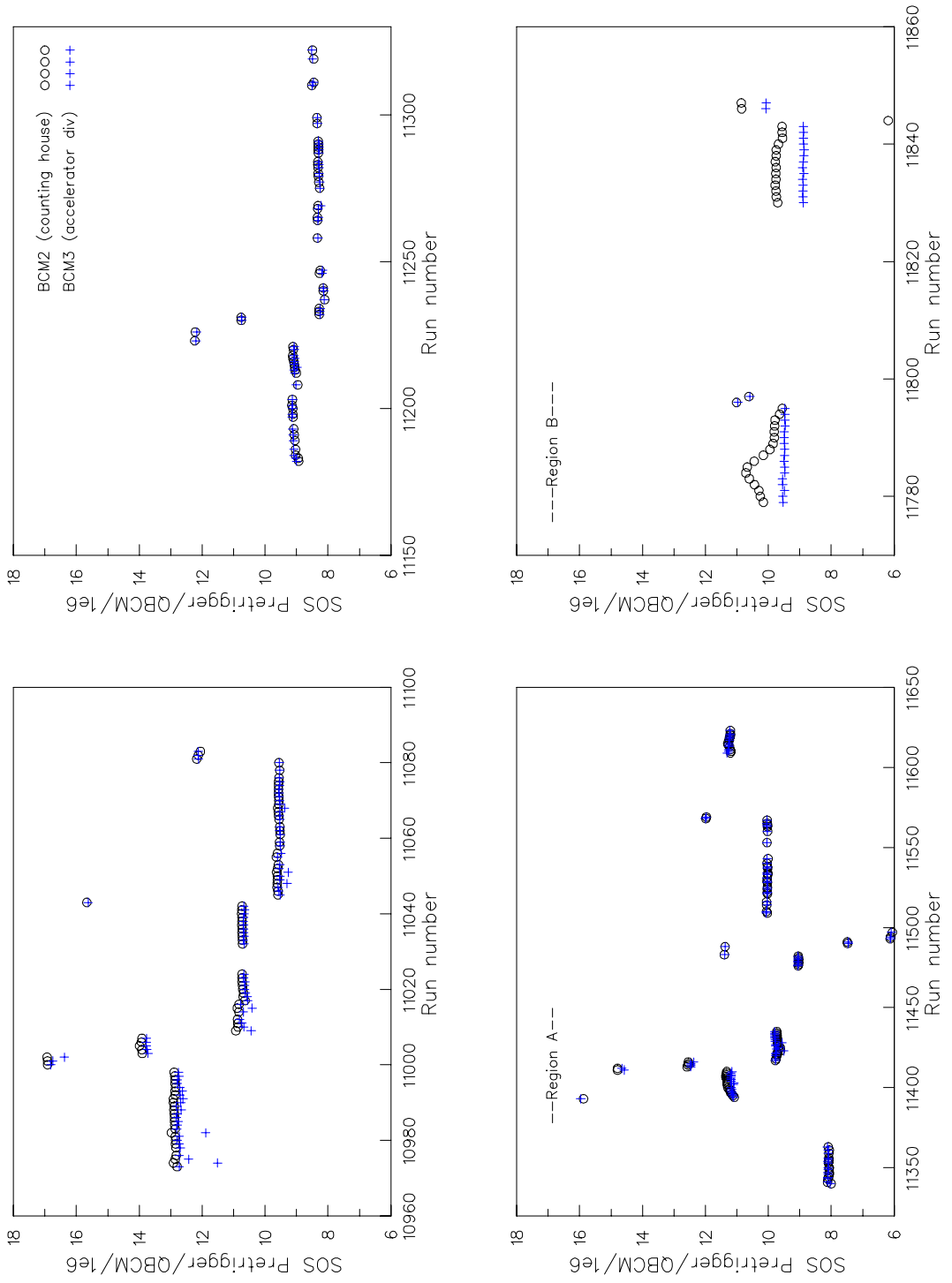

Figure 3.16: Ratio of SOS pretriggers to charge measured from BCM2 and BCM3. The figure is discussed in Section 3.6.11.

the scattered runs that appeared to have an improper BCM2/BCM3 ratio in the earlier portion of the experiment were a result of changes in BCM3. These were presumably small changes in the BCM calibrations made by the accelerator crew during running [Mac99].

As a result, the charge read from BCM2 was used for all runs excepting those for Points 2 and 5 (Region A), Point 7b, Point 11 (Region B), and Point 12. The charge from BCM3 was used for these particular runs, although for Points 2, 5, and 7b it should be noted that the magnitude of the fluctuations on BCM2 were less than $\pm 2\%$. Because at least one of the BCMs was always stable, it was unnecessary to increase any errors associated with the charge measurement. The error on the charge measurement was thus taken to be 1.5%.

Chapter 4

Monte Carlo Simulation

4.1 Overview

The present analysis required a detailed Monte Carlo simulation of the experiment in order to extract cross section information from the data. The simulation modeled the optical properties of both spectrometers, multiple scattering, energy loss from passage through materials, kaon decay, and radiative processes.

The simulation code used for this E93-018 analysis was largely based upon the code SIMULATE [Mak94] used by the SLAC NE-18 experiment. The code was modified to include spectrometer models of the HMS and SOS, and renamed to SIMC. The SIMC code uses the Plane Wave Impulse Approximation (PWIA) to model A(e,e′p) for various nuclei, incorporating radiative corrections.

In order to test the validity of the Monte Carlo, elastic scattering (e,e′) and (e,e′p) data were taken and compared with the results from SIMC. After

the spectrometer models were verified in this manner, the code was modified to simulate kaon electroproduction from hydrogen, and was renamed to SIMK. The details and use of the Monte Carlo will be discussed in this chapter. Note that as a matter of convention, the term "data" always refers to the measured experimental data yields, and the term "MC" always refers to the simulated events and yields.

4.2 Event Generation

The SIMK event generator first picks a random target interaction point in the beam-coordinate system (x_B, y_B, z_B) consistent with the target length and raster amplitudes. The beam energy is selected based on the value given in the input file with a resolution dE/E of 0.5%. Then, the quantities $(Q^2, W, \phi_e, \theta^*_{qK}, \phi)$ are randomly generated for each event*. These coincidence events were generated with unit cross section in the phase space $\Delta V^5_{\rm gen} \equiv \Delta Q^2 \Delta W \Delta\phi_e \Delta\Omega^*_K$ with limits that extended beyond the physical acceptances of the spectrometers.

With the scattered electron quantities (Q^2, W, ϕ_e) generated (and after the effects of radiative corrections are considered as in Section 4.4) the virtual photon four-vector q^μ is completely specified. Using Equations B.12 and B.13, one can perform a Lorentz transformation to obtain the CM virtual photon four-vector, $(q^\mu)^*$, in the CM frame of the virtual photon and proton.

For the kaon side, the Monte Carlo input file specifies which hyperon

*These quantities are all defined in Appendix B.

$Y = (\Lambda, \Sigma^0)$ is being generated. Because the kaon-hyperon production is a two-body reaction, the momentum of the outgoing kaon in the CM frame is fixed by knowledge of W as

$$|\mathbf{p}^*_{\mathbf{K}}| = \sqrt{\left(\frac{(W^2 + m_K^2 - m_Y^2)}{2\,W}\right)^2 - m_K^2}\ . \tag{4.1}$$

The remaining components of the kaon four-vector in the CM frame, $(p_K^\mu)^*$, are determined using the quantities (θ^*_{qK}, ϕ). Then, the kaon is Lorentz boosted back to the lab frame in a coordinate system in which the z-axis is along the $\mathbf{q}$ vector (see Section B.4). Finally, a coordinate rotation is performed to yield the "spectrometer" values of momentum and angles of the kaon at the interaction vertex (henceforth referred to as "vertex quantities").

4.3 Spectrometer Models

After the momenta and angles of both the electron and kaon are converted to outgoing vertex quantities in the lab frame, each particle is transported forward through a COSY INFINITY [COS91] model of its respective spectrometer. Ionization energy loss in the target is accounted for using the Bethe-Bloch equation [Leo94]. For the hadron arm,

$$E_{\text{loss}} = 0.3071\,\frac{Z_{\text{eff}}}{A_{\text{eff}}}\,\frac{t}{\beta^2}\left[\ln\left(\frac{2m_e c^2\beta^2\gamma^2}{I}\right) - \beta^2\right] \tag{4.2}$$

where Z_{eff} is the effective charge of the material, A_{eff} is the effective mass number, t is the thickness traversed in g/cm^2, m_e is the electron mass, β is the

particle velocity (v/c), $\gamma = (1-\beta^2)^{-\frac{1}{2}}$, and I is the mean excitation potential ($I = 21.8$ eV for H_2). For the electron arm, the Bethe-Bloch equation is replaced by a relativistic approximation:

$$E_{\rm loss} = 0.3071 \frac{Z_{\rm eff}}{A_{\rm eff}} \frac{t}{2} \left[\ln\left(\frac{t}{\rho}\right) + 19.26 \right] \tag{4.3}$$

where ρ is the density of the material in g/cm^3, and all other quantities are as above in Equation 4.2. Typically, the electron and kaon each lose less than 1 MeV in the target.

The particle trajectory is then projected through the magnetic elements to the detector hut, taking multiple scattering effects into account [HZ98] and applying fiducial cuts on the detector sizes. An event in the HMS is considered to be a good event after reaching the third hodoscope plane, and in the SOS after reaching the aerogel detector (as discussed in Section 3.6.6). Wire chamber hits were simulated and then smeared by a Gaussian with the measured resolution of the chambers. A straight line track was then fit to these wire chamber hits to determine the focal plane quantities, ($x_{\rm fp}$, $y_{\rm fp}$, $x'_{\rm fp}$, $y'_{\rm fp}$). In practice, a second (broader and weaker) Gaussian smearing function was needed to account for events with more than six hits per chamber as these broadened the measured widths of the various focal plane spectra [Kol99]. Figures 4.1 and 4.2 show a comparison between data and MC (dotted line) focal plane quantities for p(e,e′p) using the SIMC code.

The target quantities ($x'_{\rm tar}$, $y'_{\rm tar}$, $y_{\rm tar}$, δ) are reconstructed using these focal

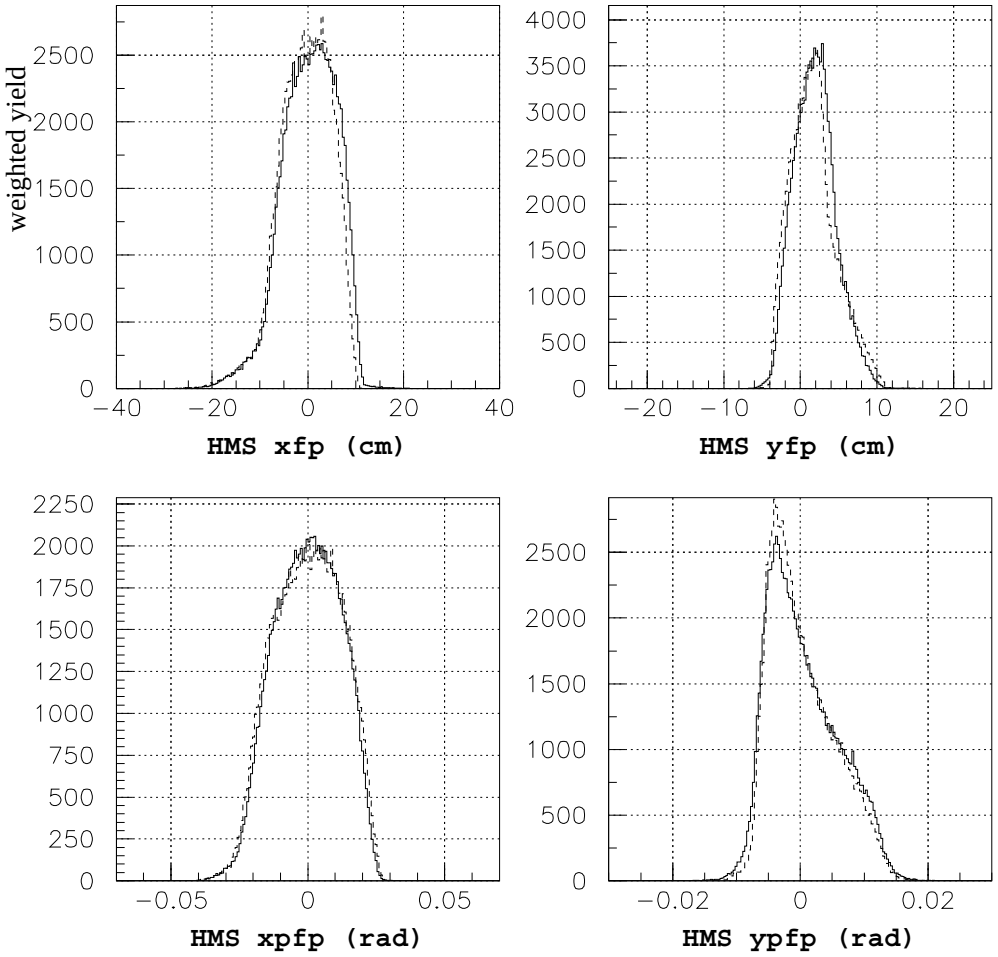

Figure 4.1: Example comparison of Data (solid line) and MC (dotted line) for HMS p(e,e′p) used in the validation of the MC optical simulation. In these plots, xfp = $x_{\rm fp}$, xpfp = $x'_{\rm fp}$, yfp = $y_{\rm fp}$, and ypfp = $y'_{\rm fp}$.

plane quantities and a set of reconstruction matrix elements which are the inverse of the forward COSY model. Comparisons of kaon data spectra with MC spectra are shown in Figures 4.3, 4.4, and 4.5. The MC spectra are weighted by the extracted cross section (i.e., they are not arbitrarily normalized to the data).

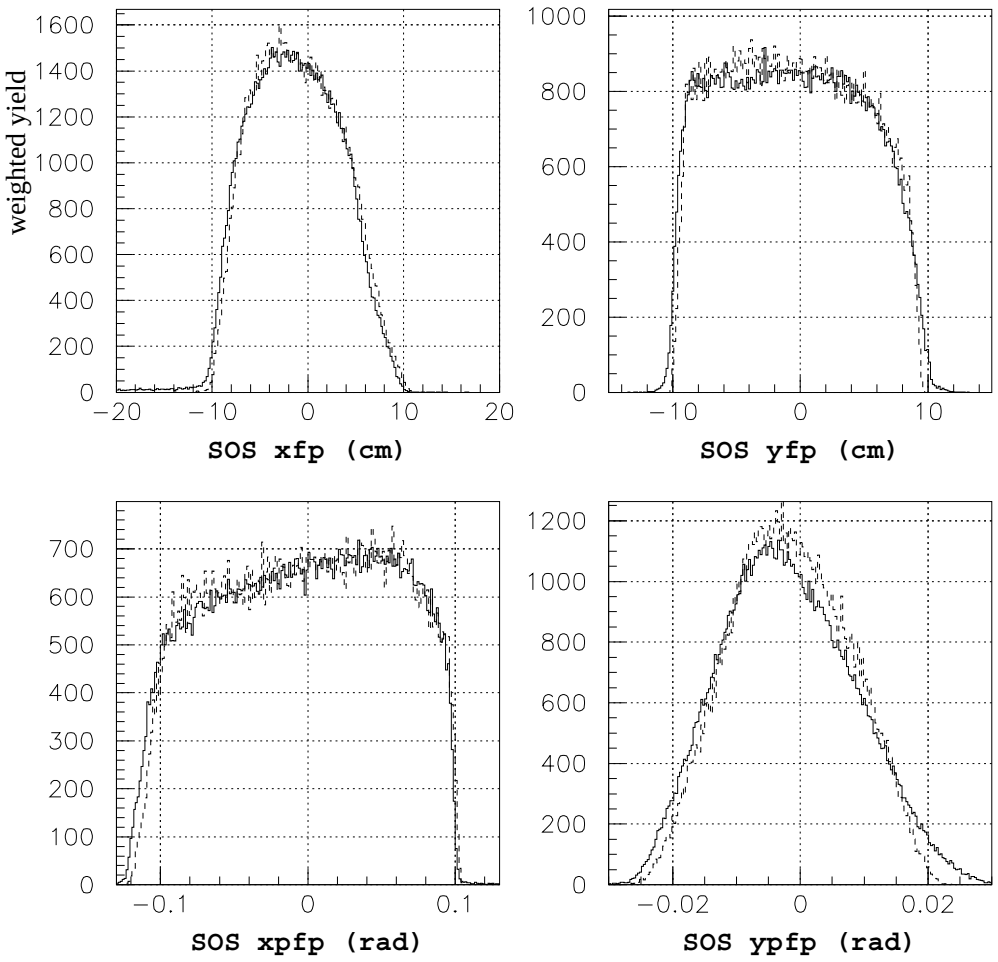

Figure 4.2: Example comparison of Data (solid line) and MC (dotted line) for SOS p(e,e′p) used in the validation of the MC optical simulation. In these plots, xfp = $x_{\rm fp}$, xpfp = $x'_{\rm fp}$, yfp = $y_{\rm fp}$, and ypfp = $y'_{\rm fp}$.

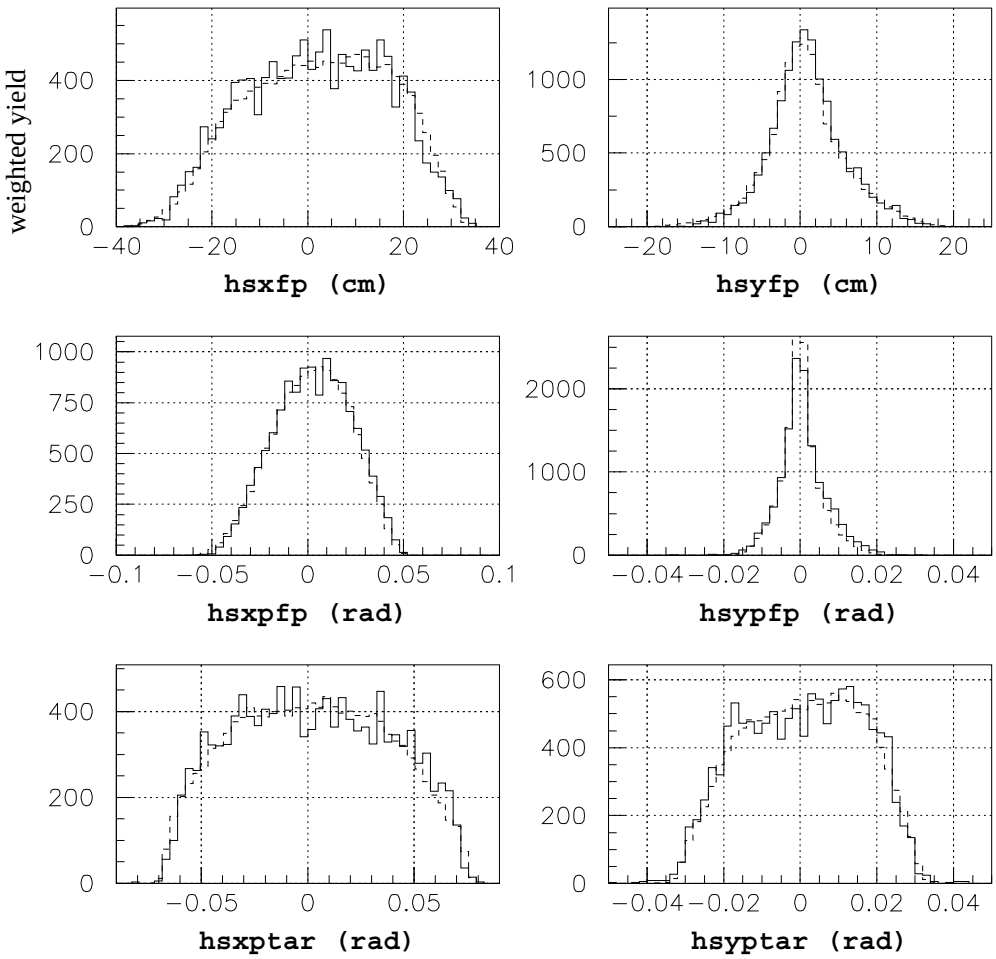

Figure 4.3: Example comparison of Data (solid line) and MC (dotted line) for HMS, p(e,e′K$^+$)Λ. In these plots, hsxfp = HMS $x_{\rm fp}$, hsxpfp = $x'_{\rm fp}$, hsyfp = $y_{\rm fp}$, hsypfp = $y'_{\rm fp}$, hsxptar = $x'_{\rm tar}$, and hsyptar = $y'_{\rm tar}$. The MC is normalized by the final extracted cross section (i.e., it is not an arbitrary normalization).

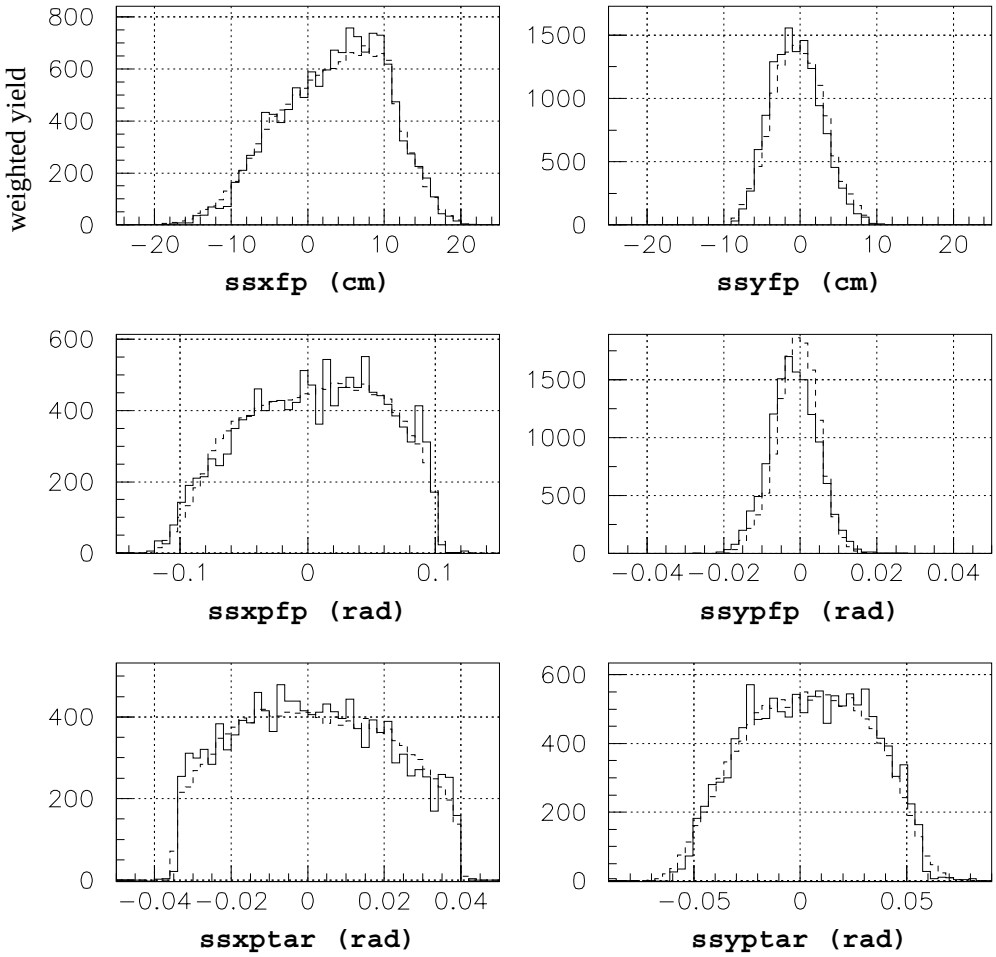

Figure 4.4: Example comparison of Data (solid line) and MC (dotted line) for SOS, p(e,e′K$^+$)Λ. In these plots, ssxfp = HMS $x_{\rm fp}$, ssxpfp = $x'_{\rm fp}$, ssyfp = $y_{\rm fp}$, ssypfp = $y'_{\rm fp}$, ssxptar = $x'_{\rm tar}$, and ssyptar = $y'_{\rm tar}$. The MC is normalized by the final extracted cross section.

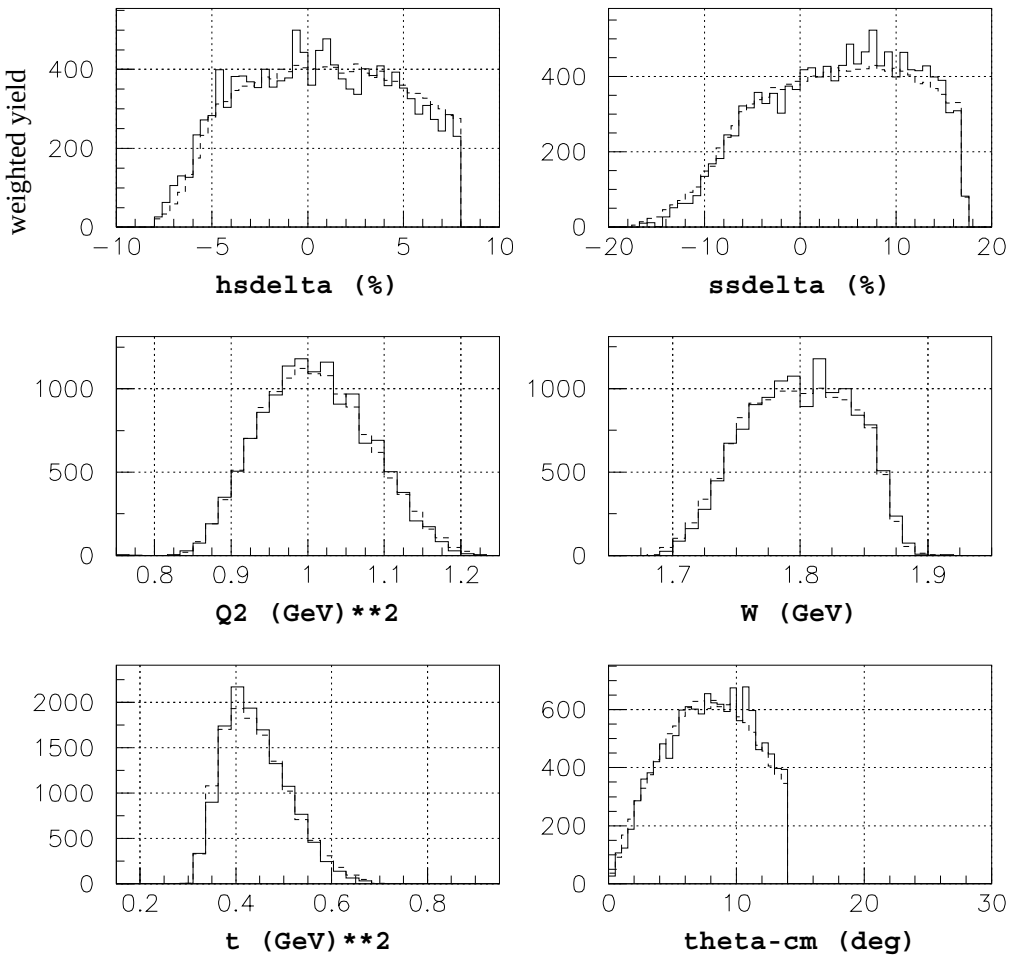

Figure 4.5: Example comparison of Data (solid line) and MC (dotted line) for physics quantities, p(e,e′K$^+$)Λ. The MC is normalized by the final extracted cross section.

4.4 Radiative Corrections

The radiative correction routines supplied in SIMC for (e,e′p) were based on the work of Mo and Tsai [MT69, Tsa61], extended to be valid for a coincidence framework. The details of the corrections are well-documented in several references [Mak94, O'N94, Arm99]. Most of this code was retained in SIMK, with modifications made to consider kaon production in place of the existing code that dealt with the production of an offshell proton. The assumption is that the diagrams involving kaons should be less significant to the correction than the electron diagrams.

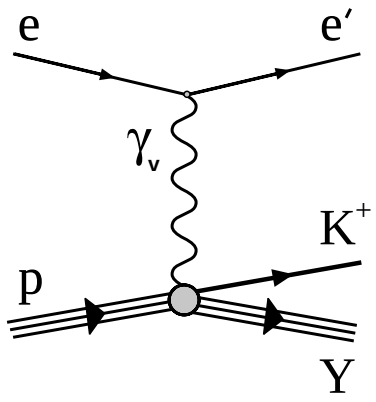

Figure 4.6: First-order Feynman diagram for kaon electroproduction.

The cross section that is to be measured is represented by the first-order Feynman diagram shown in Figure 4.6. The measurement is complicated by the fact that the charged particles involved can radiate extra photons. The emission of a real photon can change the kinematics of the reaction (leading to the tail in the missing mass spectrum in Figure 3.6), while the emission of virtual photons

result in the measurement of Feynman amplitudes other than that of Figure 4.6.

Two approximations were used to simplify the calculation of the radiative corrections. The first, called the "soft photon approximation", states that the energy of the emitted photon must be small relative to the energy of the particle which emitted it. The second, called the "extended peaking approximation", constrains the direction of the emitted photon to be along the direction of the radiating particle. The radiative corrections can be broken down into two categories: external and internal Bremsstrahlung. The internal correction can be further subdivided into soft and hard processes.

For external Bremsstrahlung, a real photon is emitted in the field of a nucleus different from the target proton. The photon emission lowers the energy of the radiating particle. If the incident electron radiates an external Bremsstrahlung photon, the effective beam energy will be lower at the interaction vertex, changing the kinematics at which the electroproduction takes place. If one of the scattered particles radiates an external Bremsstrahlung photon, the detected momentum will be lower than the actual momentum at the vertex. Because the external corrections take place away from the vertex region, the amplitudes can be added without interference.

Figure 4.7 shows the four Feynman diagrams considered for internal soft Bremsstrahlung. Again, in these processes a real photon is emitted, lowering the energy of the radiating particle. The difference between internal and external

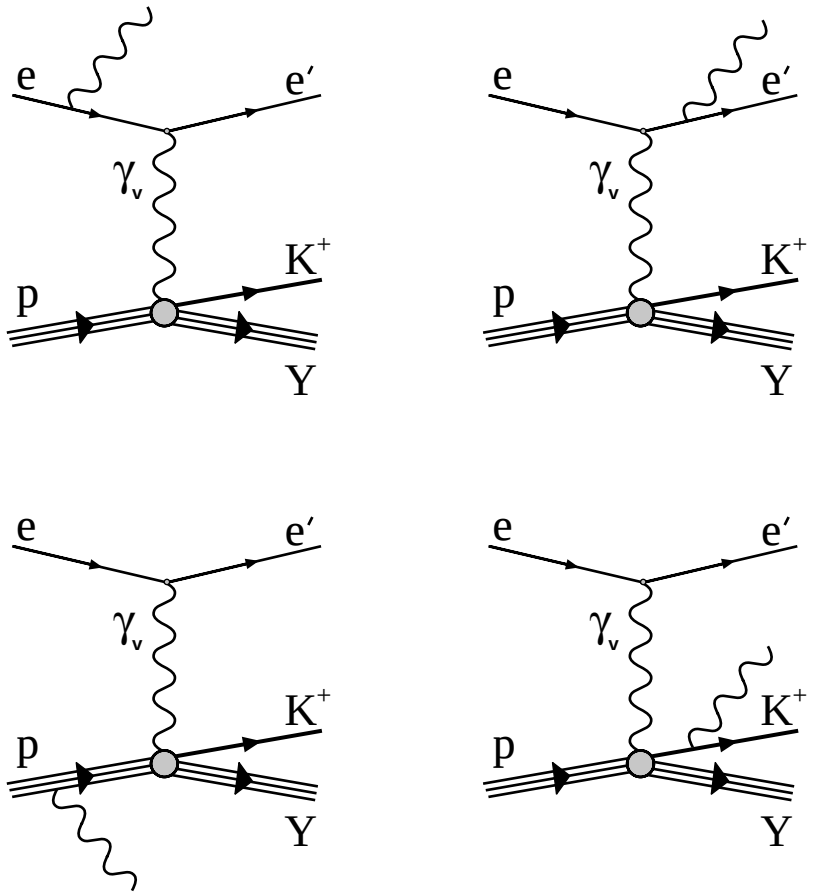

Figure 4.7: Feynman diagrams for the internal soft corrections. The effects of these diagrams have to be added coherently, leading to interference terms in the correction. See text for details.

Bremsstrahlung is that the internal amplitudes must be added coherently, leading to interference terms. Both the external and internal soft corrections can lead to modifications of the vertex kinematics, and can actually cause events to radiate into or out of the experimental acceptance.

Figure 4.8 shows the two Feynman diagrams for internal hard Bremsstrahlung that are calculable from QED (the "vertex correction" and "loop" diagrams,

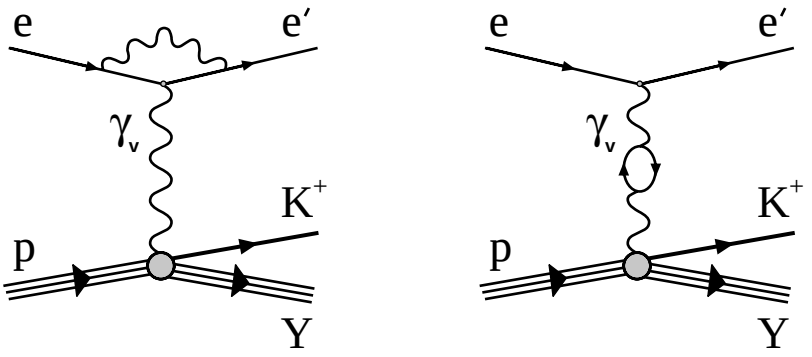

Figure 4.8: Feynman diagrams for the internal hard corrections. These are the "vertex correction" and "loop" diagrams, as described in the text.

respectively*). These diagrams do not include the emission of real photons, and as such do not modify the vertex kinematics. However, because the final state for each of these internal hard processes is indistinguishable from that of Figure 4.6, they represent a background underneath the cross section that we are trying to measure. Each event is given a multiplicative weighting factor to compensate for the influence of these diagrams.

For each event in the MC, the relative probabilities for radiation of the incident electron, scattered electron, and produced kaon are calculated. The radiated photon energy is generated using a distribution that goes as $1/\omega^{1-g}$, where g is a number less than one, related to the probability of having radiation in that particular arm. In the case where the incident electron loses energy to radiation, the vertex kinematics are recalculated using the new value of the beam

*There are diagrams that include second-order virtual photon corrections involving the hadrons, but only those terms necessary to cancel out the first-order infrared divergence are retained [Mak94, MS88].

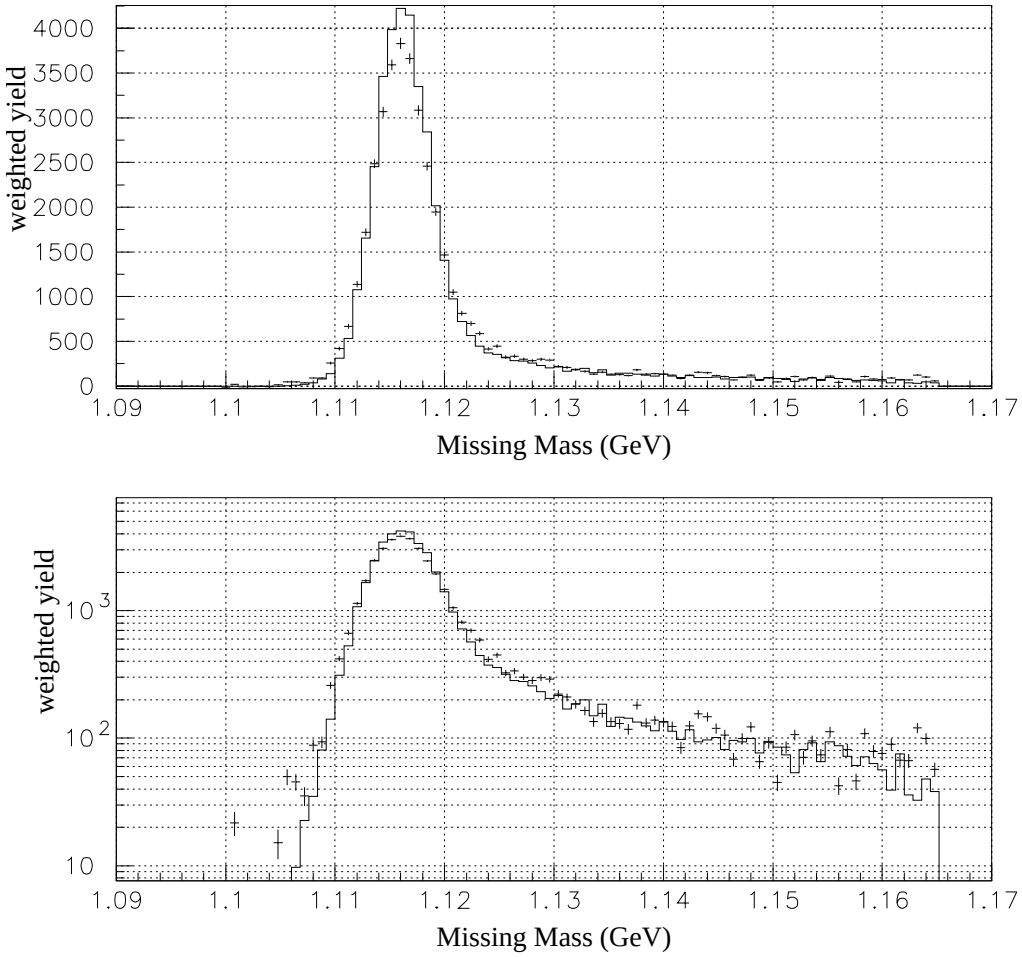

Figure 4.9: Yield spectrum of missing mass comparing MC (solid line) to data (crosses) for p(e,e′K$^+$)Λ, on both linear (top panel) and logarithmic (bottom panel) scales, normalized by the extracted cross section.

energy. If the outgoing electron or kaon radiates, its four-vector is modified but the vertex is not recalculated.

Figure 4.9 shows the cross section weighted MC calculation of the radiative tail (solid line) plotted on top of the measured data (crosses), on both linear and

logarithmic scales. One can see that the resolution of the MC peak is slightly narrower than that of the data as a result of the spectrometer model. However, outside of the peak region, the agreement between MC and data is quite good. The missing mass cut used to define the Λ is wide enough so that it is not affected by the difference in resolution. In fact, the extracted cross section is quite stable as a function of the missing mass cut (see Section 5.3), implying that the MC does a sufficient job of modeling the tail.

4.5 Equivalent Monte Carlo Yield

The equivalent experimental yield given by the MC can be expressed as

$$Y_{\rm MC} = L_H \times \int \left[\frac{d^5\sigma}{dQ^2 dW d\phi_e d\Omega_K^*}\right] A(d^5V)\, R(d^5V)\, dQ^2 dW d\phi_e d\Omega_K^* \tag{4.4}$$

where L_H is the experimental luminosity (including global efficiencies such as the tracking efficiency, dead times, etc.), A is the acceptance function (see discussion following Equation 4.8) of the coincidence spectrometer setup, and R is the radiative correction*. The experimental luminosity is given by

$$L_H = C_{\rm eff} \left(\frac{Q}{1.602 \times 10^{-19}}\right)_{\rm beam} \left(\frac{\rho\, t\, N_A}{m_p}\right)_{\rm target} \tag{4.5}$$

where $C_{\rm eff}$ is a multiplicative factor containing all the global efficiencies, Q is the accumulated charge in a given setting in Coulombs, ρ is the target density in

*By virtue of the Monte Carlo technique used to perform this integral (discussed later in this section), the quantities A and R are not available separately or on an event-by-event basis. The overall effect of the correction $A \times R$ ranged from 20-40%.

g/cm^3, t is the target thickness in cm, m_p is the target mass in amu, and N_A is Avogadro's number, 6.02×10^{23} mol^{-1}.

Then, substituting the virtual photoproduction cross section (Equation 1.7) for the full electroproduction relation yields

$$Y_{\rm MC} = L_H \times \int \left[\Gamma(Q^2, W) \left(\frac{d^2\sigma}{d\Omega_K^*} \right) \right] A(d^5V)\, R(d^5V)\, dQ^2 dW d\phi_e d\Omega_K^*. \tag{4.6}$$

Note that the general cross section can be written in terms of the cross section at a given point (called the "scaling point") $(\langle Q^2 \rangle, \langle W \rangle)$ and $\theta_{CM} = 0^\circ$ as

$$\left(\frac{d^2\sigma}{d\Omega_K^*} \right) = \left(\overline{\frac{d^2\sigma}{d\Omega_K^*}} \right) \Bigg|_{(\langle Q^2 \rangle, \langle W \rangle, \theta_{CM}=0^\circ)} \times \left(\frac{f(Q^2, W, \theta_{CM})}{f(\langle Q^2 \rangle, \langle W \rangle, \theta_{CM} = 0^\circ)} \right) \tag{4.7}$$

where $f/\langle f \rangle$ is a "scaling function" describing the behavior of the cross section across the acceptance (see Section 4.6). The resulting extracted cross section is not very sensitive to the choice of scaling functions because the cross section does not vary strongly in Q^2, W, and θ_{CM} within the acceptance. Inserting Equation 4.7 into Equation 4.6 gives the expression

$$\begin{aligned} Y_{\rm MC} = L_H \times \left(\overline{\frac{d^2\sigma}{d\Omega_K^*}} \right) \Bigg|_{(\langle Q^2 \rangle, \langle W \rangle, \theta_{CM}=0^\circ)} \times \\ \int \left[\Gamma(Q^2, W) \times \left(\frac{f(Q^2, W, \theta_{CM})}{f(\langle Q^2 \rangle, \langle W \rangle, \theta_{CM} = 0^\circ)} \right) \right] A(d^5V)\, R(d^5V)\, dQ^2 dW d\phi_e d\Omega_K^*. \end{aligned} \tag{4.8}$$

The integral is evaluated numerically via the Monte Carlo simulation. That is, each MC "count" accepted by the spectrometer is appropriately weighted with

the radiative corrections, virtual photon flux, and scaling function. The influence of the acceptance function, A, is felt through the fraction of generated events that successfully traverse the spectrometers and are reconstructed. The MC equivalent yield then reduces to

$$Y_{\rm MC} = L_H \times \left(\overline{\frac{d^2\sigma}{d\Omega_K^*}}\right)\Bigg|_{(\langle Q^2\rangle,\langle W\rangle,\theta_{CM}=0^\circ)} \times \left[\left(\frac{(\text{Number of MC successes})_{weighted}}{\text{Number of MC tries}}\right) \times \Delta^5 V_{\rm gen}\right]. \quad (4.9)$$

Finally, by setting the equivalent yields of MC and data to be equal (i.e., $Y_{\rm MC} = Y_{\rm DATA}$), the cross section at the scaling point can be extracted using Equation 4.9 as:

$$\left(\overline{\frac{d^2\sigma}{d\Omega_K^*}}\right)\Bigg|_{(\langle Q^2\rangle,\langle W\rangle,\theta_{CM}=0^\circ)} = Y_{\rm DATA} \times \frac{1}{L_H} \times \left[\left(\frac{\text{Number of MC tries}}{(\text{Number of MC successes})_{weighted}}\right) \times \frac{1}{\Delta^5 V_{\rm gen}}\right]. \quad (4.10)$$

4.6 Scaling Functions

This analysis uses the existing world data to account for the cross section behavior across the acceptance. It will be shown in the results chapter that the extracted cross sections in this analysis are not overly sensitive to the choice of scaling functions. In the paper by Bebek, *et al.* [Beb77a], the behavior of the cross section is parameterized as:

$$\frac{d^2\sigma}{d\Omega_K^*} \sim f_{\rm Bebek}(Q^2) \times f_{\rm Bebek}(W) \quad (4.11)$$

where

$$f_{\text{Bebek}}(Q^2) = \frac{1}{(Q^2 + X)^2} \tag{4.12}$$

with $X = 2.67$ for the Λ channel, and $X = 0.79$ for the Σ^0, and

$$f_{\text{Bebek}}(W) = \frac{|\mathbf{p}^*_{\mathbf{K}}|}{W(W^2 - m_p^2)}. \tag{4.13}$$

In practice, it was discovered in the analysis of Jefferson Lab experiment E91-016 [Kol99] that the scaling in W given by Equation 4.13 was not accurate at lower values of W (approaching the production threshold) for the Lambda cross section. Figure 4.10 shows the measured cross sections from that analysis with a solid curve showing the W-dependence from Equation 4.13. The dotted curve shown is fitted to a function

$$f(W) = \frac{C_1\ |\mathbf{p}^*_{\mathbf{K}}|}{W(W^2 - m_p^2)} + \frac{C_2\ (1.72)^2\,(0.10)^2}{(W^2 - (1.72)^2)^2 + (1.72)^2(0.10)^2} \tag{4.14}$$

where $C_1 = 4023.9$ GeV^2 nb/sr and $C_2 = 180.0$ GeV^2 nb/sr. This form was motivated by the hypothesis that there are possible resonance contributions to the cross section at lower W that modify the Bebek form of Equation 4.13. In this analysis, Equation 4.14 was used to scale in W, while Equation 4.12 was used to scale in Q^2.

Next, the θ_{CM} behavior can be estimated by using the results of Brauel, et al. [Bra79]:

$$2\pi \frac{d^2\sigma}{dt d\phi} \sim e^{-\xi|t|} \tag{4.15}$$

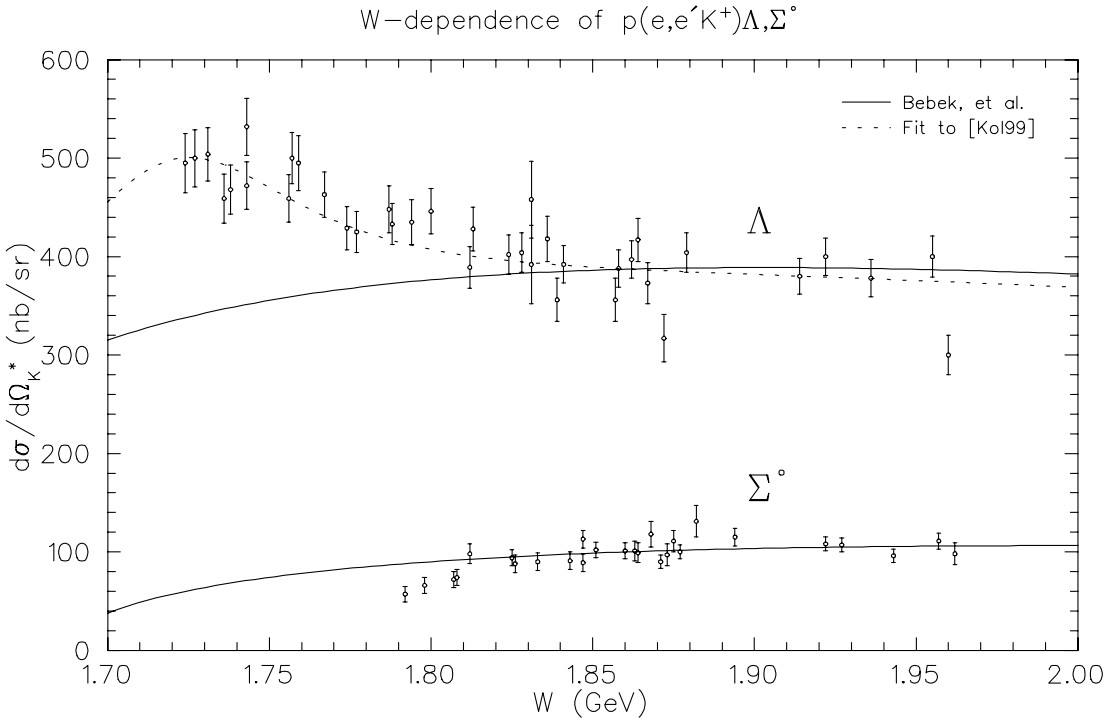

Figure 4.10: W-dependence of the differential kaon production cross section for both the Λ and Σ^0 channels [Kol99], shown with solid curves from Equation 4.13 (Bebek, [Beb77a]) and a dotted curve from Equation 4.14 ([Kol99]).

where $\xi = 2.1$ for the Λ, and $\xi = 1.0$ for the Σ^0.

We can use the fact that the Mandelstam variable t can be written as the square of the difference between the virtual photon and kaon four-vectors in either the lab or the CM frame, because t is Lorentz invariant:

$$t = -(q^\mu - p_K^\mu)^2 = -[(q^*)^\mu - (p_K^*)^\mu]^2 \ . \tag{4.16}$$

Using the CM frame variables (see Section B.1) we have

$$-t = \left((\nu^* - E_K^*), (\mathbf{q}^* - \mathbf{p}_\mathbf{K}^*)\right)^2 \ , \tag{4.17d1}$$

which after squaring and collecting terms becomes

$$-t = -Q^2 + m_K^2 - 2\,E_K^*\nu^* + 2\,|\mathbf{q}^*||\mathbf{p}_\mathbf{K}^*|\cos\theta_{CM}\ . \tag{4.17}$$

Now we can calculate the Jacobian relating $dt \leftrightarrow d(\cos\theta_{CM})$:

$$\frac{dt}{d(\cos\theta_{CM})} = -2|\mathbf{q}^*||\mathbf{p}_\mathbf{K}^*|\ . \tag{4.18}$$

Finally, the behavior of our cross section as a function of θ_{CM} can be expressed as

$$\frac{d^2\sigma}{d\Omega_K^*} = \frac{d^2\sigma}{d(\cos\theta_{CM})d\phi} = \left(\frac{d^2\sigma}{dtd\phi}\right)\left(\frac{dt}{d(\cos\theta_{CM})}\right) \tag{4.19}$$

or, using Equations 4.15 and 4.18,

$$f(\theta_{CM}) = f(t) = \frac{d^2\sigma}{d\Omega_K^*} \sim \frac{1}{2\pi} \times e^{-\xi|t|} \times -2|\mathbf{q}^*||\mathbf{p}_\mathbf{K}^*|\ . \tag{4.20}$$

At $\theta_{CM} = 0^\circ$, $-t \to -t_{min}$ given by

$$-t_{min} = -Q^2 + m_K^2 - 2\,E_K^*\nu^* + 2\,|\mathbf{q}^*||\mathbf{p}_\mathbf{K}^*|\ , \tag{4.21}$$

resulting in a scaling behavior of

$$\frac{f(\theta_{CM})}{\langle f(\theta_{CM}=0^\circ)\rangle} = \frac{e^{-\xi|t|}}{e^{-\xi|t_{min}|}} = e^{-\xi(t-t_{min})}\ . \tag{4.22}$$

Note that $-t_{min}$ is a function of Q^2 and W (through its dependence on ν^*).

Since we wish to scale the cross section to the value given at $\theta_{CM} = 0^\circ$, each event in the MC should not only be weighted by the Q^2 and W scaling functions (Equations 4.12 and 4.14), but also should be scaled to $t_{min}(Q^2, W)$ for each event using Equations 4.20 and 4.21.

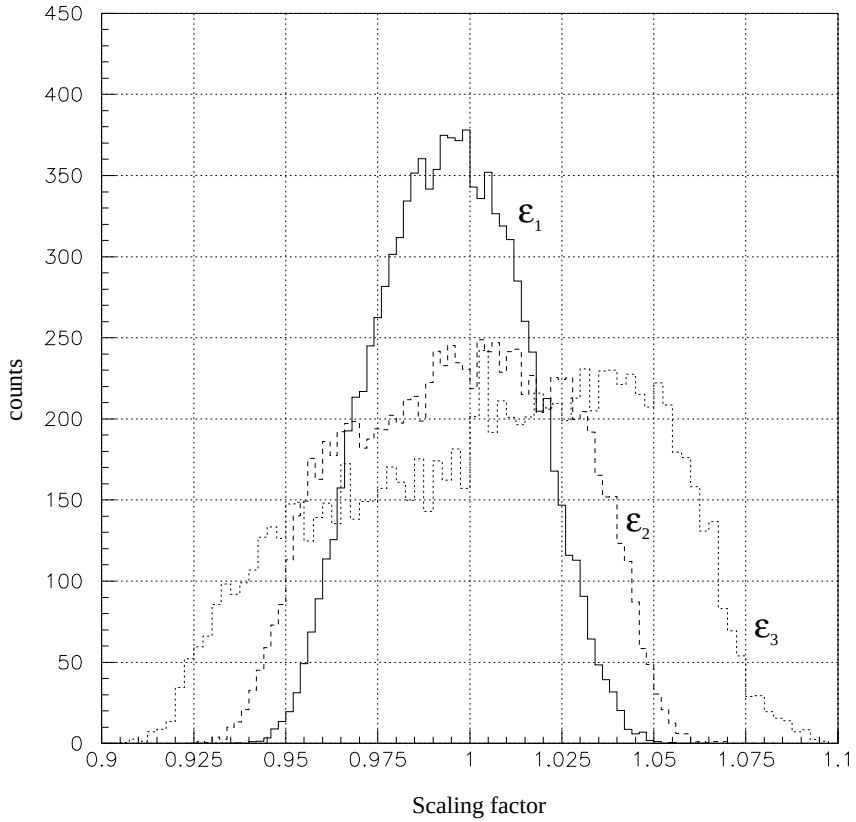

Figure 4.11: Magnitude of the MC scaling factor $f/\langle f \rangle$ for the three values of ϵ at $Q^2 = 0.52$ GeV^2 (Points 1, 2, and 3). Note that the scaling factor is typically less than $\pm 8\%$.

Figure 4.11 shows the magnitude of the scaling factor $f/\langle f \rangle$ (i.e., the product of all scaling factors in Q^2, W, and θ_{CM}) for the MC corresponding to the three values of ϵ at the $Q^2 = 0.52$ GeV^2 setting. The size of the scaling factor is largest at this lowest Q^2, and is essentially always less than $\pm 8\%$. Also, in order to minimize the sensitivity to the θ_{CM} scaling, cuts were placed on t/θ_{CM} such that the entire $\phi \in (0, 2\pi)$ region was covered symmetrically. The dependence of the extracted cross section on the form of the scaling functions will be discussed in Section 5.3.

Chapter 5

Physics Analysis and Results

5.1 Overview

This chapter ties together the discussions of Chapters 3 and 4, explaining how the unseparated cross sections were extracted in both hyperon channels. The cuts on both the data and Monte Carlo simulation are listed, and the sensitivity of the results as a function of these cuts is explored. This is followed by a summary of the sources and sizes of the errors affecting the results. The remainder of the chapter discusses the results of this analysis for unseparated cross sections, L/T separated cross sections, and various cross section ratios. On the figures showing the results, calculations from the model of Williams, Ji, and Cotanch (WJC) [WJC92], an isobaric model discussed in Chapter 1, are often shown for comparison. This is not meant as a judgment of the quality of any particular model, but simply reflects the fact that suitable calculations from the

other models were not available at the time of this writing.

5.2 Extraction of the Λ Cross Section

As discussed in the previous chapter, the cross section was extracted by forcing the ratio of data/MC yields to be unity (using Equation 4.10). A stand-alone FORTRAN code (that uses HBOOK [Gro94] and MINUIT [Jam94] routines internally) reads in the data and MC events separately, applies correction factors read in from an input database, applies the final cuts, and calculates the properly weighted yields for both data and MC. The code internally calculates the cross section in a variable number of bins in the azimuthal angle, ϕ.

After the first pass through the analysis loop, the code arrives at yields binned in reconstructed* ϕ for both data and MC. The ratio of data/MC was calculated in each bin yielding a zeroth order cross section for that bin. The procedure was then iterated, applying the extracted $(n-1)^{th}$ order cross section as a weighting factor for the yields in each ϕ bin using the *vertex* values of the MC ϕ as the bin index. From this, the n^{th} order cross section was extracted from the new data/MC ratio. The number of iterations was variable, but was selected such that the extracted cross section stabilizes to within 0.1% of its value from previous iterations (usually less than 3 iterations was sufficient). These final

*Note that the binning was done in reconstructed ϕ, which was blurred by the resolution of the spectrometers ($\Delta\phi \approx 5 - 10^{\circ}$, depending on the value of θ_{CM}).

bin-by-bin values are fitted to a constant plus a harmonic ϕ dependent function of the form $A + B\cos\phi + C\cos 2\phi$ in order to extract $A = \sigma_T + \epsilon\sigma_L$. Varying the number of ϕ bins from $1-12$ left the extracted cross section unchanged to better than 0.5%. Note that with only one ϕ bin, the ϕ dependence "naturally" cancels out because the ϕ coverage is complete. It should be noted that the ϕ dependence of the cross section, while certainly non-zero, could not be extracted in a quantitative manner due to low statistics per bin and poor ϕ reconstruction resolution.

5.3 Cut Dependences

A summary of the cuts applied to the data and MC is listed in Table 5.1. To give an impression of the relative importance of these cuts, Figure 5.1 shows the sequential effect of placing the cuts on the experimental data from a single run.

An important avenue to be investigated is the stability of the results as a function of the applied cuts. All of the cuts listed in Table 5.1 were systematically varied and their effects on the cross section noted. The standard deviation of the resulting cross sections was used as an estimate of the systematic error on the quoted cross section.

An example of a cut dependence study is shown in Figure 5.2. The results of the Λ cross section extraction are shown with the upper limit of the missing mass

Cuts placed on data and MC	
abs(ssdelta) < 17 %	SOS momentum (δ) cut
abs(hsdelta) < 8 %	HMS momentum (δ) cut
abs(hsxptar) < 0.080 mrad	HMS $x'_{\rm tar}$
abs(hsyptar) < 0.040 mrad	HMS $y'_{\rm tar}$
abs(ssxptar) < 0.040 mrad	SOS $x'_{\rm tar}$
abs(ssyptar) < 0.070 mrad	SOS $y'_{\rm tar}$
-49.0 cm $<$ saeroX < 46.0 cm	Aerogel detector fiducial cut, x
-14.0 cm $<$ saeroY < 18.0 cm	Aerogel detector fiducial cut, y
1.100 GeV $< m_Y <$ 1.155 GeV	Missing mass cut, Λ only
1.180 GeV $< m_Y <$ 1.230 GeV	Missing mass cut, Σ^0 only
Cuts placed on data only	
abs(scointim - Δt) < 0.65 ns	Coincidence timing
abs($\beta_{\rm tof}$ - $\beta_{\rm K}$) < 0.04	TOF velocity measurement
saernpe < 3.5	Aerogel number of photoelectrons
hcernpe > 2.0	HMS Gas Čerenkov number of p.e.

Table 5.1: Listing of cuts placed on the data and MC.

cut varied from 1.120−1.195 GeV. With an upper cut limit of less than about 1.135 GeV, the extracted cross section is too low as a result of the difference in resolution between the data and MC (see Figure 4.9). This is because the MC peak is narrower, and a given cut will contain more counts in the MC than in the data. Then, because the cross section is proportional to $Y_{\rm DATA}/Y_{\rm MC}$, the larger denominator results in a lowered apparent cross section. The cross section shows a stable plateau for upper cut limits between 1.145−1.175 GeV, the region in which the cut at 1.155 GeV was actually placed. For larger upper cut limits, the data cut begins to include contributions from the Σ^0 whereas the Λ-specific MC does not. Hence, the numerator of $Y_{\rm DATA}/Y_{\rm MC}$ is too large, and the apparent

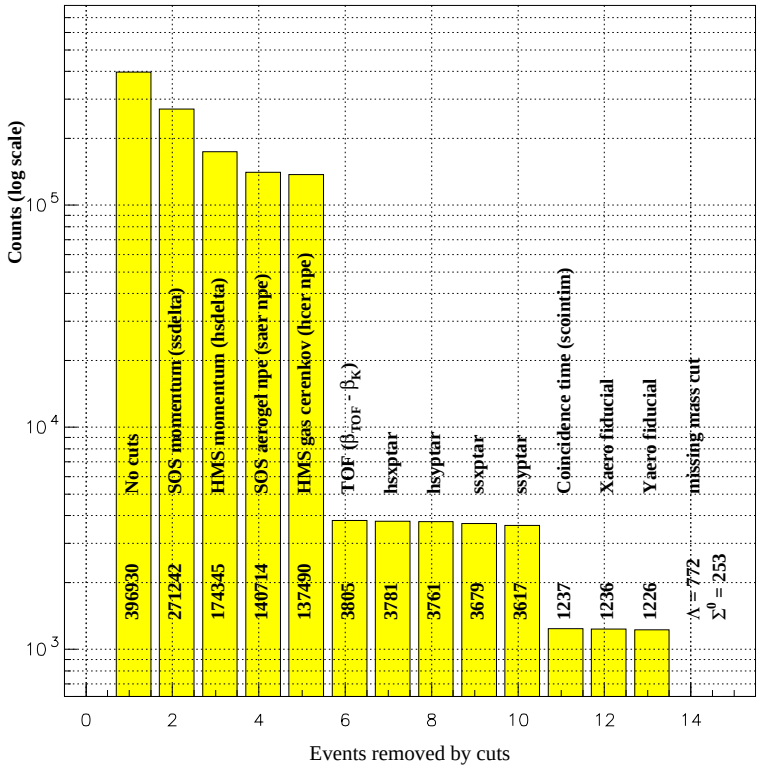

Figure 5.1: Histogram showing the cumulative effects of applying the cuts (note logarithmic scale) (Run 10986). Shown are the number of counts surviving after applying the cuts as indicated from left to right, resulting in a final yield of 772 Λ and 253 Σ^0.

cross section increases.

As mentioned earlier in Section 4.6, the extracted cross section is also dependent somewhat on the form of the scaling factor, $f/\langle f \rangle$. Table 5.2 shows the results for the cross section for Point 3 using several different variations of the scaling functions, given relative to the final value which is normalized to 100.0 to facilitate comparison. Out of all the E93-018 settings, the effects of varying the scaling technique are maximum for Point 3 because it is at the lowest Q^2 (i.e.,

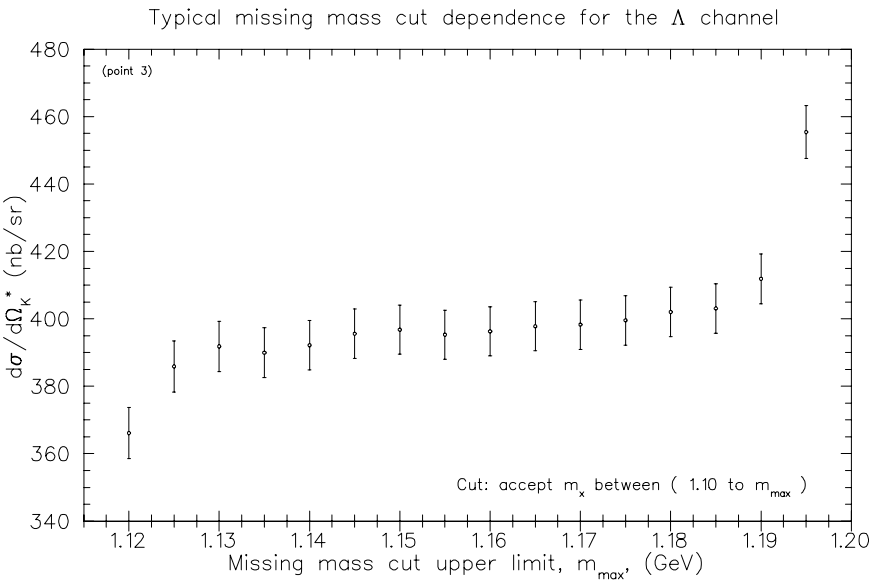

Figure 5.2: Typical dependence of the extracted Λ cross section on the missing mass cut size.

the cross section should change the most across the acceptance as per Figure 1.3) and because it has the largest Q^2 and W acceptance of the three settings at this Q^2.

The topmost section of Table 5.2, labeled "A", shows the extracted Λ cross section (with a statistical error, and normalized as stated in the previous paragraph) if the variation of the cross section across the acceptance is neglected (i.e., $f/\langle f \rangle = 1$). This is within 1% of the quoted result for Point 3.

The three sections (B, C, D) that follow within Table 5.2 show the effects of holding the two scaling techniques listed in the heading constant, while varying the third.

Section B of Table 5.2 examines the effect of the scaling t (or equally, θ_{CM}) while retaining the Q^2 and W scaling used for the final analysis. Test B.1 does

Scaling technique used	Normalized result
A: No scaling	
1. no scaling in Q^2, W, or t/θ_{CM}	100.5 ± 1.8
B: $f_{\text{Bebek}}(Q^2), f(W)$[Kol99]	
1. no t/θ_{CM} scaling (integrated $\theta_{CM} < 8^\circ$)	99.26 ($\langle\theta_{CM}\rangle = 5^\circ$)
2. above result, scaled to $\theta_{CM} = 0^\circ$	99.87
3. scaled to $\theta_{CM} = 0^\circ$ event-by-event	100.0 (final value)
4. scaled to $-t_{min}(\langle Q^2\rangle, \langle W\rangle)$, event-by-event	100.0
C: Event-by-event $\theta_{CM} = 0^\circ$, $f(W)$[Kol99]	
1. no Q^2 scaling	100.4
2. $f_{\text{Bebek}}(Q^2)$ scaling	100.0 (final value)
3. absurd $1/f_{\text{Bebek}}(Q^2)$ scaling	100.7
D: $f_{\text{Bebek}}(Q^2)$, event-by-event $\theta_{CM} = 0^\circ$	
1. no W scaling	100.8
2. $f(W)$[Kol99]	100.0 (final value)
3. $f_{\text{Bebek}}(W)$	102.3

Table 5.2: Dependence of the extracted cross section on the choice of scaling for Point 3, relative to the final quoted result (which is normalized to a value of 100.0). Results are scaled to $Q^2 = 0.52$ GeV^2 and $W = 1.84$ GeV. A detailed explanation can be found in the text.

not include any correction for t/θ_{CM}, giving a result slightly lower than the final value, but which should properly be quoted at $\langle\theta_{CM}\rangle = 5^\circ$. Test B.2 takes this value and scales it from $\theta_{CM} = 5^\circ \rightarrow \theta_{CM} = 0^\circ$, giving a new value that agrees well with the final result. Test B.3 is exactly the technique used for the final result – the results are scaled to $\theta_{CM} = 0^\circ$ as calculated from Equations 4.17, 4.21 and 4.22 using the Q^2 and W for each event. Test B.4 differs from Test B.3 in that the values ($\langle Q^2\rangle$, $\langle W\rangle$) for the scaling point are used in place of the event-by-event (Q^2, W) to calculate the value of t_{min} in Equation 4.21. These

last two techniques give results that agree better than 0.1%.

Section C of Table 5.2 explores the sensitivity of the extracted result to the Q^2 parameterization. Of note is Test C.3, in which the *inverse* of the Bebek form for the Q^2 dependence was assumed, and the result was only changed at less than the 1% level.

Section D of Table 5.2 tests the sensitivity of the results with respect to the W scaling used. In Test D.1, not accounting for the W-dependence leads to an extracted value that is less than 1% higher than the final result. In Test D.3, the use of the Bebek form for the W-dependence (given by Equation 4.13) gives a value that is higher than the final result by about 2%. This effect can be attributed to the difference between the Lambda curves for Equations 4.13 and 4.14 in Figure 4.10 over the region of W covered in E93-018, $1.75 \lesssim W \lesssim 1.95$. This sensitivity to the W function is the largest contributor to the error associated with the scaling.

5.4 Extraction of the Σ^0 Cross Section

The procedure for extracting the Σ^0 cross section is similar to that for the Λ, except that the Σ^0 yield must first be corrected for the Λ background beneath the Σ^0 peak in the missing mass spectrum (see Figure 3.6).

The Λ-specific MC was used to determine the number of background Λ counts that were within Σ^0 cuts. The Λ-specific MC was weighted with the

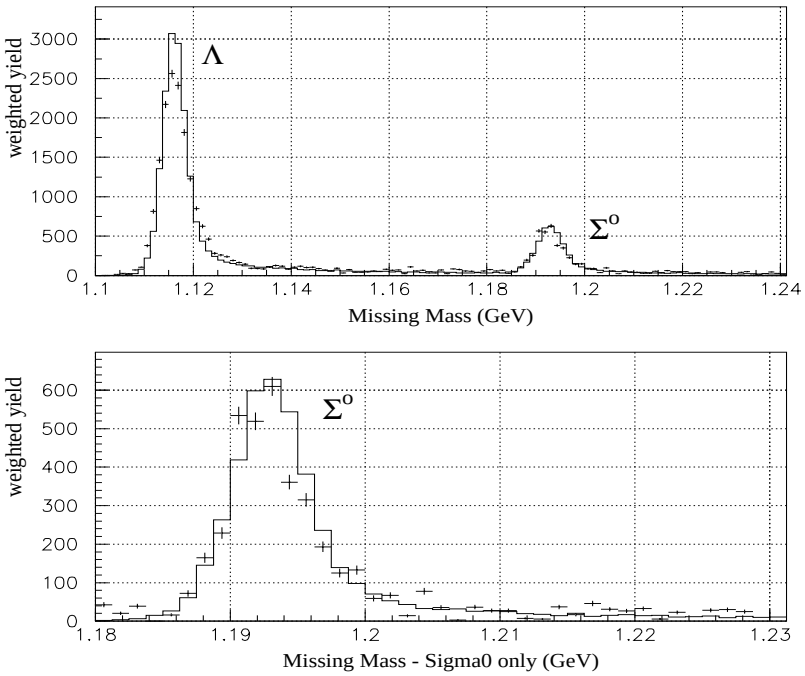

Figure 5.3: Use of the MC to correct for the Λ background below the Σ^0 missing mass peak. The upper panel shows the combination of the Λ-specific and Σ^0-specific MC simulations plotted on top of the data missing mass. The lower panel shows the remaining Σ^0 data after subtracting the Λ-specific MC, with the Σ^0-specific MC superimposed. The MC is normalized using the extracted Λ and Σ^0 cross sections.

extracted Λ cross section, binned in the same manner as the data, and was subtracted from each data bin. The upper half of Figure 5.3 shows the combination of the Λ-specific and Σ^0-specific MC simulations plotted on top of the data missing mass. The lower half of the figure shows the remaining Σ^0 data after subtracting the Λ-specific MC, with the Σ^0-specific MC superimposed.

In this technique, the extracted Σ^0 cross section depends on the magnitude of the extracted Λ cross section listed in the input file. As a measure of the

sensitivity to this, varying the Λ cross section listed in the Σ^0 input file by $\pm 10\%$ resulted in changes of less than 2% in the Σ^0 cross section. An additional scale error proportional to the Λ cross section error was thus applied to the Σ^0 results.

5.5 Summary of Errors

The size of typical corrections to the data and/or the MC and the errors in the cross section associated with those corrections is shown in Table 5.3. The statistical errors for the various settings ranged from 1.0−3.1% for the Λ, and from 4.8−5.9% for the Σ^0. The systematic errors are broken down into "random" and "scale" errors. Random errors affect each kinematic setting in an independent manner, and hence can influence the linear fit used to perform the L/T separation. For example, all of the run-by-run inefficiencies (tracking efficiencies, dead times) are random errors. Scale errors are global errors that affect all kinematic settings in the same way. An example of a global scale error is the uncertainty in the charge measurement. The sources of the errors in Table 5.3 have all been discussed elsewhere in this document, mainly in Chapter 3.

5.5.1 Goodness of Fit, χ^2_ν

This subsection is a discussion of the use of the reduced χ^2 (denoted as χ^2_ν) as a measure of the goodness of fit for the L/T separation. In a typical fitting situation, one often has the task of fitting a straight line to a large number of

Property	Typical Size of Correction	Random Error	Scale Error
HMS Acceptance	—	—	2.0 %
SOS Acceptance	—	—	2.0 %
Cut variation (acceptance)	—	0.7 - 3.1 %	—
Scaling function	0.9 - 1.1	0.5 %	2.0 %
Radiative Correction	—	1.0 %	1.0 %
Cut variation (m_Y)	—	0.5 %	—
Acceptance × Rad Corr	1.2 - 1.4 (from MC)		
HMS Tracking Efficiency	0.91 - 0.98	0.5 %	—
SOS Tracking Efficiency	0.83 - 0.93	1.0 %	—
HMS Trigger Efficiency	1.0	0.1 %	—
SOS Trigger Efficiency	1.0	0.1 %	—
Coincidence blocking	0.950 - 0.985	0.5 %	—
TOF $\beta = 0$	0.96 - 0.99	0.5 %	—
HMS Electronic Live Time	0.996 - 1.000	0.1 %	—
SOS Electronic Live Time	0.973 - 0.990	0.1 %	—
Computer Live Time	0.91 - 1.00	0.3 %	—
Cointime cut efficiency	≈ 1.0	0.1 %	—
TOF β cut efficiency	> 0.99	0.5 %	—
HMS Čerenkov Efficiency	≈ 0.998	0.2 %	—
Aerogel cut inefficiency	0.974	—	0.3 %
Kaon Absorption	0.94 - 0.97	0.5 %	0.5 %
Kaon Decay	2.5 - 4.0	1.0 %	3.0 %
Decay Product Kaon Mimic	0.990 - 0.995	0.5 %	—
Target Length/Density	—	—	0.4 %
Target Density Fluctuation	0.992	0.4 %	—
Target Purity	0.998	—	0.2 %
Charge Measurement	—	—	1.5 %
Random Subtraction	2% to 5%	0.5 %	—
Dummy Subtraction	1 - 2% Λ, 4 - 8% Σ^0	0.5 %	—
Total		2.5 - 3.9 %	5.0 %

Table 5.3: Systematic corrections and errors in the E93-018 analysis.

data points. In that case there are many degrees of freedom and one expects the value of χ^2_ν to be around 1.0 (i.e., it goes to 1.0 in the limit of an infinite number of degrees of freedom). The reason to expect this is that with a large number of

degrees of freedom, the integral of the reduced χ^2 probability distribution from $(\chi^2_\nu = 1) \rightarrow \infty$ is equal to 50% of the entire integral. In other words, if the experiment were done again, there would be a 50-50 chance that the measured values would yield a higher value of χ^2. For a given value of χ^2 and a given number of degrees of freedom, the integral

$$P_x(\chi^2;\nu) = \left(\frac{1}{2^{\nu/2}\Gamma(\nu/2)}\right) \int_{\chi^2}^{\infty} x^{(\nu-2)/2}\, e^{-x/2}\, dx \tag{5.1}$$

is called the "confidence limit" or "CL". It is a CL of 50% that is expected, not necessarily the "rule of thumb" which looks for a reduced χ^2 of 1.0.

When the number of data points is small, this distinction is important. For E93-018, we only have 3 points to fit for each Q^2, with 2 constraints (slope and intercept), leaving only *one* single degree of freedom. In this case, the value of reduced χ^2 corresponding to a CL of 50% is approximately $\chi^2_\nu = 0.45$. The values for χ^2_ν extracted in this analysis for the Λ are approximately (0.22, 0.23, 0.20, 0.17) which seemed at first glance to be extremely low, implying that the errors were highly overestimated. In fact, those values of χ^2_ν give CLs of (64%, 63%, 65%, 68%), which are reasonable. To put it in perspective, if there were ~ 200 data points with confidence limits such as these, the corresponding χ^2_ν would be approximately 0.97, and the "rule of thumb" would be correct. For further discussion, please see reference [BR92] (particularly Section C.4 regarding the reduced χ^2 distribution), and to [Bar89].

$\langle Q^2 \rangle$ (GeV^2)	$\langle W \rangle$ (GeV)	ϵ	$\sigma_T + \epsilon\sigma_L$ (nb/sr)
0.52	1.84	0.552	369.2 $\pm$ 12.1
0.52	1.84	0.771	380.2 $\pm$ 12.2
0.52	1.84	0.865	395.3 $\pm$ 12.5
0.75	1.84	0.462	346.3 $\pm$ 11.8
0.75	1.84	0.724	362.8 $\pm$ 10.9
0.75	1.84	0.834	379.2 $\pm$ 11.2
1.00	1.81	0.380	320.0 $\pm$ 10.7
1.00	1.81	0.678	343.3 $\pm$ 10.7
1.00	1.81	0.810	344.8 $\pm$ 11.6
2.00	1.84	0.363	221.8 $\pm$ 9.0
2.00	1.84	0.476	233.4 $\pm$ 8.9
2.00	1.84	0.613	237.7 $\pm$ 7.9

Table 5.4: Results for the unseparated p(e,e'K$^+$)Λ cross section used in the L/T separation (i.e., not including a scale error of 5%).

5.6 Results for the Λ Channel

The extracted p(e,e'K$^+$)Λ unseparated cross sections are shown in Table 5.4. The high-ϵ values of the unseparated cross sections are shown in Figure 5.4 plotted together with the world data (previously shown in Figure 1.3). The E93-018 results have been scaled to $\langle W \rangle = 2.15$ GeV using the scaling due to Bebek [Beb77a] (Equation 4.13) and include a 5% scale error. The previous world data shown in this plot have been scaled to ($\langle W \rangle = 2.15$ GeV, $\theta_{CM} = 0^\circ$) using Equations 4.13 and 4.22.

The unseparated cross sections are plotted as a function of ϵ in Figure 5.5. A linear least-squares fit* was performed to determine the best straight line

*The full procedure used for the linear least-squares fit is described in detail in both Chap-

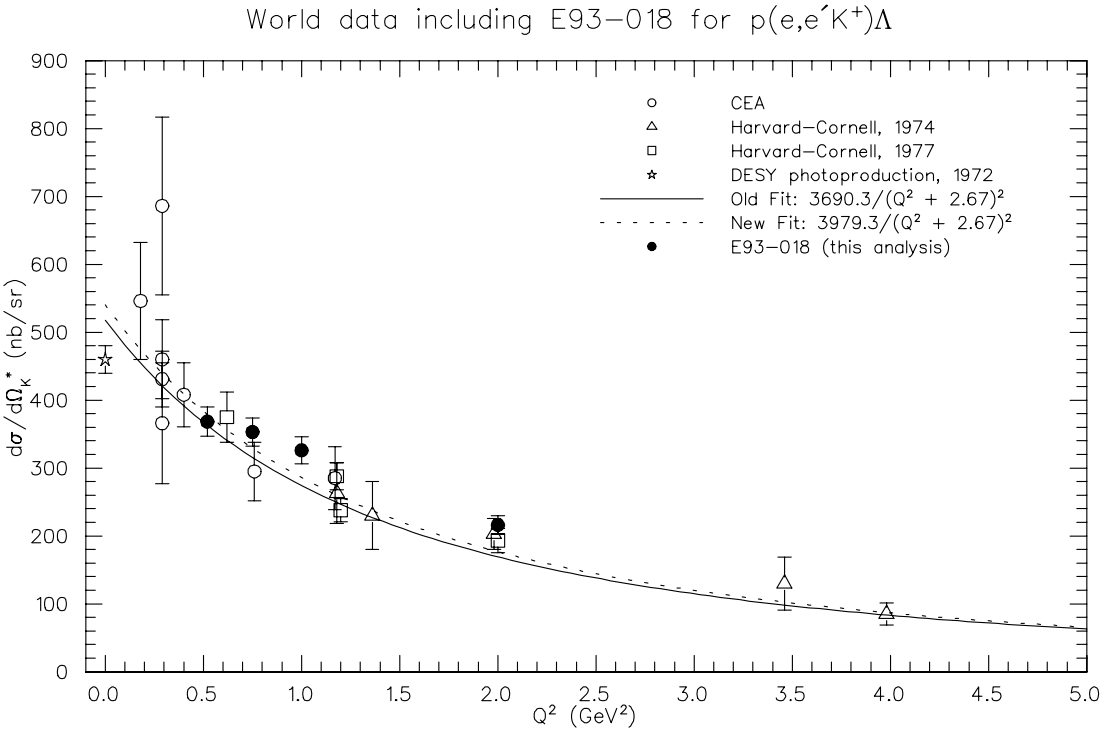

Figure 5.4: World data from Table 1.3 with the addition of the high-ϵ results of this analysis (solid points) scaled to $\langle W \rangle = 2.15$ GeV, $\theta_{CM} = 0°$, for the p(e,e′K$^+$)Λ unseparated cross sections. The "new fit" includes the results of this analysis.

($\sigma = \sigma_T + \epsilon\sigma_L$) through the points. The resulting values of σ_L, σ_T, and $R = \sigma_L/\sigma_T$ are shown in Table 5.5 as well as on Figure 5.5. The fitting procedure only includes the random and statistical errors (added in quadrature), as the scale errors are completely correlated between all epsilon points at a given Q^2 setting. The errors on σ_L and σ_T include the scale errors added in quadrature with the random errors; the quantity R is completely insensitive to scale errors.

The separated cross sections σ_L and σ_T are plotted as a function of Q^2 in Figures 5.6 and 5.7, respectively. Also, a Lambda photoproduction point

ter 6 of [BR92] and in Chapter 6 of [Bar89].

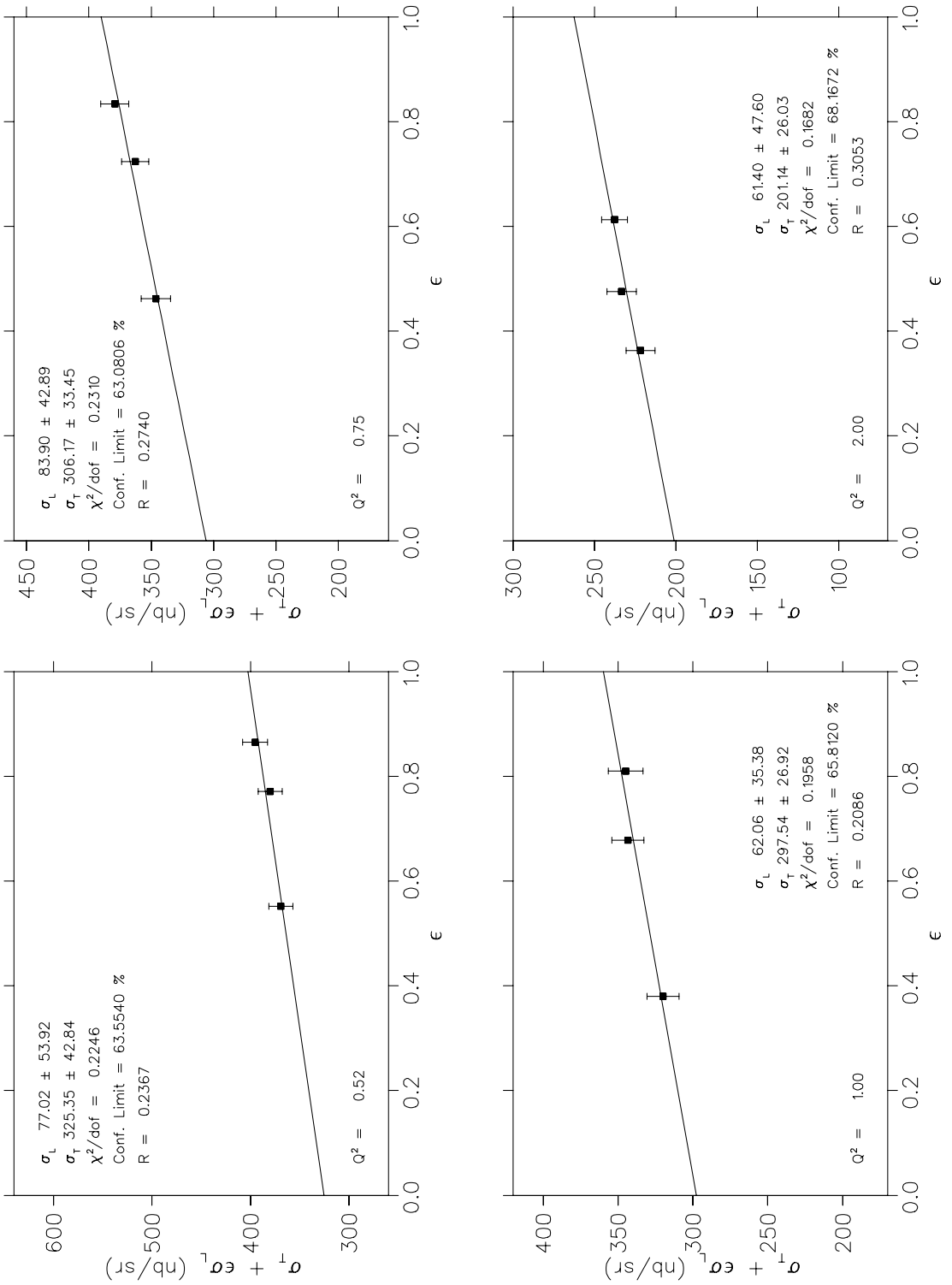

Figure 5.5: Extraction of L/T separated cross sections for p(e,e′K$^+$)Λ. For details see text.

$\langle Q^2 \rangle$	$\langle W \rangle$	σ_L (nb/sr)	σ_T (nb/sr)	R = σ_L/σ_T
0.52	1.84	77.0 ± 53.9	325.4 ± 42.8	0.24 ± 0.17
0.75	1.84	83.9 ± 42.9	306.2 ± 33.5	0.27 ± 0.14
1.00	1.81	62.1 ± 35.4	297.5 ± 26.9	0.21 ± 0.12
2.00	1.84	61.4 ± 47.6	201.1 ± 26.0	0.31 ± 0.24

Table 5.5: L/T separated cross section results from this analysis for the reaction p(e,e′K$^+$)Λ.

from [Fel72] is shown in Figure 5.7*. This photoproduction point was taken at $E_\gamma = 1.45$ GeV ($W \approx 1.90$ GeV), $\theta_{CM} = 29°$ with cross section (339 ± 16) nb/sr. For Figure 5.7 this point is scaled to $\langle W \rangle = 1.84$ GeV, $\theta_{CM} = 0°$, to yield (390 ± 18) nb/sr. Over the Q^2 range studied, σ_L is fairly constant, while σ_T shows a decrease with increasing Q^2. Figure 5.8 shows the ratio $R = \sigma_L/\sigma_T$ from this analysis as a function of Q^2, along with data from [Beb77a]. The curves shown are from the WJC model.

Along with E93-018, Jefferson Lab experiment E91-016 [Zei91] also studied the p(e,e′K$^+$)Y reaction. Part of their program entailed taking p(e,e′K$^+$)Λ data at a setting of $Q^2 = 0.50$ GeV^2, with similar W and θ_{CM} coverage to E93-018. The two analyses of that data [Kol99, Cha99] found cross sections that are consistent with those presented in this analysis, particularly if they are scaled to the same Q^2 and W using the dependences of Equation 4.12 [Beb77a] and Equation 4.14 [Kol99], respectively. Furthermore, this author analyzed the actual E91-016 data taken for "setting 0" of [Kol99] for the purposes of a direct comparison and arrived

*Photoproduction experiments use real photons, hence only σ_T contributes.

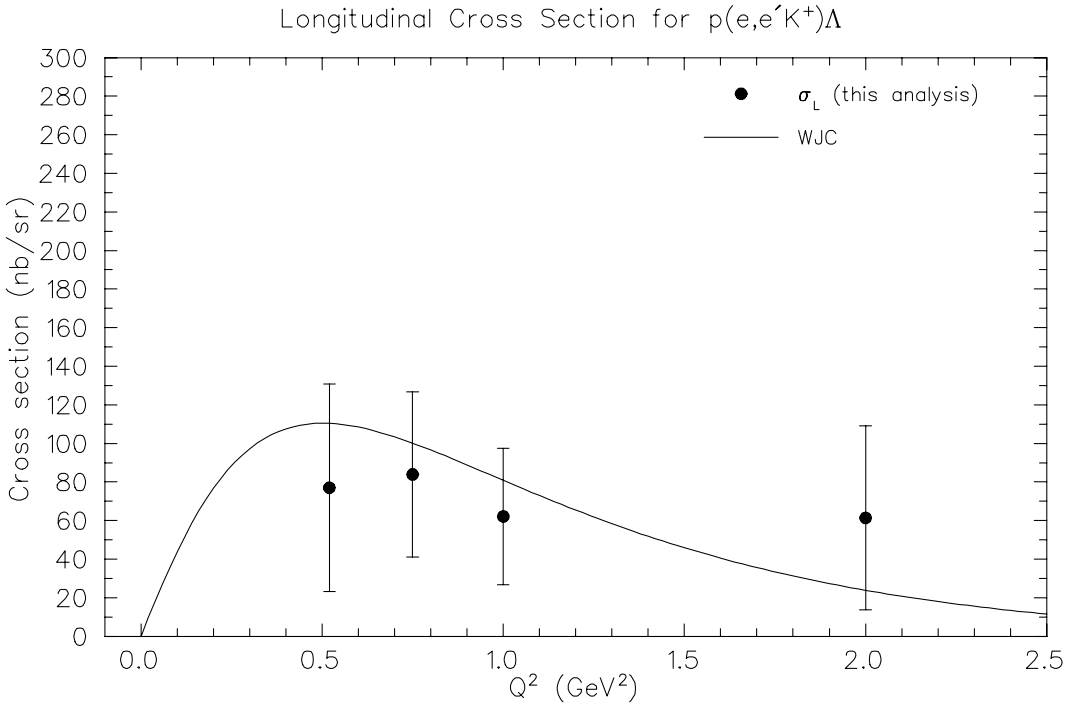

Figure 5.6: Longitudinal cross sections for p(e,e′K$^+$)Λ as a function of Q^2.

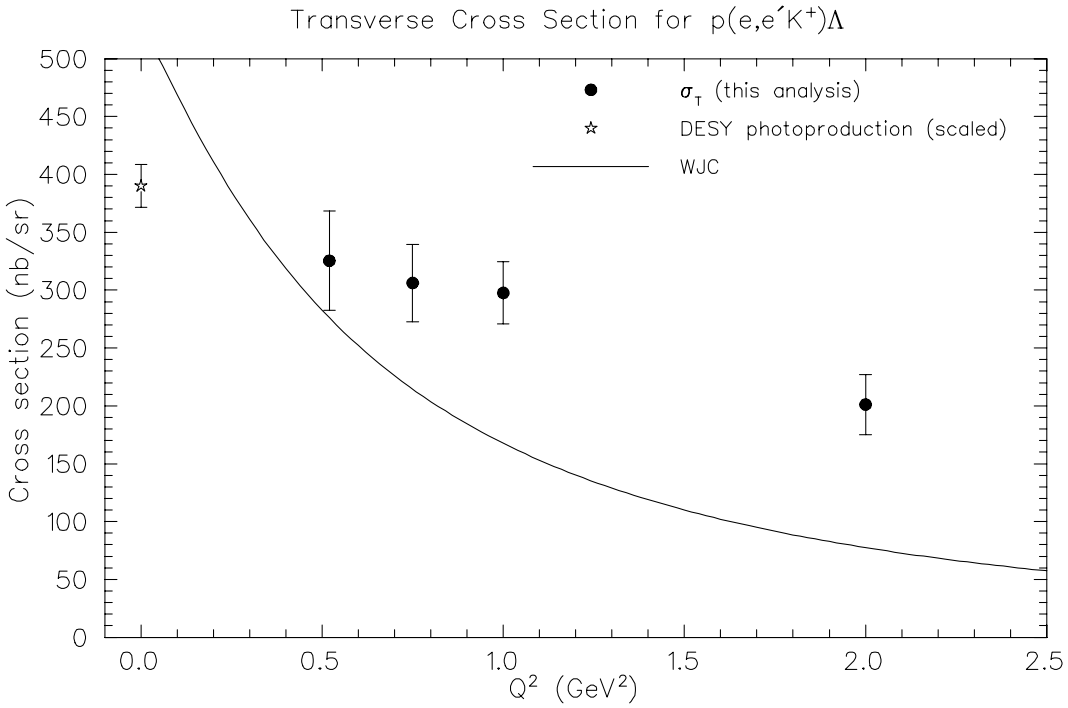

Figure 5.7: Transverse cross sections for p(e,e′K$^+$)Λ as a function of Q^2.

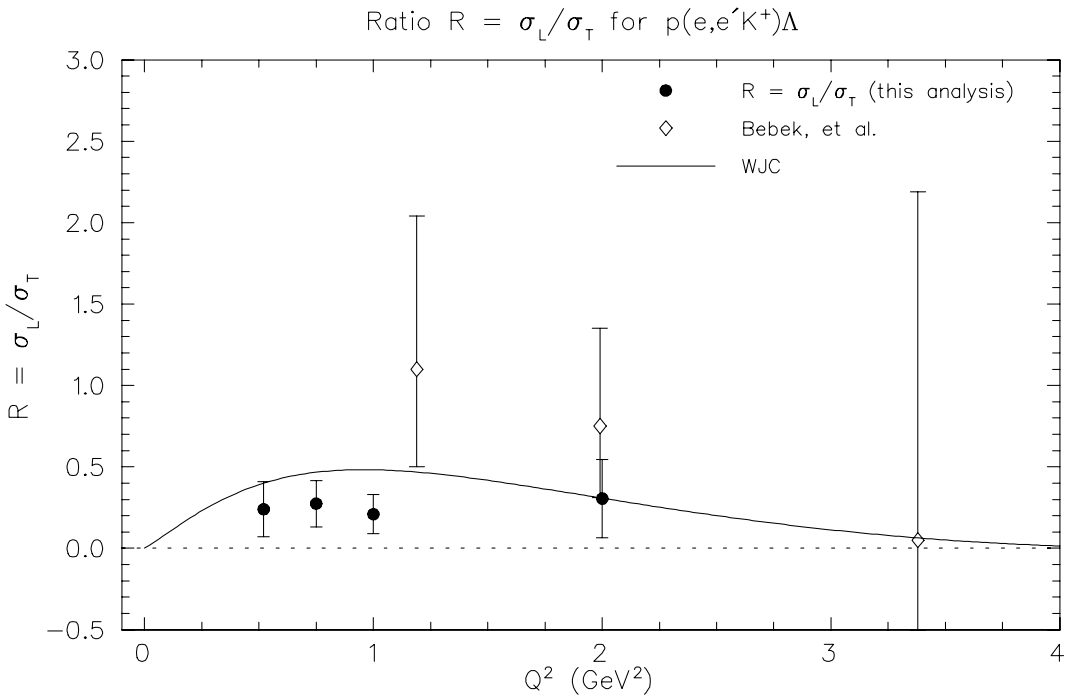

Figure 5.8: Ratio of longitudinal/transverse cross sections for p(e,e′K$^+$)Λ as a function of Q^2.

at a value of (426 ± 21) nb/sr, which agrees within 2.5% of their quoted value of (416 ± 20) nb/sr.

It should be noted that an independent analysis of the E93-018 data given in [Nic98a, Nic98b] arrived at cross sections for the Λ channel that were significantly different than those presented here (the Σ^0 channel was not analyzed) and that were also inconsistent with [Kol99, Cha99]. For example, the high-ϵ cross section at $Q^2 = 0.52$ GeV^2 (Point 3) quoted in [Nic98a] is (536.8 ± 29.7)* nb/sr, whereas the result from this analysis (including a 5% scale error) is (395.3 ± 23.4) nb/sr.

Scaling the [Nic98a] Point 3 cross section to $\langle W \rangle = 2.15$ GeV using the

*The value listed in [Nic98a] is (536.8 ± 12.8) nb/sr plus a 5% scale error.

function listed in Bebek (Equation 4.13) [Beb77a] as specified in [Nic98a], and noting that the value is quoted at $\theta_{CM} = 0°$, gives a value of 500.0 nb/sr. This value is inconsistent with the fit to the world data presented in Figure 5.4. This is also inconsistent with Figure 3 of reference [Nic98b], where a point was added to that world data plot at $Q^2 \approx 0.52$ with $d\sigma/d\Omega_K^* \approx 370$ nb/sr. The result for the high-ϵ point at $Q^2 = 2.00$ GeV^2 (Point 12) also gives a result inconsistent with the world data presented in Figure 5.4 and in Figure 3 of [Nic98b], going from a quoted 101.6 nb/sr to a W-scaled value of 94.6 nb/sr. Significant attempts were made to reconcile this analysis with [Nic98a], but these were largely unsuccessful because of the difficulty of comparing the two radically different analysis and corrections procedures.

5.7 Results for the Σ^0 Channel

The p(e,e′K$^+$)Σ^0 unseparated cross sections are shown in Table 5.6. In a manner similar to the Λ results, the high-ϵ values of the unseparated cross sections are shown in Figure 5.9 plotted together with the world data (previously shown in Figure 1.4). The E93-018 data shown in this plot have been scaled to $\langle W \rangle = 2.15$ GeV and include a 6% scale error. The world data have been scaled to ($\langle W \rangle = 2.15$ GeV, $\theta_{CM} = 0°$), using Equations 4.13 and 4.22.

The Σ^0 unseparated cross sections are plotted as a function of ϵ in Figure 5.10. The resulting values of σ_L, σ_T, and $R = \sigma_L/\sigma_T$ are shown in Table 5.7

$\langle Q^2 \rangle$ (GeV^2)	$\langle W \rangle$ (GeV)	ϵ	$\sigma_T + \epsilon\sigma_L$ (nb/sr)
0.52	1.84	0.545	70.1 ± 4.0
0.52	1.84	0.757	86.5 ± 4.8
0.52	1.84	0.851	91.4 ± 5.0
0.75	1.84	0.456	55.1 ± 3.2
0.75	1.84	0.709	65.8 ± 4.0
0.75	1.84	0.822	67.6 ± 4.1
1.00	1.81	0.375	37.2 ± 2.1
1.00	1.81	0.663	44.4 ± 2.7
1.00	1.81	0.792	47.3 ± 2.8
2.00	1.84	0.352	22.7 ± 1.5
2.00	1.84	0.461	21.7 ± 1.4
2.00	1.84	0.598	24.7 ± 1.5

Table 5.6: Results for the unseparated p(e,e′K$^+$)Σ^0 cross section used in the L/T separation (i.e., not including a scale error of 6%).

as well as on Figure 5.10. The fitting procedure and error analysis are similar to that done for the Λ in Section 5.6. The separated cross sections, σ_L and σ_T are shown as a function of Q^2 in Figures 5.11 and 5.12, respectively. A Sigma photoproduction point from [Fel72] is shown on Figure 5.12. This photoproduction point was taken at $E_\gamma = 1.31$ GeV ($W \approx 1.83$ GeV), $\theta_{CM} = 32^\circ$ with cross section (186 ± 30) nb/sr, and for Figure 5.12 was scaled to $\langle W \rangle = 1.84$ GeV, $\theta_{CM} = 0^\circ$, to yield (204 ± 33) nb/sr. Figure 5.13 shows the ratio $R = \sigma_L/\sigma_T$ from this analysis as a function of Q^2, along with data from [Beb77a]. Again, the curves shown are from the WJC model.

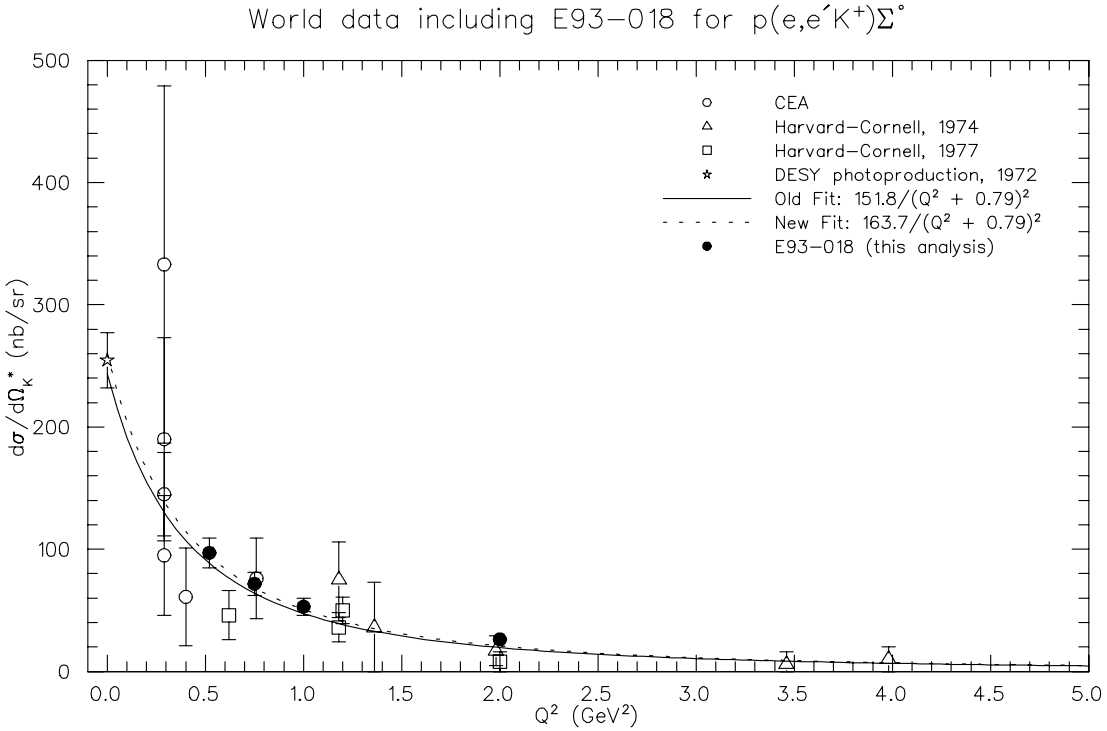

Figure 5.9: World data from Table 1.3 with the addition of the high-ϵ results of this analysis (solid points) scaled to $\langle W \rangle$ = 2.15 GeV, $\theta_{CM} = 0°$, for the p(e,e′K$^+$)Σ^0 unseparated cross sections. The "new fit" includes the results of this analysis.

$\langle Q^2 \rangle$	$\langle W \rangle$	σ_L (nb/sr)	σ_T (nb/sr)	R = σ_L/σ_T
0.52	1.84	71.6 ± 20.2	31.3 ± 14.0	2.29 ± 1.20
0.75	1.84	36.1 ± 13.6	38.9 ± 9.0	0.93 ± 0.40
1.00	1.81	24.4 ± 8.1	28.1 ± 5.0	0.87 ± 0.32
2.00	1.84	8.4 ± 8.5	19.0 ± 4.2	0.44 ± 0.46

Table 5.7: L/T separated cross section results from this analysis for the reaction p(e,e′K$^+$)Σ^0.

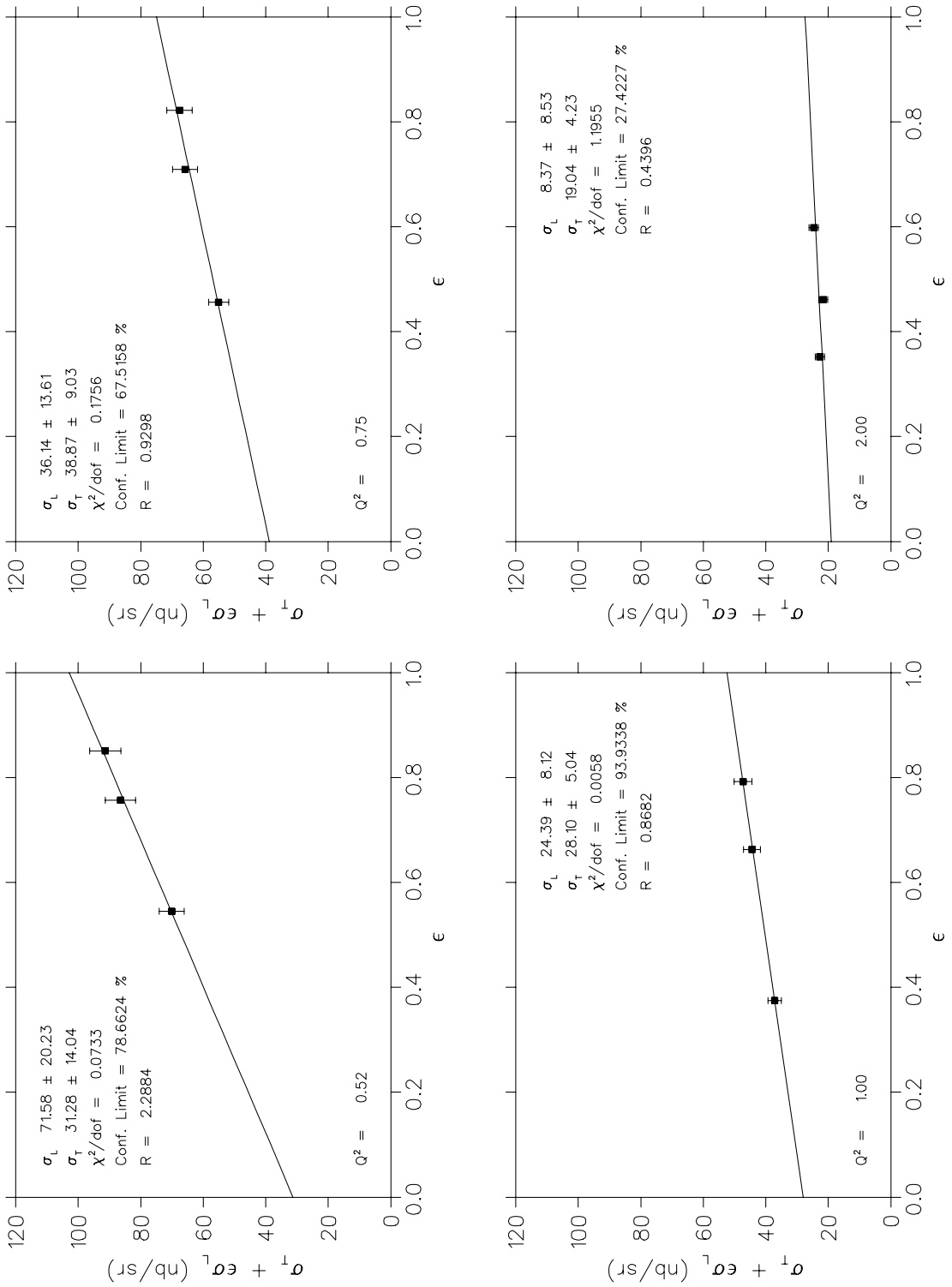

Figure 5.10: Extraction of L/T separated cross sections for $p(e,e'K^+)\Sigma^0$. For details see text.

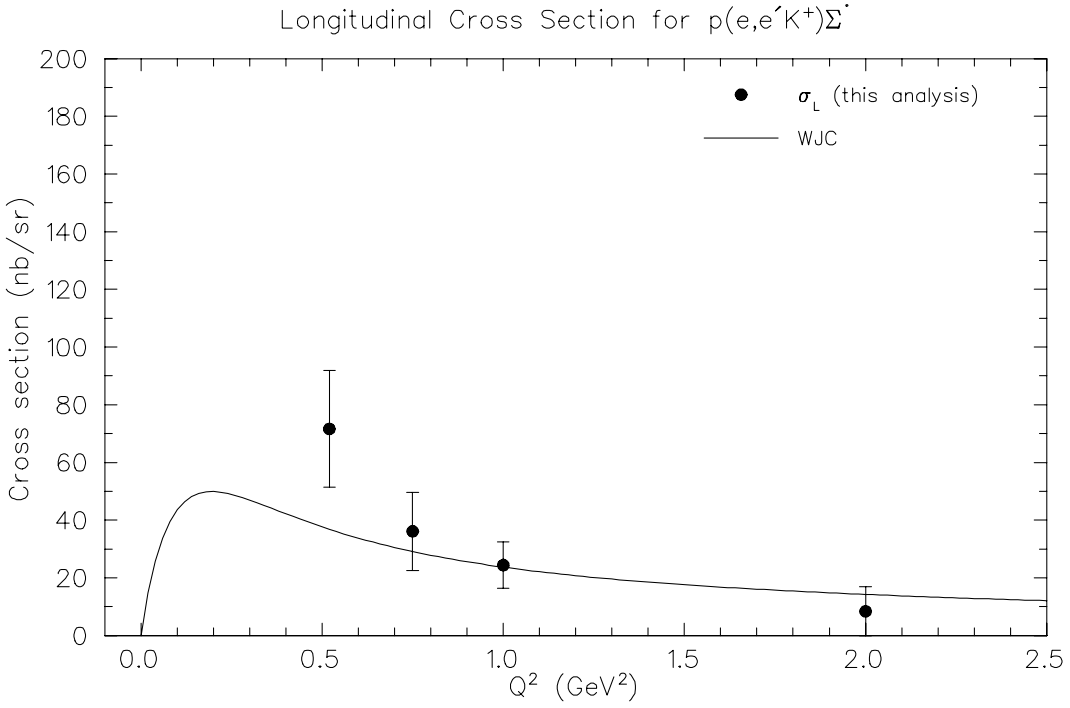

Figure 5.11: Longitudinal cross sections for p(e,e′K$^+$)Σ^0 as a function of Q^2.

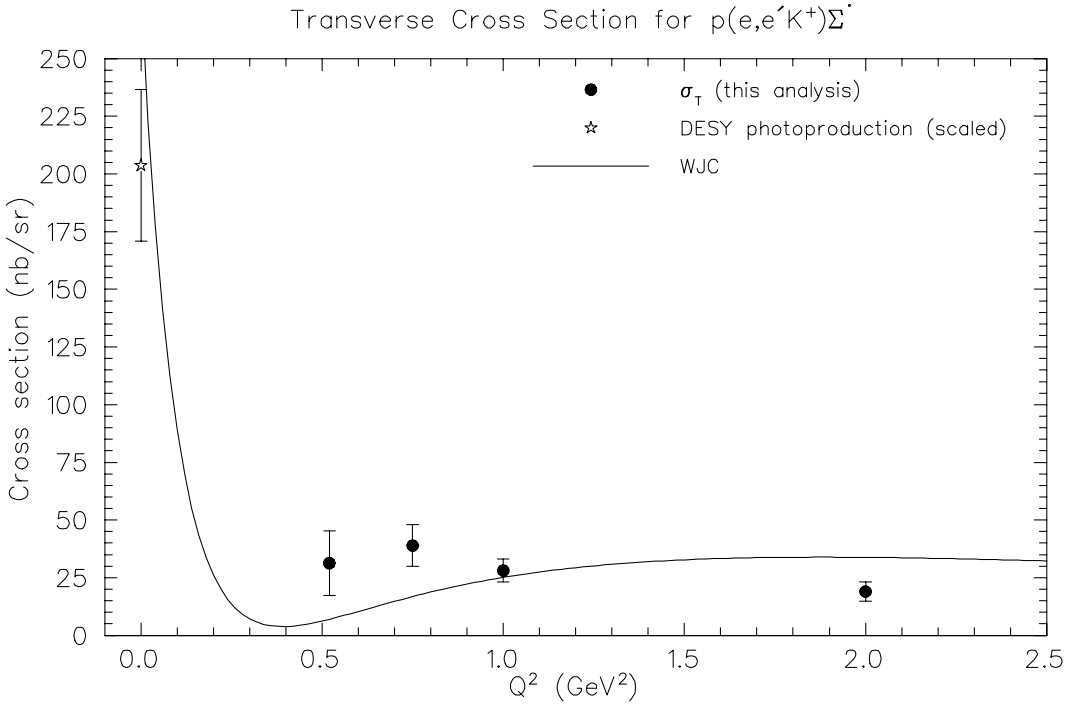

Figure 5.12: Transverse cross sections for p(e,e′K$^+$)Σ^0 as a function of Q^2.

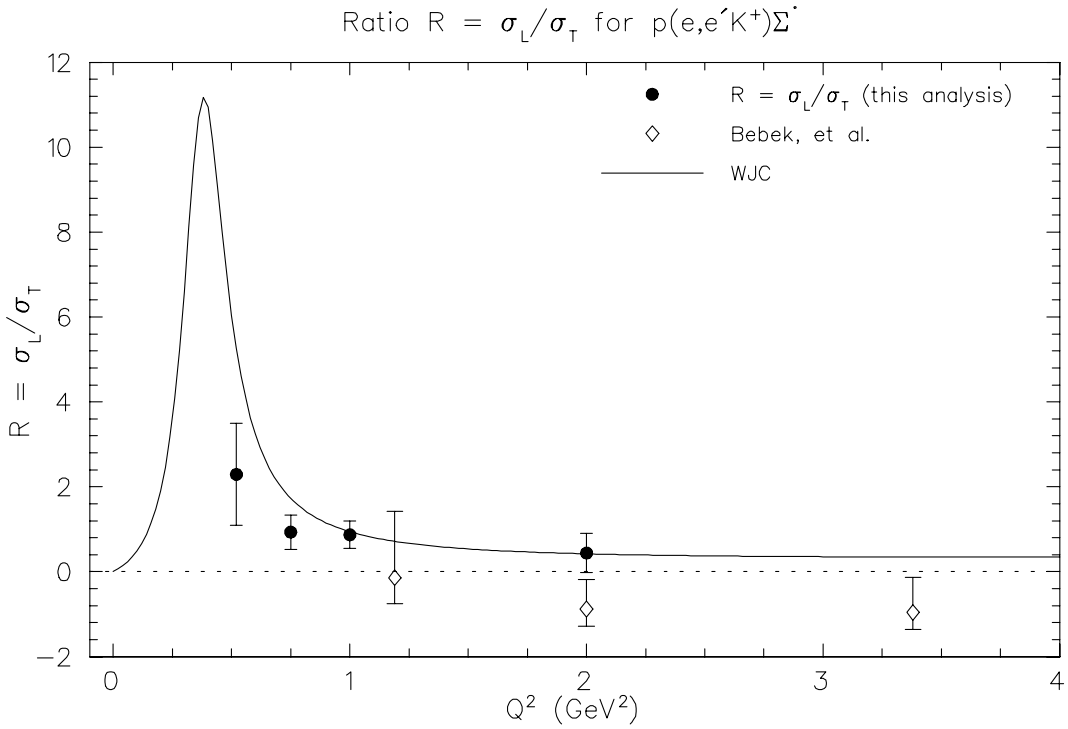

Figure 5.13: Ratio of longitudinal/transverse cross sections for p(e,e′K$^+$)Σ^0 as a function of Q^2.

5.8 Ratio of Σ^0/Λ Cross Sections

The ratio of Σ^0/Λ separated cross sections σ_L and σ_T are listed in Table 5.8, and are shown plotted vs. Q^2 in Figures 5.14 and 5.15, respectively, along with curves from the WJC model. An interesting feature is the decrease in the ratio seen for $\sigma_L(\Sigma^0)/\sigma_L(\Lambda)$, while the ratio of $\sigma_T(\Sigma^0)/\sigma_T(\Lambda)$ is fairly constant.

$\langle Q^2 \rangle$	$\langle W \rangle$	x	$\sigma_L(\Sigma^0)/\sigma_L(\Lambda)$	$\sigma_T(\Sigma^0)/\sigma_T(\Lambda)$
0.52	1.84	0.172	0.929 ± 0.702	0.096 ± 0.045
0.75	1.84	0.232	0.431 ± 0.274	0.127 ± 0.033
1.00	1.81	0.294	0.393 ± 0.259	0.094 ± 0.019
2.00	1.84	0.444	0.136 ± 0.175	0.095 ± 0.024

Table 5.8: L/T separated results from this analysis for the ratio of Σ^0/Λ cross sections.

5.9 Discussion of Results and WJC Model

The parameters of the WJC model are constrained by global fits to the existing data, virtually none of which were L/T separated results, so it is not surprising that the model does not completely describe the features of the data [Cot99]. However, the model does do well in some aspects, as will be discussed in this section.

For $p(e, e'K^+)\Lambda$, the model reproduces the behavior of the longitudinal part of the cross section (Figure 5.6), but fails to reproduce the transverse part (Figure 5.7). The inability to reproduce the transverse part leads to problems reproducing the ratio $R = \sigma_L/\sigma_T$ in Figure 5.8. One possible cause for the difference between the model and the data for the transverse cross section as a function of Q^2 could be the lack of knowledge of the baryonic form factors entering in the s-channel. For example, very little data exists from which form factors for strange baryons can be extracted.

For $p(e, e'K^+)\Sigma^0$, the model does a fair job of reproducing the trends of

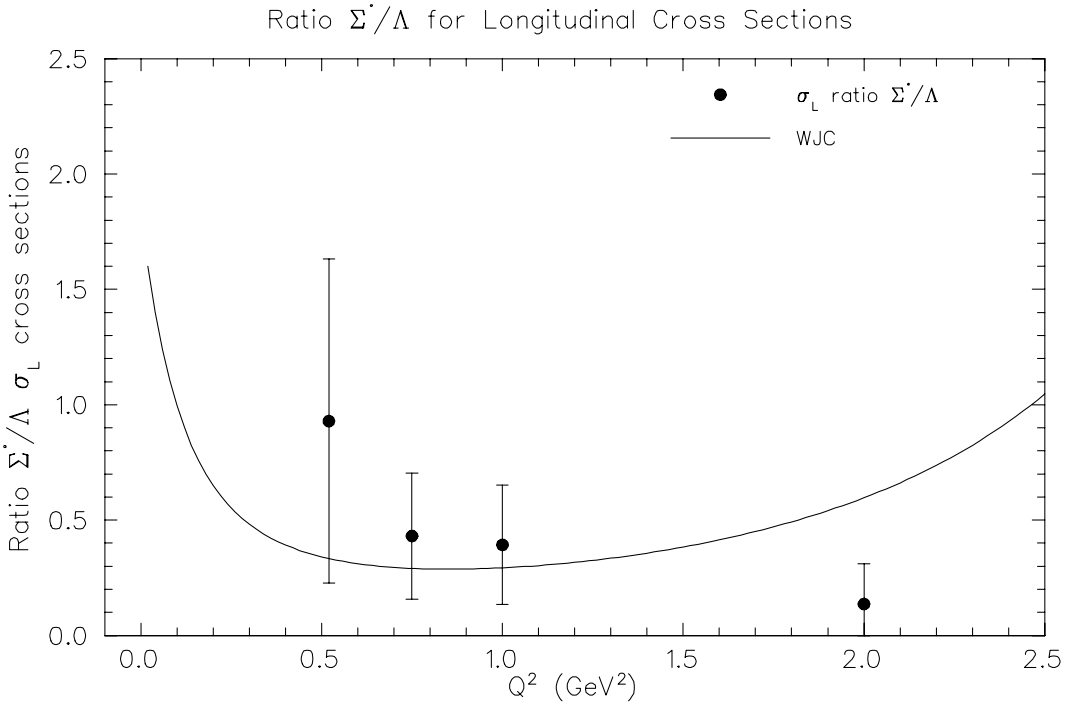

Figure 5.14: Ratio of Σ^0/Λ longitudinal cross sections as a function of Q^2.

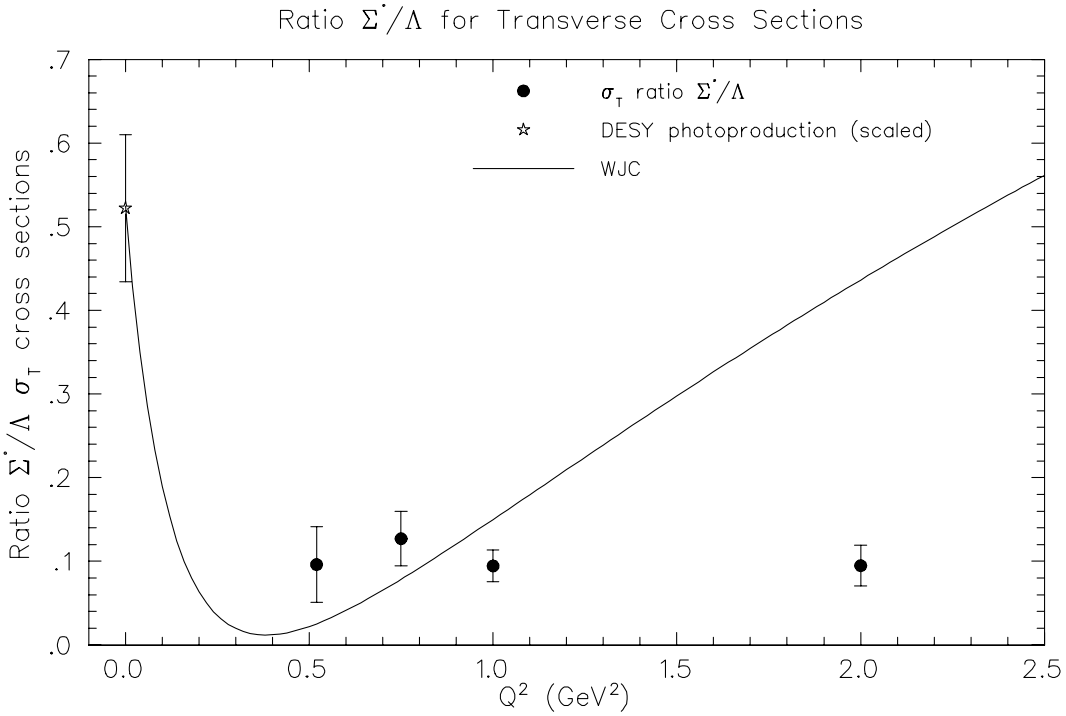

Figure 5.15: Ratio of Σ^0/Λ transverse cross sections as a function of Q^2.

the data in both the longitudinal and transverse channel (Figures 5.11 and 5.12, respectively). The model also shows the proper trend in the ratio $R = \sigma_L/\sigma_T$ (Figure 5.13). Again, it seems reasonable to expect that the form factors and the strengths of the various resonances entering the model could be modified in order to give better agreement with the data. The magnitude of the large peak in the model for R located at $Q^2 \approx 0.5$ GeV^2, for example, is very sensitive to the CM energy, W, of the reaction, indicating that there are strong resonance contributions in the model. In general, the model for the Σ^0 is harder to tune than for the Λ because of the influence of the isovector Δ resonances (of spin 1/2 and 3/2 in the model) in the Σ^0 channel.

The ratio of the longitudinal cross sections for Σ^0/Λ (Figure 5.14) shows a decrease as Q^2 is raised, although the errors are such that the degree of the decrease is not certain. As mentioned in the introductory chapter, a decrease in this ratio could be due to a decrease in the ratio of $g_{\Sigma NK}/g_{\Lambda NK}$. The ratio of the transverse cross sections for Σ^0/Λ (Figure 5.15) does not show any appreciable decrease above $Q^2 \approx 0.52$ GeV^2. However, the inclusion of a DESY photoproduction point on the plot shows that there is a rapid decrease in the transverse part for $Q^2 < 0.52$ GeV^2. The extracted values for the ratio of transverse cross sections listed in Table 5.8 are within the limits described by the simple model of Nachtmann and Cleymans/Close shown in Figure 1.10.

5.10 Conclusions

Experiment E93-018 measured kaon electroproduction on hydrogen in two hyperon channels, p(e,e′K$^+$)Λ and p(e,e′K$^+$)Σ^0. Data in both channels were taken at three (3) different values of the virtual photon transverse linear polarization, ϵ, for each of four (4) values of Q^2 = (0.52, 0.75, 1.00, 2.00) GeV^2. Cross sections averaged over the azimuthal angle, ϕ, were extracted (i.e., $\sigma_T + \epsilon\sigma_L$) at each of these twelve points for each hyperon. Rosenbluth separations were performed to separate the longitudinal and transverse production cross sections.

The results presented here are the most precise measurements of the separated cross sections σ_T and σ_L made to date, particularly for the Σ^0 channel, and can possibly serve to constrain theoretical calculations of these electroproduction processes. For example, a comparison of the WJC model to the results can yield information about the coupling strengths of contributing resonances within the framework of the model as well as perhaps information about the form factors and offshell vertex corrections entering the diagrams. These data will also hopefully be used in conjunction with other models to learn more about the reaction dynamics.

With regard to future experimental work, the results of this analysis show that there may be interesting physics in the region $0 < Q^2 < 0.5$ GeV^2. However, the taking of such data is a difficult proposition for a double-arm spectrometer experiment such as E93-018 because of the available beam energies and physical

limitations of the spectrometers. For example, at the lowest Q^2 measured for E93-018, small angles of approximately 13° were needed for both spectrometers. The physical bulk of the spectrometers makes it difficult to arrange them at the even smaller angles necessary to achieve a lower Q^2 L/T separation. However, similar measurements performed at higher W, possibly at Jefferson Lab after the beam energy is upgraded to 6 GeV, could be combined with the present results to examine the changing strengths of resonance contributions to the cross sections.

Other related measurements (photoproduction, electroproduction, as well as kaon-atomic electron scattering) are either just completed, currently running, or scheduled to run at laboratories worldwide. Additionally, other types of experiments (e.g., electroweak parity violation, hypernuclear spectroscopy, ϕ-meson production) also give a window into the physics of strangeness. The strategy of this experiment (and those of our companion experiment, E91-016) is only one of the many important perspectives from which strangeness physics should be viewed, with the ultimate goal of providing a more thorough understanding of the composition of nuclear matter and subnuclear reaction dynamics.

APPENDICES

Appendix A

The SOS Aerogel Čerenkov Detector

A.1 Introduction: Čerenkov radiation

As mentioned in Section 2.6.3, charged particles will emit "Čerenkov radiation" when traversing a material at a speed greater than the speed of light in that material, $\beta = 1/n$, where n is the index of refraction. A simple visualization of the process is shown in Figure A.1. In the left figure, a particle traveling less than the speed of light in a material is shown at several equally spaced times t_0 through t_5. The electromagnetic waves emanating from it at the times t_0 through t_5 travel at the speed of light in the medium and are thus unable to overlap one another. However, if the particle is moving faster than the speed of light in the medium as in the right half of Figure A.1, the different electromagnetic waves do overlap each other. The waves will constructively interfere with each other along a wave-front traveling at an angle θ_C relative to the motion of the particle. The

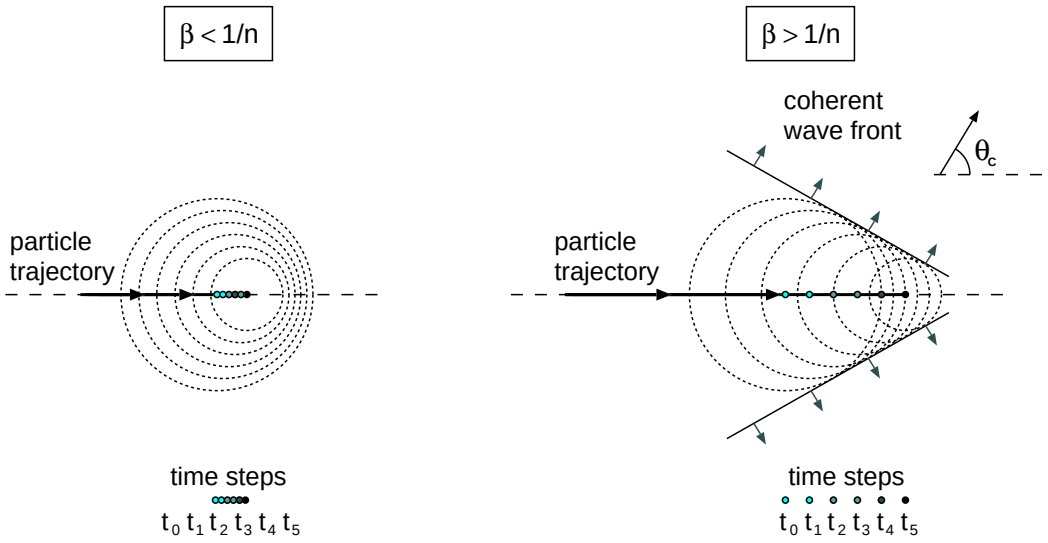

Figure A.1: Qualitative depiction of the Čerenkov radiation mechanism (based on [Jac75]).

condition for this angle can be seen from this geometric construction to be

$$\cos\theta_C = \frac{1}{\beta n} \ . \tag{A.1}$$

Of course, the properties of Čerenkov radiation can be derived properly from classical electrodynamics. In two-dimensions (for simplicity), the energy (E) and angular distribution of the light emitted by a particle of charge ze can be given (as in [Leo94]) in terms of the emitted frequency, ω and the solid angle, Ω as

$$\frac{d^2E}{d\omega\, d\Omega} = \frac{z^2\,\alpha\,\hbar}{c}\, n\,\beta^2\, \sin^2\theta \left| \frac{\omega\, L}{2\pi\,\beta\, c} \frac{\sin\xi(\theta)}{\xi(\theta)} \right|^2 \tag{A.2}$$

with

$$\xi(\theta) = \frac{\omega\, L}{2\pi\,\beta\, c}(1 - \beta\, n\, \cos\theta) \ . \tag{A.3}$$

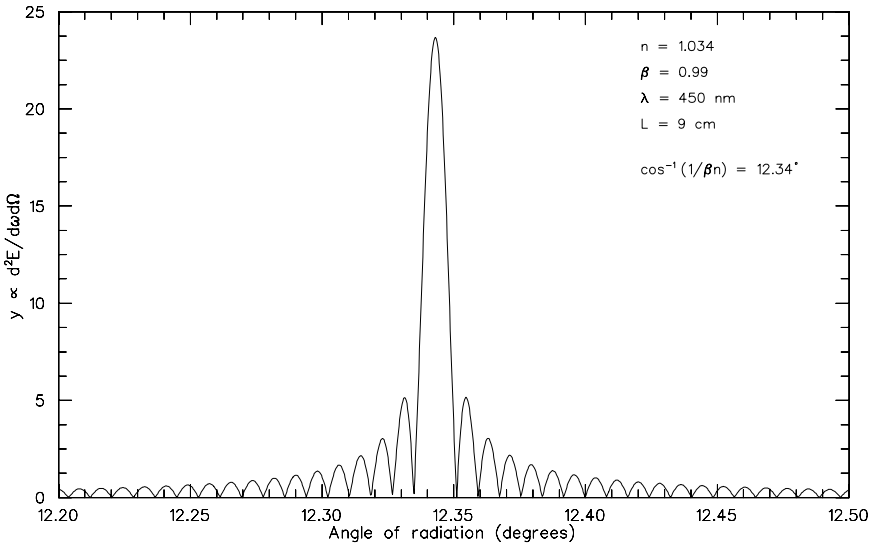

Figure A.2: Angular spectrum of Čerenkov radiation given by Equation A.2 showing the similarity to a Fraunhofer (far-field) diffraction pat-tern.

where θ is the polar angle of the emitted light, L is the length of material traversed, and $\beta = v/c$ is the velocity of the particle.

The angular distribution of energy at $\lambda = 2\pi/\omega = 450$ nm from Equation A.2 is shown in Figure A.2 for a particle traveling at $\beta = 0.99$ through 9 cm of aerogel with $n = 1.034$. The radiation is peaked at θ_C as given by Equation A.1, with an angular distribution similar to that of far-field diffraction. In the limit of $L \gg \lambda$, the function $\omega L \sin(\xi)/\xi$ becomes proportional to the delta function $\delta(1 - \beta n \cos\theta)$, yielding the exact condition of Equation A.1.

For the Hall C aerogel Čerenkov detector, the angular distribution is not as important as is the number of photons generated by a particle traveling above the threshold velocity. The number of photons per unit wavelength emitted per unit length traversed can be obtained by integrating Equation A.2 over the entire solid

angle (assuming $L \gg \lambda$ to simplify the integral), and dividing by $\hbar\omega$, yielding

$$\frac{d^2N}{d\lambda\, dx} = \frac{2\pi\, z^2\, \alpha}{\lambda^2} \left(1 - \frac{1}{\beta^2\, n^2(\lambda)}\right) . \tag{A.4}$$

Integrating over a typical range of detectable wavelengths (e.g., 300−600 nm for the Burle 8854 PMT [Inc89]), and approximating that the index of refraction is independent of wavelength yields the number of photons per unit length traversed:

$$\frac{dN}{dx} = 2\pi\, z^2\, \alpha \left(1 - \frac{1}{\beta^2\, n^2}\right) \int_{300\,\mathrm{nm}}^{600\,\mathrm{nm}} \frac{d\lambda}{\lambda^2} . \tag{A.5}$$

For a $z = 1$, $\beta = 1$ particle passing through aerogel with $n = 1.034$, this expression yields approximately 50 photons/cm, neglecting attenuation. Attenuation can be incorporated by the inclusion of an exponential decay factor, such as

$$\frac{dN}{dx} = 2\pi\, z^2\, \alpha \left(1 - \frac{1}{\beta^2\, n^2}\right) e^{-x/l_o} \int_{\lambda_1}^{\lambda_2} \frac{d\lambda}{\lambda^2} , \tag{A.6}$$

where l_o is the attenuation length, here assumed to be independent of wavelength. Aerogels typically have an attenuation length on the order of a few cm [Poe86].

For practical applications, the generated light is measured by photomultiplier tubes (PMTs) mounted in a detector, such as in Figure 2.16 and Figure 2.17. The detector itself absorbs some of the light, and the PMTs themselves are not 100% efficient at converting light into photoelectrons. Based on [Car79], the number of photoelectrons ($\mathrm{N_{pe}}$) for a $z = 1$ particle can be found by integrating Equation A.6 over the length of aerogel from (0−L) and adding a detector efficiency term:

$$\mathrm{N_{pe}} = \left(1 - \frac{1}{\beta^2\, n^2}\right) K'\, l_o\, (1 - e^{-L/l_o}) \left(\frac{\varepsilon}{1 - \eta\,(1 - \varepsilon)}\right) \tag{A.7}$$

where ε is the effective fraction of the container area covered by PMTs, η is the reflectivity of the container walls, L is the aerogel thickness, and K is an empirical factor accounting for the PMT efficiencies given by

$$K' = 2\pi\,\alpha \int_{\lambda_1}^{\lambda_2} \frac{q(\lambda)}{\lambda^2}\, d\lambda \ , \tag{A.8}$$

where $q(\lambda)$ is the effective quantum efficiency of the photocathode of each PMT.

Note that if attenuation is not included explicitly* in Equation A.6 (the approach taken in [Car79]), the resulting expression for $\mathrm{N_{pe}}$ is simply

$$\mathrm{N_{pe}} = \left(1 - \frac{1}{\beta^2\, n^2}\right) K\, L \left(\frac{\varepsilon}{1 - \eta\,(1-\varepsilon)}\right) \ . \tag{A.9}$$

A.2 Operation and Testing of the Detector

A.2.1 Physical Design, High Voltages

The physical design for the Hall C SOS aerogel Čerenkov detector was based on the aerogel detector in the MEPS spectrometer at the MIT/Bates Laboratory [Bay82]. A diffusion box arrangement was chosen because the lack of directionality of the Čerenkov light due to scattering in the aerogel material makes mirrors hard to use.

The phototubes were roughly gain-matched on an oscilloscope. The high voltages applied to the tubes ranged from 2440 to 2850 Volts (see Hall C Logbook

*In this case, attenuation is included as part of the factor K which must be determined from experiment. In the case where attenuation is ignored, $K = K'$ given by Equation A.8.

#10, p.197). In fact, it should be noted that the aerogel HV values were all originally ∼100 Volts higher, but were purposely lowered during E91-016/E93-018 as a conservative precaution to protect the tubes from the high rate (up to ∼300 kHz) of Čerenkov light-producing particles.

A.2.2 Summary of Detector Testing

At the design stage, calculations based on the performance of earlier detectors predicted about 13 photoelectrons (p.e.) to be generated for a $\beta = 1$ electron [Nap92]. Bench tests were performed using cosmic rays, with scintillator paddles set up above and below the detector to identify hits. The first tests used a single $(9 \times 20 \times 10)$ cm^3 stack of aerogel, and showed a yield of about 6-7 photoelectrons. The detector was then temporarily installed in the SOS so that it could be tested with scattered electrons, and once again only 6-7 p.e. were measured for $\beta = 1$ particles.

The detector was then brought back to the University of Maryland for further diagnostics. Two major changes were made at this point: First, as discussed in [Car79], the PMT bases were modified to raise the photocathode-to-1st-dynode voltages up to about 1 kV. Second, and most importantly, the aerogel tiles were baked in an oven at about 500°C for 5 hours, following a prescription given by [Hen96]. In comparison to the freshly baked tiles, the unbaked tiles had an obvious brownish tint – a surprising result as the tiles were factory sealed upon

receipt.

The detector was reassembled and bench tests indicated an approximately threefold gain in p.e. for $\beta = 1$. Tests with the detector installed in the SOS verified this result, giving a response of approximately 20.4 photoelectrons for $\beta = 1$ particles. This result was found with the higher set of PMT high voltages mentioned earlier in Section A.2.1. A slightly lower value of 19.3 photoelectrons for $\beta = 1$ particles was found for the lowered HV (see Section A.4).

To test the index of refraction and determine the threshold, π^+ and π^- data were taken at a setting of $P_{SOS} = 0.530$ GeV/c. At that setting, the pions were distributed in β such that they straddled the Čerenkov threshold velocity. A plot of the number of photoelectrons detected versus the pion velocity (as calculated from measured momentum as in Equation 3.2) is shown in Figure A.3.

The "turn on" of the Čerenkov light at threshold is clearly visible. The response of the detector for velocities below threshold is mainly due to light produced from scintillation as the particles pass through the dry nitrogen gas in the diffusion box. Taking a weighted average of the response below threshold gives a response due to scintillation of 0.28 ± 0.03 photoelectrons*. From the β dependence the index of refraction was determined to be 1.034 ± 0.001, implying $\beta_{threshold} \approx 0.967$. This corresponds to a kaon momentum of 1.875 GeV/c and

*In order to avoid accumulating background from events which scintillated but did not radiate Čerenkov light, PMTs with less than 0.3 p.e. for a given event were not included in the aerogel software sum.

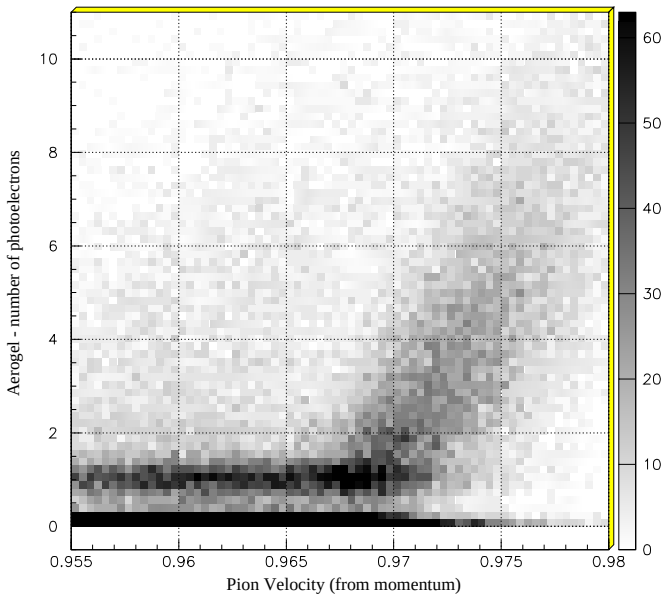

Figure A.3: Number of counts as a function of the number of photoelectrons detected and particle velocity for π^+ with a momentum of 530 MeV (Run 9973). The z-axis scale is shown to the right of the figure. The aerogel Čerenkov threshold occurs at a velocity of $\beta \approx 0.967$.

a pion momentum of 0.530 GeV/c. Some of the background response in Figure A.3 is thought to be due to muons arising from pion decay, which due to their smaller mass will achieve threshold velocity at a lower momentum than pions.

The aerogel detector was originally located at the position of the SOS gas Čerenkov detector (which would have been removed from the hut) in Figure 2.13. At that z-position, the fringe fields from the second SOS dipole magnet were measured with a Gaussmeter to be on the order of several Gauss. These fields were strong enough to cause up to 90% degradation in the collection efficiency of the aerogel PMTs, despite attempts to shield the PMTs using μ-metal. The

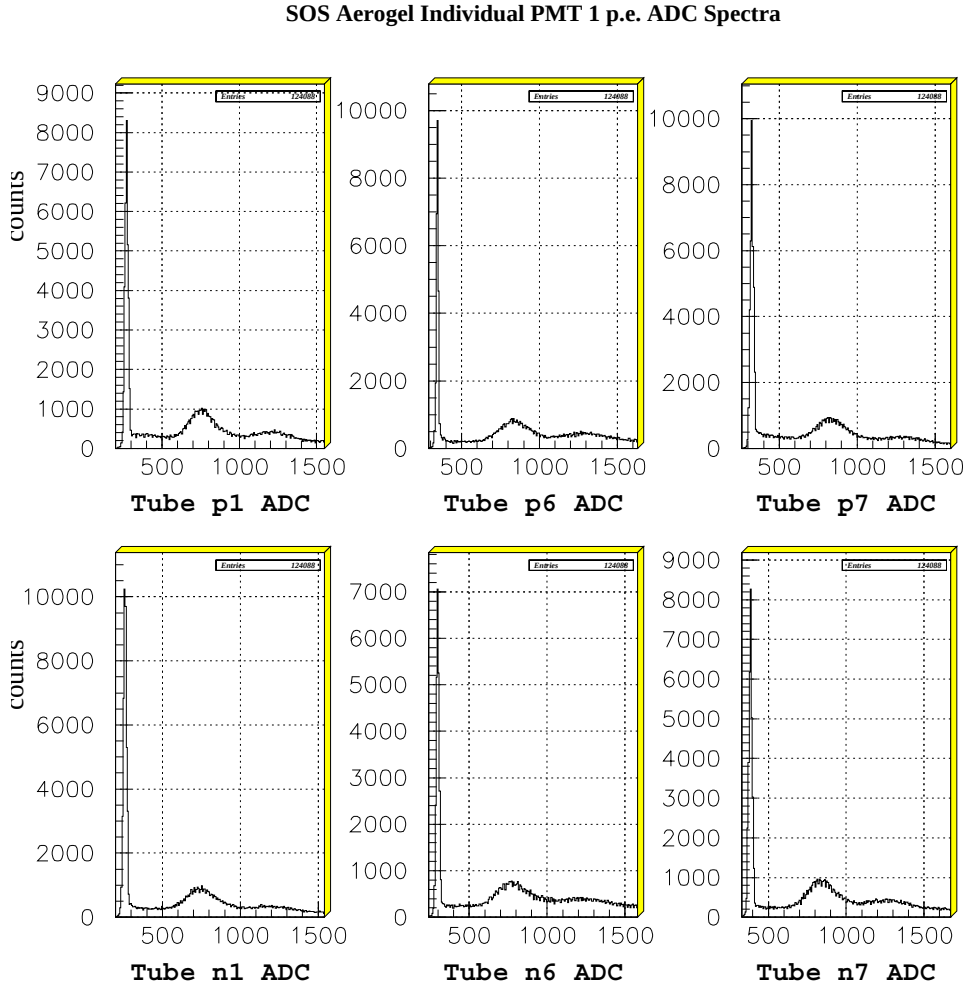

Figure A.4: Single photoelectron ADC signals from selected aerogel detector phototubes.

detector was then repositioned further back in the hut between hodoscope planes S2Y and S2X, where the fields were measured to be less than 1 Gauss.

A.3 Single Photoelectron Calibration

A selection of single PMT ADC spectra are shown in Figure A.4. The pedestal, single photoelectron peak, and even the double photoelectron peak are

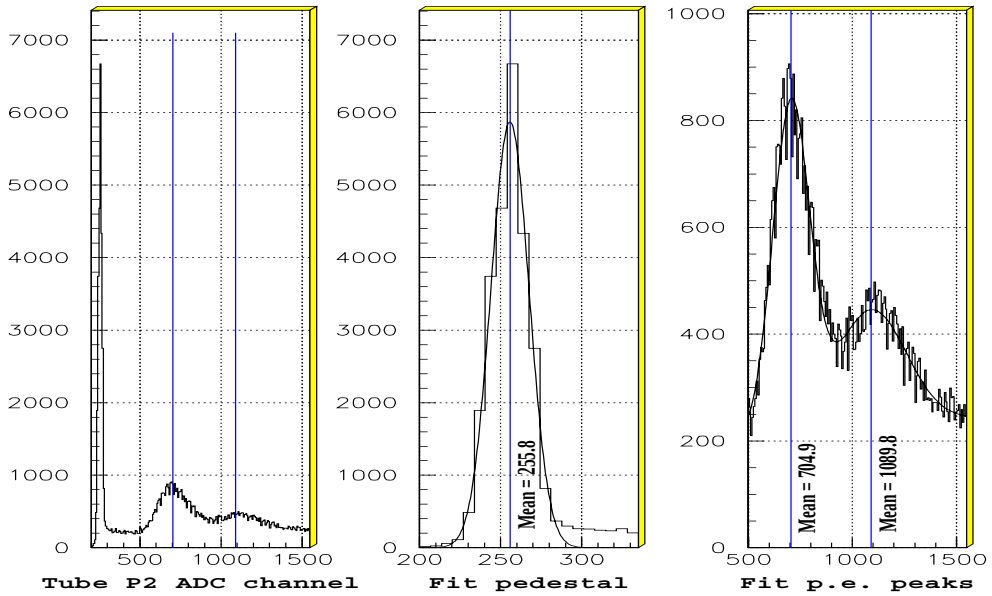

Figure A.5: Fitting the pedestals and first/second photoelectrons from the ADC signals from a single aerogel detector phototube as described in the text.

easily seen. Figure A.5 shows the procedure used to find the parameters necessary to convert ADC channels into number of photoelectrons. The value of the pedestal was found by fitting the lower region of the ADC spectrum by a Gaussian, as shown in the central panel of Figure A.5. The single and double photoelectron peaks are found by fitting the spectrum above the pedestal region to three independent Gaussians, one for each peak, and a third, weak, broader distribution to account for any (small) background. This procedure was consistently used for all of the PMT calibrations.

A.4 Response for $\beta = 1$ Particles

Prior to data taking for E93-018, but after the high voltages were lowered on the aerogel PMTs, the response the $\beta = 1$ particles was verified. Figure A.6 is a histogram of the number of photoelectrons seen in the aerogel detector for $\beta = 1$ electrons. The curve is a fit to a Poisson distribution, fit up to 25 photoelectrons, yielding $\langle \mathrm{N_{pe}} \rangle = 19.3$. Backgrounds due to other processes including knock-on electrons (delta rays) contribute to the higher channels.

Figure A.7 is a histogram of the number of PMTs firing with greater than 0.3 p.e. per tube, for the same electron run as in Figure A.6, showing a similar spectrum to that of Figure A.6.

A.5 Parameterization of $\mathrm{N_{pe}}$

In order to extract a rough estimate of the aerogel detector response as a function of aerogel material thickness traversed, an estimate of the attenuation length is needed. Reference [Car79] lists measurements of the response of several previous detectors. That paper references a detector reasonably similar to the Hall C detector [Bar77] that has the empirical factor K extracted for $\beta = 1$ particles traversing different lengths of aerogel, particularly $L = 4.5$ cm and $L = 9$ cm, with ε, η, and n held constant. From this knowledge, the ratio $\mathrm{N_{pe}}(L = 9\ \mathrm{cm})/\mathrm{N_{pe}}(L = 4.5\ \mathrm{cm})$ can be extracted using Equation A.9. Then,

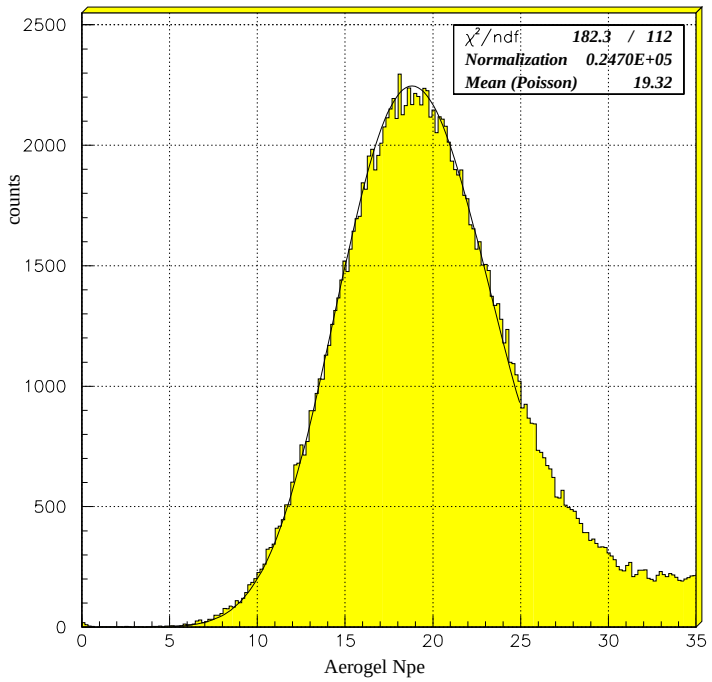

Figure A.6: Number of photoelectrons measured by the aerogel detector for $\beta = 1$ electrons, shown with a fit to a Poisson distribution (Run 10298).

this ratio can be used to solve Equation A.7 to give an effective attenuation length for that detector, $l_o = 7.37$ cm.

Using this value* of l_o, an expression based on Equation A.7 can be constructed by normalizing N_{pe} at $\beta = 1$ to the measured value of $N_{pe} = 19.3$ photoelectrons at a length of $L = 9$ cm. The quantities K', ε, and η are accounted for in the overall normalization. The result is:

$$\langle N_{pe} \rangle = 423.49 \times (1 - \frac{1}{\beta^2 \, n^2}) \times (1 - e^{-L/7.37}) \; . \tag{A.10}$$

*This assumes that the aerogel from that detector was of similar quality and that the larger N_{pe} detected by the Hall C detector is primarily a result of better collection efficiency.

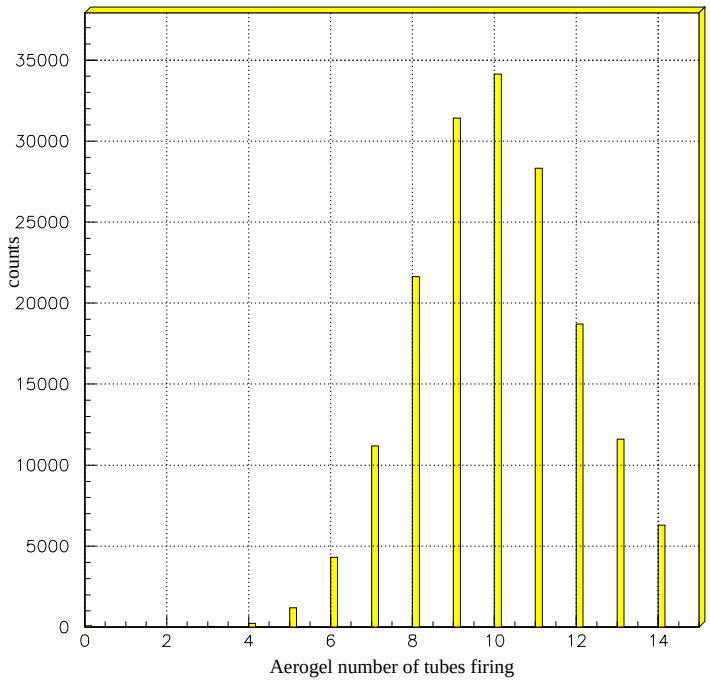

Figure A.7: Histogram showing the number of tubes firing at more than 0.3 p.e. per tube for $\beta = 1$ electrons (Run 10298).

As discussed in Section 3.6.6, the motivation for this expression was to estimate the minimum length of traversed aerogel material necessary for a decay product traveling at a velocity above threshold before a signal larger than the software cut of $N_{pe} < 3.5$ was generated. Figure A.8 shows the behavior of Equation A.10 in response to pions with velocities above threshold (i.e., $\beta > 0.967$). Based on this figure, even a $\beta = 1$ particle must travel through at least 1 cm of aerogel before it makes a sufficiently large signal to be cut at $N_{pe} < 3.5$.

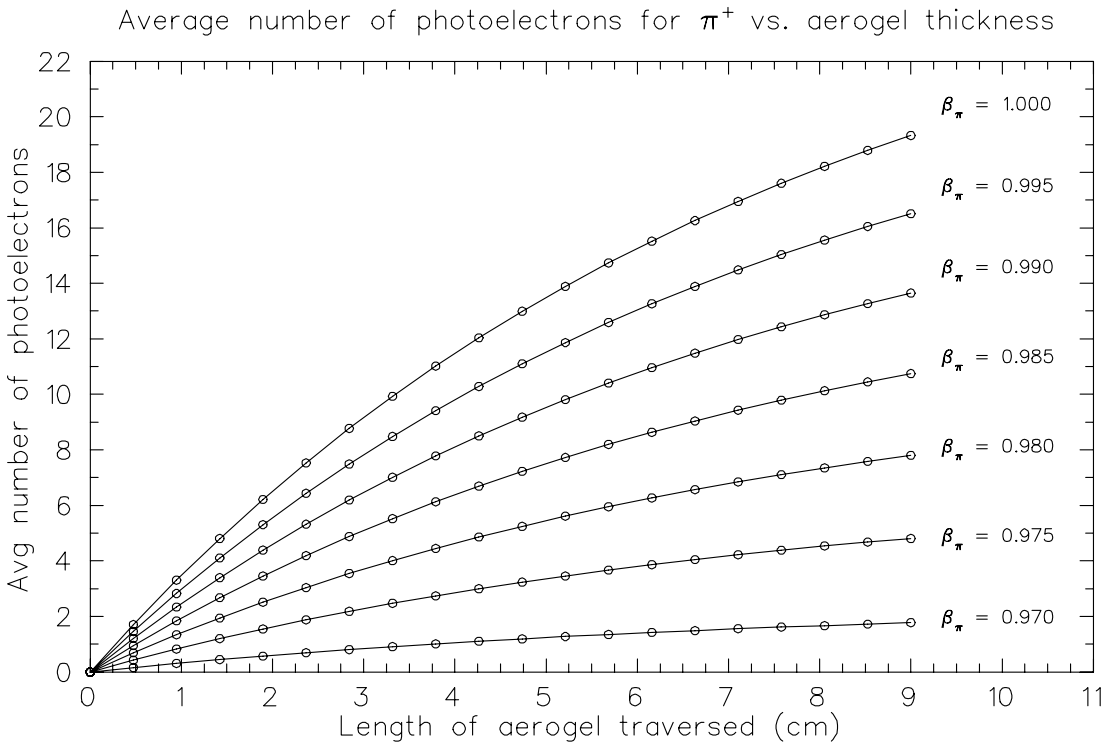

Figure A.8: Aerogel NPE as a function of aerogel thickness and pion velocity as given by Equation A.10.

A.6 Aerogel Pretrigger

The SOS aerogel pretrigger is discussed in some detail in Section 2.8. The purpose of the aerogel pretrigger was to establish a very conservative means of rejecting pions at the hardware level. In other words, the pretrigger was not implemented to eliminate all of the pion background, but rather only about $50 - 80\%$ of it, so as to not risk accidentally rejecting kaons.

The effect of inserting the aerogel veto signal into the hardware trigger is shown in Figure A.9. The left panel shows the raw ADCs from the half-sums A and B output by the aerogel summing module (see Figure 2.18) plotted against

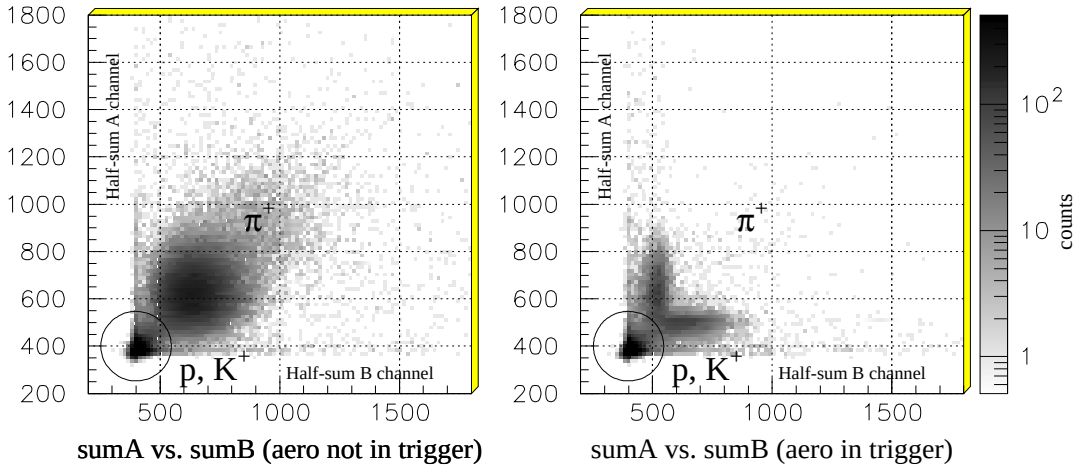

Figure A.9: Counts as a function of the raw ADC channels from aerogel summing module outputs A and B. In the left panel, the aerogel veto is not included in the pretrigger logic (Run 11695), whereas in the right panel it is included in the pretrigger (Run 11694). The few pions with more than 3.5 p.e. per half-sum that were accepted by the **PIPRE** path of the SOS pretrigger for diagnostics can also be seen in the right panel.

one another. The protons and kaons generate a very small aerogel signal for both A and B, and appear in the encircled region in the lower left corner. The pions generate a significant signal in each half-sum, and appear as a "balloon" in the left hand panel.

The right panel shows the same quantities plotted, except with the aerogel veto in place in the SOS pretrigger. Recall that the discriminators that determined the aerogel veto were set to reject events with more than 3.5 p.e. in either half-sum. The protons and kaons are left unchanged in the encircled region, but a large fraction of the pions have been eliminated by the two independent cuts on the half-sums A and B. Of course, it is the software aerogel cut that is responsible

for the final elimination of pions (see Section 3.5.2).

A.7 Aerogel Detector Fiducial Region

In order to determine the active fiducial region of the aerogel detector, negative polarity runs (mostly electrons) were taken with the SOS magnets purposely defocused and with the trigger restriction relaxed to simply **S1X** AND **S1Y**. This was done so that a reasonably large sample of particles would pass through the detector stack outside of the aerogel fiducial region.

Considering the transverse dimension (y) first, from the physical dimensions of the detector, particles more than approximately ± 20 cm away from the central ray cannot actually hit any aerogel material. In fact, it turns out that particles that pass through the outer side edges of the diffusion box in the y-direction may actually hit the phototube faces directly. When this occurs, a very large signal is generated in the struck PMT resulting in an ADC overflow. The left panel of Figure A.10 shows a plot of x vs. y projected to the z location of the aerogel detector for the events showing an ADC overflow. There is some background (presumably multiple tracks due to the non-restrictive trigger condition), but one can clearly see the locations of 13 of the 14 PMT faces (the 14th tube was not read during this run), delimiting the usable transverse region of the aerogel detector.

Likewise, in the dispersive direction (x), events that miss the detector by

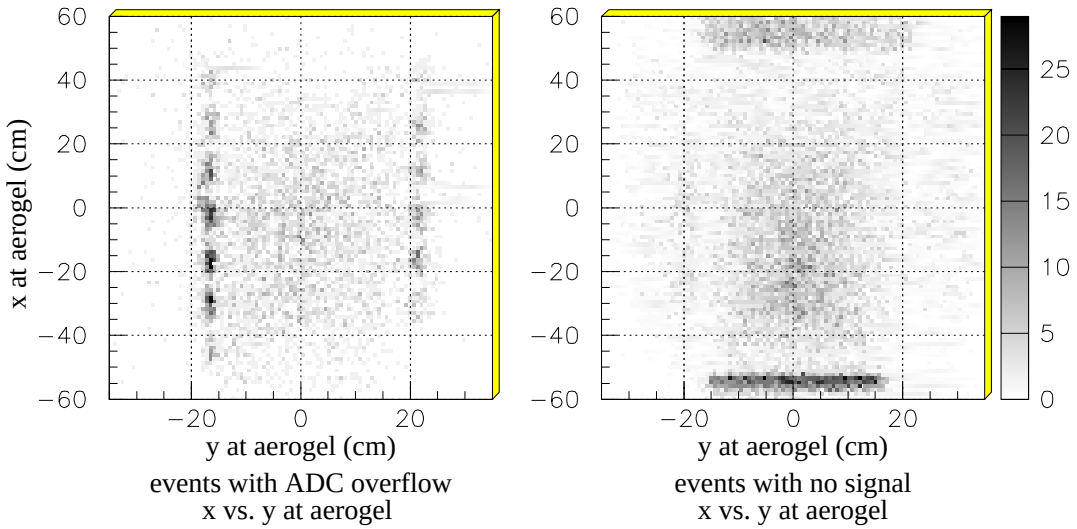

Figure A.10: Determination of the aerogel detector fiducial region. The left panel shows events gated by ADC overflows, revealing the positions of the phototube faces. The right panel shows events with no aerogel signal, revealing the upper and lower edges of the diffusion box.

traveling either below it or above it should generate no signal whatsoever in the detector. The right panel of Figure A.10 shows a plot of x vs. y projected to the z location of the aerogel detector for the events with no signal. Again, ignoring the background particles, one can clearly see two ridges defining the vertical edges of the detector.

Figure A.11 shows the approximate location of the detector as determined from the one-dimensional projections of the data in Figure A.10. The fiducial region (x at aerogel)=(-49.0 cm, 46.0 cm) and (y at aerogel)=(-14.0 cm, 18.0 cm) was defined and implemented as a cut in the final analysis to ensure that particles were capable of having generated an aerogel signal. In fact, after placing all of

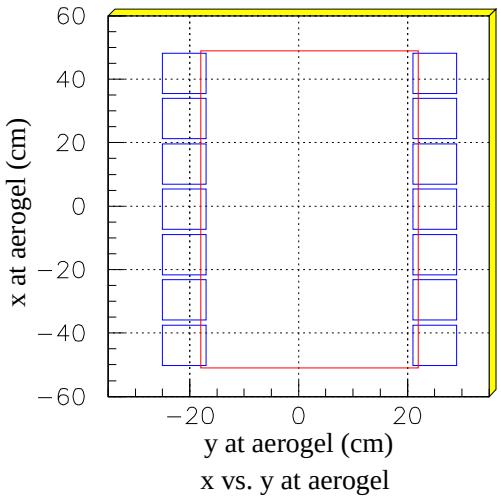

Figure A.11: Approximate physical location of the aerogel detector determined from the data of Figure A.10.

the other cuts (i.e., cuts on δ, m_Y, N_{pe}, β_{tof}, etc...), in turns out that the aerogel fiducial cut had very little impact (see Figure 5.1) on the number of counts accepted.

Appendix B

Miscellaneous

B.1 Notations and Kinematic Quantities

This section is given as a reference containing definitions and/or derivations of some of the kinematic quantities used throughout the document. Many of the relevant constants and notations used in this document are listed in Tables B.1, B.2, and B.3.

First of all, using the notation of Figure 1.2 and Table B.2, the total invariant energy of the (virtual photon + proton) CM system, W, is given by

$$W^2 = \left[(\nu, \mathbf{q}) + (m_p\,, \mathbf{0})\right]^2 \tag{B.1d1}$$

$$= \Big((\nu + m_p), \mathbf{q}\Big)^2 \tag{B.1d2}$$

$$= \nu^2 - |\mathbf{q}|^2 + 2m_p\nu + m_p^2 \tag{B.1d3}$$

$$W = \sqrt{m_p^2 + 2m_p\nu - Q^2}\ . \tag{B.1}$$

Constant	Definition	Value [HZ98]
m_e	Electron mass	0.511 MeV
m_π	π^+, π^- mass	139.57 MeV
m_K	K^+, K^- mass	493.677 MeV
m_p	Proton mass	938.272 MeV
m_Λ	Λ mass	1115.683 MeV
m_{Σ^0}	Σ^0 mass	1192.642 MeV
$c\tau_\pi$	π^+, π^- proper mean lifetime	7.805 m
$c\tau_K$	K^+, K^- proper mean lifetime	3.713 m
$c\tau_\Lambda$	Λ proper mean lifetime	0.0789 m
$c\tau_{\Sigma^0}$	Σ^0 proper mean lifetime	2.22×10^{-11} m
e	Electron charge	1.602×10^{-19} C
c	Speed of light *in vacuo*	2.998×10^{8} m/s
$\hbar = h/2\pi$	Planck constant, reduced	6.582×10^{-22} MeV s
$\alpha = e^2/4\pi$	Fine structure constant	1/137.036
N_A	Avogadro's number	6.022×10^{23} mol^{-1}

Table B.1: Listing of constants relevant to this analysis.

The squared four-momentum transfer carried by the virtual photon, Q^2, is given by

$$Q^2 = -q^\mu q_\mu = -(k_i^\mu - k_f^\mu)^2 = -(\nu, \mathbf{q})^2 = -\nu^2 + \mathbf{q}\cdot\mathbf{q} \tag{B.2d1}$$

$$= -E^2 + -E'^2 + 2EE' + |\mathbf{k_i}|^2 + |\mathbf{k_f}|^2 - 2|\mathbf{k_i}||\mathbf{k_f}|\cos\theta_e \ , \tag{B.2d2}$$

or, neglecting the mass of the electron (i.e., $E = |\mathbf{k_i}|$ and $E' = |\mathbf{k_f}|$),

$$Q^2 = 4EE'\sin^2\left(\frac{\theta_e}{2}\right) \ . \tag{B.2}$$

Variable	Definition
$k_i^\mu = (E, \mathbf{k_i})$	Initial electron four-momentum (Lab frame)
$k_f^\mu = (E', \mathbf{k_f})$	Scattered electron four-momentum (Lab frame)
θ_e	Scattered electron polar angle (Lab frame)
ϕ_e	Scattered electron azimuthal angle (Lab frame)
Ω_e'	Solid angle of scattered electron in the Lab frame
$p_p^\mu = (m_p, \mathbf{0})$	Target proton four-momentum
ν	Energy of the virtual photon, $(E - E')$
$\mathbf{q}$	Three-momentum of the virtual photon, $(\mathbf{k_i} - \mathbf{k_f})$
$q^\mu = (\nu, \mathbf{q})$	Virtual photon four-momentum (Lab frame), $k_i^\mu - k_f^\mu$
$Q^2 = -q^\mu q_\mu$	Virtual photon four-momentum transfer squared
W	Total (invariant) available energy of the (γ_v + p) system
ϵ	Virtual photon transverse linear polarization
Γ_0	Virtual photon flux as a function of (E', Ω_e')
Γ	Virtual photon flux as a function of (Q^2, W)
$p_K^\mu = (E_K, \mathbf{p_K})$	Kaon four-momentum (Lab frame)
θ_{qK}	Angle between the kaon and virtual photon (Lab frame)
$\theta_{CM} \equiv \theta_{qK}^*$	Angle between the kaon and virtual photon (CM frame)
ϕ	Azimuthal angle between the scattering and reaction planes
Ω_K^*	Solid angle of produced kaon in the CM frame
$p_Y^\mu = (E_Y, \mathbf{p_Y})$	Hyperon four-momentum (Lab frame)
m_Y	Generic hyperon mass, or the calculated missing mass
β	Velocity given as v/c
γ	Lorentz factor, $1/(1-\beta^2)^{-\frac{1}{2}}$
$\mathbf{p_{cm}^*}$	Three-momentum of the CM frame relative to the Lab
β_{cm}	Velocity of the CM frame relative to the Lab

Table B.2: Listing of selected notations used in this document. Note that a superscript "$*$" is used throughout to represent the Center-of-Momentum (CM) frame equivalent of any Lab frame variable. The CM frame referred to is always that of the (virtual photon + proton) system.

Variable	Definition
$s = (q^\mu + p_p^\mu)^2 = W^2$	Mandelstam variable (CM frame energy squared)
$t = -(q^\mu - p_K^\mu)^2$	Mandelstam variable (Section 4.6)
$u = (q^\mu - p_Y^\mu)^2$	Mandelstam variable
(x_B, y_B, z_B)	Incident beam coordinate system
(x_H, y_H, z_H)	HMS Transport coordinate system
(x_S, y_S, z_S)	SOS Transport coordinate system
$\mathrm{P_{HMS}}$, $\mathrm{P_{SOS}}$	HMS (SOS) central momentum setting
θ_H, θ_S	HMS (SOS) angle setting
β_{tof}	Velocity as calculated using the TOF information
β_{mom}	Velocity as calculated from the momentum
$\beta_{\mathrm{threshold}}$	Threshold velocity for Čerenkov radiation
$\mathrm{N_{pe}}$	Number of photoelectrons detected (Appendix A)

Table B.3: Further listing of selected variables relevant to the data analysis.

B.1.1 Definition of Missing Mass

In the experiment, the four-vector quantities k_i^μ, k_f^μ, and p_K^μ were measured. The four-momentum of the undetected hyperon could then be deduced by requiring the total four-momentum to be conserved in Figure 1.2:

$$(k_i^\mu + p_p^\mu) = (k_f^\mu + p_K^\mu + p_Y^\mu) \tag{B.3d1}$$

$$(q^\mu + p_p^\mu) = (p_K^\mu + p_Y^\mu) \tag{B.3d2}$$

$$p_Y^\mu = (q^\mu + p_p^\mu - p_K^\mu) \tag{B.3d3}$$

or in expanded notation,

$$\left(E_Y, \mathbf{p_Y}\right) = \left((\nu + m_p - E_K), (\mathbf{q} - \mathbf{p_K})\right) . \tag{B.3d4}$$

Squaring both sides and collecting terms gives

$$m_Y^2 = (\nu^2 - |\mathbf{q}|^2) + (E_K^2 - |\mathbf{p_K}|^2) + 2\,\nu\,m_p - 2\,E_K(\nu + m_p) - 2\,\mathbf{q}\cdot\mathbf{p_K}\ . \tag{B.3d5}$$

Finally, replacing the relevant terms with Q^2 and the kaon mass yields the expression for the missing mass as

$$m_Y^2 = -Q^2 + m_K^2 + 2\,\nu\,m_p - 2\,E_K(\nu + m_p) - 2\,\mathbf{q}\cdot\mathbf{p_K}\ . \tag{B.3}$$

B.2 Hall C Coordinate Systems

The different coordinate systems that were used in the course of this analysis are presented in this section. First, the "Beam coordinate system" is shown in Figure B.1, and is defined such that the positive z-axis is in the direction of the incident beam. The positive y-axis is defined as the true vertical (i.e., opposite of gravity), and the positive x-axis is selected so as to form a right-handed coordinate system (i.e., to the left of the beam).

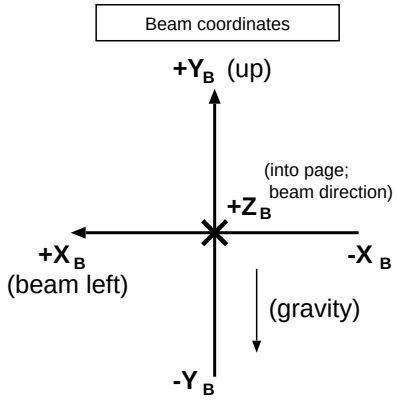

Figure B.1: Definition of the Beam coordinate system (beam's-eye view).

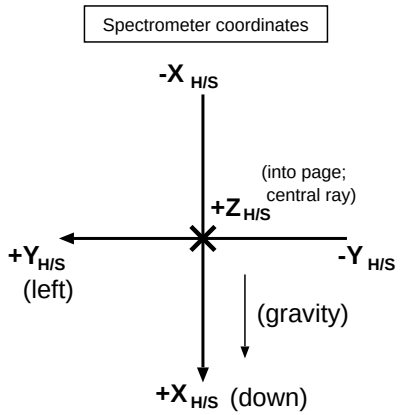

Figure B.2: Definition of the HMS/SOS Transport spectrometer coordinate system, (particle's-eye view).

Second, the coordinates of the particles as they traverse the HMS or SOS are given with reference to the "Transport spectrometer coordinate system" for each spectrometer as shown in Figure B.2. For each spectrometer, the positive z-axis is defined to be in the direction of the central ray emanating from the target. The positive x-axis is taken in the dispersive direction of the spectrometer towards higher momentum, which for both HMS and SOS is downward (i.e., in the direction of gravity). The positive y-axis is selected so as to form a right-handed coordinate system (i.e., to the left of the particle direction). Further details regarding the use of the "Transport" program can be found in [Bro80].

Figure B.3 shows a top view of relating these two coordinate systems. Converting between the Beam coordinate system and the HMS Transport coordinate

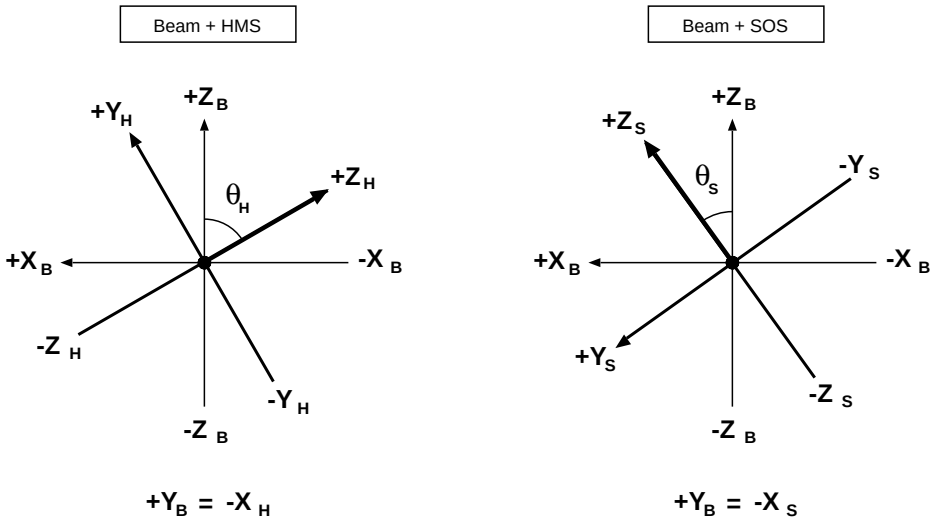

Figure B.3: Relation of the Beam coordinate system to HMS/SOS Transport spectrometer coordinate system (top view).

system is done via

$$x_{_H} = -y_{_B} \tag{B.4}$$

$$z_{_H} = z_{_B}\cos\theta_{_H} - x_{_B}\sin\theta_{_H}$$

$$y_{_H} = z_{_B}\sin\theta_{_H} + x_{_B}\cos\theta_{_H}\ ,$$

and the inverse,

$$y_{_B} = -x_{_H} \tag{B.5}$$

$$z_{_B} = z_{_H}\cos\theta_{_H} + y_{_H}\sin\theta_{_H}$$

$$x_{_B} = -z_{_H}\sin\theta_{_H} + y_{_H}\cos\theta_{_H}\ .$$

Likewise, converting between the Beam coordinate system and the SOS Transport

coordinate system is done via

$$x_S = -y_B \tag{B.6}$$

$$z_S = z_B \cos\theta_S + x_B \sin\theta_S$$

$$y_S = -z_B \sin\theta_S + x_B \cos\theta_S \ ,$$

and the inverse,

$$y_B = -x_S \tag{B.7}$$

$$z_B = z_S \cos\theta_S - y_S \sin\theta_S$$

$$x_B = z_S \sin\theta_S + y_S \cos\theta_S \ .$$

B.2.1 Definition of x', y', $y_{\rm tar}$, and δ

The particle trajectories are usually given in terms of their slopes $(x'_{\rm tar}, y'_{\rm tar})$ at the target, or $(x'_{\rm fp}, y'_{\rm fp})$ at the focal plane, with reference to the Transport spectrometer coordinate system. Figure B.4 shows the definition of x' and y' for a given trajectory in the SOS. In words, x' is the slope of the projection of the trajectory in the x-z plane, and y' is the slope of the projection of the trajectory in the y-z plane.

The quantity $y_{\rm tar}$ is used to describe the position of the interaction vertex along the length of the target cell. The quantity $y_{\rm tar}$ is given with respect to the Transport spectrometer coordinate system and is equivalent to $y_H(y_S)$ for the HMS (SOS), whereas the length of the target is typically given in the Beam coordinate system. The $\sim$4 cm LH_2 target is centered at $z_B = 0$ and extends from

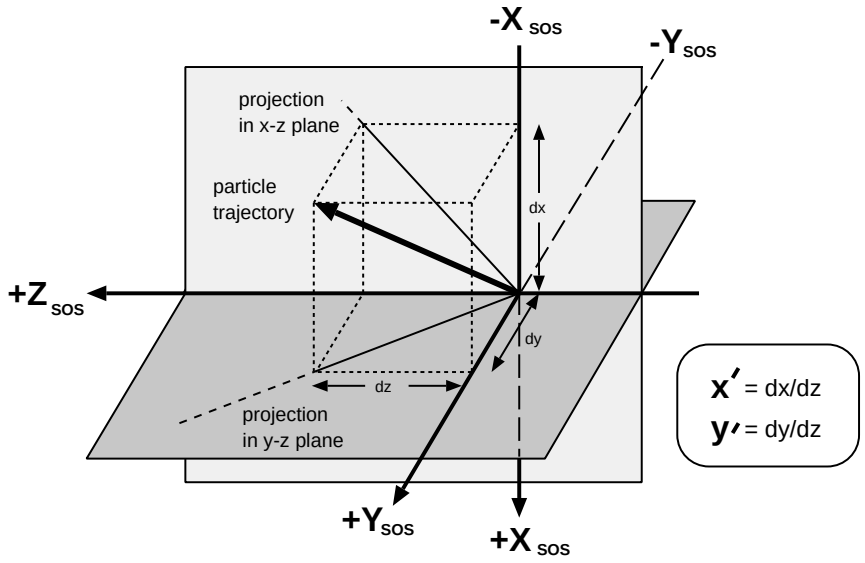

Figure B.4: Definition of x' and y', shown for the SOS.

$z_B = (-2.18$ cm, $+2.18$ cm). Taking the HMS as an example and using Equation B.4 (with $x_B = 0$), for a spectrometer angle of $\theta_H = 15^\circ$ this corresponds to a range of $y_{\rm tar} = (-1.128$ cm, $+1.128$ cm). Likewise, for an angle of $\theta_H = 45^\circ$, $y_{\rm tar} = (-1.54$ cm, $+1.54$ cm). Figure B.5 shows the relationship between $y_{\rm tar}$ and z_B from the perspective of the HMS.

The quantity δ is used to describe the percentage deviation of the detected momentum, $|\mathbf{p}|$, of a particle from the central momentum setting of the spectrometer. For the HMS, δ is given by

$$\delta = \frac{(|\mathbf{p}| - P_{\rm HMS})}{P_{\rm HMS}} \times 100 \ . \tag{B.8}$$

with an analogous form for the SOS. In order to convert the reconstructed value of δ into an absolute momentum the inverse of the above equation is used,

$$|\mathbf{p}| = P_{\rm HMS} \times (1 + \delta/100) \ . \tag{B.9}$$

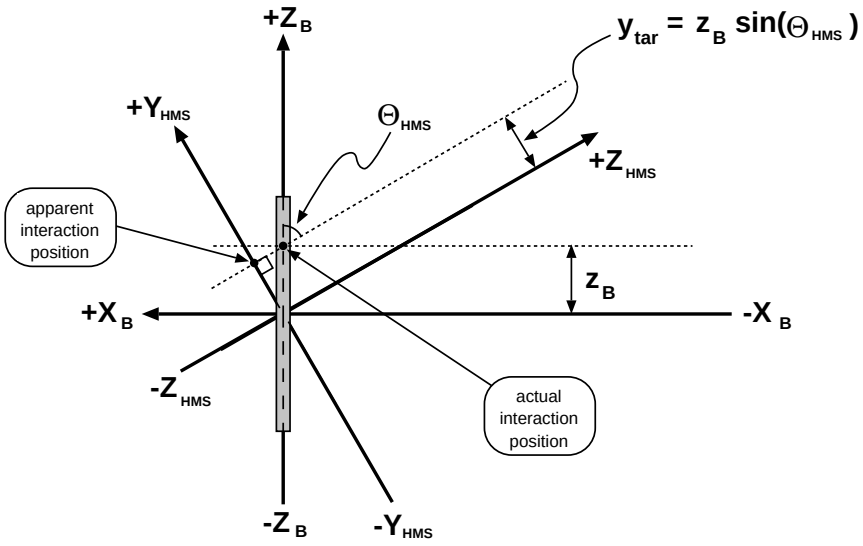

Figure B.5: Geometrical definition of the apparent interaction position, $y_{\rm tar}$, from the perspective of the HMS (top view such that the y_B axis points into the page).

B.3 Virtual Photoproduction in the CM Frame

The virtual photoproduction reaction is shown in the CM frame in Figure B.6. The three-momentum of both the virtual photon and the proton in the CM frame can be shown* to be given by

$$|\mathbf{p}^*_{\mathbf{cm}}| \equiv |\mathbf{q}^*| = |\mathbf{p}^*_{\mathbf{p}}| = \frac{m_p\,|\mathbf{q}|}{W}\ . \tag{B.10}$$

Because the proton is at rest in the lab, the proton velocity in the CM frame is equal to the velocity of the CM frame itself, and is given by

$$\beta_{cm} = \frac{|\mathbf{p}^*_{\mathbf{cm}}|}{E^*_p} = \frac{|\mathbf{p}^*_{\mathbf{cm}}|}{\sqrt{m_p^2 + |\mathbf{p}^*_{\mathbf{cm}}|^2}}\ . \tag{B.11}$$

*For example, see Exercise 11.20 in [Jac75].

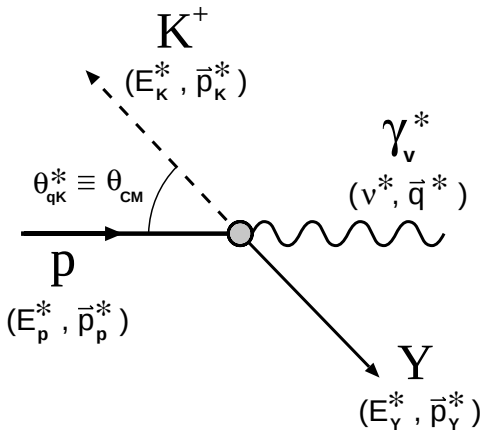

Figure B.6: Virtual photoproduction in the CM frame.

This expression can be reduced to

$$\beta_{cm} = \frac{|\mathbf{q}|}{(\nu + m_p)} \ , \tag{B.12}$$

for the velocity of the CM frame, and

$$\gamma_{cm} = \frac{(\nu + m_p)}{W} \ , \tag{B.13}$$

for the Lorentz factor of the CM frame.

With knowledge of β_{cm} and γ_{cm}, particle momenta can be transformed between the Lab and CM frames easily using a simple Lorentz transformation, as will be demonstrated in Section B.4.

B.4 Lab $\leftrightarrow$ CM Transformation

For the analysis it was necessary to convert the measured Laboratory (Lab) quantities into their Center-of-Momentum (CM) frame equivalents, and

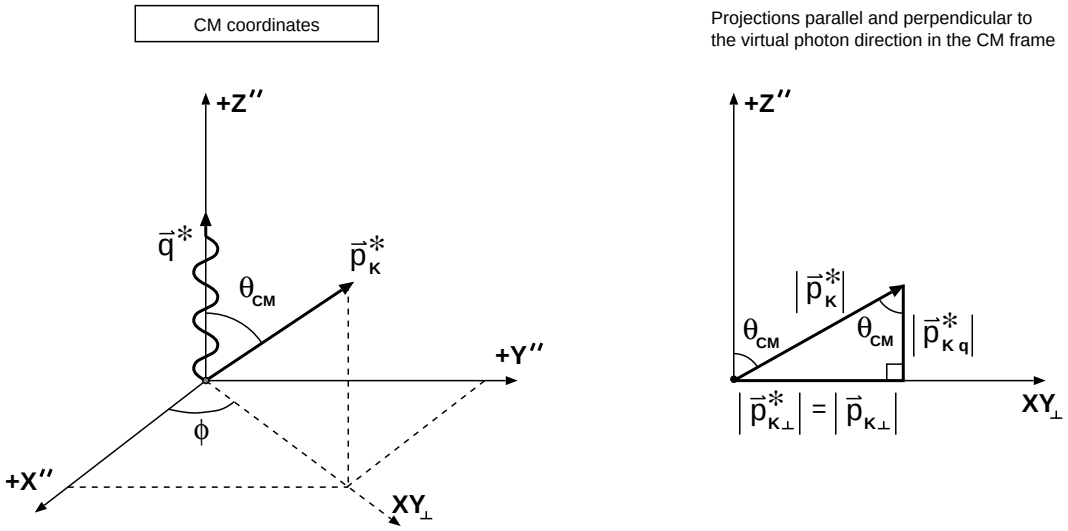

Figure B.7: Components of the kaon three-momentum in the CM frame with respect to the $\hat{\mathbf{q}}^*$ vector.

vice versa. Data were taken in the Lab frame, and results were needed in the CM frame of the (virtual photon + proton) system. For the Monte Carlo simulation, physics events were first generated in the CM frame and needed to be boosted to the Lab frame prior to being transported through the spectrometer models. After reconstruction in the Monte Carlo, these Lab quantities again needed to be transformed into their CM counterparts.

The Lorentz transforms were performed with the "z"-axis for each frame taken to be along the direction of the virtual photon ($\hat{\mathbf{q}}$ or $\hat{\mathbf{q}}^*$, as they are equivalent in this case). The CM $\rightarrow$ Lab frame transformation is discussed first, although the inverse transform is approached in a completely analogous manner.

The left half of Figure B.7 shows the coordinate system and relevant variables for the produced kaon in the CM frame. The right half of Figure B.7 shows

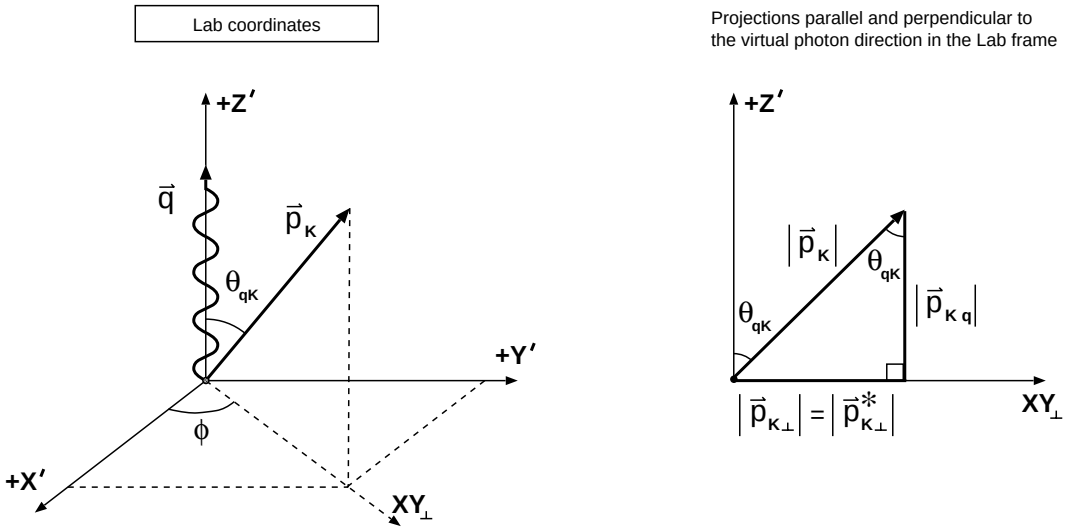

Figure B.8: Components of the kaon three-momentum in the Lab frame with respect to the $\hat{\mathbf{q}}$ vector.

the kaon three-momentum, $\mathbf{p}^*_{\mathbf{K}}$, its projection onto the z''-axis (i.e., $\widehat{\mathbf{q}}$-axis), $\mathbf{p}^*_{\mathbf{Kq}}$, and its projection onto the x''-y'' plane, $\mathbf{p}^*_{\mathbf{K}_\perp}$.

The components of the kaon momentum in the Lab frame, $\mathbf{p}_{\mathbf{K}}$, are similarly depicted in Figure B.8. Because the motion of the CM frame relative to the Lab frame is in the direction of $\widehat{\mathbf{q}}$, the components of the kaon momentum in the Lab frame can immediately be written as

$$|\mathbf{p}_{\mathbf{K}_\perp}| = |\mathbf{p}^*_{\mathbf{K}_\perp}| \tag{B.14}$$

and

$$|\mathbf{p}_{\mathbf{Kq}}| = \gamma_{cm}\,(|\mathbf{p}^*_{\mathbf{Kq}}| + \eta\,\beta_{cm}\,E^*_K) \tag{B.15d1}$$

$$|\mathbf{p}_{\mathbf{Kq}}| = \gamma_{cm}\,(|\mathbf{p}^*_{\mathbf{K}}|\cos\theta_{CM} + \eta\,\beta_{cm}\,E^*_K) \tag{B.15}$$

where β_{cm}, γ_{cm} are given by Equations B.12 and B.13, as

$$\beta_{cm} = \frac{|\mathbf{q}|}{(\nu + m_p)}\ , \tag{B.16}$$

and

$$\gamma_{cm} = \frac{1}{\sqrt{1-\beta_{cm}^2}} = \frac{(\nu + m_p)}{W} \ , \tag{B.17}$$

and $\eta = +1$ or -1, depending on whether the projection $\mathbf{p_{Kq}}$ is parallel or anti-parallel to the $\widehat{\mathbf{q}}$ vector*. The quantity η is frame independent, and can be expressed as

$$\eta = \frac{(\mathbf{p^*_{Kq}}) \cdot (\mathbf{q}^*)}{|\mathbf{p^*_{Kq}}|\,|\mathbf{q}^*|} = \frac{(\mathbf{p_{Kq}}) \cdot (\mathbf{q})}{|\mathbf{p_{Kq}}|\,|\mathbf{q}|} \ . \tag{B.18}$$

The reverse transformation,

$$|\mathbf{p^*_{Kq}}| = \gamma_{cm}\left(|\mathbf{p_K}|\cos\theta_{qK} - \eta\,\beta_{cm}\,E_K\right) \tag{B.19}$$

can be used to calculate the CM quantities from the Lab frame values. Equation B.19 can be used to obtain the kaon angle with respect to the virtual photon direction in the CM frame, θ_{CM}, via

$$\tan\theta_{CM} \equiv \tan\theta^*_{qK} = \frac{|\mathbf{p^*_{K\perp}}|}{|\mathbf{p^*_{Kq}}|} = \frac{|\mathbf{p_{K\perp}}|}{|\mathbf{p^*_{Kq}}|} = \frac{|\mathbf{p_K}|\sin\theta_{qK}}{|\mathbf{p^*_{Kq}}|} \ . \tag{B.20}$$

*In practice, $\eta = +1$ for all settings in E93-018. This is because the central momentum of the SOS was set to accept the higher momentum "forward" (parallel) kaons, and the ± 20% momentum acceptance excluded the slower "backward" (anti-parallel) kaons.

B.5 The Jefferson Lab E93-018 Collaboration

D. Abbott[1], A. Ahmidouch[2,3], Ts. A. Amatuni[4], P. Ambrozowicz[5], T. Angelescu[6], C. S. Armstrong[7], K. Assamagan[2], S. Avery[2], K. Bailey[8], O. K. Baker (Spokesman)[1,2], K. Beard[2], S. Beedoe[9], E. Beise[10], H. Blok[11], H. Breuer[10], R. Carlini[1], J. Cha[2], C. C. Chang[10], N. Chant[10], E. Cisbani[12], G. Collins[10], W. Cummings[8], S. Danagoulian[9], R. De Leo[12], F. Duncan[10], J. Dunne[1], D. Dutta[13], T. Eden[2], R. Ent[1], L. Ewell[10], L. Eyraud[14], M. Finn[7], T. Fortune[15], V. Frolov[16], S. Frullani[12], C. Furget[14], F. Garibaldi[12], D. Gaskell[17], D. Geesaman[8], P. Guèye[2], K. K. Gustafsson[10], J.-O. Hansen[8], M. Harvey[2], W. Hinton[2], E. Hungerford[18], M. Iodice[12], C. Jackson[9], C. Keppel[1,2], W. Kim[19], K. Kino[20], D. Koltenuk[15], S. Kox[14], L. Kramer[21], K. Lan[18], T. Leone[12], G. Lolos[12], A. F. Lung[10], D. Mack[1], R. Madey[2,3], M. Maeda[20], S. Majewski[3], P. Markowitz[21], C. J. Martoff[5], D. Meekins[7], A. Mihul[6], J. Mitchell[1], H. Mkrtchyan[4], R. M. Mohring[10], S. Mtingwa[9], J. Napolitano[16], G. Niculescu[2], I. Niculescu[2], R. Perrino[12], D. Potterveld[8], J. W. Price[16], B. A. Raue[21], J.-S. Real[14], J. Reinhold[8], P. Roos[10], T. Saito[20], G. Savage[2], R. Sawafta[9], R. Segel[13], S. Stepanyan[4], P. Stoler[16], V. Tadevosian[4], L. Tang[1,2], L. Teodorescu[6], T. Terasawa[20], H. Tsubota[20], G. M. Urciuoli[12], J. Volmer[11], W. Vulcan[1], P. Welch[17], R. Williams[2], S. Wood[1], C. Yan[1], B. Zeidman[8]

[1]Jefferson Lab, Newport News, VA 23606
[2]Hampton University, Hampton, VA 23668
[3]Kent State University, Kent, OH 44242
[4]Yerevan Physics Institute, Yerevan, Armenia 375306
[5]Temple University, Philadelphia, PA 19122
[6]Bucharest University, Bucharest, Romania R76900
[7]College of William and Mary, Williamsburg, VA 23187
[8]Argonne National Laboratory, Argonne, IL 60439
[9]North Carolina A & T State University, Greensboro, NC 27411
[10]University of Maryland, College Park, MD 20742
[11]Free University, Amsterdam, The Netherlands 1081
[12]INFN, Rome, Italy I-00161
[13]Northwestern University, Evanston, IL 60201
[14]ISN, Grenoble, France 38026
[15]University of Pennsylvania, Philadelphia, PA 19104
[16]Rensselaer Polytechnic Institute, Troy, NY 12180
[17]Oregon State University, Corvallis, OR 97331
[18]University of Houston, Houston, TX 77204
[19]Kyungpook National University, Taegu, Republic of Korea
[20]Tohoku University, Sendai 982, Japan
[21]Florida International University, Miami, FL 33199

BIBLIOGRAPHY

[Abb95] D. Abbott et al., Proceedings of the 1995 IEEE Conference on Real-Time Computing Applications in Nuclear, Particle, and Plasma Physics (1995), 147.

[ADW97] K. A. Assagaman, D. Dutta, and P. Welch, *Hall C Matrix Element Optimization Package*, JLab Hall C Internal Report (unpublished) (1997).

[Amb00] P. Ambrozewicz, Ph.D. thesis, Temple University, 2000, (unpublished).

[Arm95] C. S. Armstrong, *Hall C Time-of-Flight Fitting Code*, JLab Hall C Internal Report (unpublished) (1995).

[Arm99] C. S. Armstrong, Ph.D. thesis, College of William & Mary, 1999, (unpublished).

[Arr98] J. Arrington, Ph.D. thesis, California Institute of Technology, 1998, (unpublished).

[AS90] R. Adelseck and B. Saghai, Phys. Rev. C **42** (1990), no. 1, 108.

[Bak93] O. K. Baker, *Proposal for JLab Experiment E93-018*, (unpublished) (1993).

[Bak95] O. K. Baker et al., Nucl. Instr. and Meth. **A367** (1995), 92.

[Bar77] A. Baracat et al., Saclay Report DPh PE 77-10 (1977), (referred to by [Car79]).

[Bar89] R. J. Barlow, *Statistics*, John Wiley & Sons, Chichester, 1989.

[Bay82] M. Bayer, Master's thesis, Massachusetts Institute of Technology, 1982, (unpublished).

[Beb74] C. J. Bebek et al., Phys. Rev. Lett. **32** (1974), no. 1, 21.

[Beb77a] C. J. Bebek et al., Phys. Rev. D **15** (1977), no. 11, 3082.

[Beb77b] C. J. Bebek et al., Phys. Rev. D **15** (1977), no. 3, 594.

[Bod74] A. Bodek et al., Phys. Lett. **B51** (1974), 417.

[BR92] P. R. Bevington and D. K. Robinson, *Data Reduction and Error Analysis for the Physical Sciences, 2nd edition*, McGraw-Hill, New York, 1992.

[Bra79] P. Brauel et al., Z. Phys. C **3** (1979), 101.

[Bro72] C. N. Brown et al., Phys. Rev. Lett. **28** (1972), no. 16, 1086.

[Bro80] K. L. Brown et al., *Transport: A Computer Program For Designing Charged Particle Beam Transport Systems*, CERN 80-04, Super Proton Synchrotron Division, 18-Mar-1980 (1980).

[Car79] P. J. Carlson et al., Nucl. Instr. and Meth. **160** (1979), 407.

[CC75] J. Cleymans and F. E. Close, Nucl. Phys. **B85** (1975), 429.

[Cha99] J. Cha, private communication (1999).

[Clo74] F. E. Close, Nucl. Phys. **B73** (1974), 410.

[Clo79] F. E. Close, *An Introduction to Quarks and Partons*, Academic Press, London, 1979.

[Col77] P. D. B. Collins, *An Introduction to Regge Theory and High Energy Physics*, Cambridge University Press, Cambridge, 1977.

[COS91] *COSY INFINITY*, Proceedings of the 1991 Particle Accelerator Conference, also see, `http://bt.nscl.msu.edu/cosy/index.htm` .

[Cot89] S. R. Cotanch, *Quarks, Mesons and Nuclei II, Electroweak Interactions*, Spring School on Medium- and High-Energy Nuclear Physics, May 16-21, 1988, Taipei, Taiwan (W.-Y. P. Hwang and E. M. Henley, eds.), 1989, pp. 190–236.

[Cot99] S. R. Cotanch, private communication (1999).

[CWJ93] S. R. Cotanch, R. A. Williams, and C.-R. Ji, Physica Scripta **48** (1993), 217.

[DDW97] F. Duncan, J. Dunne, and S. A. Wood, *Hall C Cryogenic Target*, JLab Hall C Internal Report (unpublished) (1997).

[DFLS96] J. C. David, G. Fayard, G. H. Lamot, and B. Saghai, Phys. Rev. C **53** (1996), no. 6, 2613.

[DL72] R. C. E. Devenish and D. H. Lyth, Phys. Rev. D **5** (1972), no. 1, 47.

[Dun97a] F. Duncan, *Hall C Cryogenic Target User Manual*, JLab Hall C Internal Report (unpublished) (1997).

[Dun97b] J. Dunne, *Cryo and Dummy Target Information*, JLab Hall C Internal Report (unpublished) (1997).

[Dur96] B. M. Durham, *Jefferson Lab, A Status Report*, JLab TechNote ACC96-01 (unpublished) (1996).

[Dut95] D. Dutta et al., *Beam Energy Determination Using Kinematic Methods*, JLab Hall C Internal Report (unpublished) (1995).

[Dut99] D. Dutta, Ph.D. thesis, Northwestern University, 1999, (unpublished).

[Fel72] P. Feller et al., Nucl. Phys. **B39** (1972), 413.

[Fey72] R. P. Feynman, *Photon-Hadron Interactions*, Addison-Wesley, New York, 1972.

[GLV97a] M. Guidal, J.-M. Laget, and M. Vanderhaegen, Nucl. Phys. **A627** (1997), 645.

[GLV97b] M. Guidal, J.-M. Laget, and M. Vanderhaegen, Nucl. Phys. **B400** (1997), 6.

[GLV99] M. Guidal, J.-M. Laget, and M. Vanderhaegen, submitted to Phys. Rev. Lett. (1999), also see Los Alamos e-Print Archive, `http://xxx.lanl.gov` : hep-ph/9904511.

[Gro93] CERN Application Software Group, *PAW – Physics Analysis Workstation, The Complete Reference*, CERN Program Library Long Writeup Q121, Version 2.03 (1993).

[Gro94] CERN Application Software Group, *HBOOK – Reference Manual*, CERN Program Library Long Writeup Y250, Version 4.22 (1994).

[GS94] W. Greiner and A. Schäfer, *Quantum Chromodynamics*, Springer-Verlag, Berlin, 1994.

[GTY96] P. Guèye, M. Tiefenback, and C. Yan, *Hall C Beam Energy Measurement*, JLab Hall C Internal Report (unpublished) (1996).

[Guè96] P. Guèye, *Status of the Actual Beam Position Monitors in the Hall C Beamline*, JLab Hall C Internal Report (unpublished) (1996).

[Gus96] K. Gustafsson, *Cryotarget Density Dependence on Beam Current*, JLab Hall C Internal Report (unpublished) (1996).

[GW94] D. F. Geesaman and S. Wood, *Hall C Analysis Software Vade Mecum*, JLab Hall C Internal Report (unpublished) (1994).

[HCD] *Hall C Document Repository*, Internal ∼`cdaq/documents` directory on Jefferson Lab central computer systems.

[Hen96] S. Henning, private communication (1996), Airglass AB, Box 150, S-245 00, Staffanstorp, Sweden.

[HM84] F. Halzen and A. D. Martin, *Quarks & Leptons*, John Wiley & Sons, New York, 1984.

[HZ98] D. Haidt and P. M. Zerwas, European Phys. Journal C **3** (1998), no. 1-4, Particle Data Book.

[Inc89] Burle Technologies, Inc., *Technical Specifications for Burle 8854 Photomultiplier*, (unpublished) (1989).

[Jac75] J. D. Jackson, *Classical Electrodynamics, 2nd edition*, John Wiley & Sons, New York, 1975.

[Jam94] F. James, *MINUIT – Function Minimization and Error Analysis, Reference Manual*, CERN Program Library Long Writeup D506, Version 94.1 (1994).

[JC88] C.-R. Ji and S. R. Cotanch, Phys. Rev. C **38** (1988), no. 6, 2691.

[JC90] C.-R. Ji and S. R. Cotanch, Phys. Rev. D **41** (1990), no. 7, 2319.

[KMT59] A. Kerman, H. McManus, and R. Thaler, Ann. Phys. **8** (1959), 551.

[Kol99] D. M. Koltenuk, Ph.D. thesis, University of Pennsylvania, 1999, (unpublished).

[Lab93] A. W. Labrador et al., Proceedings of the 23rd International Cosmic Ray Conference **2** (1993), 524.

[Leg96] R. Legg, *Operating Experience at CEBAF*, JLab TechNote PR96-013 (unpublished) (1996).

[Leo94] W. R. Leo, *Techniques for Nuclear and Particle Physics Experiments, 2nd edition*, Springer-Verlag, Berlin, 1994.

[LMR73a] N. Levy, W. Majerotto, and B. J. Read, Nucl. Phys. **B55** (1973), 493.

[LMR73b] N. Levy, W. Majerotto, and B. J. Read, Nucl. Phys. **B55** (1973), 513.

[Mac97] D. J. Mack, private communication (1997).

[Mac99] D. J. Mack, private communication (1999).

[Mak94] N. C. R. Makins, Ph.D. thesis, Massachusetts Institute of Technology, 1994, (unpublished).

[Mar94] P. Markowitz et al., *Proposal for JLab Experiment E94-108*, (unpublished) (1994).

[MBHW95] T. Mart, C. Bennhold, and C. E. Hyde-Wright, Phys. Rev. C **51** (1995), no. 3, R1074.

[Mee99] D. Meekins, Ph.D. thesis, College of William & Mary, 1999, (unpublished).

[MH93] M. Mestayer and K. Hicks, *Proposal for JLab Experiment E93-030*, (unpublished) (1993).

[Mkr96] H. Mkrtchyan, private communication (1996).

[MS88] F. Mandl and G. Shaw, *Quantum Field Theory*, Wiley-Interscience, Chichester, 1988.

[MT69] L. M. Mo and Y. S. Tsai, Rev. Mod. Phys. **41** (1969), 205.

[Nac72] O. Nachtmann, Nucl. Phys. **B38** (1972), 397.

[Nac74] O. Nachtmann, Nucl. Phys. **B74** (1974), 422.

[Nap92] J. Napolitano, AIP Conference Proceedings **269** (1992), no. 1, 535.

[Nic95] G. Niculescu, *Resonant Cavities used as Beam Current Monitors*, JLab Hall C Internal Report (unpublished) (1995).

[Nic97] I. Niculescu, *Shower Counter and Čerenkov Efficiencies*, JLab Hall C Internal Report (unpublished) (1997).

[Nic98a] G. Niculescu, Ph.D. thesis, Hampton University, 1998, (unpublished).

[Nic98b] G. Niculescu et al., Phys. Rev. Lett. **81** (1998), no. 9, 1805.

[NL90] S. Nozawa and T.-S. H. Lee, Nucl. Phys. **A513** (1990), 511.

[O'N94] T. G. O'Neill, Ph.D. thesis, California Institute of Technology, 1994, (unpublished).

[Poe86] G. Poelz, Nucl. Instr. and Meth. **A248** (1986), 118.

[Ree97] C. E. Reece, *Operating Experience With Superconducting Cavities at Jefferson Lab*, Invited contribution to The Eighth Workshop on RF Superconductivity, Abano Terme, Italy (1997).

[Tan95] L. Tang et al., Nucl. Instr. and Meth. **A366** (1995), 259.

[Ter99] B. Terburg, Ph.D. thesis, University of Illinois, 1999, (unpublished).

[Tsa61] Y. S. Tsai, Phys. Rev. **122** (1961), 1898.

[VGL98] M. Vanderhaegen, M. Guidal, and J.-M. Laget, Phys. Rev. C **57** (1998), 1454.

[VW99] D. Van Westrum, Ph.D. thesis, University of Colorado, 1999, (unpublished).

[Wis97] M. Wiseman et al., *High Power Electron Beam Dumps at CEBAF*, JLab TechNote ACT-97-02 (unpublished) (1997).

[WJC90] R. Williams, C.-R. Ji, and S. R. Cotanch, Phys. Rev. D **41** (1990), no. 5, 1449.

[WJC91] R. A. Williams, C.-R. Ji, and S. R. Cotanch, Phys. Rev. C **43** (1991), no. 2, 452.

[WJC92] R. A. Williams, C.-R. Ji, and S. R. Cotanch, Phys. Rev. C **46** (1992), no. 5, 1617.

[Won90] S. S. M. Wong, *Introductory Nuclear Physics*, Prentice-Hall, New Jersey, 1990.

[Yan94] C. Yan, *User Manual of Hall C Beamline*, JLab Hall C Internal Report (unpublished) (1994).

[Zei91] B. Zeidman, *Proposal for JLab Experiment E91-016*, (unpublished) (1991).